SYNTHESIS AND BIOLOGICAL APPLICATIONS OF POROUS AND ANISOTROPIC METALLIC NANOSTRUCTURES

SOURABH SHUKLA

UNDER THE GUIDANCE OF

Dr. ARCHANA PUNDLE

BIOCHEMICAL SCIENCES DIVISION
NATIONAL CHEMICAL LABORATORY
PUNE 411 008 INDIA

AND CO-GUIDANCE OF

Dr. MURALI SASTRY

MARCH 2007

SYNTHESIS AND BIOLOGICAL APPLICATIONS OF POROUS AND ANISOTROPIC METALLIC NANOSTRUCTURES

THESIS SUBMITTED TO THE UNIVERSITY OF PUNE

FOR THE DEGREE OF

DOCTOR OF PHILOSOPHY

IN

BIOTECHNOLOGY

BY

SOURABH SHUKLA

BIOCHEMICAL SCIENCES DIVISION
NATIONAL CHEMICAL LABORATORY
PUNE 411 008
INDIA

MARCH 2007

CERTIFICATE

This is to certify that the work discussed in the thesis entitled **"SYNTHESIS AND BIOLOGICAL APPLICATIONS OF POROUS AND ANISOTROPIC METALLIC NANOSTRUCTURES"** by **SOURABH SHUKLA**, submitted for the degree of ***Doctor of Philosophy in Biotechnology*** was carried out under my supervision at the Biochemical Sciences and the Materials Chemistry Divisions of the National Chemical Laboratory, Pune, India. Such materials as have been obtained by other sources have been duly acknowledged in this thesis. To the best of my knowledge, the present work or any part thereof has not been submitted to any other University for the award of any other degree or diploma.

Date: **Dr. (Mrs.) Archana Pundle**

Place: Pune (Research Guide)

CERTIFICATE

This is to certify that the work discussed in the thesis entitled **"SYNTHESIS AND BIOLOGICAL APPLICATIONS OF POROUS AND ANISOTROPIC METALLIC NANOSTRUCTURES"** by **SOURABH SHUKLA**, submitted for the degree of ***Doctor of Philosophy in Biotechnology*** was carried out under my joint supervision at the Biochemical Sciences and the Materials Chemistry Divisions of the National Chemical Laboratory, Pune, India. Such materials as have been obtained by other sources have been duly acknowledged in this thesis. To the best of my knowledge, the present work or any part thereof has not been submitted to any other University for the award of any other degree or diploma.

Date: **Dr. Murali Sastry**

Place: Pune (Research Co-Guide)

DECLARATION

I hereby declare that the work described in this thesis entitled **"SYNTHESIS AND BIOLOGICAL APPLICATIONS OF POROUS AND ANISOTROPIC METALLIC NANOSTRUCTURES"** submitted for the degree of ***Doctor of Philosophy in Biotechnology*** has been carried out by me at the Biochemical Sciences and the Materials Chemistry Divisions of the National Chemical Laboratory, Pune, India under the joint supervision of Dr. (Mrs.) Archana Pundle and Dr. Murali Sastry. Such materials as have been obtained by other sources have been duly acknowledged in this thesis. The work is original and has not been submitted in part or full by me for award of any other degree or diploma in any other University.

Date: **Sourabh Shukla**

Place: Pune (Research Student)

Acknowledgement

The work presented in this thesis has been made possible by the association of many people and I would like to take this opportunity to acknowledge their contributions.

First and foremost among them is my research advisor and co-guide Dr. Murali Sastry whose guidance and motivation has been inspirational in making this thesis possible. His constant support and openness to new ideas has helped a great deal in designing new experiments during the course of my thesis. His tireless enthusiasm and in-depth knowledge has been invaluable in making this thesis possible. He has provided us with excellent exposure to the field by encouraging and facilitating participation in national as well as international conferences, for which I would like to extend my gratitude towards him. I cherish my fruitful association with him that has introduced me to the exciting field of nanotechnology and has opened several new avenues for me.

I would also like to thank my research guide Dr. A. Pundle for her constant support, guidance and encouragement throughout my stay at the National Chemical Laboratory. Her suggestions regarding my work have been crucial in the completion of this thesis. I would like to thank her for all the help that she has provided, often going out of her way.

I would also like to thank Dr. S. Sivram, Director, NCL and Dr. Sourav Pal, HOD, Physical Chemistry Division, for allowing me to carry out research at this institute and providing with the required facilities. I am thankful to CSIR, Govt. of India, for the research fellowship.

My sincere thank goes to Dr. B. L. V. Prasad for his support encouragement and cooperation. His suggestions pertaining to the work have been of great help. I would like to thank him for his affectionate advices and friendly interactions.

My thesis has involved a lot of collaborative work both in NCL and outside of it. I am thankful to Dr. K. N. Ganesh and Mr. A. Gaurishankar from the OCS division for the ITC related work. At the same time, I am extremely thankful to Dr. R. R. Bhonde and Dr. Meenal Banerjee from the National Center of Cell Sciences, Pune for their significant help in the cell imaging part of the thesis. I would also like to acknowledge Dr. P. V. Satyam and Mr. Ghatak from IOP, Bhubaneshwar for their assistance with the HRTEM analysis. My sincere thanks goes to Dr. M. I. Khan for allowing me to use the fluorescence spectrophotometer in his lab. I would like to extend my sincere thanks to Mrs. Renu Pasricha for training me in TEM operations.

I would also like to thank Dr. Satish Ogale, Dr. Asmita Prabhune, Dr. Absar Ahmad and Dr. Pankaj Poddar for their valuable suggestions and useful inputs during the course of the thesis. I would like to extend my thanks to Mrs. Suguna Adhayanthaya for helping with the day-to-day laboratory issues and her elderly suggestions. I also thank Prof. S.P. Gejji from the Chemistry department, University of Pune for being the member of the work evaluation committee.

I would like to thank my former and current lab-mates for their support in the work and encouragement during the thesis. I extend my thanks to Dr. Ashvini, Dr. Debabrata, Dr. Sumant, Dr. Anita, Dr. Saikat, Dr. Kannan, Dr. Shankar, Dr. Senthil, Hrushi, Ambrish, Akhilesh, Amit, Tanushree, Atul, Vipul, Mrs. Pasricha, Ritwik, Manasi, Deepti, Prathap, Sanjay, Minakshi, Maggie, Imran, Priyanka, Anil, Sheetal, Dr.Vijay, Umesh, Ramya, and Boisakhi. I had a good time with all of them in the lab and outside of it. I have really enjoyed their company in the lab and at the cricket ground and badminton courts, lunches and dinners, movies and trips. I would like to acknowledge Maggie and Manasi once more for helping me with the thesis corrections.

Besides, I would also like to acknowledge Dr. Ankamwar, Dr. Bapu, Mrs. Usha Raghvan, Annie, Ganesh, Ram, Avinash, Mugdha, Gauri and many other project students who have been part of the nanoscience group for their support. I would like to mention Annie's name in particular for the dedicated efforts she put in the transmetallation and DNA work as a project student.

I would like to thanks Mr. Deepak, Mr. Punekar and Mr. Pardesi from the Physical Chemical Division office for helping me extensively with the routine official and administrative work. I would also like to thank NCL Library staff, administrative staff, and technical staff at CMC for their assistance in the administrative issues during this time.

This thesis would not have been possible without the strong faith, support and encouragement of my family. I wish to express my deep sense of gratitude to my father for being supportive and for his trust, patience, affection and blessings, I could not have done this without him being there all the time. I would also like to thank my sister, my brother, sister-in-law and brother in-law for all their affection and love and would like to express my thanks to my in-laws for their blessings and encouragement. At the end, I want to thank my friend, collaborator and wife Meenal for being there all these years with her love, trust, support and understanding. I am indeed lucky to have her as a life partner.

…Sourabh Shukla

Table of Contents

Chapter I: Introduction

1.1.	Introduction to Nanotechnology	2
1.2.	Historical perspective	3
1.3.	Properties of nanoparticles and applications thereof	3
1.4.	Synthesis of nanoparticles	8
1.5.	Synthesis of anisotropic nanoparticles	11
1.6.	Nanoparticle assemblies: Route to higher order architectures	12
1.7.	DNA: The '***generic***' material of nanotechnology	17
1.8.	Bimetallic porous / hollow shell nanoparticles: synthesis and applications	22
1.9.	Outline of the thesis	27
1.10.	References	30

Chapter II: Characterization techniques

2.1	Introduction	54
2.2	Uv-vis-NIR spectroscopy	54
2.3	Fluorescence spectroscopy	56
2.4	X-ray photoelectron spectroscopy (XPS)	57
2.5	Phase contrast microscopy	59
2.6	Fluorescence microscopy	61
2.7	Confocal laser scanning microscopy (CFLSM)	62
2.8	Transmission electron microscopy (TEM)	63
2.9	Scanning probe microscopy (SPM)	65
2.10	Energy dispersive X-ray analysis (EDX)	67
2.11	Isothermal titration calorimetry (ITC)	68
2.12	Fluorescence activated cell sorting (FACS)	70
2.13	References	72

Chapter III: Sequence dependent DNA metallization:
An isothermal titration calorimetric approach

3.1 Introduction 74
3.2 Isothermal titration calorimetric (ITC) measurements 77
3.3 UV-vis spectroscopy and TEM analysis 84
3.4 Sequence dependent DNA metallization 91
3.5 Discussion 95
3.6 Conclusions 96
3.7 References 97

Chapter IV: Synthesis of porous metal nanostructures

4.1 Introduction 102
4.2 Synthesis of porous nanospheres of gold, platinum and palladium 107
4.3 Synthesis of anisotropic porous nanostructures 131
4.4 Discussion 143
4.5 Conclusions 145
4.6 References 147

Chapter V: Biological applications of porous nanoparticles

5.1 Introduction 153
5.2 Porous gold nanoparticles for cell imaging applications 157
5.3 Porous gold nanoparticles for enzyme immobilization 168
5.4 Cytotoxicity of porous gold nanoparticles 173
5.5 Discussion 178
5.6 Conclusions 181
5.7 References 183

Chapter VI: Conclusions

6.1 Summary of the work 193
6.2 Scope for future work 195

List of Publications

Chapter 1

Introduction

This chapter is an introduction to the thesis and gives a brief overview of nanotechnology. The chapter discusses the unique properties of nanoparticles, their applications and methods of preparation and focuses on the parameters that could alter nanoparticle properties. Further, nanoparticle assemblies have been discussed in detail with particular emphasis on the importance of DNA based assemblies. This chapter also discusses bimetallic nanostructures, their properties and synthesis protocols along with their numerous technological applications. Towards the end, the chapter summarizes the outline of the thesis, division of chapters and its salient features.

1.1 Introduction to Nanotechnology

Nanotechnology is the science of manipulating objects at nanoscale lengths. The term 'nano' is Greek for 'dwarf' and nanometer refers to the billionth part of a meter. To put this in perspective, a single human hair measures 75,000 nm across and 10 hydrogen atoms lined together would make up 1 nm.

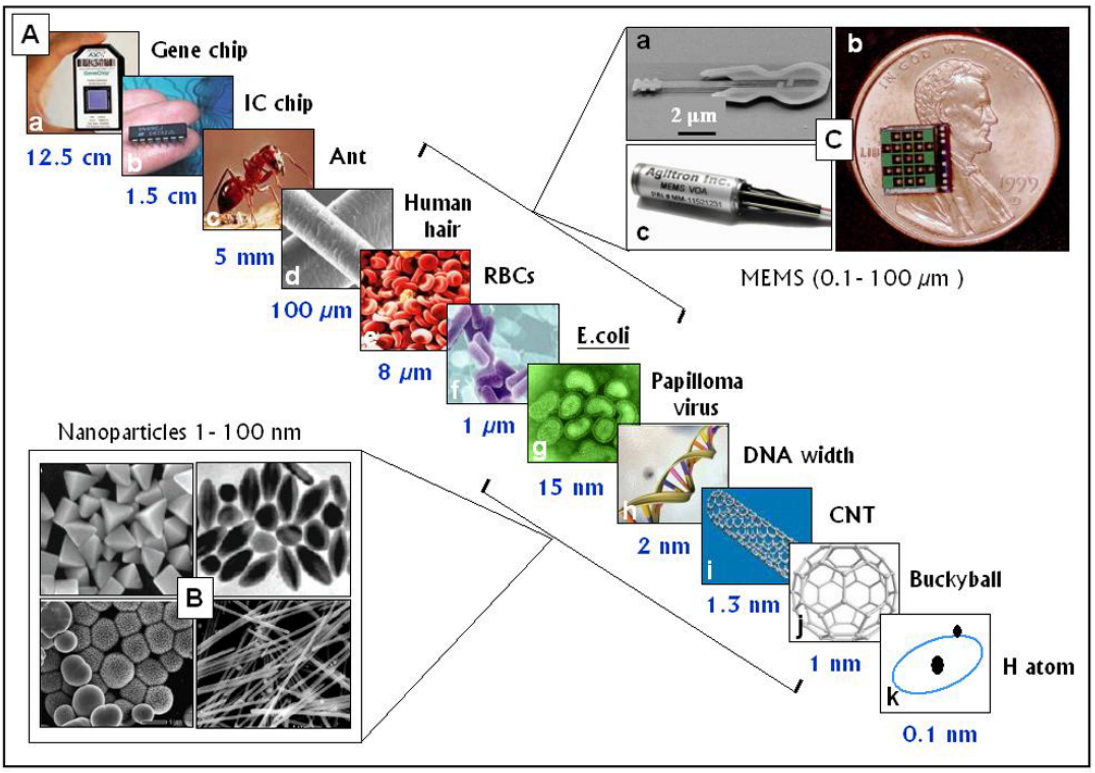

Figure 1.1 *"The nanoscale": size comparison of nanoparticles with other 'small' entities. (Images courtesy: A (a-k): various sources at http://images.google.com; B: Wiley, B. et al., Chem. Eur. J.* ***2005****, 11, 454; C-a, b: www.news.cornell.edu/science.html; C-c: www.agiltron.com).*

However, Nanotechnology is not merely creating and observing 'dwarf' objects, the working definition of nanotechnology as described by the National Nanotechnology Initiative of US, encompasses the following:

1. Nanotechnology involves research and technology developments at 1 -100 nm ranges.
2. Nanotechnology creates and uses objects that have unique properties because of their small size.
3. Nanotechnology builds on the ability to control or manipulate at atomic scales.

Figure 1.1 compares the size of nanoparticles with those of other 'small' objects, both artificial and natural, that we are familiar with. These comparisons give a glimpse of the scales that one needs to manipulate when working with nanoparticles.

It's the plethora of exotic properties offered by the smaller forms of materials that is the motivating force behind the miniaturization overdrive. These novel properties have not only generated new technology but also have given a totally new dimension to existing technologies.

1.2 Historical perspective

Applications of nanotechnology preceded the current understanding by many centuries. Be it the colored windows of the chapels and palaces [1] or the decorative Lycurgus cup of fourth century AD [2], the healing sols of gold and silver in the traditional medicines [3] or the Damascus Saber [4] used against the crusaders, people realized that a certain form of material could generate exceptional colors, healing power and strength, much more than anything they had known till then. Mayan civilization witnessed the use of nanoparticles in wall paintings, colors that would last for centuries [1].

It was only with Faraday's pioneering work on systematic synthesis of gold sols in the year 1857 [5], that nanotechnology as a discipline started to swell, and in the next three decades, engrossed people from pure sciences, engineering and medicine alike, into the exciting world of nanotechnology. Significant contributions also came from researchers such as Thomas Graham [6] and Norio Taniguchi [7] who coined the terms 'colloids' and 'nanotechnology', respectively. More recently, Richard Feynaman's plenary talk titled, 'There's plenty of room at the bottom', discussed the potential advances nanotechnology could bring about and is considered to be the foundation for modern nanoscience research [8]. The progress has been made possible by the emergence of tools and technologies that have made visualization and manipulation of nanoparticles possible.

1.3 Properties of nanomaterials and applications thereof

As mentioned above, the surge in nanotechnology research over the last few decades was fueled by the set of interesting properties shown by the nanomaterials.

These novel properties have thrown open avenues for new technologies and applications that were not achievable with bulk materials.

The transformations in the properties of materials, as one reduces the size from bulk to nano domain, are the manifestation of changes in the electronic state of the matter. As the size of the materials approaches atomic dimensions, energy level bands are slowly transformed into quantised discrete energy levels. Since the changes in the electronic structure occur in the nanometer region, it gives an insight as to how the properties evolve from the molecular or atomic level to the bulk. Also the reduction in size would confine the electronic motion, which is therefore evident in terms of unique physical and chemical properties of the material [9].

Although, the changes in the properties with the reduction in size holds true for all materials, this thesis is focused on the studies of such phenomena in the metal nanoparticles and emphasize on the properties, synthesis and application of the metal nanostructures.

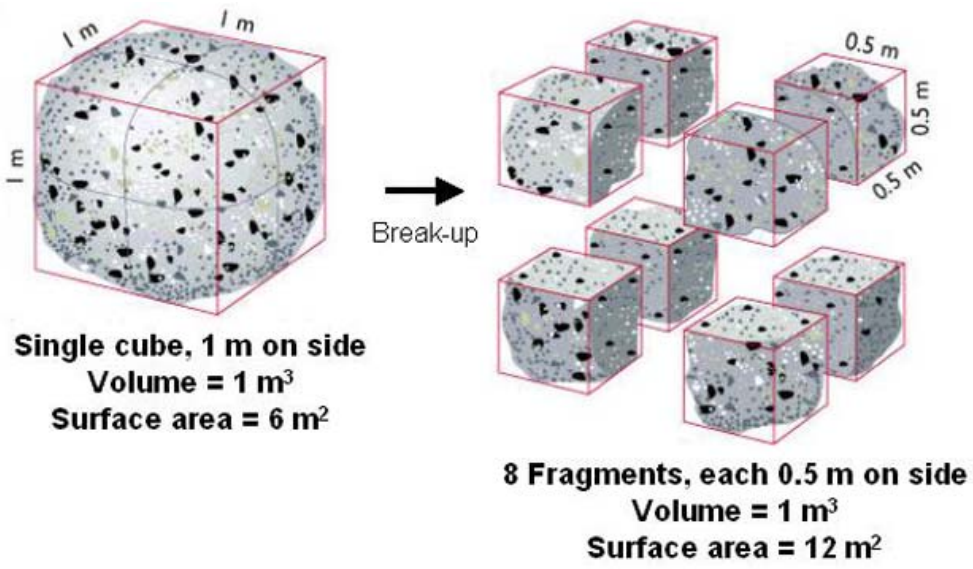

Figure 1.2 *Schematic representation of increasing surface area with reducing size. (Image courtesy: http://piru.alexandria.ucsb.edu/collections/geography3b/p-s/ps06-05a.jpg).*

The most apparent change resulting from the size reduction is the enormous increase in the surface-to-volume ratio of metal nanoparticles as depicted in Figure 1.2. What it means in atomic terms is that the percentage of the surface atoms increases and so does the surface energy, making the nanoparticles surface highly

active. For instance, iron nanoparticles of sizes 3 nm, 10 nm and 30 nm will have 50 %, 10 % and 5 % of atoms on the surface, respectively [9]. Thus, it is evident that the properties obtained at the nanoscale could vary with the changes in the particles size. Interestingly, size is only one of the parameters that govern the properties of nanoparticles, others being shape, composition, dielectric properties of the particles and surrounding medium and interparticle interactions. Such remarkable variations exist because of the comparable dimensions of nanoparticles to the de Broglie wavelength of the charge carriers and their high surface to volume ratio [10]. Varying one or all of these parameters provides tunability of the nanoparticle properties and has generated extensive research interest.

One of the most interesting aspects of metal nanoparticles is their optical property. The optical properties of metal nanoparticles can be attributed to the phenomenon of surface plasmon resonance (SPR) i.e., the coherent charge density oscillations [11]. The electric field of the incoming radiation induces the formation of a dipole in the nanoparticle, and there is a restoring force due to the positive polarization charge that tries to compensate it, so that a unique resonance frequency matches this electron oscillation within the nanoparticle (Figure1.3, A). The surface plasmons are characterized by strong field enhancement at the interface, while the electric field vector decays exponentially away from the surface (in the nm range) [12a, b]. When the dimensions of the conductor are reduced, boundary and surface effects become very important, and for this reason, the optical properties of small metal nanoparticles are dominated by such a collective oscillation of conduction electrons in resonance with incident electromagnetic radiation [12c]. The plasmon frequency for metals such as Pb, Hg, In and Cd lies in the UV region and therefore does not show color effects. However, for coinage metals Au, Ag and Cu, which form air stable colloids, the d-d band transitions push the plasmon frequency into the visible part of the spectrum, giving them their characteristic colors.

Plasmon resonance of nanoparticles being a surface phenomenon is affected by any change in the electron density of the surface layer and surrounding medium [12d]. Other factors that influence the surface plasmon are the particle size, shape and composition. For non-spherical particles, such as rods, the resonance wavelength

depends on the orientation of the electric field relative to the particle, and thus, oscillations either along (longitudinal) or across (transversal) the rod are possible [13a] (Figure 1.3, B). Because of the dimensionality of anisotropic shapes, the frequencies associated with the various resonance modes can be quite different, and thus the optical properties can be largely affected.

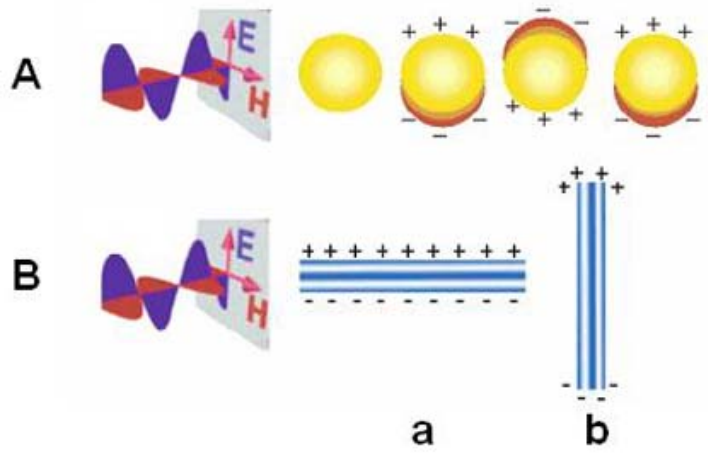

Figure 1.3 *Plasmon oscillation in spherical nanoparticles (A); transversal (B-a) and longitudinal (B-b) oscillation of electrons in metal nanorods. (Figure courtesy: 13a).*

The transverse plasmon band shows a linear relation with the aspect ratio (ratio of length to width) and the dielectric constant of the medium [12d, 13b]. With an increase in the aspect ratio, the energy separation between the two plasmon bands also increases [13c]. In certain cases, another peak in between the two plasmon peaks has also been reported, which has been attributed to the in-plane quadrupole mode of plasmon resonance [14]. Since these resonances arise from the particular dielectric properties of the metals, they can be easily modeled using the equations derived by Mie for the resolution of Maxwell equations for the absorption and scattering of electromagnetic radiation by small spheres [15a] and their modification by Gans for ellipsoids [15b]. The theoretical aspects pertaining to optical properties of metal nanoparticles have been further studied in many reviews [15c-f]. Mie theory describes the light absorption characteristic of spherical metal nanoparticles [15a], which shows that in the size range 3 to 10 nm, the absorption does not depend strongly on the size of the particle. This is due to the fact that the higher order terms in the Mie formula become insignificant in this size range. Thus, only the dipole term becomes relevant, which depends only on the total metal concentration and not the size of the particles.

The absorption spectrum of particles in a given solvent can be calculated from the optical constants of the bulk metal [15f]. The absorption coefficient, α ($mol^{-1}Lcm^{-1}$) can be calculated according to the relation

$$\alpha = \frac{18\pi}{\ln 10} \frac{10^5}{\lambda} \frac{Mn_0^3}{\rho} \frac{\varepsilon_2}{(\varepsilon_1 + 2n_0^2) + \varepsilon_2^2} \quad \ldots\ldots\ldots (1.1)$$

where λ is the wavelength of light, M and ρ are the molecular weight and density of the metal, n_o is the refractive index of the solvent and ε_1 and ε_2 are the real and imaginary parts of the dielectric constant of the metal. For particles smaller than the mean free path of the electrons, the absorption profile is explained using corrected values of ε_2 [15f]

$$\varepsilon_2 = \varepsilon_{2(bulk)} + \left(\omega_p^2 / \omega^3\right) (V_F / R) \quad \ldots\ldots\ldots (1.2)$$

where ω is the frequency of light, ω_p the plasmon frequency, V_F the electron velocity at the Fermi level and R the particle radius (R/V_F, mean time of the free movement of the electrons). The plasmon frequency can be expressed as following

$$\omega_P = \frac{Ne^2}{m\varepsilon_0} \quad \ldots\ldots\ldots (1.3)$$

where N is the concentration of free electrons in the metal, e is charge on one electron and m is the effective mass of an electron [15c]. In order to satisfy the resonance condition with the incident light, ε_1 should be twice the negative value of dielectric constant of the medium,

$$\varepsilon_1 = -2\varepsilon_m \quad \ldots\ldots\ldots (1.4)$$

The strong correlation of the optical properties with the size, shape, and composition of the nanoparticles is well established and in fact, plasmon absorption bands are used as optical signatures for nanoparticles of different morphology and composition [16].

The increased surface area also renders metal nanoparticles such as gold (which, in bulk form, is an inert metal), platinum and palladium highly catalytic [17]. The unique surface, electronic structure, high surface area and lower work function

make nanoparticles attractive candidates for homogenous catalysis in solution or heterogeneous catalysis on a solid support. Dependence of catalytic efficiency on the nanoparticle shape has also been reported and is attributed to the preferential adsorption of the reactants to certain faces of the nano-crystals [18]. Similarly, composition of the nanoparticles also affects the catalytic efficiency and many processes have been improved using bimetallic nanoparticles [19].

Likewise, other properties such as magnetism [20], electronic properties [21] and melting point [22] of the nanomaterials are characteristic of their morphology, composition, interparticle interaction and surrounding medium and have been studied in great details [23].

Owing to these unique and interesting properties, there has been an ever-growing interest in developing applications of the nanoparticles. It was the applications of nanoparticles without much understanding of their chemical and physical behavior that lead to the vast areas of nanotechnology research, after which, it has been a synergistic relationship between understanding new properties and developing new applications, one driving the other. Today, nanotechnology has been used in not just developing new techniques and tools, it has played crucial role in improving existing technologies. There is a huge literature on the application of nanoparticles in sensors [24], catalysis [25], diagnostic tools [26], therapeutic agents [27], drug/gene delivery vehicles [28], solar cells [29], plasmonics devices [30], cosmetics [31], coatings [32] cell imaging [33], fuel cells [34], photonic band gap materials [35], single electron transistors [36], nonlinear-optical devices [37] and surface enhanced Raman spectroscopy [38].

1.4 Synthesis of nanoparticles

As discussed above, properties of the nanoparticles are a manifestation of their shape, size and composition. Therefore, not surprisingly, synthesis of nanoparticles with control over these parameters has been and will remain, the most challenging aspect of nanotechnology research. Even though, numerous methods have been developed for the synthesis of nanoparticles, they follow either of the two principles: ‘top-down’ approach or a ‘bottom-up’ approach. As apparent from the term, ‘top-down approach’ refers to breaking down materials to sub-micron sizes and was used

by mankind to make their earliest tools and materials. Although perfected over time, top-down approach is often limited by the precision one can achieve while working at the nanoscale. A typical example of the top-down approach is the generation of patterned surfaces on SiO_2 surfaces by electron beam lithography [39] (Figure 1.4, A

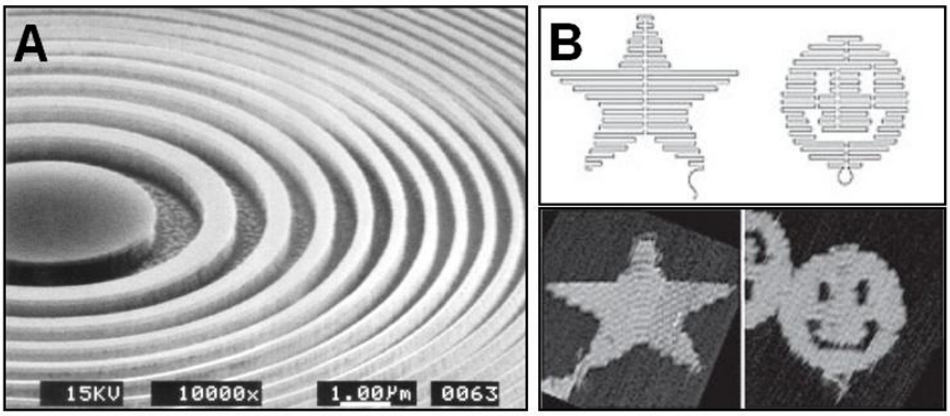

Figure 1.4 *The 'top-down' and 'bottom-up' approach of materials synthesis. 'A' illustrates the pattern etched on silicon substrate by electron beam lithography, a typical 'top-down' approach. 'B' corresponds to star and smiley fabricated by assembling short DNA molecules (Images curtsey: A- www.iu-bremen.de*; *B-Rothemund, P. Nature,* ***2006****, 440, 297).*

A), which literally etches away the surface, much like chiseling of stones by a sculptor. The 'bottom-up' approach on the other hand, works by assimilating smaller units to fabricate larger structures such as the DNA origami developed by Rothmund [40] (Figure 1.4, B) by assembling short complementary DNA strands. Bottom-up approach is able to impart excellent precision over the shape and size of the nano-architectures.

Synthesis protocols can be broadly divided into physical, chemical and biological routes. Different methods that comprise these routes have been surmised in scheme 1.1. Physical methods for the synthesis of inorganic nanoparticles includes vapor deposition [41], thermal decomposition [42], spray pyrolysis [43], photoirradiation [44], laser ablation [45], ultrasonication [46], radiolysis [47] and solvated metal atom dispersion [48].

Chemical methods offer much more control over the synthesis procedures and therefore have been widely accepted as most efficient methods. Some of the common chemical routes include sol-gel method [49], solvothermal synthesis [50], micelles based synthesis [51] and galvanic replacement reaction [52].

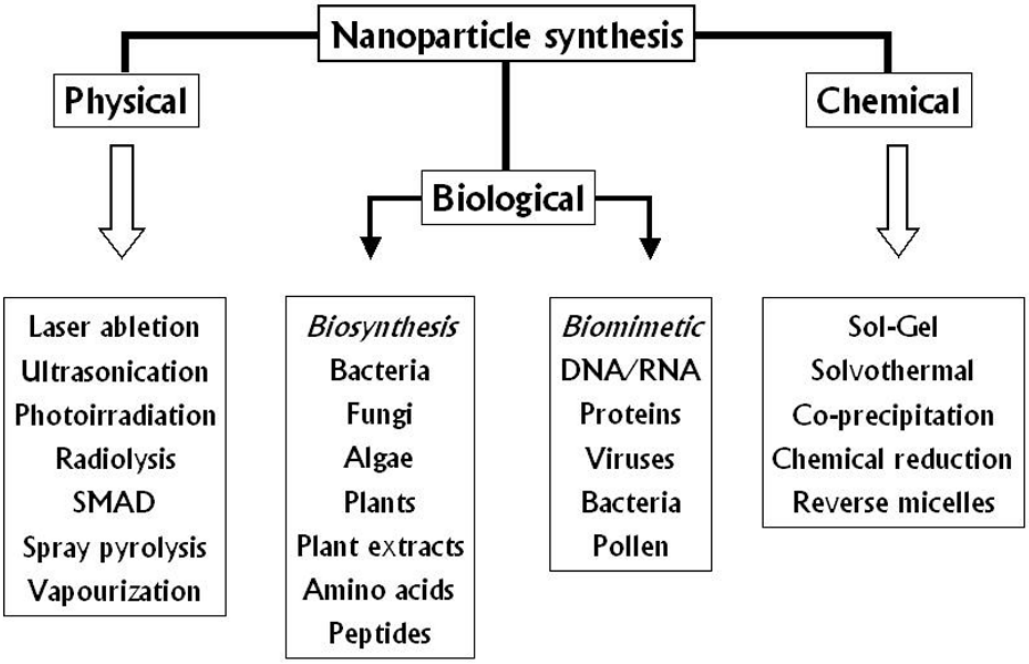

Scheme 1.1 *Schematic outlining the various approaches for the synthesis of nanoparticles.*

Chemical reduction has been the most popular route towards synthesis of metal nanostructures due to easy protocols and the exquisite shape and size control provided by this method. The control of size, shape, stability and the assembly of nanoparticles have been achieved by using different capping agents, solvents and templates. Various types of capping agents have been used ranging from ions [53] to polymeric molecules [54] and even biomolecules [55]. Although water has been used primarily for synthesis protocols, several reports on use of organic solvents [56], ionic liquids [57] and super critical fluids [58] are also available. Similarly, different templates such as micelles [59], polymers [60], mesoporous materials [61], carbon nanotubes (CNTs) [62], biomolecules [63] and microorganisms [64] have been used for the synthesis of nanoparticles on the surface or in confined spaces.

Despite the advantages associated with the chemical procedures, concern over the use of toxic chemicals and solvents along with the high cost factor involved in maintaining temperatures and pressures have forced materials scientists to take the biological and biomimetic routes for nanomaterials synthesis. The abundance of biologically synthesized functional nanomaterials throughout the natural world has been the inspiration to create nanomaterials under ambient conditions of temperature,

pressure and pH [65-68]. Therefore, growing number of reports of biologically synthesized nanomaterials using bacteria [69], fungi [70], yeast [71] and plant extracts [72] are appearing in the literature. Similarly, biomimetic approaches involving protein-mediated synthesis of various inorganic nanocrystals have been reported including peptides such as silaffins [73] and silicateins [74] along with some other peptides like frustulins [75] and pleuralins [76]. Besides proteins, other macromolecules such as nucleic acids (both DNA and RNA) and even viruses have been used as templates for inorganic nanoparticles synthesis.

1.5 Synthesis of anisotropic nanoparticles

As the synthesis protocols have evolved over the years, a high degree of control over the nanoparticles morphology has been achieved. There are a number of examples of physical [78], chemical [79] as well as biological routes [72f, g] where well-established protocols exist for the synthesis of specific anisotropic nanoparticles. Controlling size, shape, and structural architecture of the nanocrystals requires manipulation of the kinetic and thermodynamic parameters of the systems via utilization of various additives, light and thermal energies, and their various combinations [80].

Thus, nanoparticles of many anisotropic shapes such as nanorod/nanowires [81], nanotubes [82], nanodumbbells [83], nanocubes [84], nanohexagons [85], tetrahedrals [86], decahedrons [87], multipods [88], star-shaped [89], nanodiscs [90], nanotriangles [91], dendritic-shaped [92], etc. have been synthesized. Various strategies have been applied for the controlled synthesis of anisotropic shape metal nanoparticles. The usual methods include: 1) synthesis in micellar/surfactant solutions, 2) synthesis using soft and rigid templates, 2) controlling the growth of the nanoparticles using physical confinements 3) physical processes such as nanosphere lithography, vacuum vapor deposition, 4) direct synthesis in solution in presence or absence of additives and 5) morphological transformations of the preformed nanoparticles by thermal, photoirradiation or ion irradiation process. Besides, Sastry and co-workers have also demonstrated that plant extracts could also be used to impart shape anisotropy leading to extremely thin and atomically flat gold

nanotriangles while Murphy and co-workers have established seedless and surfactant less protocols for gold nanowires synthesis [93].

1.6 Nanoparticle assemblies: route to higher order architectures

Nanoparticles exhibit size and shape dependent optical and electronic properties and as discussed previously, there are well-established protocols for synthesis of nanoparticles with discrete morphology. However, another factor governing nanoparticle properties and to a great extent, their functionality, is their assembly. The physical properties of nanoparticles can be strongly influenced by surrounding nanoparticles, some new properties often emerge from the aggregates that are distinctly different from those of the corresponding isolated nanoparticles. For example, when clusters of metal nanoparticles are placed in close proximity to one another, the electrostatic coupling between particles becomes very important [12, 13]. Neighboring nanoparticles can affect the resonance frequency in a distance-dependent manner, allowing electromagnetic energy to propagate along linear arrays. The controlled organization of metallic nanoparticles into one-dimensional, two-dimensional, or three-dimensional arrays offers a promising route to tailor the flux of surface plasmon [12e].

Study of nanoparticle assemblies is also of interest as it provides insight into the laws governing nanoparticle behavior under different conditions. The most common methods employed for such ordered ensembles of metal and semiconductor nanoparticles are solvent evaporation, molecular cross-linking and template patterning. Some of these modes of nanoparticle assemblies have been discussed below.

1.6.1 Spontaneous organization by solvent evaporation

Several groups have demonstrated the formation of spontaneous ordered arrays of nanoparticles on solid substrates by solvent evaporation [94]. The success of the method depends on various parameters such as nanoparticle concentration, rate of solvent evaporation, narrow size distribution, ionic strength and surfactant concentration. The relatively weak attractions between nanocrystals, which are efficiently screened in solution, become manifest as the solvent evaporates, initiating

assembly of intricate, slowly evolving structures [95].

Moreover, the capping material stabilizing the nanoparticles also determines the interparticle distances of such self-assembled structures [96]. Greater chemical control over the interparticle separation between the has been achieved by using bifunctional ligands [97], which are bound to the surface of the nanoparticles and can bind to a neighbouring particle during the assembly process via the second functional group. There are several examples in the literature for the evaporation induced 2D and 3D assembly of alkanethiol/alkylamine capped gold and silver nanoparticles [98]. Kiely *et al.,* have shown that it is possible to produce ordered arrays of nanoparticles even from bimodal distribution of sizes of the same metal [99] and also of different metals [100].

1.6.2 Nanoparticle assemblies through electrostatic interactions

Using electrostatic interactions, Iler showed that oppositely charged silica and alumina particles could be electrostatically self-assembled in multilayer structures by alternatively immersing the substrate in the two colloidal solutions [101]. Decher and co-workers have demonstrated an alternate layer-by-layer deposition of oppositely charged polyelectrolytes and nanoparticles [102]. The electrostatically driven layer-by-layer assembly has been extensively used to realize polyelectrolye/inorganic nanoparticle sandwich structures with nano-magnetite [103], TiO_2/CdS [104], SiO_2, TiO_2 and CeO_2 [105], CdSe [106] and Au [107] as well as alternating layers of positively charged gold and negatively charged silver particles [108]. Sastry and co-workers have shown that amino acid capped gold nanoparticles can be electrostatically assembled in a layer-by-layer fashion by suitably changing the pH [109]. On the other hand, Murphy and co-workers have demonstrated assembly of gold nanorods on glass substrates using electrostatic interactions via charged polymers [110].

1.6.3 Dielectrophorectic deposition

Dielectrophoretic assembly technique also offers a convenient and rapid method for organizing nanoparticles in macro-dimensions. In the process, the particle mobility and interactions are imparted by an alternating electrical field applied

through two metal electrodes (usually indium tin oxide electrode) immersed in a small glass cell containing colloidal solution. The charged nanoparticles migrate under the influence of electric field and get deposited on the electrode. The use of external fields offers a combination of speed, easy control, and precision, which may not be readily available through the inherent particle-particle colloidal interactions. Electric fields have been used in the assembly of complex particles [111], colloidal crystals [112], biosensors [113] and linear particle aggregates [114].

1.6.4 Self-assembled monolayers (SAMs)

Although 3-dimensional (3-D) systems are structurally and electrically well characterized, with respect to future applications the nanoparticles have to be organized in 2 (2-D) and 1-dimension (1-D). Here, one needs to take into account that not only the control over the deposition rate and density, but also the degree of order or disorder, respectively, which is vital for any kind of further technological developments. Self-assembled monolayers (SAMs), therefore, are interesting for generation of 2-D assemblies. SAMs can be prepared using different types of molecules and different substrates. Widespread examples are alkylsiloxane monolayers, fatty acids on oxidic materials and alkanethiolate monolayers.

Indeed, SAM formation provides one easy route towards surface functionalisation by organic molecules (both aliphatic and aromatic) containing suitable functional groups like –SH, –CN, –COOH, $–NH_2$ and silanes on selected metallic (Au, Cu, Ag, Pd, Pt, Hg and Co) as well as semiconducting surfaces (Si, GaAs, indium coated tin oxide etc.)[115]. Due to the highly ordered nature and tight packing, these monolayers on metallic surfaces are also important for several practical applications such as chemical sensing [116], control of surface properties like wettability and friction [117], corrosion protection [118], patterning [119], semiconductor passivation [120], and optical second harmonic generation [121]. SAM formation provides one of the easiest ways to obtain ordered monolayers through strong chemisorption between the substrate head group of a desired compound and the metal surface leading to the preparation of thermodynamically stable monolayers [122] as compared to the Langmuir–Blodgett (LB) and other techniques, where only physisorbed, thermally unstable mono/multilayer films are obtained.

1.6.5 Assembly of nanoparticles at the air water interface

As a tool for two-dimensional organization of nanoparticles LB technique has been an area of extensive research. The LB technique consists the formation of monomolecular layers of amphiphilic molecules at the air-water interface and their subsequent transfer onto solid substrates. These films have been used as templating organic structures for the synthesis of several nanostructures by exploiting their highly ordered lamellar structure to provide nanocrystals formation in a confined reaction geometry [123]. Nanoparticles of metals such as silver and gold [124], semiconductor quantum dots such as CdS and CdTe [125], oxides such as SiO_2, TiO_2, Fe_3O_4 and γ-Fe_2O_3 [126] have been assembled from solution at the air-water interface using electrostatic interactions.

1.6.6 Nanolithography

Nanolithgraphy has emerged as an indispensable tool for modern nanotechnology research. It refers to the ability to define patterns on surfaces at small length scales and is central to the research fields such as microelectronics, nano-electromechanical (NEMS) systems and biomedical applications.

A large number of variants of the nanolithography techniques have been developed such as extreme unltraviolet lithography [127], electron beam lithography (EBL) [128], focused ion beam lithography [129], dip-pen nanolithography [130] and microcontact printing [131]. Song *et al.,* have fabricated nanoparticle gradient assemblies using contact printing based approach [132]. Such assemblies are excellent combinatorial tools for quick determination of adsorption and/or interaction selectivity for nanoparticles. In addition, spacing between the density gradient particles can also be varied, thus the assemblies can be applied as filters for selecting molecules (i.e. DNA or enzyme) or particles for a given size. Furthermore, micro or meso-scaled nanoparticle gradient assemblies, due to their steep gradients, open new opportunities that have not been explored for designing nanodevices and nanosystems as well as discovering new phenomena and properties associated with the size and spatial organization of the materials or assemblies. Other direct writing techniques such as robocasting, ink jet printing, hot-melt printing and micro-pen writing have

been developed that involve assembly via a layer-by-layer deposition of particle based inks [133].

1.6.7 Templated assemblies of nanoparticles

A variety of templates, synthetic as well as natural, have been used for directed assemblies of nanoparticles in one and two dimensions with well-defined geometries, spacing and properties as depicted in Figure 1.5. Polymer beads/membranes [134], block co-polymers [135], carbon nanotubes [136], synthetic peptides [137] and several organic molecules [138] have been used for nanoparticles assembly. Similarly, large-scale assemblies of nanoparticles have also been achieved on nanotrench templates formed on the surfaces [139]. Several polyelectrolytes such as poly (diallyldimethylammonium) (PDDA), poly (allylamine hydrochloride) (PAH), polyaniline and poly- (Phenylene-pyridyl) dendrimers [140] have been used to assemble metal nanostructures.

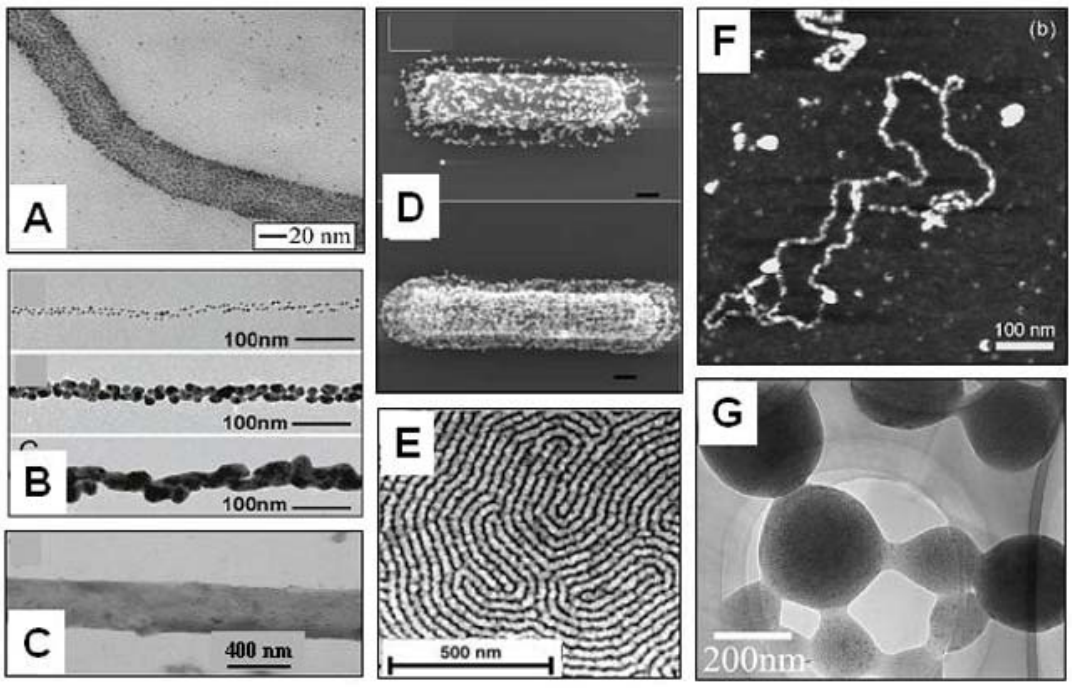

Figure 1.5 *Templated assemblies of nanoparticles on carbon nanotubes (A) [136], viral proteins (B) [145], lipid tubules (C) [142], bacteria (D) [143], block copolymers (E) [135], plasmid DNA (162) and polymers (G) [140].*

However, merger of biological molecules with nanoparticles is a more intriguing and promising aspect of nanotechnology. The specificity and information

content of biomolecular interactions offer much more than a mere template for the nanoparticle assemblies. Similarity in the size regime of biomolecules and nanoparticles and the potential applications of nanotechnology in biological science has fueled tremendous amount of research in this direction. Assemblies of nanoparticles on biological templates such as proteins [141], microtubules [142], bacterial S-layer/ bacterial cells [143], virus coat proteins [145] and nucleic acids have therefore attracted lot of researchers as evident by the vast literature available in this field. These biological templates provide high degree of programmability and reproducibility to the nanoparticle assemblies. Amongst these biological templates, nucleic acids (both DNA and RNA)-mediated nanoparticle assemblies have been studied extensively and the details of which are discussed in the following section.

1.7 DNA: The '*generic*' material of nanotechnology

Biological self-assembly has stimulated biomimetic " bottom up" approaches for the development of artificial nanometer-scaled elements that are required commercially to produce microelectronics and micromechanical devices of increasingly small dimensions in the range of 5-100 nm. Amongst the biomolecules, Deoxy Ribose Nucleic Acid (DNA) is arguably the most studied and intriguing system in context of nanotechnology research.

The vary properties of DNA that makes it the blue print of life, makes it the most intriguing material for nanoparticles assemblies too. The outstanding molecular recognition capabilities of the DNA molecule have paved the way for its interesting applications in nanotechnology research. The uniqueness of DNA lies in the ability of its fundamental building blocks, the nucleobases, to base pair with high degree of specificity [146]. Besides, the high aspect ratio of the DNA molecule (diameter of double helix is 2 nm; helical repeat is 3.5 nm) along with the robustness of the structure and uniform charge density presented by the sugar phosphate backbone renders excellent templating capabilities to the DNA molecule. Reversibility of base pairing depending on the temperature provides programmability to the nanostructures constructed using DNA. Advances in the molecular biology techniques pertinent to synthesis, detection, amplification and manipulation of nucleic acids also have contributed in development of the DNA based nanotechnology [147].

Seeman and co-workers reported one of the earliest works employing DNA as a material where they fabricated linear and 2D nanostructures by the hybridization of complimentary short DNA sequences [148]. These structures were entirely formed of short DNA strands added sequentially under conditions that favored the formation of Watson-Crick base pairing through short stick ends, leading to the formation of distinct structures. The same group later generated periodic structures with higher complexity in 3D with great success [149]. Similar work by other groups such as those of Mao and Rothmund have taken such structural arrays of DNA to another level [150, 40]. Adleman, who combined the information content of DNA using standard biotechnology operations to solve a Hamiltonian path problem, took this programmed array of DNA ahead of being mere structural curiosity to DNA-based computation [151]. Following it, many varieties of DNA based computation have been proposed and the field is steadily developing.

However, Mirkin and co-workers integrated nanoparticles and DNA for the first time when they demonstrated that the distance dependent optical properties of oligonucleotides functionlized gold nanoparticles (Au NPs) could be used in calorimetric assays for DNA detection [152]. This assay was based on the recognition of the complimentary DNA strands immobilized on the gold nanoparticles, which would result in the cohesion of the two strands, thereby aggregating the nanoparticles, the event that can be monitored optically as a shift in the plasmon resonance absorption of gold nanoparticles. The sharp melting transitions of such assemblies revealed that imperfect hybridization events could be distinguished from the perfect ones efficiently. The assay known as Northwestern spot assay has since been commercialized as a diagnostic kit.

Similarly, many groups have developed chip-based DNA detection assays. Keating *et al.,* used Au NPs probes to amplify changes in the SPR of gold films using DNA hybridization to capture strands [153]. Subsequently, Mirkin and co-workers developed a sandwich assay for DNA detection where the trapped c-DNA Au NPs probes were treated with ionic silver. The reduction of silver ions to silver nanoparticles mediated by the Au NPs amplify the probe signals due to greater scattering by the silver nanoparticles on the chip surface [154]. Commercially

available Genicon DNA chip employs Au NPs functionlized with anti-biotin IgG, which are used to label biotinylated DNA targets of interest. Here the light-scattering properties of Au NPs with different sizes and shapes are used as the read-outs [155].

Size dependent scattering of light by Au NPs has also been used in the two colour labeling of oligonucleotide arrays [156]. Other detection protocols developed by nanoparticles DNA conjugates include electrical detection of DNA with Au NPs in chip-based assay. Such detection assay are based on the changes in the electrical behavior of the circuits i.e., changes in the conduction or resistance of the circuits and are more efficient than the optical assays and were shown to have sensitivities to approx. 500 fM. Willner and co-workers developed a surface-based DNA assay where Faradic impedance spectroscopy or microgravimetric measurements using Au-electrodes and Au-quartz crystals were used for target hybridization and detection [157].

Also noteworthy are the SNP detection assay based on the DNA-Au NP conjugates and Raman spectroscopy analysis in the chip-based assay in a highly sensitive manner [158]. Besides DNA and RNA detection, Mirkin and co-workers have also developed protein detection assays using biobarcodes that are specific synthetic DNA molecules corresponding to proteins [159]. Similarly, short specific DNA sequences called aptamers have also been used in conjugation with metal nanoparticles for detection of molecules such as cocaine [160].

Another exciting role that DNA could play in nanotechnology is that of a template for the assembly of nanoparticles. In particular, DNA metallization has generated tremendous interest. Fabrication of devices built upon the nanotechnology platform has been the most important goal in nanotechnology research. The prerequisite for such devices is the miniaturization of components that make up the devices. Metallic interconnects of nanoscale dimension are one of the components that are required for such device fabrication. DNA molecule, due to its high aspect ratio could be therefore used as templates for metallic nanowires formation. Metallization of DNA is required to overcome the inherited non-conducting nature of the biomolecules [161]. The challenge in the metallization process on a biomolecular template like DNA is that of facilitating a controlled growth of inorganic material on

the surface of the biomolecules. Many such reports on the controlled metallization of DNA are present in the literature. The protocols that have been applied to achieve metallization include immobilization of preformed nanoparticles or their precursors on the DNA followed by chemical or photo-induced reduction to generate conducting metallic nanowires.

Thus, platinum, palladium, copper, silver and even quantum dots have been grown on both the linear dsDNA templates as well as on the circular plasmid DNA molecules [162]. Binding of metal precursors to the DNA templates has made use of the electrostatic interactions of the metal cations with the negatively charged sugar phosphate backbone [163]. Uri Sivan and co-workers and Facci and co-workers have used similar approaches to bind silver ions along the length of the linear lambda DNA followed by its reduction [164]. Sivan's group has used hydrazine vapors for the reduction of ionic silver, while Facci and co-workers have reduced the bound silver ions by UV radiation. Silmilarly, Sastry and co-workers have used amino acid capped gold nanoparticles for assembly on the DNA template [165].

However, the electrostatic assembly of the cations on the negative sugar phosphate backbone would result into the nonspecific binding of the ionic precursors over the entire length of the DNA. Such limitations were overcome by Keren *et al.,* by using sequence specific Rec A probe nucleoprotein [166]. The Rec A nucleoprotein, in a sequence specific manner, protects certain specific regions against metal ion binding and the subsequent reduction leading to the metallization of DNA. In another method, the same group achieved sequence dependent protection of DNA against metallization by placing sequence specific reducing agent on the stretched lambda DNA [167]. By doing this it was ensured that DNA metallization took place only at locations along the length of DNA where the reducing agent was placed.

This thesis deals with a related issue, i.e., sequence specific DNA metallization. Most of the strategies employed so far for DNA metallization have exploited the uniform negative charge density of the sugar phosphate backbone for binding of the precursor ions and their subsequent reduction to metal form. However, the information content of the fundamental building blocks of DNA molecule, the nitrogenous bases, makes DNA the blue print of life. Although quite similar

chemically, the four bases of the DNA have subtle differences in their structures. There is an extensive literature on the differential interactions of the nucleobases with metal ions, molecules, intercalators etc. The differences in the binding abilities of the nucleobases with metal ions have been studied in great details and have covered specific interactions of nucleobases, nucleosides and nucleotides with metal cations including those from the first transition series such as chromium, manganese, iron, cobalt, nickel and copper as well as other metals such as zinc, silver, cadmium, platinum, lead and mercury [168]. Many of these studies have explained in details the interaction of the metal cations with particular nucleobases, nucleosides and nucleotides. Some of these metals such as cobalt and nickel have an affinity towards the phosphate backbones of the DNA molecules while others such as silver have preferential binding with nucleobases [169].

In another study, Mirkin and co-workers have used temperature programmed desorption (TPD) to study the interaction of DNA bases and nucleosides with gold thin films and demonstrated the different strength of the nucleobase adsorption on the thin films [170]. Sastry and co-workers have made use of highly sensitive isothermal titration calorimetry (ITC) to determine the strength of the interaction of nucleobases and its peptide analogues with nanogold in solution [171]. ITC measures the heat of interaction between two molecules when they are reacted in solution and therefore is a more direct analytical tool.

Other previous studies on understanding the nature of interaction of nucleobases with nanoparticle surfaces have made use of various spectroscopic techniques such as surface enhanced Raman spectroscopy (SERS), Fourier transform infrared (FTIR) and reflection absorption infrared (RAIR) spectroscopies, which are clearly indirect methods for estimation of the strength of the above-mentioned interactions [172].

Despite the extensive literature, such differential interactions of nucleobases with metal nanoparticles and their precursor ions have not been used for fabrication of materials templated on DNA. A part of the thesis is thus devoted to quantitation of the nucleobases-metal ions interactions and using these very interactions to fabricate patterned molecular wires on DNA templates.

1.8 Bimetallic porous/hollow shell nanoparticles: synthesis and applications

In addition to the size and shape dependent properties of metal nanoparticles discussed in the previous sections, compositional variations also leads to significant alterations in nanoparticles properties. Bimetallic nanoparticles constitute a special class of nanomaterials, which have attracted a lot of attention pertaining to the unique optoelectronic properties exhibited by them [173]. Bimetallic nano-clusters have been widely accepted as better catalysts than the monometallic counterparts and have been studied extensively. For example, Sinfelt and co-workers have studied inorganic oxide supported bimetallic systems for their catalytic applications [174]. However, metal nanoparticles without inorganic support have added advantages over the supported ones in terms of improved monodispersity and controlled intrinsic properties [175].

The different structural forms in terms of the atomic distribution of the constituent metals that bimetallic nanoparticles could acquire are alloys, intermetallic particles, core shell particles and cluster in cluster bimetals. Where as random alloys are formed when the two constituent metals have similar atomic sizes, intermetallic particles are formed when the atomic sizes are different. Core shell nanoparticles are characterized by separation of the constituent metal atoms in such a way that one metal forms a core that is surrounded by the shell of the second metal. Cluster in cluster nanoparticle may be considered as a modification of the core shell structures where nanoclusters of one type of metal are surrounded by the second metal clusters that act as a binder [175].

Depending on these structural forms, bimetallic nanoparticles vary in their properties and have found exciting applications that includes catalysis [176], Surface Enhanced Raman Spectroscopy (SERS) based molecular detection [177], diagnostics [178], non-linear optics and magnetic applications [179] etc. These applications are dependent on the special properties that are brought about by the changes on surface and structure caused by alloying. Therefore, preparations and characterization of bimetallic nanoparticles comprising of various combinations of noble metals such as Au-Ag, Au-Pd, Au-Pt, Ag-Pd, Ni-Co, etc [180] have been subject of intensive studies. In general, bimetallic nanoparticles can be prepared by simultaneous reduction or by

successive reduction of two metal ions in the presence of suitable stabilization strategy such as steric hindrance and static-electronic repulsive force. However, control of the reduction, nucleation, and aggregation rates of the two components may be effective to control the size, structure, and composition distribution of bimetallic nanoparticles [175].

An important class of bimetallic nanoparticles is the hollow shell/porous nanoparticles. Besides unique optoelectronic properties, these nanoparticles have added advantages of enhanced specific surface area, low density and cost effectiveness. Hollow metal nanoparticles also exhibit large surface permeability without much sacrifice of mechanical/thermal stability [181]. Porous structures that can be of inorganic, organic, and inorganic–organic composite materials are of scientific and technological importance because of the ability of the pore wall to interact with atoms, ions, molecules and supermolecules, together with the capacity of controllable pore space to load or capture liquid and gas molecules, and solid particles. The tailorable pore size and pore wall surface make porous materials highly attractive in frontier research.

Metallic hollow shell nanoparticles, particularly gold shell nanoparticles have been studied extensively for their interesting and often, highly applicable optical properties. The hollow gold shells depicts surface plasmon absorption band in the Near Infra red (NIR) region of the electromagnetic spectrum. These unusual optical properties have been attributed to the presence of two dipolar plasmon modes; the low-energy (long-wavelength) mode ω^- corresponds to a symmetric coupling of the cavity plasmon on the inner surface and the sphere surface plasmon on the outer surface while the higher-energy (short-wavelength) mode ω^+ corresponds to antisymmetric coupling [182]. These effects have been studied extensively and numerous theoretical models are in place to explain the unusual optical properties.

Halas and co-workers have illustrated that by increasing particle size at a constant wall thickness, the absorption band is red-shifted as the plasmon oscillation decreases in energy. However, increasing wall thickness at constant particle size will blue-shift the absorption band. The band shifts to higher energy because as the inner diameter of the hollow gold shell decreases it takes on more solid-particle-like

properties. Because solid gold particles at these sizes have plasmon bands at approximately 520 nm, the absorption will always shift in this direction as wall thickness increases [182, b]. Thus, Nanoshells can be designed and fabricated with optical resonances from the visible to the midinfrared regions of the spectrum [183], easily spanning the NIR region of the spectrum (700-1300 nm), where optical transmission through tissue is optimal [184].

Both chemical and physical methods have been employed for the synthesis of hollow shell and porous nanoparticles. Deposition of preformed nanoparticles or their precursors on removable templates such as silica or polymeric or ceramic beads, microemulsion droplets, liquid crystals, liquid droplets, surfactant vesicles and polymer micelles followed by the removal of the core by chemical etching or calcination was one of the earliest methods devised for the fabrication of hollow shell nanoparticles [185]. Layer-by-layer assembly has also been used extensively to synthesize a range of polymeric core inorganic shells nanoparticles [186]. Hollow nanocrystals have also been synthesized by the Kirkendall effect in which pores form because of the difference in the diffusion rate of two components [187]. There are also reports on chemical methods involving seed mediated Ag-Au bimetallic core-shell nanoparticles growth using surfactants [188]. Suslik and co-workers have developed sonochemical methods for the synthesis of hollow gold nanoparticles [189]. Song and co-workers reported formation of hollow Ni nanospheres via the redox reaction of nickel dodecylsulfate with NaH_2PO_2 in a micelle system [190]. Tang and co-workers have assembled Fe_3O_4 nanoparticles to form hollow nanospheres in ehthylene glycol in the presence of Dodecylamine [191]. Similarly, Wong and co-workers have shown the charge driven flocculation of poly L-lysine capped gold nanoparticles to form hollow spheres [192].

One of the most popular approaches used for the fabrication of the hollow nanoparticles is the galvanic replacement process that has been illustrated by many groups for the synthesis of a wide variety of bimetallic hollow nanoparticles. The galvanic replacement reaction makes use of the differences in the redox potentials of the two metals to reduce one (with the higher reduction potential) at other's expense, which is oxidized. The latter acts as a sacrificial reducing template and a reducing

agent, leading to the reduction and deposition of the first metal as a shell. The following equation represents the transmetallation reaction between silver nanoparticles and ionic gold:

$$3Ag + HAuCl_4 \longrightarrow Au + 3AgCl + HCl$$

Xia and co-workers have used the galvanic replacement reaction for the synthesis of hollow gold and platinum nanoparticles using silver nanoparticles of different morphologies as the sacrificial templates [193]. Chun Li Bai and co-workers, on the other hand, employed sacrificial cobalt nanoparticles for the synthesis of hollow platinum nanoparticles for improved catalysis [194]. Mirkin has used similar process for the synthesis of hollow nanoframes of gold [195]. Sastry and co-workers have illustrated the utility of such process in organic medium for the generation of hollow gold and platinum nanoparticles [196]. Alivisatos and co-workers have reported the formation of gold hollow octahedral nanoparticles from solid silver nanoparticles using the galvanic replacement reactions [197]. Cheon and co-workers have used transmetalation reactions to prepare CoAu, CoPt, CoPd and CoCu core shell magnetic nanoparticles [198].

The volume confined by the hollow shell nanoparticles is empty and is accessible to various sensing and spectroscopic applications at the nanometer scale. Thus, many such interesting applications have been developed. Most noticeable of applications have been the development of immunogold shell mediated cancer detection and therapy by Drezek and co-workers [199]. This report demonstrated a novel nanoshell-based all-optical platform technology for integrating cancer imaging and therapy applications. Immunotargeted nanoshells were engineered to both scatter light in the NIR enabling optical molecular cancer imaging and to absorb light, allowing selective destruction of targeted carcinoma cells through photothermal therapy. Nanoshells functionlized by anti HER2 antibodies were used to detect and destroy breast carcinoma cells that overexpressed HER2, a clinically relevant biomarker [199]. Similarly, West and co-workers have developed gold nanoshell based whole blood immunoassay. Nanoshells decorated with antigen induces aggregation in the whole blood, which can be detected via the spectral red shifting in the near-infrared, where blood is more transmittive thereby permitting detection of

nanoshell aggregation in the whole blood. This immunoassay is capable of detecting sub-nanogram-permilliliter quantities of various anylates in different media within 10-30 min. [200].

The larger optical cross section of gold nanoshells over the conventional NIR chromophores such as indocyanine green renders them potentially applicable in biological sensing and imaging applications such as Optical Coherent Tomography (OCT) [201] and Reflectance confocal microscopy (RCM) [202]. Encapsulation of fluorophore by the hollow metal nanoparticles also leads to better photostability of the fluorophore [203]. Xia and co-workers have also demonstrated that the surface plasmon sensitivity of the hollow gold nanoparticles towards environmental changes is higher than the solid gold nanoparticles [204]. Gold nanoshells have also been applied in techniques such as photo-oxidation inhibition in photoluminescent polymer films [205], Raman sensors that can be optimized to specific pump laser wavelengths [206], optically triggered drug delivery [207] and optomechanical materials [208].

Apart from gold nanoshells that have increasingly found application in biological research due to its biocompatibility with living systems, other hollow shell nanoparticles have also been used in applications in various fields including catalysis, magnetic storage devices etc. The enhanced specific surface area of and low density makes hollow/porous palladium and platinum and nickel nanoparticles efficient catalysts. Numerous catalytic reactions such as Suzuki coupling reaction, electrocatalytic oxidation of methanol etc have been shown to have become more efficient and cost effective with the introduction of porous forms of the conventional catalytic materials [209].

A lot of research is also focused on the development of increased hydrogen storage capacities using the porous forms of platinum and palladium nanoparticles [210]. Chen and co-workers have also used nickel hollow shells as catalysts in the acetone hydrogenation reaction [211]. The reduced use of metals has been demonstrated in making conductive composites consisting of hollow nanostructures as metallic fillers [212]. Other applications of metallic and nonmetallic hollow nanospheres include artificial cells, coatings for controlled drug release, cosmetics, inks and dyes [213].

1.9 Outline of the thesis

The work presented in the thesis is focused on developing a new strategy for the sequence dependent metallization of DNA, which is based on the differential binding abilities of the silver ions with nucleobases. The heat of Ag^+ - nucleobases interactions measured by an extremely sensitive ITC analysis has been employed to establish the distinct abilities of nucleobases to bind with silver ions. These differences have been exploited to impart sequence dependence in the DNA metallization process. This is a significant diversion from the conventional metallization approach that is based on the localization of charged particles and their precursors on the negatively charged sugar phosphate backbone of the DNA.

The second part of the thesis establishes a novel method of synthesizing porous metal nanostructures by a galvanic replacement process across a semi-permeable dialysis membrane. The method offers an excellent control over the reaction kinetics and thereby leads to a better insight into the formation of cavities within the nanoparticles. Unlike the previous galvanic replacement protocols, our method leads to room temperature synthesis of phase pure porous nanostructures.

Porous gold nanostructures fabricated by the above-mentioned methods have been shown to possess an enhanced surface area over its solid gold counterparts and have been applied for cell imaging protocols and enzyme immobilization. We have established that the porous gold nanoparticles could confine ligands within the cavities and deliver them much like the 'Trojan horse'. The chapter wise discussion of these studies is as follows:

The ***Second chapter*** describes the various techniques used for the experimental characterization during the synthesis of nanomaterials and studying their interactions with different ligands. Thus, the chapter gives an overview of the physical principle of techniques such as Uv-visible-NIR Spectroscopy, Transmission Electron Microscopy (TEM), Isothermal titration Calorimetry (ITC), Fluorescence Spectroscopy, Fluorescence Assisted Cell Sorting (FACS), Confocal Microscopy, Atomic Force Microscopy (AFM), Energy Dispersive Analysis of X-ray (EDAX), X-ray Photoelectron Spectroscopy (XPS) and High Resolution Transmission

Microscopy (HRTEM). The importance of these techniques in the work described in the thesis has been illustrated.

The ***Third chapter*** explores the importance of nucleic acids in general, and DNA in particular, in the field of nanotechnology. The chapter describes studies pertaining to the interactions of the nucleobases with metal nanoparticle precursors with the help of extremely sensitive Isothermal Titration Calorimetry (ITC) analysis. This analysis reveals the differential strengths of interactions of the nucleobases with metal nanoparticle precursor ions. These interactions have been compared with the respective short oligonucleotides and the significance of the nucleobases in nanoparticle-DNA interaction has been highlighted. Based on these differential affinities of nucleobases towards metal ions, a new strategy for sequence based DNA metallization and patterned nanowires has been put forward and as a proof of concept experiment, customized single stranded DNA sequences have been used to develop patterned molecular wires of silver.

The ***Fourth chapter*** is dedicated to development of a novel process for the room temperature synthesis of porous bimetallic nanostructures. The chapter begins with an introduction to bimetallic structures with an emphasis on porous metal nanostructures, previously developed methodologies for their synthesis and their characteristic properties. Thereafter, a novel protocol for the synthesis of porous bimetallic structures has been described wherein a semi permeable dialysis membrane is used for a controlled galvanic replacement reaction between a sacrificial metal nanoparticle and a metal ion system. Using UV-vis-NIR spectroscopy and TEM analysis, excellent control over the reaction kinetics has been demonstrated. The versatile nature of the method has been established by fabrication of different elemental combinations of porous nanostructures and also applying the method for obtaining anisotropic porous nanostructures. Further, HRTEM and EDX analysis of these bimetallic nanoparticles has been performed to establish the presence and distribution of the bimetal in the nanostructures.

The ***Fifth chapter*** explores the potential applications of the porous metallic nanostructures in cell imaging, enzyme immobilization and drug delivery applications. Using tools such as confocal laser scanning microscopy, the chapter

illustrates the importance of enhanced surface area and nano-cavities offered by the porous metallic nanostructures in cell imaging protocols as well as enzyme immobilization applications. The biocompatibility issues of the porous gold nanoparticles have also been addressed using mammalian cell lines and microbial cultures.

The ***Sixth chapter*** concludes the thesis by highlighting the results and observations of the previous chapters and discusses the future prospects of the work carried out in the thesis.

1.10 References

1. Fulhame, M. *An Essay on Combustion with a View to a New Art of Dying and Painting*; J. Cooper: London, **1794**.
2. (a) Savage, G. *Glass and Glassware*, Octopus Book, London **1975**.
3. (a) Antonii, F. Panacea Aurea–Auro Potabile, Bibliopolio Frobeniano, Hamburg, **1618**. (b) Kunckels, J. Nuetliche Observationes oder Anmerkungen von Auro und ArgentoPotabili, Schutzens, Hamburg **1676**. (c) Helcher, H. H. Aurum Potabile oder Gold Tinstur, J. Herbord Klossen, Breslau and Leipzig **1718**. (d) Lloyd, J.U. *Elixirs and Flavoring Extracts: Their History, Formulae, and Methods of Preparation*, **1892**, New York: William Wood and Company.
4. Reibold, M. *et al., Nature* **2006**, *446*, 226.
5. Faraday, M. *Philosophy Trans.* **1857**, *147*, 145.
6. Graham, T. *Philos. Trans. R. Soc*. **1861**, *151*, 183.
7. Taniguchi, N. **1974**. On the Basic Concept of 'Nano-Technology'. In: *Proceedings of the international conference on production engineering. Tokyo, Part II,* Japan Society of Precision Engineering, **1974**: 18-23: Tokyo: JSPE.
8. Feynman, R. P. *Engg. Sci.* **1960**, *23*, 22.
9. 'Nanoscale Materials in Chemistry' Klabunde, K. J. (Ed.), John Wiley, New York (**2000**).
10. (a) Raimondi, F.; Scherer, G. G.; Kötz, R.; Wokaun, A. *Angew. Chem. Int. Ed.* **2005**, *44*, 2190. (b) Henry, C. R. *Surf. Sci. Rep.* **1998**, *31*, 231. (c) Zhang, J. H. *Acc. Chem. Res.* **1997,** *30*, 423.
11. (a) Raimondi, F.; Scherer, G. G.; Kötz, R.; Wokaun, A. *Angew. Chem. Int. Ed.* **2005**, *44*, 2190. (b) Henry, C. R. *Surf. Sci. Rep.* **1998**, *31*, 231. (c) Zhang, J. H. *Acc. Chem. Res.* **1997,** *30*, 423.
12. (a) Ritchie, R. H. *Phys. Rev.* **1957**, *106*, 874. (b) Barnes, W. L.; Dereux, A.; Ebbesen, T. W. *Nature* **2003**, *424*, 824. (c) Kreibig, U.; Vollmer, M. *Optical*

Properties of Metal Clusters; Springer- Verlag: Berlin, **1996**. (d) Burda, C.; Chen, X.; Narayanan, R.; El-Sayed, M.A. *Chem. Rev.* **2005**, *105*, 1025.

13. (a) Pe´rez-Juste, J.; Pastoriza-Santos, I.; Liz- Marzan, L. M.; Mulvaney, P. *Coord. Chem. Rev.* **2005**, *249*, 1870. (b) Link, S; El-Sayed, M. A. *Annu. Rev. Phys. Chem.***2003**, *54*, 331. (c) Van der Zande, B. M. I.; Bohmer, M. R.; Fokkink, L. G. J.; Schonenberger, C. *J. Phys. Chem. B* **1997**, *101*, 852. (d) Yu, Y. Y.; Chang, S. S.; Lee, C. L.; Wang, C. R. C. *J. Phys. Chem. B* **1997**, *101*, 6661. (e) Liz-Marzan, L. M. *Langmuir* **2006,** *22,* 32.

14. Millstone, J. E.; Park, S.; Shuford, K. L.; Qin, L.; Schatz, G. C.; Mirkin, C. A. *J. Am. Chem. Soc.* **2005**, *127*, 5312.

15. (a) Mie, G. *Ann. Phys.* **1908**, *25*, 377. (b) Gans, R. *Ann. Phys.* **1912**, *37*, 881. (c) Mulvaney, P. *Langmuir* **1996**, *12*, 788. (d) Link, S.; El-Sayed, M. A. *J. Phys. Chem. B* **1999**, *103*, 8410. (e) Mulvaney, P.; Liz-Marzan, L. M. *Top. Curr. Chem.* **2003**, *226*, 225. (f) Johnson, P.B.; Christy, R.W. *Phys. Rev. B* **1972**, *6*, 4370.

16. (a) Burda, C.; Chen, X.; Narayanan. R.; El-Sayed, M. A. *Chem. Rev.* **2005,** *105*, 1025. (b) El-Sayed, M. A. *Acc. Chem. Res.* **2001**, *34*, 257. (c) Murphy, C. *et al., J. Phys. Chem. B* **2005**, *109*, 13857.

17. (a) Haruta, M.; Daté M. *Appl. Catal. A* **2001**, *222*, 427. (b) Zhong, C.J., Maye, M.M. *Adv. Mater*. **2001**, *13*, 1507. (c) Lewis. L.N. *Chem. Rev.***1993**, *93*, 2693. (d) Astruc, D.; Lu, F.; Aranzaes, J.R. *Angew. Chem. Int. Ed.* **2005**, *44*, 7852.

18. (a) Wang, Z.L.; Ahmad, T.S.; El-Sayed, M.A. *Surf. Sci.,* **1997**, *380*, 302. (b) Narayanan, R.; El-Sayed, M.A. *Nano Lett.* **2004**, *4*, 1343. (c) Narayanan, R.; El-Sayed, M.A. *J. Phys. Chem. B* **2004**, *108*, 5726.

19. (a) Shephard, D.S. *et al., Angew. Chem. Intl. Ed.* **1997**, *36*, 2242. (b) Zhang, X.; Chan, K. Y. *Chem. Mater.* **2003**, 15, 451. (c) Deivaraj, T. C.; Chen, W.; Lee, J. Y. *J. Mater. Chem.* **2003**, *13*, 2555.

20. (a) Kleemann, W *et al., Phy. Rev. B* **2001**, *63*, 1344231. (b) Park, J, I.; Cohen, J. *J. Am. Chem. Soc.* **2001**, *123*, 5743. (c) Liu, S. M. *Chem. Commun*. **2004**, *10*, 2726.

21. (a) Andersen, N. A.; Lian, T. *Ann. Rev. Phy.Chem.* **2005**, *56*, 491. (b) Kamat, P. V. *J. Phys. Chem. B* **2002**, *106*, 7729. (c) McConnell, W. P. *et al., J. Phys. Chem. B* **2000**, *104*, 8925.

22. (a) Qu, J. R.; Hu, M. A.; Chen, J. Z.; Han, W. *J. China Univ. Geosci*. **2005**, *30*, 195. (b) Willert, M.; Rothe, R.; Landfester, K.; Antonietti, M. *Chem. Mater*. **2001**, *13*, 4681.

23. (a) Jensen, T.; Kelly, L.; Lazarides, A.; Schatz, G. C. *J. Cluster Sci.***1999**, *10*, 295. (b) Fiorani, D.; Testa, A. M.; Lucari, F.; D'Orazio, F.; Romero, H. *Physica B* **2002**, *320*, 122. (c) Dormann, J. L. *et al., J. Magnet. Magnet. Mater.* **1998**, *187*, L139. (d) Jiang, C.; Markutsya, S.; Tsukruk, V. V. *Langmuir* **2004**, *20*, 882. (e) Saponjic, Z. V. *et al., Adv. Mater.* **2005**, *17*, 965.

24. (a) Haes, A. J.; Van Duyne, R.P. *Anal.Bioanal.Chem.* **2004**, *379*, 920. (b) Niemeyer, C. M. *Angew. Chem. Int. Ed.* **2001**, *40*, 4128. (c) Niemeyer, C. M. *Angew. Chem. Int. Ed.* **2003**, *42*, 5974. (d) Parak, W. J.; Gerion, D.; Pellegrino, T.; Zanchet, D.; Micheel, C.; Williams, S. C.; Bodreau, R.; Gros, M. A. L.; Larabell, C. A.; Alivisatos, A. P. *Nanotechnology* **2003**, *14*, R15. (e) Caski, A.; Maubach, G.; Born, D.; Reichert, J.; Fritzsche, W. *Single Mol.* **2002**, *3*, 275.

25. (a) Roucoux, A.; Schulz, J.; Patin, H. *Chem. Rev.* **2002,** *102,* 3757. (b) Lewis, L. N. *Chem. Rev.* **1993**, 93, 2693.

26. (a) Rosi, N. L.; Mirkin, C. A. *Chem. Rev.* **2005**, *105*, 1547. (b) Lawrie, G. *et al., Langmuir* **2006**, *22*, 497.

27. (a) Liu, G. *et al., Biochim. Biophysic. Acta* **2005**, *1741*, 246. (b) Loo, C. *et al., Tech. Cancer Res. Treat*. **2004**, *3*, 33. (c) Liu, C. *et al., Neuroscience Lett*. **2006**, *406*, 189. (d) Chan, W. C. W. *Biol. Blood Marrow. Trans*. **2006**, *12*, 87.

28. (a) Otsuka, H.; Nagasaki, Y.; Kataoka, K. *Adv. Drug Delivery Rev*. **2003**, *55*, 403. (b) McAllister, D. V. *Proc. Natl. Acad. Sci. USA.* **2003**, *100*, 13775.

29. (a) Andersen, N. A.; Lian, T. *Ann. Rev. Phys. Chem*. **2005**, *56*, 491. (b) Yae. S. *et al., Solar Energy Mater. Solar Cells* **2007**, *91*, 224.

30. (a) Zou, S.; Schatz, G. C. *Phy. Rev. B* **2006**, *74*, 125111. (b) Maier, S. A.; Friedman, M. D.; Barclay, P. E.;Painter, O. *Appl. Phys. Lett.* **2005**, *86*, 1. (c) Maier, S. A. *et al., Adv. Mater*. **2001**, *13*, 1501.

31. (a) Cengiz, E.; Wissing, S. A.; Muoller, R. H.; Yazan, Y. *Intl. J. Cosmetic Sci.* 2006, 28, 371. (b) Villalobos-Hernández, J. R.; Muoller-Goymann, C. C. *Int. J. Pharmaceutics.* **2006**, *322*, 161.

32. (a) Pradell, T.; Molera, J.; Bayés, C.; Roura, P. *Appl. Phys. A* **2006**, *83*, 203. (b) José-Yacamán, M.; Rendón, L.; Arenas, J.; Serra Puche, M. C. *Science* **2006**, *273*, 223. (c) Baglioni, P.; Giorgi, R. *Soft Matter* **2006**, *2*, 293.

33. (a) Yelin, D.; Oron, D.; Thiberge, S.; Moses, E.; Silberberg, Y. *Optics Express*, **2003**, *11*, 1385. (b) Wang, Y. *et al., Nano Lett.* **2005**, *4*, 1689. (c) Sokolov, K. *et al., Cancer Res.* **2003**, *63*, 1999. (d) El-Sayed, I. H.; Huang, X.; El-Sayed, M. A. *Nano Lett.* **2005**, *5*, 829. (e) Grainger, R. G. *Brit. J. Rad.* **1882**, *55*, 1.

34. Fichtner, M. *Adv. Engg. Mater.* **2005**, *7*, 443.

35. Moran, C. E.; Steele, J. M.; Halas, N. J. *Nano Lett*. **2004**, *4*, 1497.

36. a) Simon, U. In *Nanoparticles: From Theory to Application*, Schmid, G., Ed. Wiley-VCH, Weinheim, **2004**. b) *Nanomaterials: Synthesis, Properties, and Applications*, edited by A. S. Edelstein and R. C. Cammarata (Institute of Physics Publishing, Bristol, U.K., **1996**).

37. a) Maier, S. A.; Brongersma, M. L.; Kik, P. G.; Meltzer, S.; Requicha, A. A. G.; Atwater, H. A. *Adv. Mater.* **2001**, *13*, 1501. b) Maier, S. A.; Brongersma, M. L.; Kik, P. G.; Atwater, H. A. *Phys. Rev. B*, **2002**, *65*, 193408. c) Wang, Y. *Acc. Chem. Res.* **1991**, *24*, 133. (b) Yoffe, A. D. *Adv. Phys.* **1993**, *42*, 173.

38. Li, X.; Xu, W.; Zhang, J.; Jia, H.; Yang, B.; Zhao, B.; Li, B.; Ozaki, Y. *Langmuir* **2004**, *20*, 1298.

39. (a) Chen, A.; Chua, S. J.; Chen, P.; Chen, X. Y.; Jian, L. K. *Nanotechnology* **2006**, *17*, 3903. (b) Dreeskornfeld, L *et al., J. Electrochem. Soc.* **2003**, *150*, G702.

40. Rothemund, P. W. K. *Nature* **2006**, *440*, 297.

41. (a) Wegner, K.; Walker, B.; Tsantilis, S.; Pratsinis, S. E. *Chem. Eng. Sci.* **2002**, *57*, 1753. (b) Oha, S.; Choi, C.; Kwon, S.; Jin, S.; Kim, B.; Park, J. *J. Magn. Magn. Mater.* **2004**, *280*, 147. (c) Chevallier, J. *Thin Solid Films* **1977**, *40*, 223. (d) Perekrestov, V. I. *Tech. Phys. Lett.* **2005**, *31*, 830.

42. (a) Wang, Y.; Zhang, L.; Meng, G.; Liang, C.; Wang, G.; Sun, S. *Chem. Commun.* **2001**, 2632. (b) Teng, X.; Black, D.; Watkins, N.J.; Gao, Y.; H. Yang, *Nano Lett.* **2003**, *3*, 261. (c) Hou, Y.; Kondoh, H.; Kogure, T.; Ohta, T. *Chem. Mater*. **2004,** *16,* 5149.

43. (a) Kim, J. H.; Germer, T. A.; Mulholland, G. W.; Ehrman, S. H. *Adv. Mater.* **2002**, *14*. 518. (b) Okuyama, K.; Lenggoro, I. W. *Chem. Eng. Sci.* **2003**, *58*, 537. (c) Suh, W. H.; Suslick, K. S. *J. Am. Chem. Soc.* **2005**, *127*, 12007.

44. (a) Zhou, Y.; Wang, C.Y.; Zhu, Y.R., Chen, Z.Y. *Chem. Mater.* **1999**, *11*,2310. (b) Li, H.X.; Lin, M.Z.; Hou, J.G. *J. Crystal Growth* **2000**, *212*, 222. (c) Mallick , K.; Wang , Z.L.; Pal, T. *J. Photochem. Photobiol. A* **2001**, *140*, 75. (d) Chen, W.X.; Lee, J.Y.; Liu, Z. *Chem. Commun.* **2002**, 2588. (e) Jin, R.; Cao, Y.C.; Hao, E.; Métraux, G.S.; Schatz, G.C.; Mirkin, C.A. *Nature* **2003**, *425*, 487. (f) Sakamoto, M.; Tachikawa, T.; Fujitsuka, M.; Majima, T. Langmuir, **2006**, *22,* 6361.

45. (a) Amendola, V.; Polizzi, S.; Meneghetti, M. *J. Phys. Chem. B* **2006,** *110,* 7232. (b) Amendola, V.; Rizzi, G.A.; Polizzi, S.; Meneghetti, M. *J. Phys. Chem. B* **2005**, *109*, 23125. (c) Balchev, I.; Minkovski, N.; Marinova, Ts.; Shipochka, M.; Sabotinov, N. *Mater. Sci. Eng. B* **2006**, *135*, 108. (d) Mafuné, F.; Kohno, J.; Takeda, Y.; Kondow, T. *J. Phys. Chem. B* **2000**, *104*, 8333. (e)

Zhu, X.P.; Suzuki, T.; Nakayama, T.; Suematsu, H.; Jiang, W.; Niihara, K. *Chem. Phys. Lett.* **2006**, *427*, 127.

46. (a) Chen, W.; Cai, W.; Lei, Y.; Zhang, L. *Mater. Lett.* **2001**, *50*, 53. (b) Chen, W.; Cai, W.; Zhang, L.; Wang, G.; Zhang, L. *J. Colloid Interface Sci.* **2001**, *238*, 291. (c) Dhas, N. A., Raj, C. P., Gedanken, A. *Chem. Mater.* **1998,** *10,* 1446. (d) Fujimoto, T.; Terauchi, S.; Umehara, H.; Kojima, I.; Henderson, W. *Chem. Mater.* **2001,** *13,* 1057. (e) Nemamcha, A.; Rehspringer, J.; Khatmi, D. *J. Phys. Chem. B* **2006,** *110,* 383. (f) Pol, V. G.; Grisaru, H.; Gedanken, A. *Langmuir* **2005,** *21,* 3635.

47. (a) Kurihara, K.; Kizing, J.; Stenius, P.; Fender, J. H. *J. Am. Chem.Soc.* **1983**, *105*, 2574. (b) Mulvaney, P.; Henglein, A. *J. Phys. Chem.* **1990**, *94*, 4182. (c) Joshi, S. S.; Patil, S. F.; Iyer, V.; Mahumuni, S. Nanostruct. Mater. **1998**, *7*, 1135. (d) Henglein, A.; Giersig, M. *J. Phys. Chem. B* **1999,** *103,* 9533. (e) Dimitrijevic, N. M.; Bartels, D.M.; Jonah, C.D.; Takahashi, K.; Rajh, T. *J. Phys. Chem. B* **2001,** *105,* 954. (f) Doudna, C.M.; Bertino, M. F.; Blum, F. D.; Tokuhiro, A. T.; Lahiri-Dey, D.; Chattopadhyay, S.; Terry, J. *J. Phys. Chem. B* **2003**, *107,* 2966.

48. (a) Stoeva, S. I.; Prasad, B. L. V.; Uma, S.; Stoimenov, P. K.; Zaikovski, V.; Sorensen, C. M.; Klabunde, K. J. *J. Phys. Chem. B* **2003,** *107,* 7441. (b) Ponce, A. A.; Klabunde, K. J. *J. Mol. Catal.* **2005**, 225, 1. (c) Smetana, A. B.; Klabunde, K. J.; Sorensen C. M. *J. Colloid Interface Sci.* **2005**, *284*, 521. (d) Klabunde, K. J.; Timms, P. S.; Skell, P. S.; Ittel, S. *Inorg. Synth.* **1979**, *19*, 59. (e) Davis, S. C.; Klabunde, K. J. *Chem. Rev.* **1982**, *82*, 153. (f) Stoeva, S.; Klabunde, K. J.; Sorensen, C. M.; Dragieva, I. *J. Am. Chem. Soc.* **2002**, *124*, 2305.

49. (a) Armelao, L.; Bertoncello, R.; De Dominicis, M. *Adv. Mater.* **1997**, *9*, 736. (b) Devarajan, S.; Bera, P.; Sampath, S. *J. Colloid Interface Sci.* **2005**, *290*, 117. (c) Shukla, S.; Seal, S. *Nanostructured Mater*. **1999**, *11*, 1181.

50. (a) Gao, F.; Lu, Q.; Komarneni, S. *Chem. Mater.* **2005,** *17,* 856. (b) Rosemary, M. J.; Pradeep, T. *J. Colloid Interface Sci.* **2003**, *268*, 81.

51. (a) Bronstein, L. M.; Chernyshov, D. M.; Timofeeva, G. I.; Dubrovina, L. V.; Valetsky, P. M.; Obolonkova, E. S.; Khokhlov, A. R. *Langmuir* **2000**, *16*, 3626. (b) Bronstein, L. M.; Sidorov, S. N.; Valetsky, P. M.; Hartmann, J.; Cölfen, H.; Antonietti, M. *Langmuir* **1999**, *15*, 6256. (c) Lee, C. L.; Wan, C. C.; Wang, Y. Y. *Adv. Funct. Mater.* **2001**, *11*, 344.

52. (a) Sun, Y.; Xia, Y. *J. Am. Chem. Soc.* **2004**, *126*, 3892 (b) Sun, Y.; Mayers, B. T.; Xia, Y. *Adv. Mater.* **2003**, *15*, 641. (c) Sun, Y.; Xia, Y. *Nano Lett.* **2003**, *3*, 1569 (d) Jin, Y.; Dong, S. *J. Phys. Chem. B* **2003,** *107,* 12902 (e) Sun, Y.; Mayers, B. T.; Xia, Y. *Nano Lett.* **2002**, *2*, 481. (f) Chen, J. *et al., Nano Lett.* **2005**, *5*, 473 (g) Liang, H. P.; Guo, Y. G.; Zhang, H. M.; Hu, J. S.; Wan, L. J.; Bai, C. L. *Chem. Commun.* **2004**, 1496. (h) Selvakannan, P. R.; Sastry, M. *Chem Commun*. **2005**, 1684. (i) Metraux, G. S.; Cai, Y. C.; Jin, R.; Mirkin, C. A. *Nano. Lett.* **2003**, *3*, 519.

53. (a) Cliffel, D. E.; Zamborini, F. P.; Gross, S. M.; Murray, R. W. *Langmuir* **2000**, *16*, 9699. (b) Yonezawa, T.; Onoue, S.; Kimizuka, N. *Langmuir* **2000**, *16*, 5218. (c) Thomas, K.G.; Zajicek, J.; Kamat, P.V. *Langmuir* **2002,** *18,* 3722.

54. (a) Henhar, R. S.; Norstern, T. B.; Rotello, V. M. *Adv. Mater.* **2005**, *17*, 657. (b) Cheng, J.; Teply, B. A.; Sherifi, I.; Sung, J.; Luther, G.; Gu, F. X.; Levy-Nissenbaum, E.; Radovic-Moreno, A. F.; Langer, R.; Farokhzad, O.C. *Biomaterials* **2007**, *28*, 869. (c) Hoppe, C. E.; Lazzari, M.; Pardiñas-Blanco, I.; López-Quintela, M. A. *Langmuir* **2006,** *22,* 7027. (d) Qian, X. F.; Yin, J.; Feng, S.; Liu, S. H.; Zhu, Z. K. *J. Mater. Chem.* **2001**, *11*, 2504. (e) Sidorov, S. N.; Bronstein, L. M.; Valetsky, P. M.; Hartmann, J.; Cölfen, H.; Schnablegger, H.; Antonietti, M. *J. Colloid Interface Sci.* **1999**, *212*, 197. (f) Xiong, Y.; Washio, I.; Chen, J.; Cai, H.; Li, Z. Y.; Xia, Y. *Langmuir* **2006,** *22,* 8563. (g) Mu, X.; Evans, D.G.; Kou, Y. *Catal. Lett.* **2004**, *97*, 151.

55. (a) Selvakannan, PR.; Mandal, S.; Phadtare, S.; Pasricha, R.; Sastry, M. *Langmuir* **2003,** *19,* 3545. (b) Selvakannan, PR.; Mandal, S.; Phadtare, S.; Gole, A.; Pasricha, R.; Adyanthaya, S. D.; Sastry, M. *J. Colloid Interface Sci.* **2004**, *269*, 97. (c) Zhong, Z.; Patskovskyy, S.; Bouvrette, P.; Luong, J. H. T.;

Gedanken, A. *J. Phys. Chem. B* **2004,** *108,* 4046. (d) Huang, Y. F.; Lin, Y.-W.; Chang, H. T. *Nanotechnology* **2006**, *17*, 4885. (e) Naka, K.; Itoh, H.; Tampo, Y.; Chujo, Y. *Langmuir* **2003,** *19,* 5546. (f) Fan, J.; Chen, S.; Gao, Y. *Colloids Surf. A* **2003**, *28*, 199. (g) Fujiki, Y.; Tokunaga, N.; Shinkai, S.; Sada, K. *Angew. Chem. Int. Ed.* **2006**, *45*, 4764. (h) Aubin-Tam, M.; Hamad-Schifferli, K *Langmuir* **2005,** *21,* 12080. (i) You, C. C., De, M., Han, G., Rotello, V.M. *J. Am. Chem. Soc.* **2005**, *127*, 12873. (j) Bhargava, S. K.; Booth, J. M.; Agrawal, S.; Coloe, P.; Kar, G. *Langmuir* **2005,** *21,* 5949. (k) Sanyal, A.; Mandal, S.; Sastry, M. *Adv. Funct. Mater.* **2005**, *15*, 273. (l) Selvakannan, PR.; Swami, A.; Srisathiyanarayanan, D.; Shirude, P. S.; Pasricha, R.; Mandale, A. B.; Sastry, M. *Langmuir* **2004,** *20,* 7825. (m) Joshi, H.; Shirude, P. S.; Bansal, V.; Ganesh, K. N.; Sastry, M. *J. Phys. Chem. B* **2004,** *108,* 11535.

56. (a) Brust, M.; Fink, J.; Bethell, D.; Schiffrin, D. J.; Kiely, C. J. *J. Chem. Soc., Chem. Commun*. **1995**, 1655. (b) Knecht, M. R.; Garcia-Martinez, J. C.; Crooks, R. M. *Langmuir* **2005,** *21,* 11981. (c) Cardenas-Trivino, G.; Klabunde, K. J.; Dale, E. B. *Langmuir* **1987**, *3*, 986. (d) Mandal, S.; Das, A.; Srivastava, R.; Sastry, M. *Langmuir* **2005,** *21,* 2408. (e) Schlotterbeck, U.; Aymonier, C.; Thomann, R.; Hofmeister, H.; Tromp, M.; Richtering, W.; Mecking, S. *Adv. Funct. Mater.* **2004**, *14*, 999. (f) Cozzoli, P.D.; Comparelli, R.; Fanizza, E.; Curri, M.L.; Agostiano, A.; le Laub, D. *J. Am. Chem. Soc.* **2004**, *126*, 3868.

57. (a) Kim, K. S.; Demberelnyamba, D.; Lee, H. *Langmuir*, **2004**, *20*, 556. (b) Wang, Y.; Yang, H. *Chem. Commun.* **2006**, 2545. (c) Zhao, D.; Fei, Z.; Ang, W. H.; Dyson, P. J. *Small* **2006**, *2*, 879. (d) Scheeren, C. W.; Machado, G.; Teixeira, S. R.; Morais, J.; Domingos, J. B.; Dupont, J. *J. Phys. Chem. B* **2006,** *110,* 13011.

58. (a) Sun, Y.; Riggs, J. E.; Rollins, H. W.; Guduru, R. *J. Phys. Chem. B* **1999,** *103,* 77. (b) Cason, J. P.; Roberts, C. B. *J. Phys. Chem. B* **2000**, *104,* 1217. (c) Cason, J. P.; Khambaswadkar, K.; Roberts, C. B. *Ind. Eng. Chem. Res.* **2000,** *39,* 4749. (d) Ohde, H.; Hunt, F.; Wai, C. M. *Chem. Mater.* **2001,** *13,* 4130. (e)

Clarke, N. Z.; Waters, C.; Johnson, K. A.; Satherley, J.; Schiffrin, D. J. *Langmuir* **2001,** *17,* 6048. (f) Morley, K. S.; Marr, P. C.; Webb, P. B.; Berry, A. R.; Allison, F. J.; Moldovan, G.; Brown, P. D.; Howdle, S. M. *J. Mater.Chem.* **2002**, *12*, 1898. (g) Ye, X. R.; Lin, Y.; Wang, C.; Engelhard, M. H.; Wang, Y.; Wai, C. M. *J. Mater. Chem.* **2004**, *14*, 908. (h) Morley, K. S.; Licence, P.; Marr, P. C.; Hyde, J. R.; Brown, P. D.; Mokaya, R.; Xia, Y.; Howdle, S. M. *J. Mater. Chem.* **2004**, *14*, 1212. (i) Esumi, K.; Sarashina, S.; Yoshimura, T. *Langmuir* **2004,** *20,* 5189. (j) Hou, Z.; Theyssen, N.; Brinkmann, A.; Leitner, W. *Angew. Chem. Int. Ed.* **2005**, *44*, 1346. (k) Sun, Z.; Fu, L.; Liu, Z.; Han, B.; Liu, Y.; Du, J. *J. Nanosci. Nanotechnol.* **2006**, *6*, 691.

59. (a) Bronstein, L.; Krämer, E.; Berton, B.; Burger, C.; Förster, S.; Antonietti, M. *Chem. Mater.* **1999,** *11,* 1402. (b) Jana, N. R. *Small* **2005**, *1*, 875. (c) Pileni, M. P. *Supramol. Sci.* **1998**, *5*, 321. (d) Pileni, M. P.; Ninham, B. W.; Gulik-Krzywicki, T.; Tanori, J .; Lisiecki, I.; Filankembo, A. *Adv. Mater.* **1999**, *11*, 1358. (e) Pileni, M.P.; Gulik-Krzywicki, T.; Tanori, J.; Filankembo, A.; Dedieu, J. C. *Langmuir* **1998,** *14,* 7359.

60. (a) Balogh, L.; Valluzzi, R.; Laverdure, K. S.; Gido, S. P.; Hagnauer, G. L.; Tomalia, D. A. *J. Nano. Res.* **1999**, *1*, 353. (b) Zhao, M.; Crooks, R. M. *Angew. Chem. Int. Ed.* **1999**, *38*, 364. (c) Chechik, V.; Zhao, M.; Crooks, R.M. *J. Am. Chem. Soc.* **1999,** *121,* 4910. (d) Zhao, M.; Sun, L.; Crooks, R. M. *J. Am. Chem. Soc.* **1998,** *120,* 4877. (e) Niu, Y.; Crooks, R. M. *Chem. Mater.* **2003,** *15,* 3463. (f) Scott, R. W. J.; Wilson, O. M.; Crooks, R. M. *J. Phys. Chem. B* **2005,** *109,* 692.

61. (a) Fukuoka, A.; Higuchi, T.; Ohtake, T.; Oshio, T.; Kimura, J.; Sakamoto, Y.; Shimomura, N.; Inagaki, S.; Ichikawa, M. *Chem. Mater.* **2006,** *18,* 337. (b) Fukuoka, A.; Araki, H.; Sakamoto, Y.; Sugimoto, N.; Tsukada, H.; Kumai, Y.; Akimoto, Y.; Ichikawa, M. *Nano Lett.* **2002**, *2*, 793. (c) Fukuoka, A.; Araki, H.; Kimura, J.; Sakamoto, Y.; Higuchi, T.; Sugimoto, N.; Inagaki, S.; Ichikawa, M. *J. Mater. Chem.* **2004**, *14*, 752. (d) Joo, S. H.; Choi, S. J.; Oh, I.; Kwak, J.; Liu, Z.; Terasaki, O.; Ryoo, R. *Nature* **2001**, *412*, 169.

62. (a) Chen, P.; Wu, X.; Lin, J.; Tan, K. L. *J. Phys. Chem. B.* **1999**, *103*, 4559. (b) Quinn, B. M.; Dekker, C.; Lemay, S. G. *J. Am. Chem. Soc.* **2005**, *127*, 6146. (c) Guo, D. J.; Li, H. L. *J. Colloid Interface Sci.* **2005**, *286*, 274. (d) Qu, J.; Shen, Y.; Qu, X.; Dong, S. *Chem. Commun.* **2004**, 34. (e) Day, T. M.; Unwin, P. R.; Wilson, N. R.; Macpherson, J. V. *J. Am. Chem. Soc.* **2005**, 127, 10639. (f) Govindaraj, A.; Satishkumar, B. C.; Nath, M.; Rao, C. N. R. *Chem. Mater.* **2000,** *12*, 202. (g) Kyotani, T.; Tsai, L.; Tomita, A. *Chem. Commun*. **1997**, 701. (h) Pradhan, B. K.; Kyotani, T.; Tomita, A. *Chem. Commun*. **1999**, 1317. (i) Sloan, J.; Wright, D. M.; Woo, H. G.; Bailey, S.; Brown, G.; York, A. P. E.; Coleman, K. S.; Hutchison, J. L.; Green, M. L. H. *Chem. Commun.* **1999**, 699.

63. (a) Wong, K. K. W.; Douglas, T.; Gider, S.; Awschalom, D. D.; Mann, S. *Chem. Mater.* **1998**, *10*, 279. (b) He, J.; Kunitake, T. *Chem. Mater.* **2004,** *16,* 2656. (c) Mark, S. S.; Bergkvist, M.; Yang, X.; Angert, E. R.; Batt, C. A. *Biomacromolecules* **2006,** *7*, 1884. (d) Willner, I., Baron, R., Willner, B. *Adv. Mater.* **2006**, *18*, 1109. (e) Zhu, H.; John, G.; Wei, B. *Chem. Phys. Lett.* **2005**, *405*, 49. (f) Klem, M. T.; Willits, D.; Solis, D. J.; Belcher, A. M.; Young, M.; Douglas, T. *Adv. Funct. Mater.* **2005**, *15*, 1489.

64. (a) Pollmann, K.; Merroun, M.; Raff, J.; Hennig, C.; Selenska-Pobell, S. *Lett. Appl. Microbiol.* **2006**, *43*, 39. (b) Douglas, T.; Young, M. *Nature* **1998**, *393*, 152. (c) Konishi, Y.; Tsukiyama, T.; Ohno, K.; Saitoh, N.; Nomura, T.; Nagamine, S. *Hydrometallurgy* **2006**, *81*, 24. (d) Nam, K.T.; Kim, D. W.; Yoo, P.J.; Chiang, C. Y.; Meethong, N.; Hammond, P. T.; Chiang, Y. M.; Belcher, A. M. *Science* **2006**, *312*, 885. (e) Lee, S. K.; Yun, D. S.; Belcher, A. M. *Biomacromolecules* **2006,** *7*, 14. (f) Peelle, B. R.; Krauland, E. M.; Wittrup, K. D.; Belcher, A. M. *Langmuir* **2005,** *21,* 6929. (g) Reiss, B. D.; Mao, C.; Solis, D. J.; Ryan, K. S.; Thomson, T.; Belcher, A. M. *Nano. Lett.* **2004**, *4*, 1127.

65. (a) Mann, S. *Nature*, **1993**, *365*, 499. (b) Oliver, S.; Kupermann, A.; Coombs, N., Lough, A.; Ozin, G. A. *Nature*, **1995**, *378*, 47. (c) Kröger, N.; Deutzmann, R.; Sumper, M., *Science*, **1999**, *286*, 1129.

66. Young, J. R.; Davis, S. A.; Bown, P. R.; Mann, S. *J. Struct. Biol.* **1999**, *126*, 195.

67. Balkwill, D.; Marata, D.; Blakemore, R. P. *J. Bacteriol.* **1980**, *141*, 1399.

68. (a)Lovley, D. R.; Stolz, J. F.; Nord, G. L.; Phillips, E. J. P. *Nature*, **1987**, *330*, 252. (b) Spring, H.; Schleifer, K. H. *Sys. Appl. Microbiol*. **1995**, *18*, 147. (c) Dickson, D. P. E. *J. Magn. Magn. Mater.* **1999**, *203*, 46.

69. (a) Bharde, A. *et al., J. Am. Chem. Soc*. **2005**, *127*, 9326. (b) Mandal, D.; Bolander, M. E.; Mukhopadhyay, D.; Sarkar, G.; Mukherjee, P. 2006, *Appl. Microbiol. Biotechnol.* **2006**, *69*, 485. (c) Banerjee, I. A. *et al., Adv. Mater.* **2005**, *17*, 1128. (d) Torres de Araujo, F. F.; Pires, M. A.; Frankel, R. B.; Bicudo, C. E. M. *Biophys. J.* **1986**, *50*, 375. (e) Bazylinski, D. A.; Frankel, R. B. *Biomineralization* (Ed.: E. Baeuerlein), Wiley-VCH, Weinheim **2000**, 41.

70. (a) Mukherjee, P.; Ahmad, A.; Mandal, D.; Senapati, S.; Sainkar, S. R.; Khan, M. I.; Ramani, R.; Parischa, R.; Ajayakumar, P. V.; Alam, M.; Sastry, M.; Kumar, R. *Angew. Chem. Int. Ed.* **2001**, *40*, 3585. (b) Mukherjee, P.; Senapati, S.; Mandal, D.; Ahmad, A.; Khan, M. I.; Kumar, R.; Sastry, M. *Chembiochem* **2002**, *3*, 461. (c) Kowshik, M.; Ashtaputre, S.; Kharrazi, S.; Vogel, W.; Urban, J.; Kulkarni, S. K.; Paknikar, K. M. *Nanotechnology* **2003**, *14*, 95. (d) Mukherjee, P.; Ahmad, A.; Mandal, D.; Senapati, S.; Sainkar, S. R.; Khan, M. I.; Ramani, R.; Parischa, R.; Ajayakumar, P. V.; Alam, M.; Sastry, M.; Kumar, R. *Angew. Chem. Int. Ed.* **2001**, *40*, 3585. (e) Mukherjee, P.; Ahmad, A.; Mandal, D.; Senapati, S.; Sainkar, S. R.; Khan, M. I.; Parischa, R.; Ajayakumar, P. V.; Alam, M.; Kumar, R.; Sastry, M. *Nano. Lett.* **2001**, 1, 515. (f) Senapati, S.; Ahmad, A.; Khan, M. I.; Sastry, M.; Kumar, R. *Small* **2005**, *1*, 517. (g) Bharde, A. *et al., Small* **2006**, *2*, 135. (h) Bansal, V. *et al., J. Mater. Chem*. **2005**, *15*, 2583. (i) Bansal, V.; Poddar, P.; Ahmad, A.; Sastry, M. *J. Am. Chem. Soc*. **2006**, *128*, 11958.

71. (a) Kowshik, M.; Vogel, W.; Urban, J.; Kulkarni, S. K.; Paknikar, K. M. *Advanced Materials* **2002**, *14*, 815. (b) Kowshik. M. *et al., Nanotechnology* **2003**, *14*, 95.

72. (a) Gardea-Torresdey, J. L.; Parsons, J. G.; Gomez, E.; Peralta-Videa, J.; Troiani, H. E.; Santiago, P.; Yacaman, M. J. *Nano Lett.* **2002**, *2*, 397. (b) Gardea-Torresdey, J. L.; Gomez, E.; Peralta-Videa, J. R.; Parsons, J. G.; Troiani, H.; Yacaman, M. J. *Langmuir* **2003,** *19,* 1357. (c) Shankar, S. S.; Rai, A.; Ahmad, A.; Sastry, M. *J. Colloid Interface Sci.* **2004**, *275*, 496. (d) Shankar, S. S.; Ahmad, A.; Sastry, M. *Biotechnol. Prog.* **2003,** *19,* 1627. (e) Armendariz, V.; Herrera, I.; Peralta-Videa, J. R.; Jose-Yacaman, M.; Troiani, H.; Santiago, P.; Gardea-Torresdey, J. L. *J. Nano. Res.* **2004**, *6*, 377. (f) Ankamwar, B.; Damle, C.; Ahmad, A.; Sastry, M. *J. Nanosci. Nanotech.* **2005**, *5*, 1665. (g) Shankar, S. S.; Rai, A.; Ankamwar, B.; Singh, A.; Ahmad, A.; Sastry, M. *Nature Mater.* **2004**, *3*, 482.

73. (a) Mann, S. *Angew. Chem. Int. Ed.* **2000**, *39*, 3392. (b) Hecky, R. E.; Mopper, K.; Kilham, P.; Degans, E. T. *Mar. Biol.* **1973**, *19*, 323. (c) Nakajima, T.; Volcani, B. E. *Science* **1969**, *164*, 1400. (d) Swift, D.; Wheeler, A. *J. Phycol.* **1992**, *28*, 202.

74. (a) Kröger, N.; Deuzmann, R.; Sumper, M. *Science* **1999**, *286*, 1129. (b) Kröger, N.; Deuzmann, R.; Sumper, M. *J. Biol. Chem.* **2001**, *276*, 26066. (c) Kröger, N.; Deuzmann, R.; Bergsdorf, C.; Sumper, M. *Proc. Natl. Acad. Sci. USA* **2000**, *97*, 14133.

75. (a) Shimizu, K.; Cha, J.; Stucky, G. D.; Morse, D. E. *Proc. Natl. Acad. Sci. USA* **1998**, *95*, 6234. (b) Cha, J.; Shimizu, K.; Zhou, Y.; Christiansen, S. C.; Chmelka, B. F.; Stucky, G. D.; Morse, D. E. *Proc. Natl. Acad. Sci. USA* **1999**, *96*, 361.

76. Kroger, N.; Bergsdorf, C.; Sumper, M. *Eur. J. Biochem.* **1996**, *239*, 259.

77. Kroger, N.; Wetherbee, R. *Protist* **2000**, *151*, 263. (b) Kroger, N.; Lehmann, G.; Rachel, R.; Sumper, M. *Eur. J. Biochem.* **1997**, *250*, 99.

78. (a) Tsuji, M. *et al., Chem. Eur. J*. **2005**, *11*, 440. (b) Callegari, A.; Tonti, D.; Chergui, M. *Nano Lett*. **2003**, *3*, 1565. (c) Yamada, k.; Tokumoto, Y.; Nagata, T.; Mafune, F. *J. Phys. Chem. B* **2006**, *110,* 11751.

79. (a) Murphy, C. J. *et al., J. Phys. Chem. B* **2005**, *109*, 13857. (b) Wiley, B.; Sun, Y.; Mayers, B.; Xia. Y. *Chem. Eur. J*. **2005**, *11*, 454.

80. Sau, T.; Murphy, C. J. *J. Am. Chem. Soc.* **2004**, *126*, 8648.

81. Jana, N. R.; Gearheart, L. A.: Murphy, C. J. *Chem. Commun*. **2001**, 617.

82. Qu, L.; Shi, G.; Wu, X.; Fan, B. *Adv. Mater*. **2004**, *16*, 1200.

83. Huang, C. C.; Yang, Z.; Chang, H. T. *Langmuir* **2004,** *20,* 6089.

84. Xiong, Y.; Chen, J.; Wiley, B.; Xia, Y.; Yin, Y.; Li, Z. Y. *Nano Lett.* **2005**, *5*, 1237.

85. Kuo, C. H.; Chiang, T. F.; Chen, L. J.; Huang, M. H. *Langmuir* **2004**, *20*, 7820.

86. Ahmadi, T. S.; Wang, Z. L.; Green, T. C.; Henglein, A.; El-Sayed, M. A. *Science* **1996**, *272*, 1924.

87. Chen, Y.; Gu, X.; Nie, C. G.; Jiang, Z. Y.; Xie, Z. X.; Lin, C. J. *Chem. Commun.* **2005**, 4181.

88. Teng, X.; Yang, H. *Nano Lett.* **2005**, *5*, 885.

89. Sau, T. K.; Murphy, C. J. *J. Am. Chem. Soc.* **2004**, *126*, 8648.

90. Maillard, M.; Giorgio, S.; Pileni, M. P. *Adv. Mater.* **2002**, *14*, 1084.

91. Jin, R.; Cao, Y. W.; Mirkin, C. A.; Kelly, K. L.; Schatz, G. C.; Zheng, J. G *Science* **2001**, *294*, 1901.

92. Jian, G. H. *et al., J. Mater. Sc*. **2005**, *40*, 1681.

93. Caswell, K. K.; Bender, C. M.; Murphy, C. J. *Nano Lett.* **2003**, *3*, 667.

94. (a) Murray, C. B.; Kagan, C. R.; Bawendi, M. G. *Science* **1995**, *270,* 1335. (b) Vossmeyer, T. *et al., Science* **1995**, *267,* 1476. (c) Wang, Z. L. *Adv. Mater.* **1998**, *10,* 13. (c) Rabani, E.; Reichman, D. R.; Geissler, P. L.; Brus, L. E. *Nature* **2003**, *426*, 271.

95. Tang, J.; Ge, G.; Brus, L. E. *J. Phys. Chem. B* **2002**, *106*, 5653.

96. (a) Collier, C. P.; Vossmeyer, T.; Heath, J. R. *Ann. Rev. Phys. Chem*. **1998**, *49*, 71. (b) Wang, Z. L. *Adv. Mater.* **1998**, *10*, 13.

97. Andres, R. P.; Bielefeld, J. D.; Henderson, J. I.; Janes, D. B.; Kolagunta, *V. R. Science.* **1996**, *273*, 1690.

98. (a) Selvakannan, PR.; Mandal, S.; Pasricha, R.; Sastry, M. *J. Colloid Int. Sci .* **2004**, *279*, 124. (b) Sarathy, K. V.; Raina, G.; Yadav, R. T.; Kulkarni, G. U.; Rao, C. N. R. *J. Phys. Chem. B* **1997**, *101*, 9876. (c) Brown, L. O.; Hutchison, J. E. *J. Phys. Chem. B* **2001**, *105*, 8911. (d) He, S.; Yao, J.; Jiang, P.; Shi, D.; Zhang, H.; Xie, S.; Pang, S.; Gao, H.; *Langmuir.* **2001**, *17*, 1571.

99. Kiely, C. J.; Fink, J.; Brust, M.; Bethell D.; Schiffrin, D. J. *Nature*. **1998**, *396*, 444.

100. Kiely, C. J.; Fink, J., Zheng, J. G.; Brust, M.; Bethell D.; Schiffrin, D. J. *Adv. Mater.* **2000**, *12*, 640.

101. Iler, R. K. *J. Colloid Interface Sci.* **1966**, 21, 569.

102. (a) Decher, G.; Hong, J. D.; Schmitt, J. *Thin Solid Films* **1992**, *210*, 504. (b) Lvov, Y.; Essler, F.; Decher, G.; *J. Phys. Chem.* **1993**, *97*, 13773.

103. Mamedov, A.; Ostrander, J.; Aliev, F.; Kotov, N.A. *Langmuir*. **2000**, *16*, 3941.

104. Hao, E.; Yang, B.; Ren, H.; Qian, X.; Xie, R.; Shen, J.; Li, D. *Mater. Sci. Engg. C.* **1999**, *10*, 119.

105. Lvov, Y.; Ariga, K.; Onda, M.; Ichinose, I.; Kunitake, T. *Langmuir.* **1997**, *13*, 6195.

106. Cassagneau, T.; Mallouk, T. E.; Fendler, J. H. *J. Am. Chem. Soc.* **1998**, *120*, 7848.

107. (a) Maya, L.; Muralidharan, G.; Thundat, T.G.; Kenik, E.A. *Langmuir*. **2000**, *16*, 9151. (b) Feldheim, D. L.; Grabar, K. C.; Natan, M. J.; Mallouk, T. E. *J. Am. Chem. Soc.* **1996**, *118*, 7640. (c) He, J. A.; Valluzzi, R.; Yang, K.; Dolukhanyan, T.; Sung, C.; Kumar, J.; Tripathy, S. K.; Samuelson, L.; Balogh, L.; Tomalia, D. A. *Chem. Mater.* **1999**, *11*, 3268.

108. Kumar, A.; Mandale, A.B.; Sastry, M. *Langmuir.* **2000**, *16*, 6921.

109. Kumar, A.; Mukherjee, P.; Guha, A.; Adyantaya, S. D.; Mandale, A. B.; Kumar, R.; Sastry, M. *Langmuir* **2000**, *16*, 9775.

110. Murphy, C. J. *et al., J. Phys. Chem. B* **2005**, *109*, 13857.

111. (a) Sides, P. J. *Langmuir* **2001**, *17*, 5791. (b) Hayward, R. C.; Saville, D. A.; Aksay, I. A. *Nature* **2000**, *404*, 56.

112. (a) Rogach, A. L.; Kotov, N. A.; Koktysh, D. S.; Ostrander, J. W.; Rogoisha, G. A. *Chem. Mater.* **2000**, *12*, 2721. (b) Velev, O. D.; Kaler, E. W. *Langmuir* **1999**, *25*, 3693.

113. (a) Park, S. J.; Taton, T. A.; Mirkin, C. A. *Science* **2002**, *295*, 1503. (b) Khondaker, S. I.; Yao, Z. *Appl. Phys. Lett.* **2002**, *81*, 4613.

114. (a) Hermanson, K. D.; Lumsdon, S. O.; Williams, J. P.; Kaler, E. W.; Velev, O. D. *Science* **2001**, *294*, 1082.

115. Feldheim, D. L.; Keating, D. C. *Chem. Soc. Rev*. **1998**, 271.

116. Dorogi, M.; Gomez. J.; Osifchin, R; Andress, R. P. Reinfenberger, R. *Phys. Rev. B*, **1995**, *52*, 9071.

117. Duan, C.; Meyerhoff, M. E. *Anal. Chem*. **1994**, *66,* 1369.

118. Bain, C. D.; Whitesides, G. M. *J. Am. Chem. Soc*. **1988**, *110***,** 5897.

119. (a) Laibinis, P. E.; Whitesides, G. M. *J. Am. Chem. Soc*. **1992**, *114***,** 9022. (b) Flink, S.; Van-Veggel, C. J. M.; Reinhoudt, D. N. *Adv. Mater.* **2000**, *12***,** 1315.

120. Prime, K. L.; Whitesides, G. M. *Science* **1991,** *252*, 1164.

121. Sagiv, J. *J. Am. Chem. Soc*. **1980**, *102***,** 92.

122. (a) Heflin, J. R.; Figura, C.; Marciu, D.; Liu, Y.; Claus, R. O. *Appl. Phys. Lett.* **1999**, *74***,** 495. (b) Dannenberger, O.; Buck, M.; Grunze, M. *J. Phys. Chem. B*, **1999**, *103*, 2202.

123. Swami, A.; Kumar, A.; Selvakannan, PR.; Mandal, S.; Pasricha, R.; Sastry, M. *Chem. Mater.* **2003**, *15*, 17.

124. (a) Sastry, M.; Patil, V.; Mayya, K. S. *Langmuir*. **1997**, *13*, 4490. (b) Sastry, M.; Patil, V.; Sainkar, S. R. *J. Phys. Chem. B* **1998**, *102*, 1404. (c) Patil, V.; Sastry, M. *Langmuir*. **2000**, *16*, 2207. (d) Patil, V.; Sastry, M. *Langmuir*. **1997**, *13*, 5511. (e) Sastry, M.; Mayya, K. S.; Patil, V.; Paranjape, D. V.; Hegde, S. G. *J. Phys. Chem. B* **1997**, *101*, 4954. (f) Mayya, K. S.; Sastry, M. *J. Phys. Chem. B* **1997**, *101*, 9790. (g) Mayya, K. S.; Sastry, M. *Langmuir*. **1998**, *14*, 74. (h) Mayya, K. S.; Patil, V.; Sastry, M. *Langmuir.* **1997**, *13*, 2575. (i) Mayya, K. S.; Patil, V.; Sastry, M. *J. Chem. Soc., Faraday Trans.* **1997**, *93*, 3377. (j) Sastry, M.; Mayya, K. S. *J. Nano. Res.* **2000**, *2*, 183.

125. (a) Tian, Y.; Wu, C.; Fendler, J. H. *J. Phys. Chem.* **1995**, *98*, 4913. (b) Zhavnerko, G. K.; Agabekov, V. E.; Gallyamov, M. O.; Yaminsky, I. V.; Rogach, A. L. *Coll. Surf. A* **2002**, *202*, 233.

126. (a) Muramatsu, K.; Takahashi, M.; Tajima, K.; Kobayashi, K. *J. Colloid Interface Sci.*, **2001**, *242*, 127. (b) Lee, D. K.; Kang, Y. S.; Lee, C. S.; Stroeve, P. *J. Phys. Chem. B* **2002**, *106*, 7267.

127. Silvast, W. T.; Wood, O. R. *Microelectron. Engg*. **1988**, *8*, 3.

128. (a) Gibson, J. M.; Berger, S. D. *Appl. Phys. Lett.* **1990**, *57*, 153. (b) Harriot, J. *Vac. Sci. Technol.* **1997**, *B15*, 2130.

129. Gierak, J. *et al., Microelect. Engg*. **2005**, *78*, 266.

130. Weinberger, D. A. *et al., Adv. Mater*. **2000**, *12*, 1600.

131. Whitesides, G. M.; Xia, Y. *Ann. Rev. Mater. Sci*. **1998**, *28*, 153.

132. Song, F.; Cai, Y.; Newby, B, Z. *Appl. Surf. Sci*. **2006**, *253*, 2393.

133. (a) Chirisey, D. B. *Science* **2000**, *289*, 879. (b) Li, Q.; Lewis, J. A. *Adv. Mater*. **2003**, *15*, 1639. (c) Song, J. H.; Edirisinghe, J. R. G.; Evans, J. Am. Ceram. Soc. 1999, 82, 3374. (d) Seerden, K. A. M. *et al., J. Am. Ceram. Soc*. **2001**, *84*, 2514. (e) Morissette, S. L. *et al., J. Am. Ceram. Soc*. **2001**, *84*, 2462.

134. (a) Kwade, A. N.; Wang, J. *Electroanalysis* **2004**, *16*, 101. (b) Shenhar, R.; Norsten, T. B.; Rotello, V. M. *Adv.Mater.* **2005**, *17*, 657. (c)

135. (a) Parka, C.; Yoonb, J.; Thomas, E. L. *Polymer* **2003**, *44*, 6725. (b) Misner, M. J.; Skaff, H. Emirck, T.; Russell, T. P. *Adv. Mater*. **2003**, *15*, 221. (c) Segalman, R. A. *Mater. Sc. Engg. Reports* **2005**, *48*, 191.

136. (a) Correa-Duarte, M. A.; Liz-Marza´n, L. M. *J Mater. Chem*. **2006**, *16*, 22. (b) Kim, B.; Sigmund, W. M. *Langmuir*, **2004**, *20*, 8239. (c) Correa-Duarte, M. A.; Sobal, N.; Liz-Marzán, L. M.; Giersig, M. *Adv. Mater.* **2004**, *16*, 2179.

137. (a) Chakrabarti, R.; Klibanov, A.M. *J. Am. Chem. Soc.* **2003**, *125*, 12531. (b) Babin, J. *et al., Farad. Discuss*. **2005**, *128*, 179. (c) Reches, M.; Gazit, E. *Science* **2003**, *300*, 625.

138. (a) Yuan, J.; Zhai, J.; Jiang, L. *Prog. Chem.* **2004**, *16*, 500. (b) Huang, H.; Yang, X. *Coll. Surf. A* **2004**, *226*, 77.

139. (a) Xiong, X. *et al., Appl. Phys. Lett*. **2006**, *89*, 193108. (b) Huwiler, C. *et al., Nanotechnology* **2005**, *16*, 2045. (c) Yin, Y; Lu, Y.; Gates, B.; Xia, Y. *J. Am. Chem. Soc.* **2001,** *123,* 8718.

140. (a) Pan, M.; Tang, H.; Jiang, S. P.; Liu, Z. *J. Electrochem. Soc.* **2005**, *52*, A1081. (b) Sheeney-Haj-Ichia, L.; Cheglakov, Z.; Willner, I. *J. Phys. Chem B* **2004**, *108*, 11.

141. (a) Mann, S.; Shenton, W.; Li, M.; Connolly, S.; Fitzmaurice, D. Adv. Mater. **2000**, *12*, 46. (b) Behrens, S. *et al., Adv. Mater*. **2002**, *14*, 1621. (c) He, P.; Hu, N.; Rusling, J. F. *Langmuir* **2004**, *20*, 722.

142. (a) Price, R. R.; Dressick, W. J.; Singh, A. *J. Am. Chem. Soc*. **2003**, *125*, 11259. (b) Jung, J. H.; Rim, J. A.; Leeb, S. J.; Leeb, S. S. *Chem. Commun*. **2005**, 468.

143. (a) Gyoryary, E. *et al.,* J. Nanosc. Nanotech. **2004**, 4, 115. (b) Gyoryary, E. *et al., Nano Lett*. **2003**, *3*, 115. (c) Mark, S. S.; Bergkvist, M.; Yang, X.; Angert, E. R.; Batt, C. A. *Biomacromol.***2006**, *7*, 1884. (d) Berry, V.; Saraf, R. F. *Angew. Chem. Int. Ed*. **2005**, *44*, 6668.

144. (a) Perez, J. M.; Simeone, F. J.; Saeki, Y.; Josephson, L.; Weissleder, R. *J. Am. Chem. Soc.* **2003**, *125*, 10192. (b) Huyang, Y. *et al., Nano Lett.* **2005**, *5*, 1429. (c) Chen, C. *et al., Nano Lett.* **2006**, *6*, 1160.

145. (a) Mirkin, C. A.; Letsinger, R. L.; Mucic, R. C.; Storhoff, J. J. *Nature* **1996**, *382*, 607. (b) Alivisatos, A. P. *et al., Nature* **1996**, *382*, 609. (c) Maxwell, D. J.; Taylor, J. R.; Nie, S. *J. Am. Chem. Soc.* **2003**, *124*, 9606. (d) Sastry, M.; Rao, M.; Ganesh, K. N. *Acc. Chem. Res.* **2002**, *35*, 847. (e) Yan, H.; Park, S. H.; Finkelstein, G.; Reif, J. H.; LaBean, T. H. *Science* **2003**, *301*, 1882. (f) Nakao, H. *et al., Nano Lett.* **2003**, *3*, 1391. (g) Sharma, J.; Chhabra, R.; Liu, Y.; Ke, Y.; Yan, H. *Angew. Chem. Intl. Ed.* **2006**, *45*, 730. (h) Khaled, A.; Guo, S.; Li, F.; Guo, P. *Nano Lett.* **2005**, *5*, 1797. (i) Liu, J.; Lu, Y. *J. Fluor.* **2005**, *14*, 343.

146. Watson, J. D.; Crick, F. H. C. *Nature*, **1953**, *171*, 737.

147. (a) Seeman, N. C. *Trends Biotechnol.* **1999**, *17*, 437. (b) Niemeyer, C. M. *Curr. Opin. Chem. Biol.* **2000**, *4*, 609.

148. (a) Kallenbach, N. R.; Ma, R. I.; Seeman, N. C. *Nature* **1983**, *305*, 829. (b) Seeman, N. R. *J. Biomol. Strut. Dynam.* **1985**, *3*, 11. (c) Churchill, M. E. A.;Tullius, T. D.; Kallenbach, N. R.; Seeman, N. C. *Proc. Natl. Acad. Sci. USA.* **1988**, *85*, 4653.

149. (a) Chen, J.; Seeman, N. C. *Nature* **1991**, *350*, 631. (b) Seeman, N. C. *Clin. Chem.* **1993**, *39*, 722. (c) Mao, C.; Sun, W.; Seeman, N. C. *Nature*, **1997**, *386*, 137. (d) Ding, B.; Seeman, N. C. *Science* **2006**, *314*, 1583.

150. (a) He, Y.; Tian, Y.; Chen, Y.; Ribbe, A. E.; Mao, C. *Chem. Commun.* **2007**, *2*, 165. (b) Tian, Y.; He, Y.; Ribbe, A. E.; Mao, C. *Org. Biomol. Chem.* **2006**, *4*, 3404.

151. Adleman, L. *Science*, **1994**, *266*, 1021.

152. (a) Mirkin, C. A. *et al., Nature*, **1996**, *382*, 607. (b) Elghaanian, R. *et al., Science*, **1997**, *277*, 1078.

153. He, L. *et al., J. Am. Chem. Soc.* **2000**, *122*, 9071.

154. Cao, Y. W. C.; Jin, R. C.; Mirkin, C. A. *Science*, **2002**, *297*, 1536.

155. (a) Yguerabide, J.; Yguerabide, E. E. *J. Cell. Biochem*. **2001**, *1*, 71. (b) Yguerabide, J.; Yguerabide, E. E. *Anal. Biochem*. **1998**, *262*, 157.

156. (a) Storhoff, J. J. *et al., J. Am. Chem. Soc*. **1998**, *120*, 1959. (b) Taton, T. A.; Mirkin, C. A.; Letsinger, R. L. *Science*, **2000**, *289*, 1757.

157. (a) Patolsky, F.; Lichtenstein, A.; Willner, I. *Angew. Chem. Int. Ed*. **2001**, *40*, 2261. (b) Patolsky, F. *et al., Chem. Commun*. **2000**, 1025.

158. Bao, P.Y. *et al., Nucleic Acids Res*. **2005**, *33*, e15.

159. Nam, J. M.; Park, S. J.; Mirkin, C. A. *J. Am. Chem. Soc*. **2002**, *124*, 3820.

160. Liu, J.; Lu, Y. *Angew. Chem. Int. Ed*. **2006**, *45*, 90.

161. (a) Richter, J. *et al.,* Adv. Mater. **2000**, *12*, 507. (b) Bensimon, D.; Simon, A. J.; Croquette, V.; Bensimon, A. *Phys. Rev. Lett*. **1995**, *74*, 4754. (c) Cohen, H.; Nogues, C.; Naaman, R.; Porath, D. *Proc. Natl. Acad. Sc. USA.* **2005**, *102*, 11589.

162. (a) Mertig, M.; Ciacchi, C. L.; Seidel, W.; Pompe, W.; Vita, D. E. *Nano Lett*. **2002**, *2*, 841. (b) Richter, J. *et al., Adv. Mater*. **2000**, *12*, 507. (c) Monson. C. F.; Woolley, A. T. *Nano Lett*. **2003**, *3*, 359. (d) Zinchenko, A. A.; Yoshikawa, K.; Baigl, D. *Adv. Mater*. **2005**, *17*, 2820. (e) Stsispura, V. *Nanotechnology* **2006**, *17*, 581. (f) Fu, A. *et al., J. Am. Chem. Soc*. **2004**, *126*, 10832.

163. (a) Zinchenko, A. A.; Yoshikawa, K.; Baigl, D. *Adv. Mater.* **2005**, *17*, 2820. (b) Wei, G.; Zhou, H.; Liu, Z.; Song, Y.; Wang, L.; Sun, L.; Li, Z. *J. Phys. Chem. B* **2005**, *109*, 8738.

164. (a) Braun, E.; Eichen, Y.; Sivan, U.; Ben-Yoseph, G. *Nature* **1998**, *391*, 775-778 (b) Berti, L.; Alessandrini, A; Facci, P. *J. Am. Chem. Soc.* **2005**, *127*, 11216.

165. Kumar, A. *et al., Adv. Mater*. **2001**, *13*, 341.

166. (a) Keren, K.; Krueger, M.; Gilad, R.; Yoseph, G. B.; Sivan, U.; Braun, E. *Science* **2002**, *72*, 72.

167. Keren, K.; Berman, R. S.; Braun, E. *Nano Lett.* **2004**, *4*, 323.

168. Reed, M. I.; Christensen, J. J.; Rytting, J. H. *Chem. Rev*. **1971**, *71*, 439.

169. Luk, K. F. S.; Maki, A. H.; Hoover, R. J. *J. Am. Chem. Soc*. **1975**, *97*, 1241.

170. Demers, L. M.; Ostblom, M.; Zhang, H.; Jang, N. H.; Liedberg, B.; Mirkin, C. A. *J. Am. Chem. Soc.* **2002**, *124*, 11248

171. Gourishankar, A.; Shukla, S.; Ganesh, K. N.; Sastry, M. *J. Am. Chem. Soc*. **2004**, *126*, 13186.

172. (a) Jang, N. H. *Bull. Korean Chem. Soc.* **2002**, *23*, 1790. (b) Hiromi, K.; Petrovykh, D. Y.; Tarlov, M. J.; Whitman, L. J. *J. Am. Chem. Soc.* **2003**, *125*, 9014.

173. (a) Maroun, F.; Ozanam, F.; Magnussen, O. M.; Behm, R. J. *Science* **2001**, *293*, 1811. (b) Heemeier, M.; (b) Carlsson, A. F.; Naschitzki, M.; Schmal, M; Bäumer, M.; Freund, H. J. *Angew. Chem. Int. Ed.* **2002**, *41*, 4073. (c) Alexeev, O. S.; Gates, B. C. *Ind. Eng. Chem. Res.* **2003**, *42*, 1571. (d) Link, S.; Wang,Z. L.; El-Sayed, M. A. *J. Phys. Chem. B* **1999**, *103*, 3529. (e) Sun, S.; Murray, C. B.; Weller, D.; Folks, L.; Moser, A. *Science* **2000**, *287*, 1989.

174. (a) Sinfelt, J. H.; Via, G. H.; Lytle, F. W. *J. Chem. Phys*. **1980**, *72*, 4832. (b) Sinfelt, J. H.; Via, G. H.; Lytle, F. W. *J. Chem. Phys*. **1982**, *76*, 2779. (c) Sinfelt, J. H.; Via, G. H.; Lytle, F. W. *J. Chem. Phys*. **1981**, *75*, 5527.

175. Toshima, N.; Yonezawa, T. *New J. Chem.* **1998**, 1179.

176. (a) Heemier, M. *et al., Angew. Chem. Int. Ed.* **2002**, *41*, 4073. (b) Maye, M. M.; Zheng, W. X.; Leibowitz, F. L.; Ly, N. K.; Zhong, C. J. *Langmuir* **2000**, *16*, 490. (c) Toshima, N.; Lu, P. *Chem. Lett*. **1996**, 729. (d) Schmid, G.; Lehnert, A.; Malm, J. O.; Bovin, J. O. *Angew. Chem. Int. Ed.* **1991**, *30*, 874. (e) Lou, Y.; Maye, M. M.; Han, L.; Luo, J.; Zhong, C, Z. *Chem. Commun.* **2001**, 473.

177. (a) Lu, L. *et al., J. Mater. Chem*. **2004**, *14*, 1005. (b) Genov, D. A.; Sarychev, A. K.; Shalaev, V. M.; Wei, A. *Nano Lett.* **2004**, *4*, 153. (c) Cao, L.; Diao, P.;

Tong, L.; Zhu, T.; Liu, Z. *Chem. Phys. Chem*. **2005**, *6*, 913. (d) Mandal, M. *Curr. Sci*. **2004**, *86*, 556.

178. (a) Tang, D.; Yuan, R.; Chai, Y. *Biotechnol. Bioengg.* **2006**, *94*, 996. (b) Lee, I. *et al.,* **2006**, *128*, 10658. (c)

179. (a) Utamapanya, S.; Klabunde, K. J.; Schlup, J. R. *Chem. Mater*. **1991**, *3*, 175. (b) Maroun, F.; Ozanam, F.; Magnussen, O. M.; Behm, R. J. *Science* **2001**, *293*, 1811. (c) Heemeier, M. *et al., Angew. Chem. Int. Ed.* **2002**, *41*, 4073. (d) Alexeev, O. S.; Gates, B. C. *Ind. Eng. Chem. Res.* **2003**, *42*, 1571. (e) Link, S.; Wang, Z. L.; El-Sayed, M. A. *J. Phys. Chem. B* **1999**, 103, 3529. (f) Sun, S.; Murray, C. B.; Weller, D; Folks, L; Moser, A. *Science* **2000**, *287*, 1989.

180. (a) Luo, K.; Wei, T.; Yi, C. W.; Axnanda, S.; Goodman, D. W. *J. Phys. Chem. B* **2005**, 109, 23517. (b) Lim, S. K. *et al., Appl. Phys. Lett.* **2006**, *88*, 163102. (c) Wu, M. L.; Chen, D. H.; Huang, T. C. *J. Colloid Interface Sci*. **2001**, *243***,** 102. (d) Wu, M. L.; Lai, L. B. *Colloid Surf. A* **2004**, *244*, 149. (e) Mandal, S.; Mandale, A. B.; Sastry, M. *J. Mater. Chem.* **2004**, *14*, 2868. (f) Qian, L.; Yang, X. *Colloid Surf. A* **2005**, *260*, 79.

181. (a) Jackson, J. B.; Halas, N. J. *J. Phys. Chem. B* **2001**, *105*, 2743. (b) Sun, Y.; Xia, Y. *Anal. Chem.* **2002**, *74*, 5297. (c) Kim, S. W.; Kim, M.; Lee, Y. W.; Hyeon, T. *J. Am. Chem. Soc.* **2002**, *124*, 7642.

182. (a) Prodan, E.; Nordlander, P.; Halas, N. J. *Nano Lett.* **2003**, *3*, 1411. (b) Aizpurua, J. *et al., Phy. Rev. Lett.* **2003**, *90*, 057401-1. (c) Schwartzberg, A. M.; Olson, T. Y.; Talley, C. E.; Zhang, J. Z. *J. Phys. Chem. B* **2006**, *110,* 19935.

183. Oldenburg, S. J.; Jackson, J. B.; Westcott, S. L.; Halas, N. J. *Appl. Phys. Lett.***1999**, *111*, 2897.

184. Welch, A.; van Gemert, M. E. Optical-Thermal Response of Laser-Irradiated *Tissue*; Plenum Press: New York, **1995**.

185. (a) Chah, S.; Fendler, J. H.; Yi, J. *J. Colloid Interface Sci.* **2002**, *250*, 142. (b) Caruso, F.; Caruso, R. A.; Mohwald, H. *Science* **1998**, *282*, 1111. (c) Caruso, F.; Spasova, M.; Maceira, V.; Marzan, L. M. *Adv. Mater*. **2001**, *13*, 1090. (d) Oldenburg, S. J.; Averitt, R. D.; Westcott, S. L.; Halas, N. J. *Chem. Phys. Lett.* **1998**, *248*, 243.

186. Murthy, V. S.; Cha, J. N.; Stucky, G. D.; Wong, M. S. *J. Am. Chem. Soc.* **2004**, *126*, 5292.

187. Yin, Y.; Rioux, R. M.; Erdonmez, C. K.; Hughes, S.; Somorjai, G. A.; Alivisatos, P. *Science* **2004**, *304*, 711.

188. Qian, L.; Yang, X. *Colloids and Surfaces A* **2005**, *260*, 79.

189. Dhas, N. A.; Suslick, K. S. *J. Am. Chem. Soc*. **2005**, *127*, 2368.

190. Liu, Q. *et al., Adv. Mater*. **2005**, *17*, 1995.

191. Dabin, Y *et al., J. Phys. Chem. B* **2006**, *110*, 21667.

192. Murthy, V. S.; Cha, J. N.; Stucky, G. D.; Wong, M. S. *J. Am. Chem. Soc*. **2004**, *126*, 5292.

193. Sun, Y.; Meyers, B.; Xia, Y. *Adv. Mater*. **2004**, *15*, 651.

194. Liang, H. P.; Guo, Y. G.; Zhang, H. M.; Hu, J. S.; Wan, L. J.; Bai, C. L. *Chem. Commun*. **2004**, 1496.

195. Metraux, G. S.; Cai, Y. C.; Jin, R.; Mirkin, C. A. *Nano. Lett.* **2003**, *3*, 519.

196. Selvakannan, P. R.; Sastry, M. *Chem Commun*. **2005**, 1684.

197. Yin, Y.; Erdonmez, C.; Aloni, S.; Alivisatos, A. P. *J. Am. Chem. Soc.* **2006** *128*, 12671.

198. Lee. W. R. *et al., J. Am. Chem. Soc.* **2005**, 1*27*, 16090.

199. Loo, C.; Lowery, A.; Halas, N.; West, J.; Drezek, R. *Nano Lett*. **2005**, 5, 709.

200. Hirsch, L. R.; Jackson, J. B.; Lee, A.; Halas, N. J.; West, J. L. *Anal. Chem*. **2003**, *75*, 2377.

201. Chen, J.; Saeki, F.; Wiley, B.; Cang, H.; Cobb, M. J.; Li, Z.; Au, L.; Zhang, H.; Kimmey, M.J.; Li, X.; Xia, Y. *Nano Lett.* **2005**, *5*, 473.

202. Liao, H.; Nehl, C. L.; Hafner, J. H. *Nanomedicine* **2006**, *1*, 201. (b) Tovmachenko, O. G.; Graf, C.; Heuvel, D. J.; Blaaderen, A.; Gerristen. H. *Adv. Mater.* **2006**, *18*, 91.

203. (a) Graf, C.; Blaaderen, A. *Langmuir* **2002**, *18,* 524. (b) Skirtach, G. A. *et al., Nano Lett.* **2005**, *5*, 1371.

204. Sun, y.; Xia, Y. *Anal. Chem.* **2002**, *74*, 5297.

205. Hale, G. D.; Jackson, J. B.; Lee, T. R.; Halas, N. J. *Appl. Phys. Lett.* **2000**, *78*, 1502.

206. Oldenburg, S. J.; Westcott, S. L.; Averitt, R. D.; Halas, N. J. *J. Chem. Phys.* **1999**, *111*, 4729.

207. Sershen, S. R.; Westcott, S. L.; Halas, N. J.; West, J. L. *J. Biomed. Mat. Res.* **2000**, *51*, 293.

208. (a) Sershen, S. R.; Westcott, J. L.; West, J. L.; Halas, N. J. *Appl. Phys. B* **2001**, *73*, 379. (b) Sershen, S. R.; Westcott, S. L.; Halas, N. J.; West, J. L. *Appl. Phys. Lett.* **2002**, *80*, 4609.

209. (a) Kim, S. W.; Kim, M.; Lee, W. Y.; Hyeon, T. *J. Am. Chem. Soc.* **2002**, *124*, 7642. (b) Liang, H. P.; Zhang, H. M.; Hu, J. S.; Guo, Y. G.; Wan, L. J.; Bai, C. L. *Angew. Chem. Int. Ed.* **2004**, *43*, 1540.

210. Teng, X.; Liang, X.; Rahman, S.; Hong, Y. *Adv. Mater*. **2005**, *17*, 2237

211. Zhong, K.; Jin, P.; Chen, Q. *J. Nanomaterials*. **2006**, *37375*, 1.

212. Ohmori, M.; Matijevic, E. *J. Colloid Interface Sci*. **1992**, *150*, 594.

213. (a) Zhong, Z; Yin, Y.; Gates, B.; Yia, Y. *Adv. Mater*. **2000**, *12*, 206. (b) Bourlinos, A. B.; Karakassides, M. A.; Petridis, M. *Chem. Commun*. **2001**, 1518. (c) Zhang, D.; Qi, L.; Ma, J.; Cheng, H. *Adv. Mater*. **2002**, *14*, 1499. (d) Caruso, F.; Caruso, R. A.; Mohwald, H. *Chem. Mater.* **1999**, *11*, 3309. (e) Kawahashi, N.; Matijevic, E. *J. Colloid Interface Sci.* **1991**, *143*, 103.

Chapter II

Characterization Techniques

This chapter discusses the basic working principle of the various characterization techniques, which were used during the course of the presented work.

2.1 Introduction

This thesis broadly deals with two different systems pertaining to the nanoparticles. The first part is the study of the interactions of nanoparticle precursors with DNA and applying the outcomes of such studies in fabricating patterned nanowires. The second part of the thesis is the synthesis of porous metallic nanostructures and their biological applications.

Various characterization techniques have been used during the course of the work presented in this thesis including spectroscopic measurements such as Ultra Violet-visible-Near Infra Red (UV-vis-NIR) spectroscopy, Fluorescence spectroscopy, X-ray photoelectron spectroscopy (XPS); microscopy techniques such as Transmission Electron Microscopy (TEM), High resolution TEM (HRTEM), Atomic Force Microscopy (AFM), Confocal Laser Scanning Microscopy (CLSM), and Phase Contrast Microscopy. Besides, other techniques such as Isothermal Titration Calorimetry (ITC), Electron Dispersive Microanalysis (EDX), Fluorescence Activated Cell Sorting (FACS) and conductivity measurements have also been used. This chapter explains the basic principles of these techniques and the instruments.

2.2 UV-vis-NIR absorption spectroscopy

Absorption spectroscopy is one of the most important analytical tools [1]. Most molecules and materials show characteristic absorption in different regions of the electromagnetic spectrum, which is therefore used as a signature for their identification and analysis.

Any molecular system possesses three types of energy namely, electronic (E_{ele}), vibrational (E_{vib}) and rotational (E_{rot}) with decreasing magnitude in same order for a system. Absorption of energy leads to transition of electron from the ground state to an excited state. The absorption peak thus obtained is broad, smooth and never very sharp due to the fact that the electronic absorption is accompanied with a corresponding change in the vibrational and rotational energies as well. The relationship between the energy absorbed in an electronic transition and the frequency, ν, wavelength, λ and wavenumber, $\bar{\nu}$ of the radiation producing the transition is

$$\Delta E = h\nu = hc/\lambda = h.\ \bar{\nu}.c$$

where, h is Planck's constant, c is the velocity of light and ΔE is the energy absorbed in an electronic transition in a molecule from a low-energy state (ground state) to a high energy state (excited state). The position of absorption maxima for a molecule depends on the difference in the energy of the ground state level to that of excited state; larger the difference between the energies, higher is the frequency of absorption and thus smaller will be the wavelength. Absorption band shows two important characteristics: position of the band which depends on the energy difference between electronic level and intensity which depends on the interaction between the radiation and electronic system as well as on the energy difference between the ground and excited state. A convenient expression, which relates the absorbance with the path length that the radiation travels within the system and the concentration of the species, can be derived from the Lambert-Beer law and is given as,

$$A = a.b.c \qquad \ldots\ldots\ldots(2.1)$$

where, A is measured absorbance, a is the absorptivity, b is the path length and c is the concentration of the analyte.

Noble metal nanoparticles absorb strongly in the visible region due to surface plasmon resonance, which was discussed briefly in the previous chapter. Hence the UV–visible absorption spectroscopy is a primary characterization tool to study the metal nanoparticles formation [2]. All the UV–Visible absorption spectra presented in the thesis was carried out on Jasco V-570 dual beam spectrophotometer and HP diode array spectrophotometer operated at a resolution of 2nm [2].

In the present work, the formation of silver nanoparticles in the presence of nucleobases and short oligonucleotides was followed by measuring the UV-vis absorption. Similarly, the transmetalation reaction leading to the formation of porous gold nanoparticles was kinetically followed by the UV-vis-NIR absorption spectroscopy. Bacterial growth in the presence of different nanoparticles was also followed by recording the single wavelength spectra from the bacterial cultures.

2.3 Fluorescence spectroscopy

Fluorescence is generated when a substance absorbs light energy at a short (higher energy) wavelength and then emits light energy at a longer (lower energy) wavelength. At room temperature most molecules occupy the lowest vibrational level of the ground electronic state, and on absorption of light they are elevated to the excited states. Having absorbed energy and reached one of the higher vibrational levels of an excited state, the molecule rapidly loses its excess of vibrational energy by collision and falls to the lowest vibrational level of the excited state. In addition, almost all molecules occupying an electronic state higher than the second undergo internal conversion and pass from the lowest vibrational level of the upper state to a higher vibrational level of a lower excited state, which has the same energy. From there the molecules again lose energy until the lowest vibrational level of the first excited state is reached. From this level, the molecule can return to any of the vibrational levels of the ground state, emitting its energy in the form of fluorescence.

The length of time between absorption and emission is usually relatively brief, often on the order of 10^{-9} to 10^{-8} seconds. The fluorescence event can be shown by means of a Jablonski Diagram, named for the Ukranian born physicist Aleksander Jablonski [2] (Fig.1).

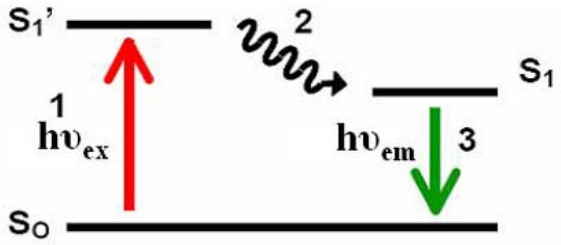

Figure 2.1 *Jablonski Diagram of a fluorescence event.*

As shown, in Stage 1 a photon of given energy $h\upsilon_{ex}$ is supplied from an outside source such as a laser or a lamp. The fluorescent molecule, lying in its ground energy state S_0, absorbs the energy creating an excited electronic singlet state S_1'. This excited state will last for a finite time, usually one to ten nanoseconds, during which time the fluorescent molecule undergoes conformational changes and can be subject to myriad potential interactions with its molecular environment. The first

phase of Stage 2 is characterized by the fluorophore partially dissipating some of the absorbed energy creating a relaxed singlet state S_1. It is from this state that the fluorophore will enter the second phase, the emission of energy, $h\upsilon_{em}$. Finally, in Stage 3, the fluorophore will return to its ground state, S_0.

In the present work, fluorescence measurements were performed to evaluate binding of Propidium Iodide (PI) on the surface of borohydride reduced gold nanoparticles and porous gold nanoparticles. Fluorescence measurements of the supernatants collected from the porous and solid gold nanoparticle solutions were performed on a Fluoroskan Ascent fluorimeter by recording the emission at 590 nm after exciting the solutions at 485 nm.

2.4 X-ray photoelectron spectroscopy (XPS)

XPS or Electron Spectroscopy for Chemical Analysis (ESCA) is a surface sensitive technique, which is used extensively for determining compositions and oxidation states. It also gives accurate quantitative information of the surface of the sample. Photoelectron spectroscopy uses monochromatic source of radiation (*i.e.* photons of fixed energy given by relation E = *hν*). In XPS, the photon of energy *hν* is absorbed by an atom *A* in a solid, leading to the ionization and emission of a core (inner shell) electron. The kinetic energy distribution of the emitted photoelectrons is measured and a photoelectron spectrum is obtained. The overall process of photo-ionization can be demonstrated as:

$$\mathbf{A + h\nu = A^{+} + e^{-}} \qquad \text{……(2.6)}$$

According to the law of conservation of energy,

$$\mathbf{E\,(A) + h\nu = E\,(A^{+}) + E\,(e^{-})} \qquad \text{……(2.7)}$$

Since the entire energy of the emitted electron will be kinetic energy (KE), equation 2.7 can be rearranged as follows,

$$\mathbf{KE = h\nu - [E\,(A^{+}) - E\,(A)]} \qquad \text{……(2.8)}$$

The term in the square bracket represents the energy difference between the ionized and the atomic state of an atom, known as the binding energy (BE), which is characteristic for an atom. The equation 2.8 is thus simplified to

$$\mathbf{KE = h\nu - BE} \quad \ldots\ldots\ldots \quad (2.9)$$

The binding energy is measured with respect to the fermi energy level in solids and thus equation 2.9 is modified incorporating the work function (ϕ) term for the solids.

$$\mathbf{KE = h\nu - BE - \phi} \quad \ldots\ldots\ldots \quad (2.10)$$

Thus, from the equation 2.10, employing the photon of known energy hν and measuring the kinetic energy of the emitted electron and with known work function ϕ, it is possible to find the binding energy, a characteristic signature of an element. Electron traveling out through the material undergo inelastic collision with the bound electron in the material resulting into energy loss. This gives a strong background to the spectrum rather than a very sharp peak. It is due to this reason that the electrons, which come out from near the surface, give the true information about the chemical composition. Such electrons are emitted from very short distance inside the material (<100 nm) and thus XPS is known to be a surface sensitive technique where the emitted photoelectrons are detected for analysis [3].

The binding energy of an electron does not only depend upon the energy level of emission but also upon the oxidation state of the concerned atom and the local surrounding to that atom. A change in either of the two factors results in a shift of the peak for that atom in the spectrum, which is called as chemical shift. Atoms of a higher positive oxidation state exhibit a higher binding energy due to the extra coulombic interaction between the photo-emitted electron and the ion core. Similarly, presence of an electronegative atom in the surrounding of the atom in question, a net partial positive charge is imparted to that atom. Thus, emission of an electron from such an atom will require higher energy, which shifts the peak to higher binding energy. This ability to discriminate between different oxidation states and chemical environments is one of the major strengths of the XPS technique.

In the work presented here, XPS has been used to confirm the formation of Au (0) from chloroaurate ions by transmetallation against silver nanoparticles. XPS does not only give a signal for presence of Au (0) in the bimetallic film but also shows the presence of Ag^{+} ions, which are formed due to the process of oxidation during the course of transmetallation. Besides, the formation of the alloy phase has also been

indicated by the appearance of the low binding energy bands. The Samples were prepared by drop-coating the solution on Si (111) and copper substrate. XPS measurements were carried out on a VG Microtech ESCA 3000 instrument at a base pressure better than 1 x 10^{-9} Torr with un-monochromatized Mg Kα radiation (1253.6 eV energy). The measurements were made in the constant analyzer energy (CAE) mode at pass energy of 50 eV and electron takeoff angle (angle between electron emission direction and surface plane) of 60°. This leads to an overall resolution of ~ 1 eV in the measurements. The chemically distinct components in the core level spectra were resolved by a non-linear least squares fitting algorithm after background removal by the Shirley method [3].

2.5 Phase contrast microscopy

Phase contrast microscopy finds application in generating high contrast image of the unstained transparent specimens such as living cells, microorganisms, thin tissue slices, lithographic patterns, and sub-cellular particles (such as nuclei and other organelles) [4]. It imparts contrast to the biological sample by transforming the phase difference of light, due to the difference in the refractive index between different sub-cellular systems, into difference in the amplitude of light. When a light ray passes through a sample with areas of different optical paths, it is retarded in phase even though the amplitude of the light remains same. Since the human eyes cannot distinguish phase difference, the information is lost. Phase contrast microscope converts this phase difference into amplitude difference to generate the contrast visible to human eye. The various components of a phase contrast microscope have been shown in the Figure 2.4.

A phase contrast has two unique components namely the “phase plate” which retards the incoming light to ¼ of wavelength in a centered, ring shaped area at the back focal plane of the objective lens and a matching “phase annulus” in the condenser consisting of a clear ring on a black field. The matching phase plate and annulus allows the direct unmodified light to pass through and be retarded by ¼ of wavelength. Since the intensity of the diffracted light will be diminished slightly due to the absorption by the sample, a neutral density coating on top of the phase ring attenuates undiffracted, background light to balance total illumination. The light ray

interacting with the sample diffract away from and do not impinge on to the phasing area of the phase plate but are focused by the objective on the image plane. It is due to this difference in the optical path of the light interacting and non-interacting with the sample that retards the refracted wave by ¼ of wavelength in phase. Light that does not interact with the specimen is collected by the objective, passed through the phase plate ring, and is retarded exactly ¼ of wavelength. Since the phase shift is not detectable to human eye, the resulting image on the image plane in the microscope appears as a normal bright background.

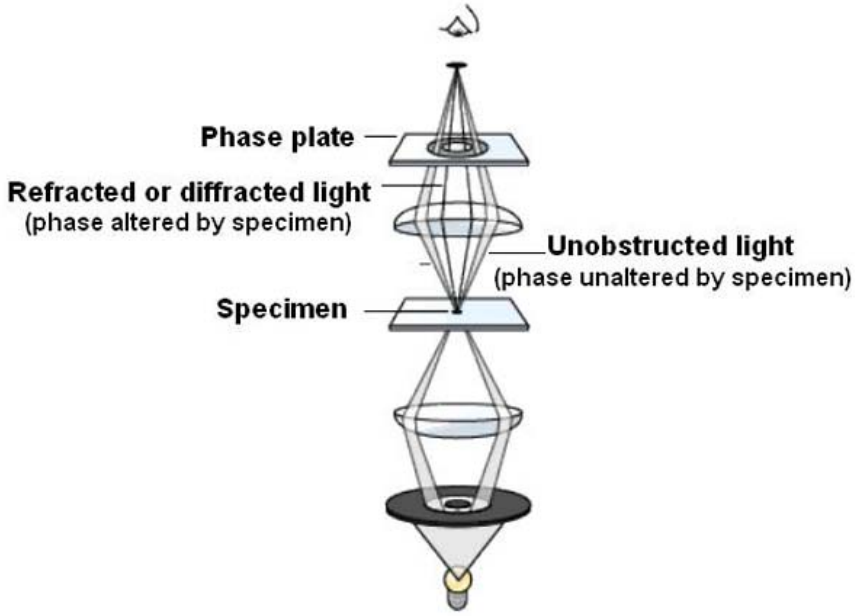

Figure 2.2 *Schematic showing different components of a phase contrast microscope (Image courtesy: http://nobelprize.org/educational_games/physics/microscopes/phase/index.html)*

Contrarily, the light passing through the specimen gets scattered due to edges and irregularities causing retardation in phase. The diffracted light diverges from the specimen filling the back focal plane of the objective and is resolved on the image plane in the microscope. The undiffracted and diffracted light interacts at the image plane causing wave interference. In negative phase contrast, a constructive interference occur between the two at the image plane resulting into bright areas depending on the difference in the refractive index within the specimen against the background of the undiffracted light. In the presented work, an inverted phase contrast microscope has been used where the specimen is positions at the top and the source of

light comes from the bottom. Such an arrangement makes the visualization of the living animal cells in culture medium easier.

In this thesis, the CHO cells were studied under the phase contrast microscope after being exposed to different concentrations/ time intervals of porous gold nanoparticles to estimate their cytotoxicity on mammalian cell lines.

2.6 Fluorescence Microscopy

Fluorescence microscopy is used to study specimens, which can be made to fluoresce. It is based on the phenomenon that certain material emits energy detectable as visible light when irradiated with the light of a specific wavelength [5]. The sample can either be fluorescing in its natural form like chlorophyll, proteins and some minerals, or treated with fluorescing chemicals or a fluorophore such as green fluorescent protein (GFP).

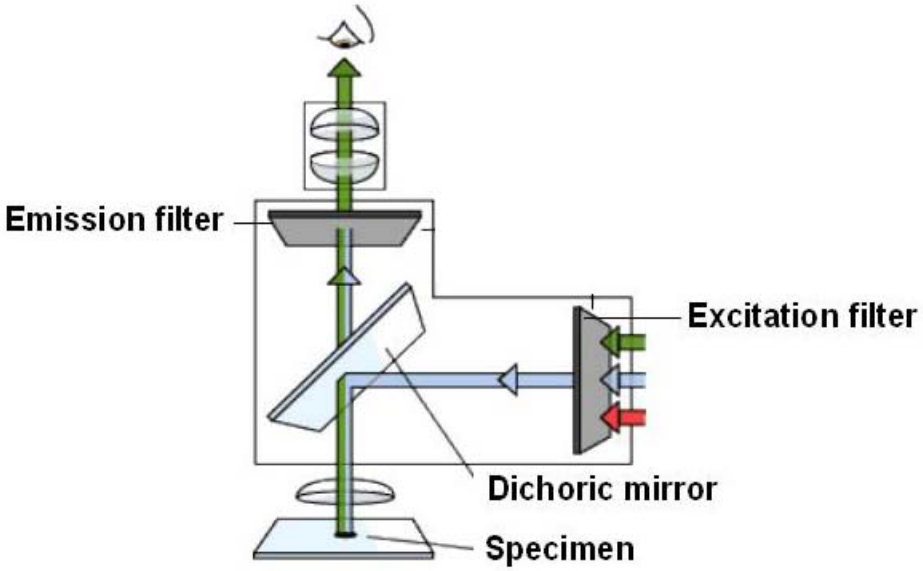

Figure 2.3 *Schematic showing the components of a fluorescence microscope. (Image courtesy: http://nobelprize.org/educational_games/physics/microscopes/fluorescence/index.htm/)*

The specimen is illuminated with light of a specific wavelength, which is absorbed by the fluorophore, causing it to emit longer wavelengths of light. The illumination light is separated from the much weaker emitted fluorescence through the use of an emission filter. The fluorescing areas can be observed in the microscope and shine out against a dark background with high contrast. Typical components of a

fluorescence microscope are the light source (Xenon or Mercury arc discharge lamp), the excitation filter, the dichoric mirror and the emission filter (Figure 2.3). The filters and the dichoric are chosen to match the spectral excitation and emission characteristics of the fluorophore used to label the specimen.

In the work presented in the thesis, a Nikon Eclipse E 600 fluorescence microscope was used to visualize CHO cells stained with PI-nanoparticles conjugates to establish the different quantities of PI loaded on the different metal nanoparticle systems.

2.7 Confocal Laser Scanning Microscopy (CFLSM)

Confocal microscopy is an imaging technique used to increase micrograph contrast and /or to reconstruct three-dimensional images by using a spatial pinhole to eliminate out-of-focus light in specimens that are thicker than focal plane [6]. In traditional wide-field epi-fluorescence microscopy, the entire specimen is subjected to intense illumination from an incoherent mercury or xenon arc-discharge lamp, and the resulting image of secondary fluorescence emission can be viewed directly in the eyepieces or projected onto the surface of an electronic array detector or traditional film plane. In contrast to this simple concept, the mechanism of image formation in a confocal microscope is fundamentally different.

The confocal principle in epi-fluorescence laser scanning microscopy is diagrammatically presented in Figure 2.4. Coherent light emitted by the laser system (excitation source) passes through a pinhole aperture that is situated in a conjugate plane (confocal) with a scanning point on the specimen and a second pinhole aperture positioned in front of the detector (a photomultiplier tube). As the laser is reflected by a dichromatic mirror and scanned across the specimen in a defined focal plane, secondary fluorescence emitted from points on the specimen (in the same focal plane) pass back through the dichromatic mirror and are focused as a confocal point at the detector pinhole aperture. The significant amount of fluorescence emission that occurs at points above and below the objective focal plane is not confocal with the pinhole (termed Out-of-Focus Light Rays in Figure 2.5) and forms extended airy disks in the aperture plane. Because only a small fraction of the out-of-focus fluorescence

emission is delivered through the pinhole aperture, most of this extraneous light is not detected by the photomultiplier and does not contribute to the resulting image.

The dichromatic mirror, barrier filter, and excitation filter perform similar functions to identical components in a wide-field epi-fluorescence microscope. Refocusing the objective in a confocal microscope shifts the excitation and emission points on a specimen to a new plane that becomes confocal with the pinhole apertures of the light source and detector.

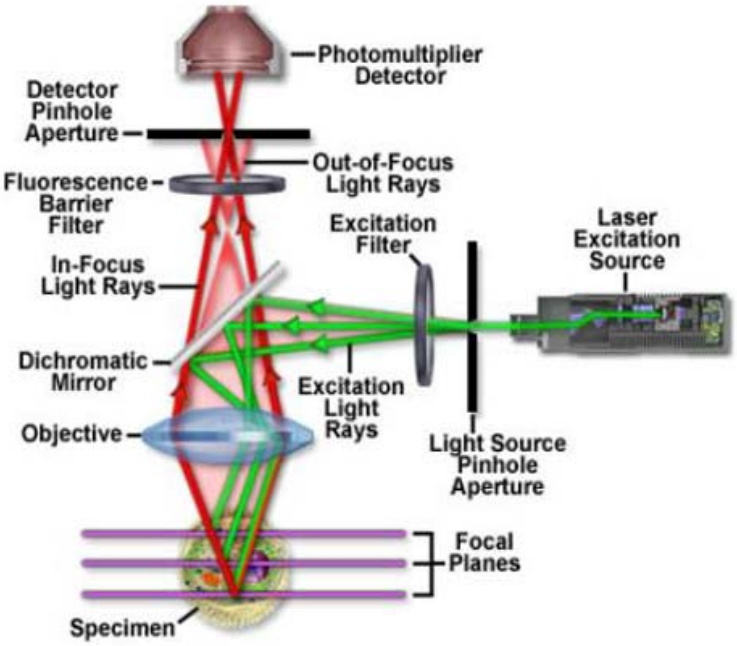

Figure 2.5 *Optical configuration of a typical laser scanning confocal microscope. (Image courtesy: http://www.olympusfluoview.com/theory/confocalintro.html)*

In the work presented in the thesis, CLSM was used to image fixed and live CHO cells stained with different flourophores loaded on the porous gold nanoparticles. All the confocal images were recorded on an LSM 510 Zeiss workstation (Carl Zeiss Meditec AG, Jena, Germany) equipped with an argon air-cooled laser (LASOS Lasertechnik GmbH, Jena, Germany).

2.8 Transmission Electron microscopy (TEM)

Electron microscopes function exactly as their optical counterparts except that they use a focused beam of electrons instead of light to "image" the specimen and can yield information on topography, morphology, composition and crystallographic

information of materials on a very fine scale [7]. Electron Microscopes were developed due to the limitations of light microscopes, which are limited by the physics of light to 500x or 1000x magnification and a resolution of 0.2 micrometers.

Resolving power of a microscope is given by the following formula

$$d = 0.5 \lambda / \sin \alpha$$

Thus, smaller the wavelength of the source, higher will be the resolution of the system. Since the wavelength of electrons is in the few angstroms, in principle, the resolution of electron microscope could go up to few angstroms. There are two different types of electron microscopes, transmission electron microscope and scanning electron microscope.

In the **transmission electron microscopy**, much smaller wavelength electrons (0.03 Å) are used instead of photons (λ > 1000 Å) providing much higher resolution. During TEM analysis, a thin sample is bathed with a collimated beam of accelerating electrons uniformly over the illuminated area. Electrons being charged in nature, can be easily deflected using an external electric or magnetic field and can be accelerated using external potential. As the electrons travel through the sample, they are either scattered or are transmitted unaffected through the sample. The probability of scattering is described in terms of the interaction cross-section or the mean free path and can be elastic or inelastic. This results into a non-uniform distribution of electrons in the beam that comes out of the sample, which contains all the structural information of the sample.

The scattered (diffracted) electrons deflected away from the optical axis of the microscope are blocked using an aperture and thus the transmitted electron beam generates a contrast on the fluorescent screen depending on its varying intensity. In the case of nanomaterials, the crystalline structures interact with the electron beam mainly by diffraction rather than absorption, though the intensity of the transmitted beam depends largely on the density and thickness of the material though which it passes. The intensity of the diffraction thus depends on the orientation of the planes of atom in the crystal relative to the electron beam. Angular distribution of electrons due to diffraction can be viewed in the form of scattering patterns, usually called diffraction patterns, and spatial distribution of electrons can be observed as contrast in

images of the sample. Figure 2.6 shows the layout of the various components of a transmission electron microscope.

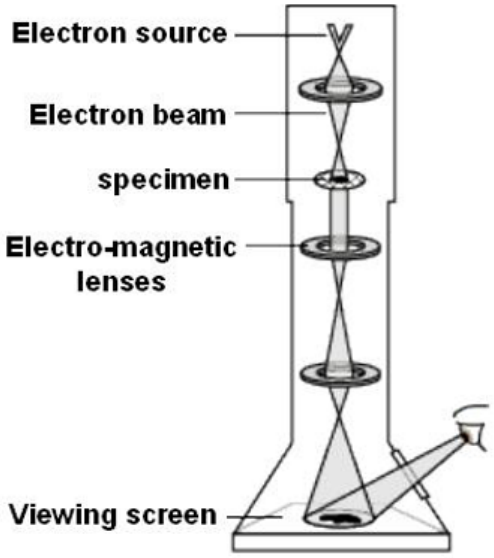

Figure 2.6 *Configuration of a typical transmission electron microscope (TEM). (Image courtesy: http://nobelprize.org/educational_games/physics/microscopes/tem/index.html).*

In this thesis, TEM has been extensively used to visualize different types of nanoparticles and kinetically follow the changes during transmetalation process. It has also been employed to obtain the selected area electron diffraction patterns that lead to the identification of nanoparticles composition. The TEM measurements were done on a JEOL model 1200EX instrument operated at an accelerating voltage of 80 kV. High resolution transmission electron microscopy (HRTEM) of the porous gold and palladium nanostructures prepared on carbon coated grids were carried on a Technai G^2 F-30 model operated at an accelerating voltage of 300 kV.

2.9 Scanning probe microscopy (SPM)

Scanning probe microscopy (SPM) is a branch of microscopy that forms images of surfaces using a physical probe that scans the specimen. An image of the surface is obtained by mechanically moving the probe in a raster scan of the specimen, line by line, and recording the probe-surface interaction as a function of position [8]. There are many advantages associated with SPM such as the resolution of the microscopes is not limilted by diffraction, but only by the size of the probe-sample interaction volume, which can be as small as a few picometer. Also, the

interaction can be used to modify the sample to create small structures. Among the various types of SPM, atomic force microscopy has been desribed below.

Atomic force microscope (AFM) is a high-resolution scanning probe microscope, with demonstrated resolution of fractions of an Angstrom. It utilizes a sharp tip at the end of cantilever that moves over the sample in a raster scan and bends in response to the force between the tip and the sample. Initial AFM was equipped with a scanning tunnelling microscope at the end of the cantilever to monitor its bending, but now, an optical lever technique is employed for the purpose, as shown in the Figure 2.7. As the cantilever bends, light from the laser is reflected onto the split photo-diode.

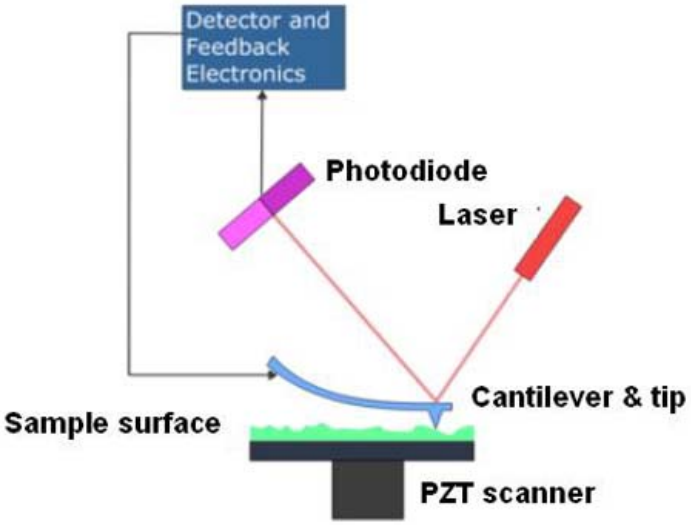

Figure 2.7 *Diagram showing the working of an AFM cantilever [7]. (Image courtesy: http://en.wikipedia.org/wiki/Atomic_force_microscopy)*

The difference in the signal is used as a measure of bending of the cantilever. The bending of the cantilever obeys the Hooke's law for small displacements and so the force between the tip and the sample can be calculated. A device made of piezo-electric ceramic in the form of a tube scanner is used to control the movement of the tip or the sample. The scanner is capable of sub-angstrom level resolution in the x, y or z direction, z being the direction perpendicular to the sample.

The AFM can be operated in two modes namely, with feedback control mode and without feedback control mode. The feedback control mode works at a constant force between the tip and the sample where the piezo which moves sample (or the tip)

responds to any change in the force between the sample and tip and alters the separation between the two to restore the original value of force. This measurement is known as height mode measurement and enables reliable topographical analysis of the sample. When the feedback control mode is off, the measurement is performed at constant height (deflection mode), which is useful in high-resolution analysis of the samples that are extremely flat. AFM incorporates several refinements such as sensitive detection, flexible cantilever, sharp tips, high resolution precise tip-sample positioning and force feedback, which enables it to achieve atomic level resolution. Since the imaging process uses the force of interaction of the atoms on the tip to that of the sample, AFM is used for imaging even the non-conducting samples.

AFM measurements can be performed in contact, tapping or non-contact modes, the difference being the extent of tip-sample interaction during the measurement. Contact mode AFM is the most commonly used method where the tip remains in close contact with the sample during the process of scanning. The force of interaction between the tip and the sample lies in the repulsive regime in the intermolecular force curve. Contact mode AFM provides 3-dimensional information of the sample non-destructively with 1.5 nm lateral and 0.05 nm vertical resolution. Tapping mode is generally used for imaging soft and poorly immobilized samples. The tip is oscillated at its resonating frequency and positioned over the sample so that it contacts the sample for a short time interval during oscillation. In the non-contact mode, the tip is oscillated at a distance from the sample so that the two are no longer in contact.

In this thesis, contact mode AFM imaging has been used to study the thickness of silver nanotriangles synthesized by a seedless-surfactant less chemical method and the porous triangles formed by the transmetalation process. The AFM measurements were done in the contact mode on a VEECO Digital Instruments multimode scanning probe microscope equipped with a Nanoscope IV controller at a scan rate of 5.086 Hz.

2.10 Energy dispersive X–rays analysis (EDX)

EDX is a chemical microanalysis technique, used most commonly in conjunction with SEM or HRTEM and utilizes the X–rays emitted from the sample during bombardment by an electron beam [9]. EDX is used to characterize the

elemental composition of the analyzed volume. Features or phases as small as about 1 μm can be analyzed. When the electron beam of SEM bombards the sample, electrons are ejected from the atoms comprising the sample's surface and another electron from a higher shell fills up the resulting electron vacancy. In this process, an X–ray photon is emitted in order to balance the energy difference between the two electrons. The EDX X–ray detector measures the number of emitted X–rays versus their energy. The energy of the emitted X–rays is characteristic of the element from which the X–ray is emitted. A spectrum of the energy versus relative counts of the detected X–rays is obtained and evaluated for qualitative and quantitative determinations of the elements (atomic number _ 4) present in the sampled volume. Combining the EDX system with the SEM allows the identification at microstructural level, of compositional gradients at grain boundaries, second phase impurities and inclusions. In the scanning mode, the SEM/EDX unit can be used to produce maps of element location, their concentration, and distribution.

In this thesis, we have used EDX measurements to determine the chemical composition (both qualitative and quantitative) of bimetallic nanoparticles formed by the galvanic replacement reactions. EDX was performed using a Phoenix EDX, attached to Leica Stereoscan – 440 SEM.

2.11 Isothermal Titration Calorimetry (ITC)

Isothermal titration Calorimetry is an extremely sensitive technique, which measures the thermodynamic parameters of a reaction between two molecules in solution and is most commonly used to determine interactions between biological molecules and their ligands including drugs, substrates, inhibitors etc [9].

An ITC instrument consist of two identical cells made of a highly efficient thermal conducting material surrounded by an adiabatic jacket (Figure 5.7). The temperature difference between the two cells is monitored via sensitive thermocouple circuits. Prior to the reaction, a constant power (<1 mW) is supplied to the reference cell. This directs a feed back circuit activating a heater located in the sample cell. During the titration, the ligand is titrated into the sample cell in precisely known aliquots, causing heat to evolve (exothermic reaction) or taken up (endothermic reaction). The time dependent power requirement to retain the temperatures of the cell

is measured. In an exothermic reaction, the temperature in the sample cell increases upon addition of ligand. This causes the feedback power to the sample cell to be decreased in order to maintain an equal temperature between the two cells while opposite occurs in an endothermic process.

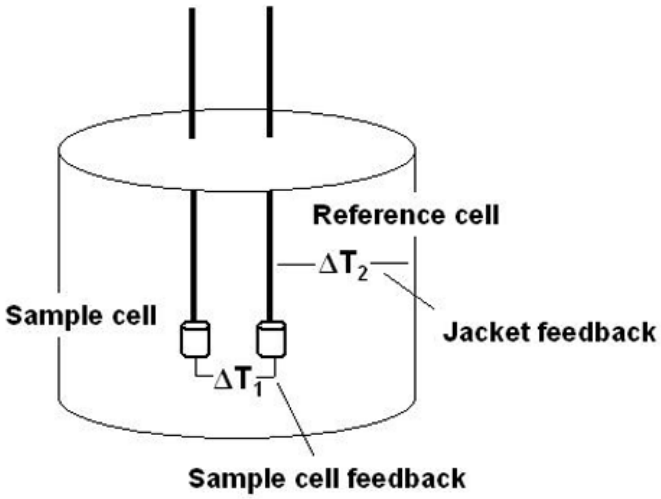

Figure 5.7 *Components of the ITC instrument (Image courtesy: http://www.microcal.com)*

Observations are plotted as the power in μcal/sec needed to maintain the reference and the sample cell at an indentical temperature. This power is given as a function of time in seconds. As a result, the raw data for an experiment consists of a series of spikes of heat flow (power), with every spike corresponding to a ligand injection. These heat flow spikes/pulses are integrated with respect to time, giving the total heat effect per injection. The pattern of these heat effects as a function of the molar ratio [ligand]/[macromolecule] can then be analysed to give the thermodynamic parameters of the interaction under study. The entire experiment takes place under computer control.

ITC is a quantitative technique that can directly measure the binding affinity (K_a), enthalpy changes (ΔH), and binding stoichiometry (n) of the interaction between two or more molecules in solution. In this chapter ITC measurements have been used to study the nucleobase-silver ions interactions and oligonucleotide-silver ions interactions and establish that the four nucleobases have different strengths of interaction with the silver ions.

2.12 Fluorescence Activated Cell Sorting (FACS)

Fluorescence-activated cell-sorting (FACS) is a specialised type of flow cytometry (FCM) [10]. It provides a method for sorting a heterogenous mixture of biological cells into two or more containers, one cell at a time, based upon the specific light scattering and fluorescent characteristics of each cell. It is a useful scientific instrument as it provides fast, objective and quantitative recording of fluorescent signals from individual cells as well as physical separation of cells of particular interest. Flow cytometry, in general, has found tremendous application in the fields of cell biology and clinical medicine. It is a versatile technique which simultaneously measures and analyses several physical properties of a single particle, usually cells, as they flow in a stream of fluid through a beam of light. It is capable of obtaining information about the cell size, cell granularity and internal complexity and relative fluorescence intensity.

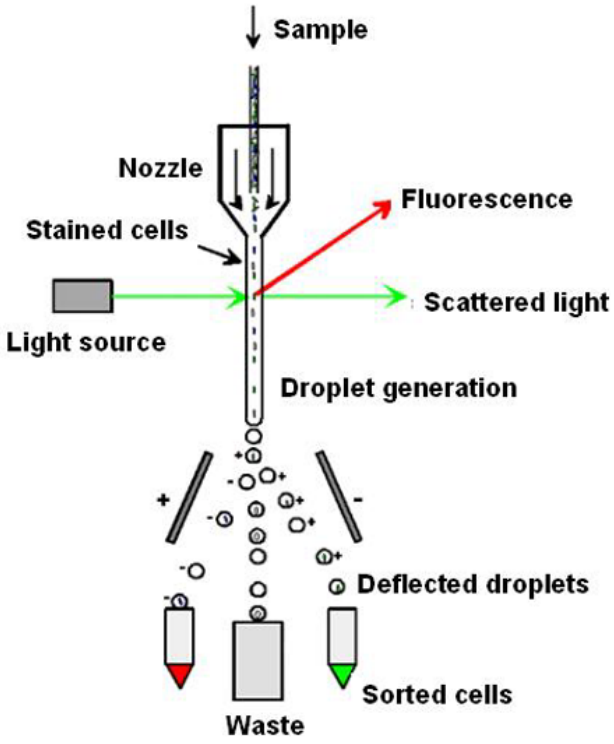

Figure 2.8 *Schematic showing the components of a typical FACS instrument. (Image courtesy: www.flow-cytometry.de/img/fcm.gif).*

For FACS analysis, the cell suspension is introduced in the centre of a narrow, rapidly flowing stream of liquid. The flow is arranged so that there is a large

separation between cells relative to their diameter. A vibrating mechanism causes the stream of cells to break into individual droplets. The system is so adjusted that just before the stream breaks into droplets, the flow passes through a fluorescence measuring station where the fluorescence character of each cell is measured. An electrical charging ring placed at the point of stream breaking into droplets, places a charge on the droplets depending on the fluorescent intensity measurement. The charged droplets then fall through an electrostatic deflection system that diverts the droplets into containers based on their charges. Thus, the technique enables us to measure the fluorescence intensity and population of cells associated with a particular fluorescence. The configuration of a typical FACS instrument has been shown in Figure 2.8.

In the thesis, FACS measurements have been used to measure the fluorescence intensity for equal number of cells incubated with PI-porous gold nanoparticle conjugate, PI-solid gold conjugates and PI-porous platinum nanoparticles conjugates. These results helps in establishing the higher loading of the fluorophore PI on the porous nanoparticles in terms of the higher mean fluorescence intensity for 10,000 cells counted.

2.9 References

1. Denney, R.C; Sinclair, R. *Visible and Ultraviolet Spectroscopy. Analytical Chemistry by open learning series*, John Wiley and Sons, USA.

2. (a) *Fluorescence and phosphorescence analysts,* Hercules, D.M., Editor Wiley-Interscience Publishers, New York, London, Sydney (**1965**). (b) *Fluoromestric analysis,* Konstantinova-Schlezinger Publishing Co., New York (**1965**).

3. (a) Shirley, D.A. *Phys. Rev. B* **1972**, *5*, 4709. (b) Kaufmann, E.N. *Characterization of materials*, John Wiley & sons, **(2003)**.

4. Bennett, A., Osterberg, H, Jupnik, H. and Richards, O., *Phase Microscopy: Principles and Applications,* John Wiley and Sons, Inc., New York, **(1951)**.

5. (a) Bradbury, S. and Evennett, P., *Fluorescence microscopy, Contrast Techniques in Light Microscopy*, BIOS Scientific Publishers, Ltd., Oxford, United Kingdom (**1996**). (b) Rost, F. and Oldfield, R., Fluorescence microscopy., Photography with a Microscope, Cambridge University Press, Cambridge, United Kingdom (**2000**).

6. (a) "*Video Microscopy*," Shinya Inoue and Kenneth R. Spring, 2nd ed., Plenum Press, **(1997)**. (b) "*Handbook of biological confocal microscopy*," edited by James B. Pawley, 2nd ed., Plenum Press, **(1995)**.

7. (a) Williams, D.B. *Transmission Electron Microscopy, A textbook for Material Science*, Plenum Press. New York and London. **(1996)**.

8. (a) R. Wiesendanger, *Scanning Probe Microscopy and Spectroscopy*, Cambridge Universtiy Press, Cambridge (**1994**). (b) Abdessamad, A.; Ladbury, J. E. *J. Mol. Recog*. **2006**, *19*, 79.

9. (a) Shapiro H. *Practical Flow Cytometry*.3rd Ed. New York, NY: Alan R. Liss; **(1994)**. (b) Givan A. L. *Flow Cytometry: First Principles* New York, NY: Wiley-Liss; **(1992)**.

Chapter III

Sequence Dependent DNA-Metallization
-An Isothermal Titration Calorimetric Approach

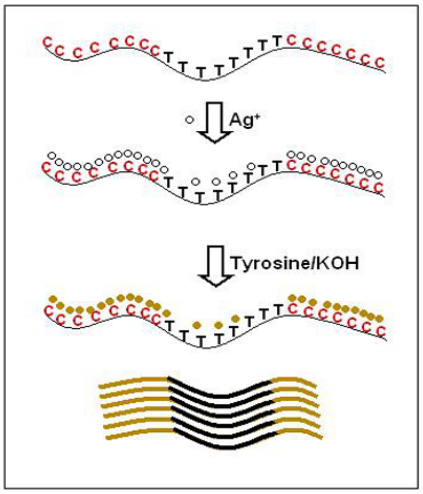

Fabrication of the active and passive components of futuristic nano-devices has generated considerable interest. This chapter discusses the use of DNA as a template for the assembly of nanoparticles leading to construction of molecular metal nanowires. We demonstrate herein the significantly different interactions of the building blocks of the DNA molecules, the nucleobases, with metal ions based on the extremely sensitive Isothermal Titration Calorimetry analysis. The distinct nature of the binding interactions of metal ions with the nucleobases, in turn, could be used to develop patterned molecular wires based entirely on the oligonucleotide sequences.

The work described in this chapter has been communicated: Shukla, S. and Sastry, M. *J. Am. Chem. Soc*. **2007**.

3.1 Introduction

One of the primary objectives of nanotechnology research is the development of technology that is miniaturized in a true sense. This implies that the tools and the components that would make up these devices be significantly downsized from their present forms. Much of current nanoscience research including synthesis of new nanomaterials, development of better processes for synthesis, controlling the morphology of the nanomaterials and tuning the optoelectronic properties of the nanomaterials, is focused on the development of constituents that would shape futuristic nano-devices. The other major area of research is the actual fabrication of final prototypes by assimilating the building blocks and already a considerable number of these products have been developed and successfully implemented in diverse fields such as optics [1], plasmonics [2], electronics [3], sensing applications [4] as well as bio-diagnostics and therapeutics [5].

The thrust, therefore, is on developing methodologies devoted to fabrication of active and passive components of nanoscale dimensions and currently includes techniques such as nanolithography [6], micro-contact printing [7], molecular self-assembly [8] and templated assemblies [9], to name a few. A wide variety of nanomaterials have been used for developing these components using the above-mentioned techniques including oxides [10], magnetic materials [11] and quantum dots [12]. Insofar as integrated circuits are concerned, there would be a need to fabricate metallic interconnects for the components in the circuit. Besides this, metal nanoparticle assemblies with controlled size, spacing and composition are also desirable for plasmonics wave-guides and which may have applications in field enhancement spectroscopy techniques such as surface enhanced Raman spectroscopy, infrared or fluorescence spectroscopy [13]. Experimental routes to nanoparticle chains have included synthesis via electron beam lithography (EBL) and manipulation of preformed particles using scanning probe tips [14]. These techniques provide excellent control over particle placement but are tedious and require sophisticated instrumentation. Alternatively, particle assemblies could be achieved in preformed channels but there is hardly any control over the interparticle distances in such techniques [15].

A more direct approach for the fabrication of metallic nano-interconnects is the template directed assembly of nanoparticles. For example, striped metal nanowires have been fabricated by the templated electrodeposition of metal in pores of alumina channels in a multistep process [16]. Other templates of choice include synthetic and natural polymers, which have been used under different conditions [17]. Of these, nucleic acids, particularly, Deoxy Ribose Nucleic Acid (DNA) perhaps, has been the most attractive template for the following reasons: (i) it has a remarkably high aspect ratio with a uniform charge density along the length, (ii) it is made up of only four building blocks, the nucleobases, with a highly predictable structural-functional relationship, (iii) the structure is flexible and yet sturdy for templated assemblies, and (iv) molecular biology techniques relevant to nucleic acids are highly developed, therefore rendering the manipulation of DNA very convenient. Besides, techniques like Polymerase Chain Reaction (PCR) provides a very efficient way of amplifying DNA, and also, DNA mediated nano architectures often have biological applications. The ability to synthesize DNA with arbitrary base sequence permits programming of inter and intra-molecular associations and thereby allows one to create simple linear structures to more complex intrinsic networks, based on which varying levels of complexity of nanoparticle assemblies could be achieved. Therefore, DNA has become increasingly relevant to nanotechnology research, not just as a template, but for three dimensional nanoparticle assemblies, complex architectures, and sensors of diagnostic importance and hence, there is extensive literature on the use of DNA for nanotechnology research [18].

Most of the strategies for DNA templated assemblies have so far relied on the binding of preformed metal nanoparticles onto double stranded DNA (dsDNA) [19] or by chemically [20-21]/photo-catalytically reducing [22] metal cations electrostatically bound to the negatively charged backbone (due to the phosphate groups in the DNA backbone) to achieve metallized molecular wires, rings [23] or networks [24]. One immediately recognizes that the non-specificity of the columbic interaction between metal cations and the phosphate backbone leads to metallization along the entire DNA segment with little opportunity to control metallization spatially. However, the structural-functional predictability of the DNA molecule lies in its nucleobases that have the ability to undergo extremely specific Watson Crick

base pairing and it's the nucleobase sequence that is responsible for diversity of DNA structure. Despite this, there have been only few attempts towards achieving any kind of sequence dependent control upon the dsDNA metallization including localization of a sequence specific DNA binding protein [25-a] or reducing agent [25-b] followed by the metallization process on the DNA. While these protocols have generated patterned molecular wires on the DNA, they require extensive multi-step modifications of the dsDNA molecule and are thus rather cumbersome.

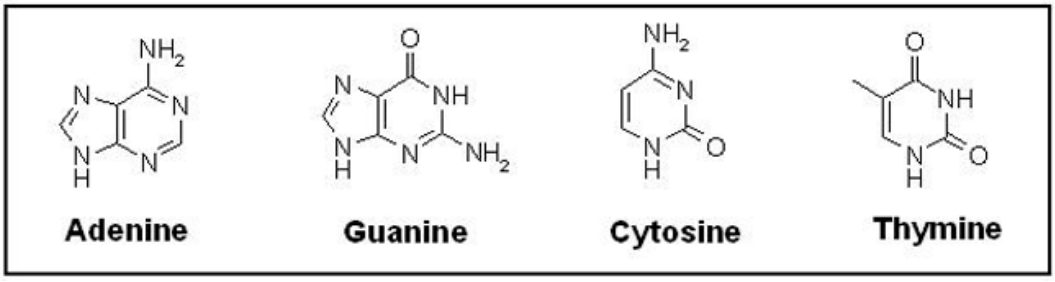

Scheme 3.1 *Chemical structures of the four DNA nucleobases.*

Nucleobases are the building blocks of the DNA molecule along with the ribose sugar and phosphate. Chemically, nucleobases or the nitrogenous bases are derivatives of purine or pyrimidine structures. Adenine and guanine are purines, while cytosine and thymine are the derivatives of pyrimidines. The chemical structures of the four nitrogenous bases are shown in scheme 3.1.

There are numerous reports on the specific interactions of nucleobases, nucleosides and nucleotides with metals cations including those from the first transition series such as chromium, manganese, iron, cobalt, nickel and copper as well as other metals such as zinc, silver, cadmium, platinum, lead and mercury [26]. Many of these studies have explained in detail the interaction of the metal cations with particular nucleobases, nucleosides and nucleotides. Some of these metals such as cobalt and nickel have an affinity towards the phosphate backbone of the DNA molecules while others such as silver have preferential binding with nucleobases [27]. Even though such information on the differential binding abilities of the bases or nucleosides with metal cations exists, they have rarely been exploited in materials chemistry, especially those related to fabrication of metal nanoparticles assemblies.

In this chapter, the interactions of one such metal cation, Ag^+, with the nucleobases have been studied using extremely sensitive Isothermal Titration Calorimetry (ITC) measurements. ITC measures the heat of reaction between two or more interacting molecules in aqueous solution and is an important tool for determining molecular interactions for biological and non-biological systems [28]. ITC therefore is a more direct approach to establish the strengths of interaction than any of the methods used earlier to establish such interactions between metals and DNA [27, 29]. We have illustrated that such differences amongst the nucleobases towards interaction with certain metal ions could be used for the fabrication of patterned molecular wires after reducing the ions to its metallic form, with excellent control over the interparticle spacing. The extensive literature available on the formation of silver nanowires, rings and networks [23, 24] based on the DNA templates was decisive in choosing Ag^+ for the present studies. We show that the subtle differences between the nucleobase structures are capable of generating significantly distinct morphologies and optical signatures. Therefore, it would be possible to fabricate pattered metal wires based entirely upon the sequences of the template DNA molecule in an easier solution based process.

3.2 Isothermal Titration Calorimetry Measurements

3.2.1 ITC measurements of nucleobases – Ag^+ interactions

Isothermal Titration Calorimetry (ITC) is an extremely sensitive technique for the analysis of thermodynamic parameters associated with non-covalent interactions between two or more molecules. In our experiments, the heat of interaction between the nucleobases and silver ions (Ag^+) and the single stranded DNA (ssDNA)-Ag^+ complexes was determined by ITC. In the first set of experiments, 100 µl of 100 µM aqueous solutions of the nucleobases were titrated in equal steps of 10 µl into 1.47 ml of 100 µM Ag_2SO_4 solution. There was a lag of 5 min between successive injections of the nucleobases. This point onwards we will refer to these experiments as the 10 injection experiments. The heat of interaction resulting from the solvation effect of the nucleobases was taken into account by performing control experiments where equivalent concentration and volumes of the respective nucleobases were titrated into 1.47 ml of Millipore water and the heat response were recorded.

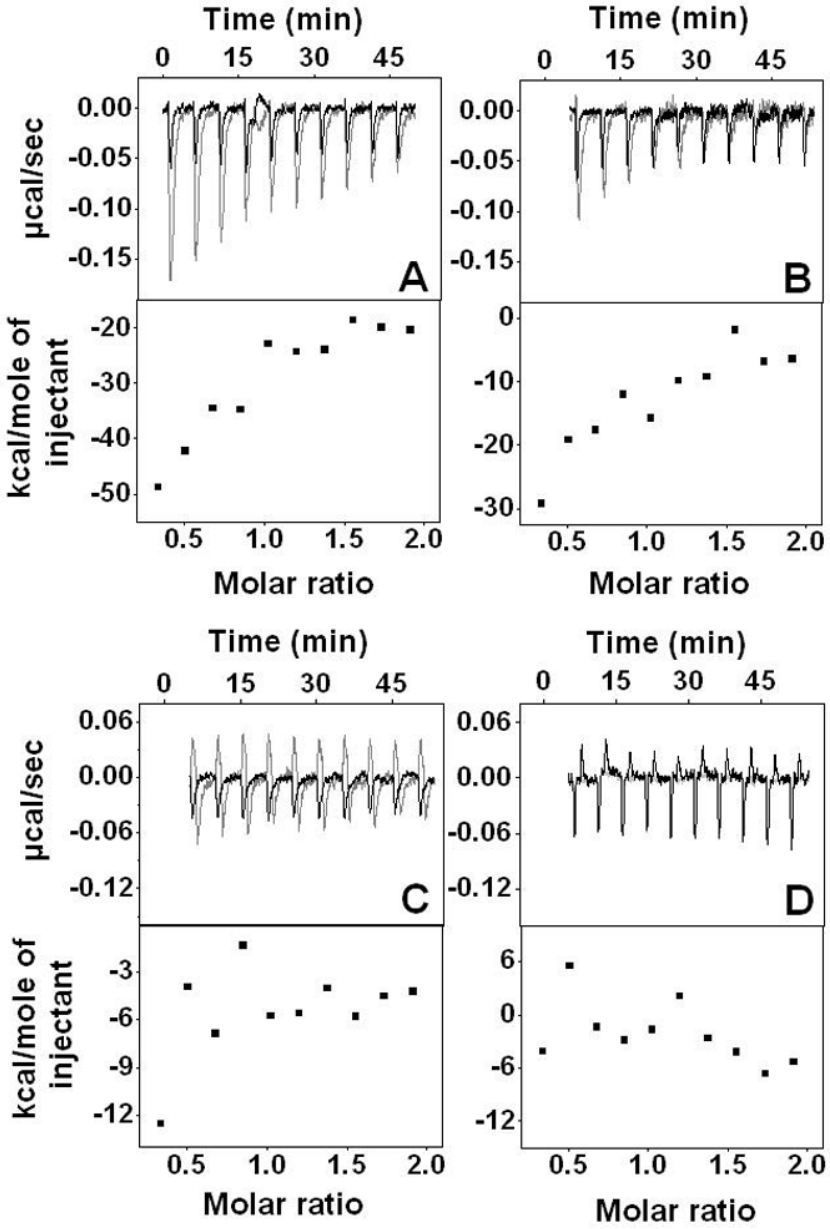

Figure 3.1 *ITC plots for the titration of the four nucleobases into the Ag^+ solution. A, B, C and D correspond to the ITC profile of cytosine, guanine, adenine and thymine respectively. The upper panels in the plots represent the heat evolved per injection of nucleobase while the lower panels show the integrated heat per injection plotted against the molar ratio of the nucleobase/Ag^+. The gray curves in each of the upper panels correspond to the experimental values while the black curves represent the control experiments for the respective nucleobases.*

The ITC measurements recorded for the four nucleobases in the 10-injection experiments are shown in the Figure 3.1. The upper panels in A, B, C and D represent the heat of reaction involved with injection, each peak corresponding to one injection. While the gray curve corresponds to the titration of nucleobases into the Ag^+ solution,

the black curve represents the control experiment where similar concentrations of nucleobases were added to 1.47 ml of Millipore water as explained earlier. The area under each curve corresponds to the total heat evolved in each injection of the ligands (nucleobases in our case) into the solvent. This integrated heat when plotted against the molar ratio of the Ag^+ ions and nucleobases, generates the lower panels of the respective ITC plots. The values of the integrated heats of the control experiments have been deducted from their respective experimental values.

It is evident from the ITC measurement of cytosine-Ag^+ titration that the interaction is exothermic as suggested by the negative values of the heat of reaction for the first few injections (Figure 3.1, A, gray curve). As successive injections of nucleobases are titrated into the cell, the quantity of heat released, which is in direct proportion to the amount of binding occurring between the nucleobase and the silver ions, decreases. As the system reaches saturation, the signal diminishes until only heats of dilution are observed. (Figure 3.1, A, gray curve). Similarly, the titration plots of guanine, adenine and thymine are also shown in Figure 3.1, B, C and D respectively. While titration of guanine against silver ions showed similarity with cytosine (Figure 3.1, B, upper panel), that of adenine and thymine did not follow a typical binding isotherm (Figure 3.1, C and D, upper panels). It is evident from the ITC profile of adenine that the exothermic response is only slightly higher than the dilution response, while in the case of thymine, the experimental and control values overlap, suggesting negligible interaction of thymine with silver ions.

Comparison between the integrated heat values for the four nucleobases clearly reveals that their binding affinities with silver ions vary significantly as reflected in the heat of interactions recorded in the ITC experiments. Thus, while cytosine shows the highest affinity to interact with silver as shown by the heat of interaction with a maximum value of - 48.74 kCal/mol, guanine, adenine and thymine followed in that order with values of - 29 kCal/mol, - 12.68 kCal/mol and - 4.46 kCal/mol, respectively (overall order being $C > G > A \geq T$). The scattered values of integrated heats in the case of adenine and thymine shows the insignificant amount of heat changes taking place upon titrating these bases with silver ions.

There is extensive literature on the interaction of cations with DNA and nucleotides, especially Ag^+ - DNA interactions [27, 29]. Combined potentiometric and spectroscopic studies have revealed the different modes of interaction between silver ions and DNA depending on the Ag^+: nucleotide ratios. However, there are no direct quantitative evidences for the differential binding abilities of nucleobases with silver ions. Our measurements therefore are significant as they clearly illustrate that the four bases behave differently in the presence of metal ions such as silver.

To compare the strengths of interactions of the nucleobases, one more set of ITC experiment was carried out with only the most strongly binding cytosine and the least binding thymine. In this experiment 300 µl of 100 µM nucleobases (cytosine and thymine) were titrated in equal steps of 10 µl into 1.47 ml of 100 µM Ag_2SO_4 solution with 2 min interval between the successive injections. This experiment hereafter, will be therefore referred to as the 30-injection experiment. The ITC plots of the 30-injection experiments are presented in Figure 3.2.

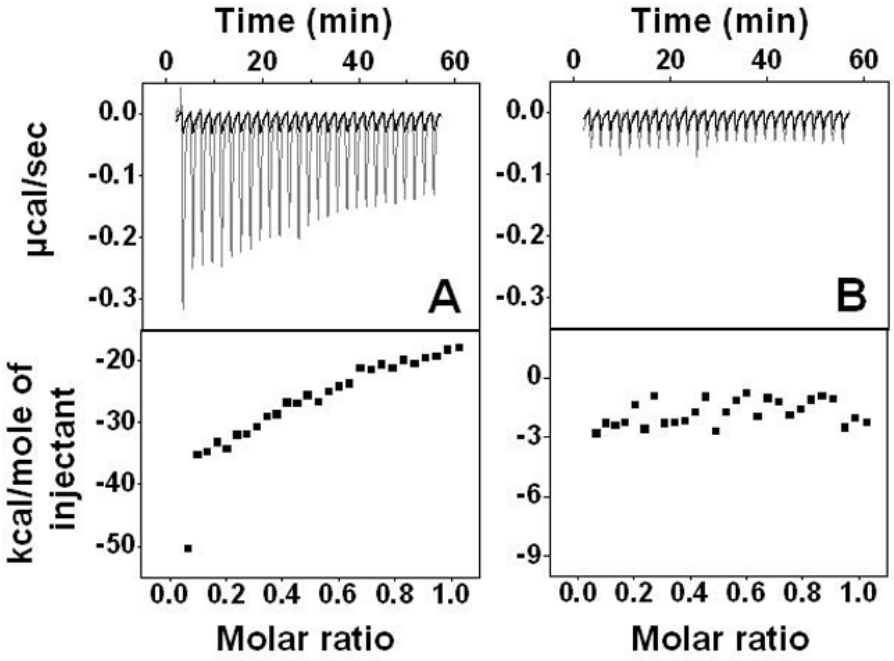

Figure 3.2 *ITC plots obtained by titrating 300 µl of 100 µM cytosine (A) and thymine (B) against 1.47 ml of 100 µM Ag_2SO_4 solution. The upper panels represent the heat liberated in each injection while the lower panels shows the integrated heat of each injection plotted against the molar ratio of the nucleobases and the silver ions. Gray curves in the upper panels depict the experimental values while the black curves are from the control experiments.*

As explained earlier, the upper panels of the plots correspond to the heat liberated with each injection of the nucleobases into the silver ions, while the lower panels are the integrated heats of each injection plotted against the molar ratios of nucleobases to the silver ions. The gray curves in the upper panels correspond to the control experiments where equivalent concentrations of the nucleobases were titrated against Millipore water.

As is clear from Figure 3.2, cytosine shows a significantly higher exothermic response to the interaction with silver ions. The 30- injections experiment leads to a binding isotherm that reaches saturation towards the end of the 30 injections (Figure 3.2, A, gray curve). The heat of dilution remains much lower and constant throughout the titration. On the other hand the heat evolved by the titration of thymine is significantly lower, and does not show a typical binding isotherm (Figure 3.2, B, upper panel) as in the case of cytosine. The small difference in the experimental curve values (gray curve) and the control values (black curve) suggests that there is no significant interaction of thymine with the silver ions in the solution and the major contribution in the heat evolved during the titration comes from the dilution effect of thymine. The magnitude of the integrated heat from the lower panels of Figure 3.2, A and 3.2, B highlights the remarkably different affinities of cytosine (-50.3 kCal/mol) and thymine (-2.7 kCal/mol) towards silver ions. The saturation of the heat liberated at the equimolar ratio of silver ions and cytosine also suggests a 1:1 binding between the two (Figure 3.2, A, lower panel).

These results are important as the nucleobases are the basic building blocks of the DNA structure and the significant differences amongst the nucleobases towards a metal cation suggest that the interaction of DNA as a whole, with metal ions could be more dynamic in terms of the association of the ions to a certain fragment of the DNA length depending on its nucleobase composition.

3.2.2 ITC measurements of oligonucleotides – Ag^+ interactions

The assumptions made above however, are not that straightforward when we talk about the DNA molecule as a whole. This is due to the fact that the DNA molecule contains, besides the nucleobases, a negatively charged sugar phosphate backbone that provides a uniform charge density for columbic interactions with any

charged moiety. In dsDNA, the hydrophobic core made up of the nucleobases remains generally inaccessible to any interacting charged species. On the contrary, a small ssDNA would offer an exposed sugar phosphate backbone as well as the nucleobases for the same (Scheme 3.2). Thus, any such interaction is now subjected to the competitive binding affinities of the phosphate sugar backbone and the nucleobases. Therefore, a ssDNA would present an excellent opportunity to compare the affinities of interactions between the nucleobases and the sugar – phosphate backbone.

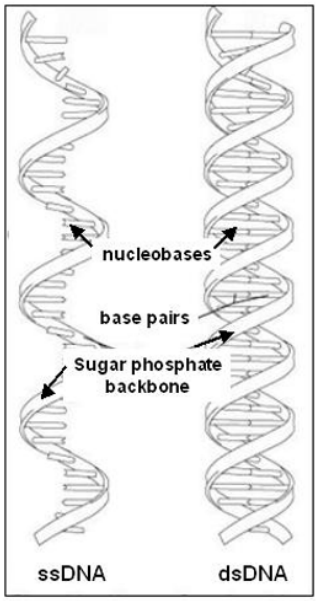

Scheme 3.2 *Comparative structure of single stranded DNA (ssDNA) and double stranded DNA (dsDNA).*

Therefore, in an experiment similar to the previous ones involving nucleobases, 300 µl of 4 µM aqueous solutions of oligo-C (C_{24}) and oligo-T (T_{24}) were titrated in equal steps of 10 µl into 1.47 ml of 100 µM Ag_2SO_4 with a time lag of 2 min between the successive injections. Control experiments similar to those mentioned above were performed where equivalent concentrations of the oligonucleotides C_{24} and T_{24} were titrated against de-ionized water. The temperature of the reaction cell was maintained at 4 ^{0}C for all the titration experiments and the pH was maintained at 7.5. The ITC plot of the titration of the oligonucleotides against silver ions with respective control experiments is shown in Figure 3.3. It is clearly seen from the ITC plots of C_{24} and T_{24} v/s Ag^+ that the interactions are exothermic, the one involving C_{24} being the stronger interaction as suggested by the more intense

heat response recorded during the titration (Figure 3.3, A, upper panel). T_{24}, in comparison, shows much lower interaction with the silver ions (Figure 3.3, B, upper panel).

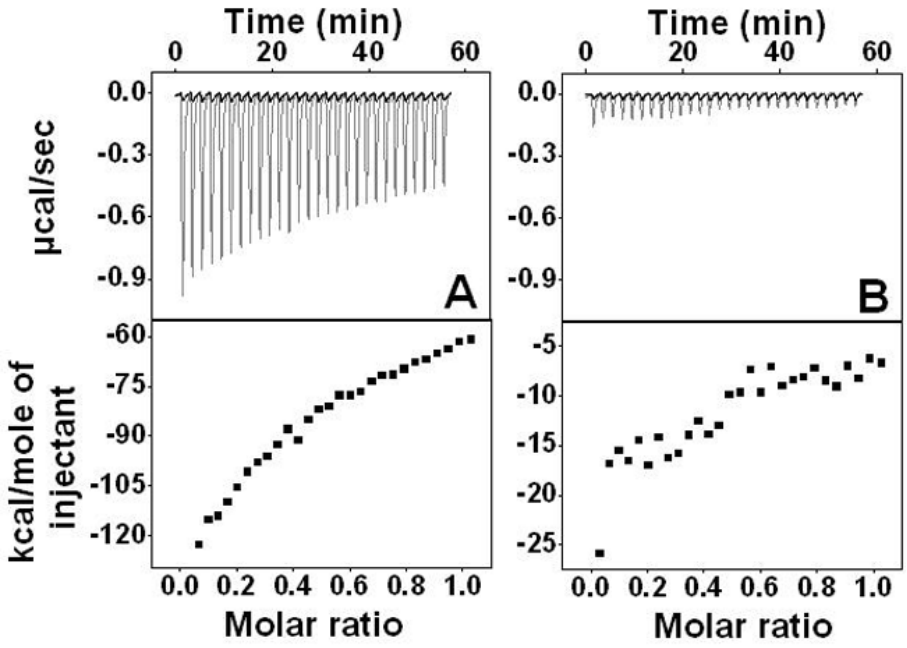

Figure 3.3 *ITC plots depicting the heat response recorded by titrating 300 µl of 4 µM oligonucleotides C_{24} (A) and T_{24} (B) against 1.47 ml of 100 µM Ag_2SO_4 in a 30-injection experiment. The upper panels show the heat liberated per injection for experiments (gray curves) and controls (black curves), while the lower panels shows the integrated heat per injection against the molar ratio of oligonucleotides/Ag^+.*

In both cases, the heat released during successive injections of the oligonucleotides decreases, indicating the saturation of binding sites on the oligos. The integrated heat per mole of the ratio of the oligonucleotides to Ag^+ gives the magnitude of difference between the affinities of C_{24} and T_{24}. Thus, while the maximum heat liberated in the case of C_{24} is - 122 kCal/mol, that for T_{24} is significantly low at - 25 kCal/mol and shows a lot of scatter suggesting that T_{24} hardly interacts with the silver ions in solution.

Interestingly, the two oligos were so chosen that they have the same length and hence similar charge density arising from the sugar-phosphate backbone. The difference between the two lies in the nucleobase composition. Since, the ITC measurements of the two oligos display significantly different exothermicity, it can be concluded that it is the nucleobases that are interacting primarily with the silver ions

and not the sugar phosphate backbone. Had it been the case that the positively charged nucleobases were interacting with the negatively charged phosphate groups, we should have obtained comparable, if not exactly similar values in the two titrations. However, the significant difference between the values for C_{24} and T_{24} illustrates that it is the differential affinity of the nucleobases, which is coming into play, as already demonstrated in the experiments involving the nucleobases directly.

These results open exciting possibilities in terms of employing DNA as a template for assembly of nanoparticles, by varying the sequences of DNA one can generate fragments where a certain metal ion or nanoparticles bind preferentially, thus developing spatially patterned assemblies.

3.3 UV-vis spectroscopy and transmission electron microscopic (TEM) analysis

3.3.1 Nucleobases - Ag^+ interactions

Reducing the silver ions in the presence of the nucleobases could further prove the apparent differences in the binding ability of the nucleobases with the silver ions and the complete binding between them at equimolar ratios. We followed a well-established protocol for the synthesis of silver nanoparticles developed by Sastry and co-workers where reduction of Ag^+ by tyrosine under alkaline conditions leads to the formation of silver nanoparticles [30]. In a typical experiment, 1 ml of 10^{-3} M aqueous solutions of nucleobases (cytosine and thymine) were mixed with 1 ml of 10^{-3} M Ag_2SO_4 and 1 ml of 10^{-3} M tyrosine and the final volume was made up to 9 ml. After bringing this solution to boil, 1 ml of 10^{-2} M KOH was added to this mixture and the boiling was continued for another five minutes. For control, equivalent concentration of silver was reduced in absence of the nucleobases following the procedure mentioned above. Similarly, silver was also reduced in the presence of a concentration of nucleobases three times higher than the above concentrations.

The UV-vis-NIR spectra recorded for the reduction of silver ions in presence and absence of the nucleobases is shown in Figure 3.4. Reduction of silver in the absence of the nucleobases cytosine and thymine leads to formation of silver nanoparticle as soon as KOH is added to the boiling mixture. The colorless aqueous

solution of the silver immediately turns to yellow, indicating the formation of colloidal silver. The UV-vis spectrum of this solution shows a sharp absorption band centered at 420 nm, which is due to the surface plasmon resonance of the colloidal silver nanoparticles [30] (Figure 3.4, curve 1).

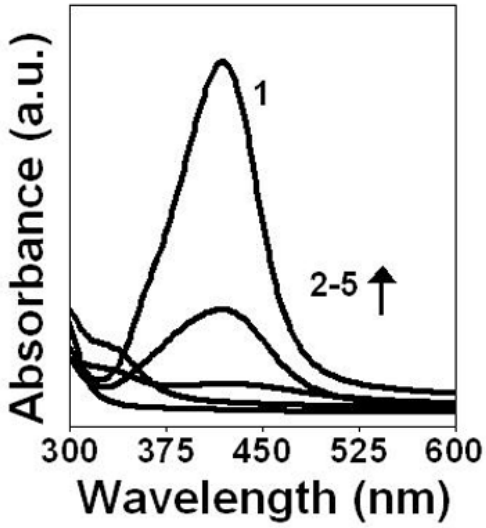

Figure 3.4 *UV-vis absorption spectra recorded for the tyrosine-KOH reduction of silver with and without the nucleobases. Curve 1 corresponds to the plasmon absorption band of 10^{-4} M silver nanoparticles in absence of the nucleobases. Curves 2-5 correspond to the reduction of varying concentration silver in presence of cytosine (curves 2 and 4; 10^{-4} M and 3 x 10^{-4} M Ag^{+}, respectively) and thymine (curves 3 and 5; 10^{-4} M and 3 x 10^{-4} M Ag^{+}, respectively).*

However, in the presence of the nucleobases, there is a clear dampening of the silver nanoparticles plasmon peak (Figure 3.4, curves 2-5). A closer look at these curves further reveals that for a silver concentration of 10^{-4} M and 10^{-4} M nucleobases concentration, the plasmon absorption band is significantly dampened (Figure 3.4, curves 2 and 3), indicating the absence of spherical silver nanoparticles, which generates a sharp surface plasmon band at 420 nm. This observation can be explained in terms of the results obtained in the ITC experiments that at equimolar concentrations, nucleobases binds tightly to the silver ions, rendering very little free silver ions for reduction by tyrosine under alkali conditions, for both cytosine and thymine. Subsequently, when the concentration of silver in the solution is significantly increased (3 x 10^{-4} M from the original 1 x 10^{-4} M), the reduction by tyrosine in alkali conditions leads to appearance of the silver plasmon band as shown in the Figure 3.4, curves 4 and 5. Thus, it can be observed that while in presence of thymine, a low intensity band centered at 400 nm is obtained (Figure 3.4, curve 5), a

very low intensity broad absorption band is obtained in the presence of cytosine (Figure 3.4, curve 4). The appearance of the surface plasmon band is indicative of the formation of silver nanoparticles in the high concentration experiments; however, the low intensity of the resultant absorption bands suggest that only the excess silver ions are reduced to form silver nanoparticles and the broad spectra reflects aggregation of silver nanoparticles so formed. These results can be further confirmed by the TEM analysis of the respective samples as shown in Figure 3.5.

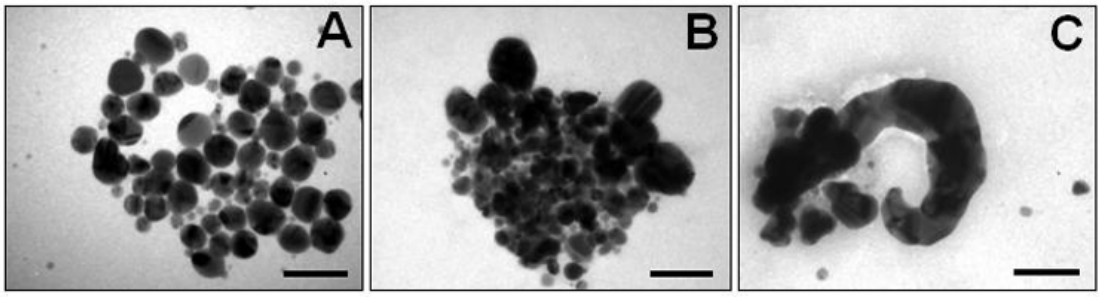

Figure 3.5 *Representative TEM images of 3 x 10^{-4} M silver ions reduced by tyrosine under alkaline conditions without the bases (A); and in the presence of 1 x 10^{-4} M thymine (B) and 1 x 10^{-4} M cytosine (C). The scale bars in TEM images correspond to 100 nm.*

Figure 3.5, A shows TEM image of the silver nanoparticles formed by the reduction of silver ions by tyrosine-KOH in absence of the nucleobases. It is clear from the image that in absence of the nucleobases spherical nanoparticles with an average diameter of 50 nm are formed without any apparent aggregation. The TEM image validates the presence of a sharp high intensity band centered at 400 nm in the UV-vis spectrum for the same (Figure 3.4, curve 1). Contrary to this, silver (3 x 10^{-4} M) reduced in the presence of thymine results in the formation of aggregated silver nanoparticles (Figure 3.5, B). The TEM is in agreement with the low intensity UV-vis absorption band observed for thymine (Figure 3.4, curve 5). Cytosine, on the other hand, under similar conditions, generates highly aggregated silver nanostructures of irregular morphologies (Figure 3.5, C). Such aggregation of silver nanoparticles by strongly binding ligands has been previously observed for phthalazine, which resulted in rapid aggregation of silver nanoparticles into clusters of irregular shapes and sizes. The aggregation is characterized by the dampening of the surface plasmon resonance absorption band of silver nanoparticles [31]. Similarly, mannose stabilized silver nanoparticles were shown to undergo rapid aggregation upon addition of

Concanavaline A, resulting in dampening of the plasmon band and has been used for bioassays [32]. The appearance of a broad absorption band with very low intensity in the UV-vis spectrum of 3 x 10^{-4} M silver ions being reduced in presence of cytosine is therefore attributed to the formation of such highly aggregated irregular structures (Figure 3.4, curve 4). It is the strong binding ability of cytosine that results in the reduction of silver ions to form large aggregates, while in the absence of any capping molecule, spherical silver nanoparticles are obtained.

3.3.2 ssDNA – Ag^+ interactions

Similar to the nucleobases, short stretches of oligonucleotides also showed differential interactions with the silver ions as demonstrated by ITC measurements explained above. The ITC analysis proved that the silver ions actually bind to the nucleobases in a ssDNA molecule and that its interaction, in such a case, with the phosphate groups present on the sugar phosphate backbone, is minimal despite the uniform charge density on the backbone. This point was further illustrated by UV-vis spectroscopy of the reaction where the silver ions are reduced in the presence of the two ssDNA with dissimilar base composition. In a typical experiment, ssDNA (C_{24} and T_{24}) were mixed with Ag^+, so as to keep their final concentrations as 4 μM and 100 μM, respectively. After incubating the mixture at 4 ^oC for 12 h, the reduction of bound Ag^+ was carried out by exposing the solution to alkaline tyrosine. For the control experiment, equivalent concentration of silver ions was reduced by tyrosine-KOH in the absence of the short oligonucleotides. The UV-vis spectra recorded is shown in Figure 3.6.

The reduction of silver in the absence of the oligonucleotides results in a sharp plasmon absorption band at 400 nm that is characteristic of spherical silver nanoparticles (Figure 3.6, curve 1). However, in the presence of the short oligonucleotides, there is a significant dampening of the silver plasmon absorption band. In the presence of T_{24}, the intensity of the 400 nm plasmon band reduces, indicating slight aggregation of the resulting silver nanoparticles. Also, in the case of C_{24} there is a drastic reduction in the silver plasmon band intensity, suggesting large aggregation of the silver nanoparticles. These results were further supported by the TEM analysis of the above reduction process shown in Figure 3.7.

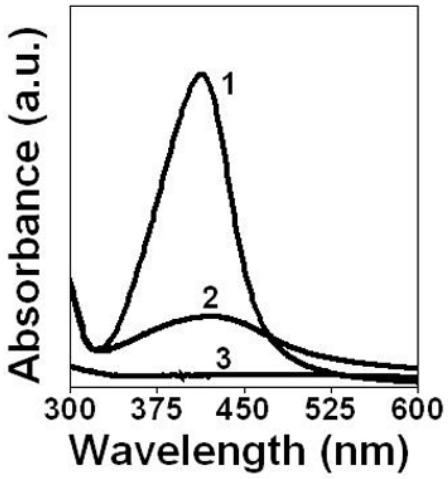

Figure 3.6 *UV-vis spectra of 100 μM Ag^+ reduced by tyrosine-KOH without any oligonucleotides (curve 1), and in presence of 4 μM of T_{24} (curve 2) and C_{24} (curve 3).*

The reduction of silver ions in the absence of the oligonucleotides results in the formation of spherical silver nanoparticles (Figure 3.7, A). The oligonucleotide on the other hand, results in various degrees of aggregation. With T_{24}, the reduced silver nanoparticles show aggregation in the form of loosely held clusters of spherical nanoparticles (Figure 3.7, B). The smaller extent of aggregation is sufficient enough to dampen the intensity of the silver plasmon band as observed in UV-vis spectroscopy (Figure 3.6, curve 2). However, the strong binding ability of the cytosine containing ssDNA C_{24} results in significant dampening of the plasmon band, which is attributed to the flat aggregated structures formed when silver is reduced in the presence of C_{24} (Figure 3.7, C). It is evident from the above experiments that the nucleobases, especially, cytosine and thymine varies drastically in the manner in which they interact with the silver ions. The differential affinity of the nucleobases towards silver ions is reflected in the way the optical absorption of the silver nanoparticles formed by reducing the ions in the presence of the bases varies.

The remarkably different interactions between the silver ions and the bases also generate entirely different morphologies of silver nanoparticles. It is also noteworthy that the nucleobases have higher affinity for silver than the phosphate groups in the sugar phosphate bonds of the DNA, which is illustrated by the persistence of the differences observed in experiments involving nucleobases in the experiments involving homo-oligonucleotides.

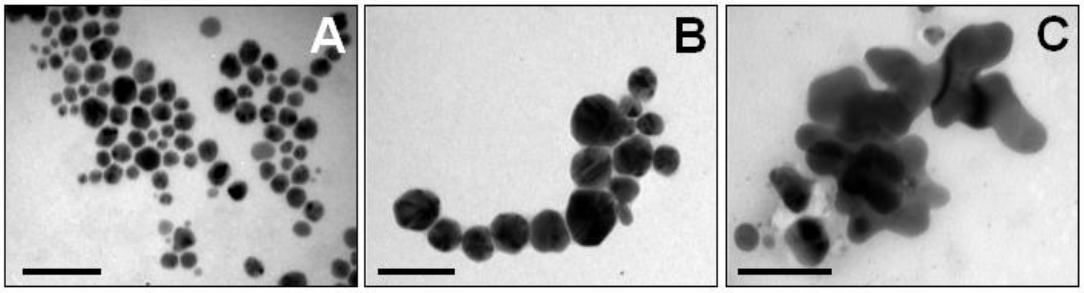

Figure 3.7 *Representative TEM images of the reduction of 100 μM Ag^+ in absence of oligonucleotides (A); and in presence of 4 μM of T_{24} (B) and C_{24} (C). The scale bars in the TEM images correspond to 50 nm.*

These evidences are in agreement with the ITC experiments, which provide the direct measure of the differential interactions of the nucleobases with silver ions.

3.3.3 Metallization of Plasmid DNA

The ability of the silver ions to differentially interact with the nucleobases and the sugar phosphate backbone could also be proved by metallization of plasmid DNA (p-DNA) that is a circular double helical DNA molecule with the nucleobases in the core and the sugar phosphate backbone around it. The nucleobases in a p-DNA are not exposed at all. However, heating the p-DNA to its melting temperature, a part of it could be uncoiled and the two strands could be separated, exposing the bases.

In a typical experiment, 0.15 μg/ml IL2 plasmid (3500 bp) was mixed with 2 μM Ag^+ at 80^o C for 5 min, after which, the reduction was achieved in solution using alkaline tyrosine. Similar experiment where the mixture of plasmid and silver ions were incubated at room temperature prior to reduction was also performed. In another experiment, after mixing the plasmid and silver ions at elevated temperature and then reducing silver by tyrosine KOH, 0.1% $NaBH_4$ was added in to the mixture. For control experiment, equivalent concentration of silver ions were reduced by tyrosine KOH at elevated temperature without the addition of plasmid. The UV-vis spectra for the above-mentioned experiments are shown as Figure 3.8.

It is clear from the UV-vis spectra for the metallization of p-DNA that 2 μM silver ions on reduction by tyrosine KOH generates a sharp plasmon absorption band at 400 nm (Figure 3.8, curve 1) which is characteristic of the silver nanoparticles. Similar concentration of silver ions when incubated with p-DNA at room temperature

followed by reduction by tyrosine KOH results in a plasmon band without any significant changes in the absorption intensity (Figure 3.8, curve 2), suggesting little

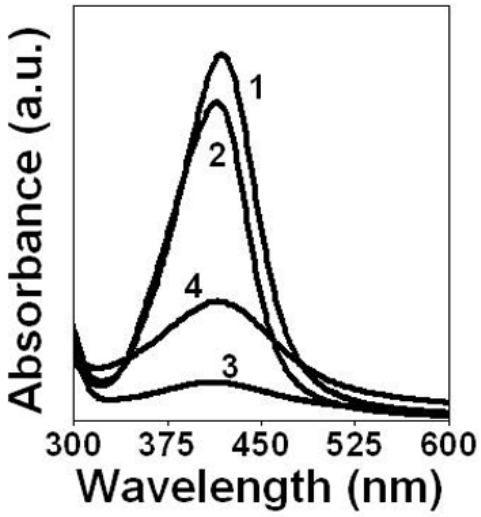

Figure 3.8 *UV-vis spectra for the reduction of silver ions in the presence and absence of p-DNA at different temperatures. Curve 1 corresponds to the spectrum of the 2 μM Ag^{+} reduced by tyrosine KOH. Curve 2 corresponds to the reduction of silver in presence of p-DNA after incubation at room temperature. Curve 3 is the reduction of silver incubated with p-DNA at 80 ^{0}C, while curve 4 is obtained after addition of 0.1 % $NaBH_4$ in 3.*

interaction between silver ions and the plasmid DNA that is still intact and highly coiled. However, when the mixture of silver ions and the p-DNA are incubated at 80 ^{0}C for 5 min prior to the reduction by tyrosine KOH, the surface plasmon band intensity of silver dampens significantly (Figure 3.8, curve 3) suggesting generation of silver nanoparticles to a lesser extent and association of the silver ions with the nucleobases. At 80 ^{0}C, which is generally the melting temperature (T_m) of a plasmid of size 3.5 kbp, some parts of the plasmid molecule are present in an uncoiled state with the two strands separated at certain places. This would expose the otherwise hidden nucleobases to the external environment where they can form association with the silver ions. Thus, a part of the silver ions population in the reaction mixture would now be bound to the exposed nucleobases, and upon reduction with tyrosine KOH, would result in aggregated silver nanoparticles embedded in the plasmid molecule. Only a small fraction of the silver ions would be reduced to form free silver nanoparticles in the solution and therefore dampened plasmon band intensity is observed in this case.

The reversibility of the association of the silver ions with the plasmid DNA is evident by the enhanced intensity of the plasmon band when a strong reducing agent sodium borohydride is added to the reaction mixture described above (Figure 3.8, curve 4). $NaBH_4$ addition to the solution leads to release of unreduced silver ions trapped in the p-DNA molecule in the solution, which are then reduced to give spherical silver nanoparticles in the solution thereby contributing to the enhancement of the plasmon band absorption over the previous case. However, the overall silver ions available for the strong reducing agent $NaBH_4$ in solution remains much lower than the control experiment, and therefore the band intensity remains lower than that of the control experiment (Figure 3.8, curve 1).

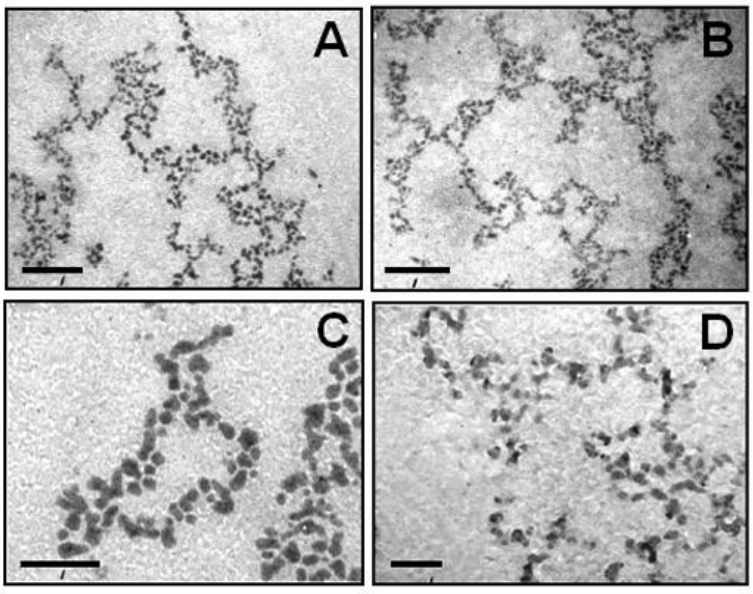

Figure 3.9 *Representative TEM images showing the formation of silver nanoparticles on the p-DNA template by reduction with tyrosine KOH. The scale bars in the A and B represents 200 nm while that in C and D correspond to 100 nm.*

The formation of aggregated silver nanoparticles of irregular shapes on the p-DNA template can be observed in the TEM images shown in the Figure 3.9.

3.4 Sequence dependent DNA metallization

The ability of the nucleobases to differentially interact with metallic ions such as silver throws open a lot of interesting possibilities of sequence dependent metallization of DNA. In the previous approaches, people have used enzymatic protection of certain fragments of the DNA molecule against deposition of metal

nanoparticles or ions and its reduction thereafter. Also, selective localization of the reducing agent on the DNA itself has also been used for the reduction of precursor ions on the DNA molecules in order to achieve metallization. However, these methods are cumbersome and involve careful modification of DNA molecule in several steps.

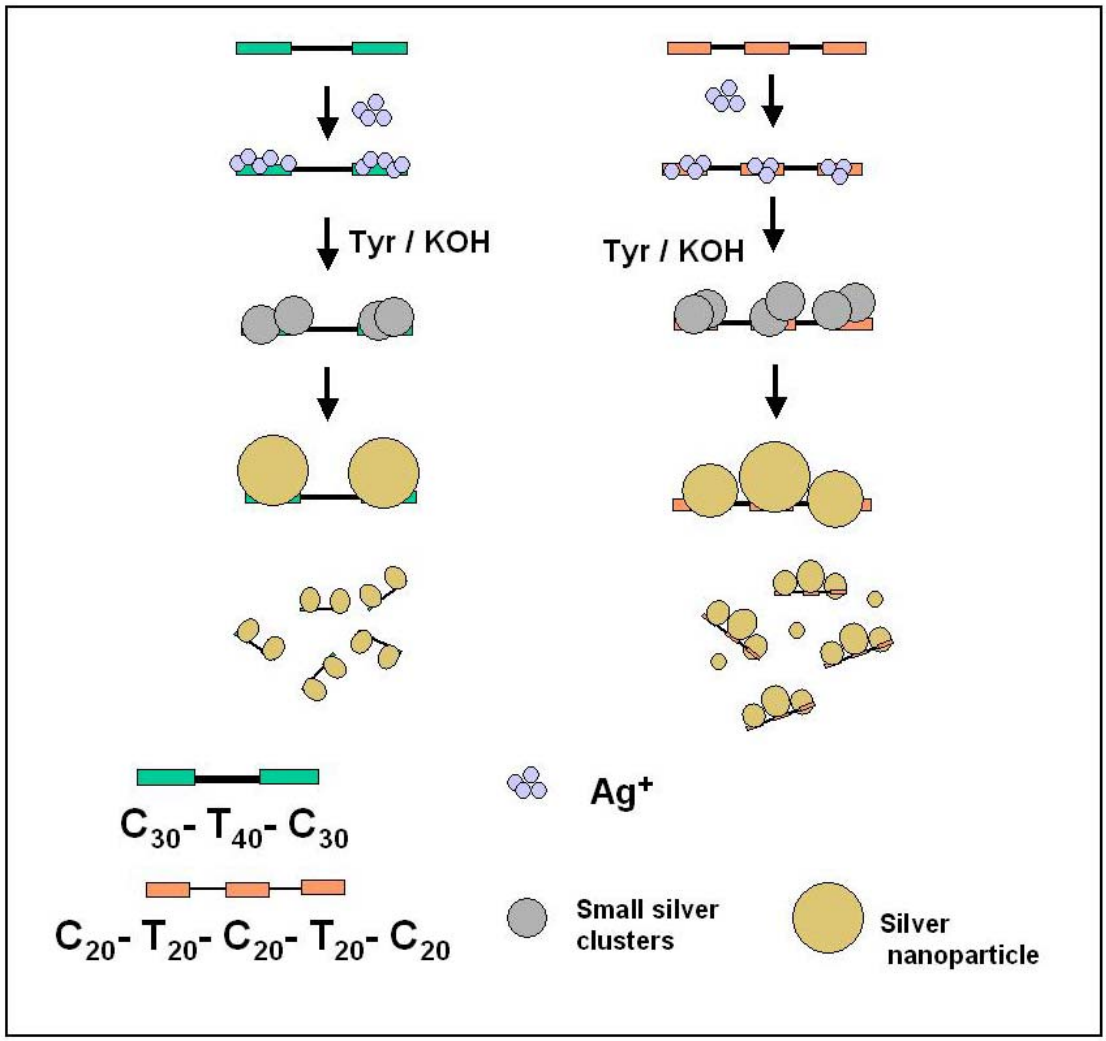

Scheme 3.3 *Experimental procedures leading to the metallization of oligonucleotides* C_{30}- T_{40}- C_{30} *and* C_{20}- T_{20}- C_{20}- T_{20}- C_{20}.

The ITC measurements have shown that despite their similar structures nucleobases clearly differ in the strengths of their interaction with the silver ions. UV-vis and TEM analysis further proved that the differences in the heat of interactions actually materialize into the varying degrees of aggregation of the resulting nanoparticles, based entirely on the nucleobases involved in the reaction. Based on

such studies, we propose a new approach to construct patterned molecular wires of silver templated on DNA, which is shown in the Scheme 3.3.

Two short oligonucleotides with sequences C_{30}- T_{40}- C_{30} and C_{20}- T_{20}- C_{20}- T_{20}- C_{20} were used to illustrate sequence dependent metallization. The sequences were so designed that the first one has two cytosine containing stretches flanking a thymine rich stretch in the middle, while the second has alternating cytosine and thymine stretches of equal lengths. In two separate experiments, 50 μM of the each oligonucleotide was mixed with 50 μM silver ions and incubated at 4 ^{0}C for 8 h. After the incubation, the reduction of silver ions was brought about by addition of 5 x 10^{-5} M tyrosine in alkaline conditions. The assembly of the silver nanoparticles so formed on the DNA template was observed under TEM and is shown in Figure 3.10 and 3.11.

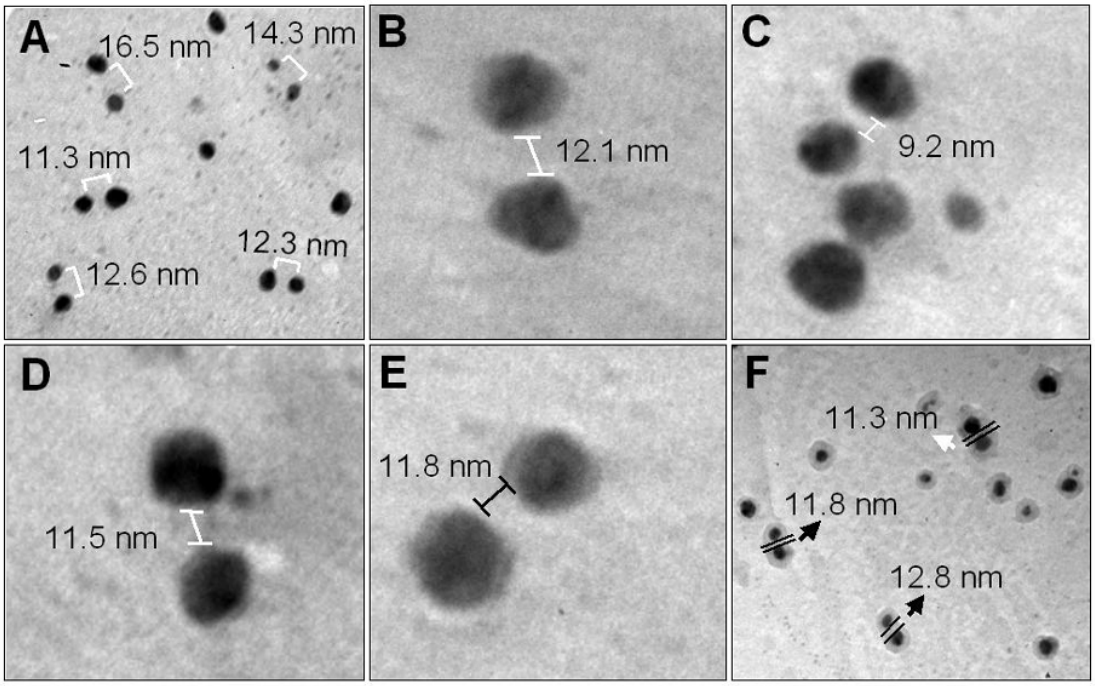

Figure 3.10 *Representative TEM images of the metallized C_{30}- T_{40} -C_{30} oligonucleotides. The formation of doublets of silver nanoparticles separated by the distance corresponding to the T_{40} stretch can be seen in images and the interparticle separation has been shown.*

It is evident from TEM analysis that the patterning on DNA template takes place as depicted in the scheme discussed above (Scheme 3.2). Thus, in the first oligonucleotide sequence (100 bases ~ 34 nm) with two cytosine stretches (C_{30}) flanking a thymine stretch (T_{40}), silver ions are trapped in the two adjoining stretches

of cytosine and are subsequently reduced to metallic silver by tyrosine in alkaline conditions (Figure 3.10). As the particles grow in size, the unoccupied thymine stretch (12.4 nm) at the center is delimited by the two particles of *ca.*15 nm each on either side. The average interparticle separation is observed to be 12.2 ± 1.7 nm, which is consistent with the length of T_{40} stretch in the middle. The metallized DNA therefore, appears in the form of doublet of nanoparticles separated by a fixed distance (Figure 3.10).

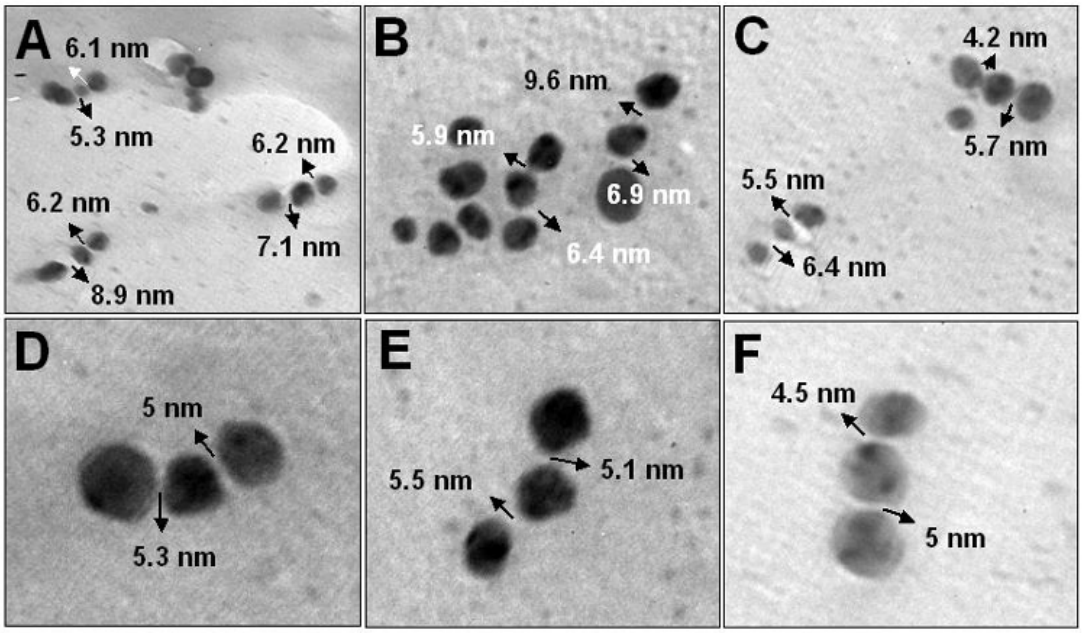

Figure 3.11 *Representative TEM images obtained from the metallized C_{20}- T_{20}- C_{20}- T_{20}- C_{20} oligonucleotide. The arrows have indicated the interparticle separation between the trimers.*

The second oligonucleotide sequence (100 bases ~ 34 nm) contains three stretches of C_{20}, alternating with two T_{20} stretches. Exposure to the reducing agent following the interaction with the silver ions leads to the appearance of short linear arrangements consisting of three silver nanoparticles (Figure 3. 11). These linear arrangements suggest that silver ions bind to three C_{20} regions in the ssDNA and subsequently forms silver nanoparticles. The alternating T_{20} regions do not bind silver nanoparticles strongly and therefore remains non-metallized. The set of three silver nanoparticles are separated by an average distance of 6.04 ± 1.33 nm, which is comparable to the length of alternating T_{20} stretches (~ 6.8 nm). Variation in the interparticle separation could result from differences in the particle size on flanking C_{20} stretches. For example, larger particles would encompass the non-metallized T_{20}

regions in the oligonucleotide and therefore would exhibit smaller separations between them.

Alivisatos and co-workers have demonstrated similar assemblies of gold nanoparticles by sequence dependent hybridization of a 5'-thiolated short oligonucleotide-gold nanocrystals conjugate with a complementary longer DNA molecule [33]. Although, their method showed spatially arranged gold nanocrystals, the process of DNA and gold nanocrystals functionalization is cumbersome. The assembly using ssDNA however, simplifies the process to a great deal. By designing appropriate oligonucleotides one can fine-tune the site of metallization and thereby control the interparticle separations. It should be also possible to develop more complex patterns of sequence based metallic nanowires by using non-liner arrays of oligonucleotides.

3.5 Discussion

Incorporation of DNA for nanoparticles assemblies has gained tremendous interest because of the large number of advantages associated with DNA over other templates [34]. This chapter was aimed at studying the ability of the nucleobases to interact with silver ions based on ITC analysis, which revealed that four nucleobases differed in their affinities towards Ag^+ remarkably, the order of strength of their interaction with silver being $C > G > A \geq T$. Similar trend in the exothermicity values was observed for single stranded oligo-cytosine and oligo-thymine sequences. The significant differences in the magnitude of interactions with silver ions despite the similarity in the sugar phosphate backbone suggest that the binding of silver ions takes place primarily with the nucleobases. This is in agreement with the previous reports that state that silver ions have affinity toward the nucleobases rather than the sugar phosphate backbone of DNA molecule [27].

The ability to differentially bind the metal ions with the nucleobases in a ssDNA presents a new approach for metallization of DNA molecule based entirely on the sequence of nucleobases. This has been realized by designing sequences consisting of the poly-cytosine and poly thymine stretches. These nucleobases exhibited the strongest and weakest binding ability with silver ions in ITC analysis. Exposing such single stranded oligonucleotides to silver ions leads to their entrapment

at the stretches rich in cytosine and the subsequent reduction event generates silver nanoparticles at these sites. Thymine rich regions remain non-metallized and acts as spacers between the silver nanoparticles at the adjoining regions. The TEM images have revealed that the interparticle separation is a function of the length and position of spacers. Such control over the sites of metallization on a DNA template had not been possible where the electrostatic assemblies of preformed nanoparticles or their precursors on the sugar phosphate backbone were employed.

The ready availability of synthetic DNA of desired sequences, and ease of manipulating it with metal ions makes this approach more promising than the previous methods requiring chemical modification of DNA molecule.

3.6 Conclusions

The chapter highlights the ability of nucleobases to differentially interact with silver ions based on the sensitive ITC measurements. These differences have been further supported by showing the varying extent of silver nanoparticle morphologies generated when the silver ions associated with the nucleobases are reduced in solution. The preferential binding of silver ions with the nucleobases over the sugar-phosphate backbone of DNA molecule has also been proved using the ITC analysis. Based on these results, we have devised a new approach for fabricating patterned nanowires of silver, where the DNA metallization can be controlled based on the sequences of the nucleobases.

3.7 References

1. (a) Warburton, R. J.; Schäflein, C.; Haft, D.; Bickel, F.; Lorke, A.; Karrai, K.; Garcia, G. M.; Schoenfeld, W.; Petroff, P. M. *Physica E* **2001**, *9*, 124. (b) Krenn, J. R.; Ditlbacher, H.; Schider, G.; Hohenau, H.; Leitner, A.; Aussenegg, F. R. *J. Microscopy.* **2003**, *209*, 167.

2. (a) Hochberg, M.; Baehr-Jones, T.; Walker, C.; Scherer, A. *Optics Express* **2004**, *12*, 5481. (b) Barrelet, C. J.; Greytak, A. B.; Lieber. C. M. *Nano Lett.* **2005**, *5*, 1779.

3. (a) Lee, T.; Liu, L.; Chen, N.; Andres, R. P.; Janes, D. B.; Reifenberger, R. *J. Nanoparticle Res*. **2000**, *2*, 345. (b) Wind, S. J.; Appenzeller, J.; Martel, R.; Derycke, V.; Avouris, P. *Appl. Phys. Lett*. **2002**, *80*, 3817**.**

4. (a) Cui, Y.; Wei, Z.; Park, H.; Lieber, C. M. *Science* **2001**, *293*, 1289. (b) Matsumiya, M.; Shin, W.; Izu, N.; Murayama, N. *Sensors and Actuators B* **2003**, *93*, 309.

5. (a) Patolsky, F.; Timko, B. P.; Yu, G.; Fang, Y.; Greytak, A. B.; Zheng, G.; Lieber, C. M. *Science* **2006**, *313*, 1100. (b) Koehne, J. E.; Chen, H.; Cassell, S. M.; Ye, Q.; Han, J.; Meyyappan, M.; Li, J. *Clinical Chem*. **2004**, *50*, 1886.

6. (a) Deng, Z.; Mao, C. *Angew. Chem. Int. Ed.* **2004**, *43*, 4068. (b) Joo, J.; Moon, S.; Jacobson, J. M. *J. Vacuum Sci. Technol. B* **2006,** *24*, 3205.

7. (a) Xu, C.; Taylor, P.; Ersoz, M.; Fletcher, P. D.; Paunov, V. N. *J. Mater. Chem.*, **2003**, *13*, 3044. (b) Thibault, C.; Berre, V. L; Casimirius, S.; Trévisiol, E.; François, J.; Vieu, C. *J. Nanobiotechnol.* **2005**, *3*:7. ; (c) Lange, S. A.; Benes, V.; Kern, D. P.; Horber, J. K. H.; Bernard. A. *Anal Chem.* **2004**, *76*, 1641. (d) Zandvliet, H. J. W.; Reinhoudt, D. N.; Poelsema, B. *J. Am. Chem. Soc*. **2006;** *128,* 15560.

8. (a) Li, M.; Schnablegger, H.; Mann, S. *Nature* **1999**, *402*, 393. (b) Rabani, E.; Reichman, D. R.; Geissler, P. L.; Brus, L. E. *Nature* **2003**, *426*, 271. (c) Ma, Y.; Zhang, J.; Zhang, G.; He, H. *J. Am. Chem. Soc.* **2004**, *126*, 7097.

9. (a) Kumar, A.; Pattarkine, M.; Bhadbhade, M.; Mandale, A. B.; Ganesh, K. N.; Datar, S. S.; Dharmadhikari, C. V.; Sastry, M. *Adv. Mater.* **2001**, *13*, 341. (b) Davis, S. A.; Breulmann, M.; Rhodes, K. H.; Zhang, B.; Mann, S. *Chem. Mater.* 2**001**, *13*, 3218.

10. (a) Dong, Q.; Su, H.; Zhang, D.; Zhu, N.; Guo, X. *Script Mater*. **2006**, *55*, 799. (b) Wakabayashi, A.; Sasakawa, Y.; Dobashi, T.; Yamamoto, T. *Langmuir* **2006**, *22*, 9260.

11. (a) Verdes, C.; Chantrell, R.W.; Satoh, A.; Harrell, J.W.; Nikles, D. *J. Mag. Mag. Mater.***2006**, *304*, 27. (b) Anderson, E.A.; Isaacman, S.; Peabody, D.S.; Wang, E.Y.; Canary, J.W.; Kirshenbaum, K. *Nano Lett.* **2006**, *6*, 1160. (c) Sun, S. *Adv. Mater.* **2006**, *18*, 393. (d) Yan, Q.; Purkayastha, A.; Kim, T.; Kroger, R.; Base, A.; Ramanath, G. *Adv. Mater*. **2006**, *89*, 2569.

12. (a) Blum, A. S.; Soto, C. M.; Wilson, C. D.; Whitley, J. L.; Moore, M. H.; Sapsford, K. E.; Lin, T.; Ratna, B. R. *Nanotechnology* **2006**, *17*, 5073. (b) Yamagiwa, M.; Mano, T.; Kuroda, T.; Tateno, T.; Sakoda, K.; Kido, G.; Koguchi, N.; Minami, F. *Appl. Phys. Lett.* **2006**, *89*, 113115.

13. (a) Moskovits, M. *Rev. Mod. Phys*. **1985**, *57*, 783. (b) Maier, S. A.; Kik, P. G.; Atwater, H. A.; Meltzer, S.; Harel, E.; Koel, B. E.; Requicha, A. A. G. *Nature Mater.* **2003**, *2*, 229. (c) Lakowicz, J. R. *Anal. Biochem*. **2001**, *298*, 1.

14. (a) Wei, Q.-H.; Su, K.-H.; Durant, S.; Zhang, X. *Nano Lett*. **2004**, *4*, 1067. (b) Maier, S. A.; Brongersma, M. L.; Kik, P. G.; Atwater, H. A. *Phys. Rev. B* **2002**, *65*, 193408. (c) Maier, S. A.; Brongersma, M. L.; Kik, P. G.; Meltzer, S.; Requicha, A. A. G.; Atwater, H. A. *Adv. Mater.* **2001**, *13*, 1501.

15. (a) Yin, Y.; Lu, Y.; Gates, B.; Xia, Y. *J. Am. Chem. Soc*. **2001**, *123*, 8718. (b) Alivisatos, A. P.; Johnsson, K. P.; Peng, X. G.; Wilson, T. E.; Loweth, C. J.; Bruchez, M. P.; Schultz, P. G. *Nature* **1996**, *382*, 609.

16. Sioss, J. A.; Keating, C. D. *Nano Lett*. **2005**, *5*, 1779.

17. Mertig, M.; Ciacchi, L. C.; Seidel, R.; Pompe, W. *Nano Lett.* **2002**, *2*, 841.

18. (a) Gothelf, K. F.; La-Bean, T. H. *Org. Biomol. Chem.* **2005**, *3*, 4023. (b) Niemeyer, C. F. *Angew. Chem. Int. Ed.* **2001**, *40*, 4128. (c) Rosi, N. L.; Mirkin, C. A. *Chem. Rev*. **2005**, *105*, 1547.

19. Monson, C. F.; Woolley, A. T. *Nano Lett.* **2003**, *3*, 359.

20. Braun, E.; Eichen, Y.; Sivan, U.; Ben-Yoseph, G. *Nature* **1998**, *391*, 775.

21. Zinchenko, A. A.; Yoshikawa, K.; Baigl, D. *Adv. Mater.* **2005**, *17*, 2820.

22. Berti, L.; Alessandrni, A.; Facci, P. *J. Am. Chem. Soc.* **2005**, *127*, 11216.

23. Zinchenko, A. A.; Yoshikawa, K.; Baigl, D. *Adv. Mater.* **2005**, *17*, 2820.

24. Wei, G.; Zhou, H.; Liu, Z.; Song, Y.; Wang, L.; Sun, L.; Li, Z. *J. Phys. Chem. B* **2005**, *109*, 8738.

25. (a) Keren, K.; Krueger, M.; Gilad, R.; Yoseph, G. B.; Sivan, U.; Braun, E. *Science* **2002**, *72*, 72. (b) Keren, K.; Berman, R. S.; Braun, E. *Nano Lett.* **2004**, *4*, 323. (c) Burley, G. A.; Gierlich, J.; Mofid,M. R.; Nir, H.; Tal, S.; Eichen, Y.; Carell, T. *J. Am. Chem. Soc*. **2006**, *128*, 1398.

26. Reed, M. I.; Christensen, J. J.; Rytting, J. H. *Chem. Rev*. **1971**, *71*, 439.

27. Luk, K. F. S.; Maki, A. H.; Hoover, R. J. *J. Am. Chem. Soc*. **1975**, *97*, 1241.

28. (a) Ladbury, J. E. *Biotechniques* **2004**, *37*, 885. (b) Arya, D. P.; Coffee, R. L.; Xue, L. Bioorg. Med. Chem. Lett. **2004**, 14, 4643. (c) Gourishankar, A.; Shukla, S.; Ganesh, K. N.; Sastry, M. *J. Am. Chem. Soc*. **2004**, *126*, 13186. (d) Joshi, H. M.; Shirude, P. S.; Bansal, V.; Ganesh, K. N.; Sastry, M. *J. Phys. Chem. B* **2004**, *108*, 11535.

29. (a) Huq, F.; Hossain, Z. *J. Inorg. Biochem.* **2002**, *91*, 398. (b) Dattagupta, N.; Crothers, D. M. *Nucleic Acids Res*. **1981**, *9*, 2971. (c) Rossetto, F. E.; Nieboer, E. *J. Inorg. Biochem*. **1994**, *54*, 167.

30. Selvakannan, P. R.; Swami, A.; Srisathiyanarayanan, D.; Shirude, P. S.; Pasricha, R.; Mandale, A. B.; Sastry, M. *Langmuir* **2004**, *20,* 7825.

31. Moskovits, M.; Vlc˘kova´, B. *J. Phys. Chem. B* **2005**, *109*, 14755.

32. (a) Schofield, C. L.; Haines, A. H.; Field, R. A.; Russell, D. A. *Langmuir* **2006**, *22*, 6707. (b) Zhang, J.; Roll, D.; Geddes, C. D.; Lakowicz, J. R. *J. Phys. Chem. B* **2004**, *108*, 12210.

33. Loweth, C. J.; Caldwell, B. W.; Peng, X.; Alivisatos, A. P.; Schultz, P. G. *Angew. Chem. Int. Ed*. **1999**, *38*, 1808.

34. (a) Gothelf, K. V.; LaBeam, T. H. *Org. Biomol. Chem.* **2005**, *3*, 4023. (b) Mirkin, C. A. *Mater. Res. Soc. Bull*. **2001**, *25*, 43.

Chapter IV

Synthesis of Porous Metal Nanostructures

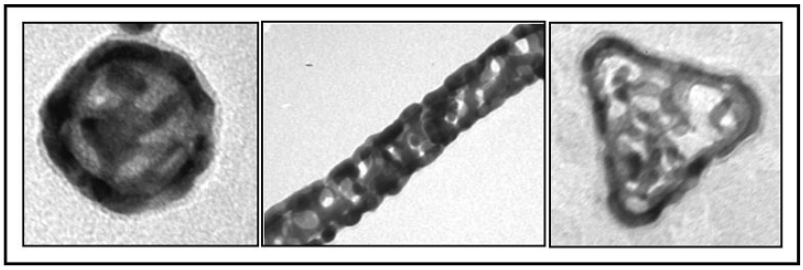

Porous metal nanostructures are a special class of bimetallic nanomaterials, which have unique electronic and optical properties arising from the presence of cavities. Thus, these materials are not just bestowed with an enormous surface area but also have low density and cost-effectiveness over solid nanomaterials of comparable size and composition. This chapter describes a novel process developed for the synthesis of such porous bimetallic metal nanostructures of varying composition as well as morphologies. The process is based on a controlled galvanic replacement reaction between a sacrificial metal nanoparticle and a metal ion species with a higher redox potential, across a semi-permeable dialysis membrane. The dialysis membrane acts as a semi-permeable barrier providing excellent control over the reaction kinetics and thereby leads to synthesis of phase-pure porous nanostructures.

Part of the work described in this chapter has been published/ communicated: (a) Shukla, S.; Priscilla, A.; Banerjee, M.; Bhonde, R. R.; Ghatak, J.; Satyam, P. V.; Sastry, M. *Chem. Mater.* **2005**, *17*, 5000. (b) Shukla, S.; Sastry, M. *Small*, **2007** (communicated).

4.1 Introduction

Synthesis of metal nanoparticles has been an active area of research for a long time now because of their unique properties that make them enormously important in applications such as electronics [1], optics [2], catalysis [3], sensing [4], diagnostics [5] and therapeutics [6]. The intrinsic properties of a nanostructured metal are mainly determined by its size, shape, composition, crystalinity and structure. In principle, therefore, accurate control over any of these parameters would allow one to fine-tune the properties of such nanostructured metals and this field presents an exciting area of research [7]. As evident from the huge interest that it has generated recently, developing new synthesis protocols with shape and size tunability, thus, is a challenging field to work in. Therefore, there are ever increasing reports on the synthesis of metal nanoparticles with control on their morphology using physical [8], chemical [9] as well as biological routes [10]. One can therefore, control the characteristic properties of metal nanoparticles such as surface plasmon resonance (SPR) by varying the shape and size, which could be tuned from the visible region to infrared region depending on the extent of anisotropy [11]. These anisotropy-induced changes could induce significant enhancement in the functionality of the metal nanoparticles, rendering them potentially more useful for specific applications.

This size, shape and structure dependent tunability of the optoelectronic properties that has lead to development of specific applications based on the morphologies. Thus, while the spherical metal nanoparticles such as gold and silver have been exploited for their visible region plasmon absorption in optical sensors [12] and as chromophores [13], other morphologies such as flat gold and silver nanotriangles with SPR absorption in the near infrared region have been used in optical coatings for thermal shields [14], cancer hyperthermia [15] and as substrates for SERS applications at longer wavelengths [16]. Similarly, other noble metal nanoparticles such as platinum nanoparticles also show catalytic specificity based on the their structures [17].

However, composition is another variable that is important in determining the nanoparticle properties and providing them with enhanced functionality. Bimetallic nanoparticles are a class of metal nanoparticles that constitute atomic clusters of two

different metals. These bimetallic nanoparticles exhibit highly improved catalytic activity, surface plasmon properties and magnetic properties arising from the structural and electronic effect of the bimetal [18]. One important subclass of bimetallic nanoparticles is hollow-shell/porous nanomaterials, which besides having advantage of high specific surface area, low density and cost effectiveness, are significant as they have unique optical and catalytic properties, different from their solid counterparts [19]. A great deal of research over the last few years is thus focused on the development of synthesis protocols leading to such hollow-shell / porous nanostructures. It is noteworthy that the presence of cavities is desirable not just in metallic nanostructures but also in polymeric and polymeric-inorganic composite nanomaterials [20]. Whereas the synthesis methods of hollow / porous polymer nanoparticles and oxide nanoparticles is well documented [21], there are only few reports on the synthesis of porous/ hollow shell metal nanostructures.

The importance of porous/ hollow metal nanostructures and the interest in developing efficient methodologies for its synthesis exists due to the unique optical and catalytic properties possessed by them. It has been established that the hollow shell SPR is dependent on the shell thickness relative to its core and is tunable from the visible to the Near Infra Red (NIR) region of the electro-magnetic spectrum by varying the shell thickness [22]. NIR absorption by the hollow-shell nanostructures is particularly interesting as in this region the tissue transmissivity is maximum due to low scattering and absorption by the intrinsic chromophores that makes the gold nano-shells attractive for *in vivo* diagnostic and therapeutic applications [23]. Also, nanostructures with hollow interior have been used as sensors based on the change in electric properties upon chemisorption of organic molecules [24].

The nano-shells also possess a large optical cross section exceeding that of conventional NIR chromophores, such as indocyanine green, by many orders of magnitude, making them potentially applicable for biomedical sensing and imaging. The higher photostability of the encapsulated fluorescent probes resulting from the metallic structure of the carrier nanoparticles also contributes to their enhanced functionality [25]. The higher scattering cross section [26] also makes the nano-shells useful for photonics based imaging applications such as Optical Coherent

Tomography (OCT) [27] and Reflectance confocal microscopy (RCM) [28]. Xia and co-workers have also demonstrated that the surface plasmon sensitivity of the hollow gold nanoparticles towards environmental changes is higher than the solid gold nanoparticles [29].

Besides the numerous advantages of gold hollow shells and porous gold nanoparticles in cell imaging, sensing and other biological applications, porous nanostructures comprising platinum and palladium are also significant in the field of catalysis and energy storage. Porous nanostructures of platinum and palladium could contribute significantly in improving the catalytic processes currently utilizing the solid forms of these nanomaterials. This is possible as the specific surface area in the case of hollow / porous nanostructures increases tremendously. Also, the reduction in the amount of the noble metal required for such applications brought about by having a surface layer of the platinum/ palladium alone, would mean introduction of cost effectiveness in the whole process. This could be very significant as the nanoparticle mediated catalysis processes despite being highly efficient, are often hampered by the high cost of metals such as platinum and palladium. While some of catalytic processes involving porous palladium, such as in Suzuki cross coupling reactions [30] and enhanced electrocatalytic oxidation of methanol by porous platinum has been demonstrated [31], others such as nano-platinum based catalytic conversion of methane to hydrogen for fuel cell applications are being developed [32]. Introduction of the porous forms of the catalytically important platinum and palladium nanostructures would therefore improve the existing processes besides opening new avenues for research in this direction.

There are only a few known methods for the fabrication of metallic hollow / porous materials. One of them is the deposition of preformed nanoparticles or their precursors on colloidal materials such as silica or polymeric and ceramic beads resulting in a core shell morphology followed by the removal of the core by chemical etching or calcination [33]. Layer-by-layer assembly has also been used extensively to synthesize a range of polymeric core inorganic shell nanoparticles [34]. Hollow nanocrystals have also been synthesized by the Kirkendall effect in which pores form because of the difference in the diffusion rate of two components [35]. There are also

reports on chemical methods involving seed mediated Ag-Au bimetallic core-shell nanoparticle growth using surfactants [36].

One of the most interesting methods for the fabrication of metallic shell nanoparticles, however, is the galvanic replacement reaction. It involves the sacrificial oxidation of a metal nanoparticle acting as a template and a consequential reduction of the second metal ion with higher redox potential leading to the formation of a shell of the latter on the former. The method has been extensively used by many research groups to form a broad range of bimetallic/ metal shell nanoparticles. Xia and co-workers have shown the synthesis of hollow Ag-Au metal nanoparticles of different morphologies by using silver nanoparticles as the sacrificial reducing agent and reducing gold ions [37]. Chun Li Bai and co-workers, on the other hand, have used cobalt nanoparticles as the sacrificial reducing agent for the synthesis of gold-platinum bimetallic nanoparticles [38]. Similarly, Mirkin's group has also fabricated gold nanoframes using sliver nanotriangles as the sacrificial templates [39]. Sastry and co-workers have used similar principles in the organic medium to synthesize hollow gold and platinum nanoparticles [40].

The popularity of this method, though, is marred by certain inherent drawbacks. For instance, in Xia `s protocol, the residual products of the redox reactions, the ions, have a tendency to form insoluble complexes that hinder the formation of purified products of interest [41]. Thus, silver ions liberated as a result of the oxidation of silver nanoparticles upon addition of gold ions, lead to the formation of silver chloride precipitates in the reaction mixture, which necessitates additional downstream steps for the purification of the hollow metal nanostructures. To avoid the formation of these impurities, one needs to carry out the reaction at a higher temperature, thereby preventing the formation of the precipitate. Also, the redox reaction underlying the transmetallation is an extremely rapid process making it challenging to control the reaction rate and the composition of the products.

This chapter discusses an exciting way out of the above-mentioned problem along with providing an excellent control of the rate of the galvanic replacement reaction. We describe here, the use of a selective semi-permeable dialysis membrane to carry out the reaction, which allows the ions to diffuse across but retains the more

bulky nanoparticles inside, thus separating the residual ions from the metal nanoparticles. The slow diffusion of the ions provide excellent control over the reaction and thereby facilitate control on the composition of the resulting hollow shell/ porous nanoparticles in terms of the constituting metals and the pore size. The method is not just simple but also is generic, applicable to a variety of redox pairs of metals – ion pairs, as well as morphologies.

The chapter begins with the illustration of the novel method developed for the synthesis of porous gold, platinum and palladium nanospheres with an emphasis on gold porous nanoparticles. This section also forays into the detailed mechanism of the cavity formation in these porous nanospheres and the affect of various parameters on the rate of the reaction. The second section, on the other hand, brings in the factor of anisotropy in the porous nanostructures. This section describes the fabrication of anisotropic template nanostructures and thereafter the galvanic replacement reactions leading to creation of the cavities within these structures. The characterization of the nanoparticles has been done using UV-vis-NIR spectroscopy, transmission electron microscopy (TEM), high resolution TEM (HRTEM), and atomic force microscopy (AFM) and is described in the chapter.

4.1.1 Experimental set-up

The porous nanostructures were synthesized by the galvanic replacement reaction taking place across the dialysis membrane, which serves as a selectively permeable barrier between the sacrificial metal nanoparticles and the suitable metallic ions.

Figure 4.1 illustrates the actual reaction set up, where the sacrificial nanoparticle solution is enclosed in dialysis tubing, which is then immersed in another solution of the second metal ions. Therefore, M-1 and I-1 are the reduced form and oxidized form of the sacrificial metal respectively, while M-2 and I-2 are the same for the second metal. For the transmetallation reaction to take place, the redox potential for the M-2/I-2 pair should be higher than the redox potential for the M-1/ I-1 pair. The set up is kept on a magnetic stirrer for uniform mixing and diffusion of the reacting species. Samples are collected intermittently for analysis from the dialysis tubing, while the reaction could be paused or terminated by simply removing the

dialysis membrane from the outer solution. The progress of the reaction could be monitored visually by the changing color of the solution inside the dialysis membrane, and also spectroscopically by monitoring the absorption spectrum of the internal and external solutions.

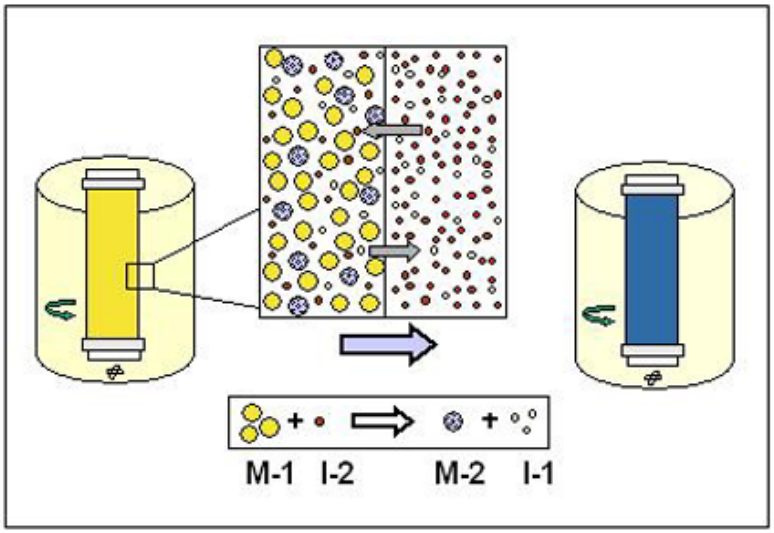

Figure 4.1 *Schematic representation of the experimental set up for the synthesis of porous nanostructures by galvanic replacement reaction across the dialysis membrane. M-1 and I-1 are the reduced and ionic forms of the sacrificial metal while M-2 and I-2 are the reduced and ionic forms of the second metal.*

4.2 Synthesis of porous nanospheres of gold, platinum and palladium

The synthesis of porous gold nanoparticles (porous Au NPs), porous platinum (porous Pt NPs) and porous palladium nanoparticles (porous Pd NPs) was carried out by the transmetallation reaction between the sacrificial silver nanoparticles (Ag NPs) and ionic solutions of gold, platinum and palladium, respectively. Tyrosine reduced silver nanoparticles were synthesized by the method developed by Sastry and co workers [42]. Briefly, 100 ml of 10^{-4} M Ag_2SO_4 solution was mixed with 10^{-4} M tyrosine and the mixture was brought to boil. Addition of 10^{-3} M KOH solution and the subsequent boiling resulted in the rapid change of the solution color from colorless to yellow, indicating the formation of the Ag NPs. The pH of the resulting Ag NPs solution was 10.2. The solution was allowed to cool and then dialyzed against Millipore water for 24 h with three water changes to get rid of all the uncoordinated tyrosine and hydroxyl ions, in the process, also bringing down the pH from 10.2 to pH

7, and was used for all the further experiments. Hereafter, Ag NPs would correspond to the dialyzed tyrosine reduced silver nanoparticles.

For the transmetallation experiment leading to the fabrication of porous Au nanoparticles, 20 ml of Ag NPs was taken inside a 12.5 kDa cut-off dialysis tubing (Sigma). Prior to this, the dialysis tubing had been washed under tap water for 5 minutes followed by boiling twice in Millipore water to remove the surface bound impurities, in accordance with the instructions provided by the manufactures. The sealed tubing containing the Ag NPs solution was then submerged in the aqueous solution of 5 x 10^{-5} M chloroauric acid ($HAuCl_4$ or Au (III) ions) in a dialysis jar and the whole set up was kept for continuous stirring on a magnetic stirrer. Aliquots were intermittently collected from within the dialysis tubing and the outer $HAuCl_4$ solution and were analyzed using UV-vis-NIR spectroscopy, Transmission Electron Microscopy (TEM), conductivity measurements, Energy Dispersive Analysis of X-rays (EDAX), and High Resolution Transmission Microscopy (HRTEM).

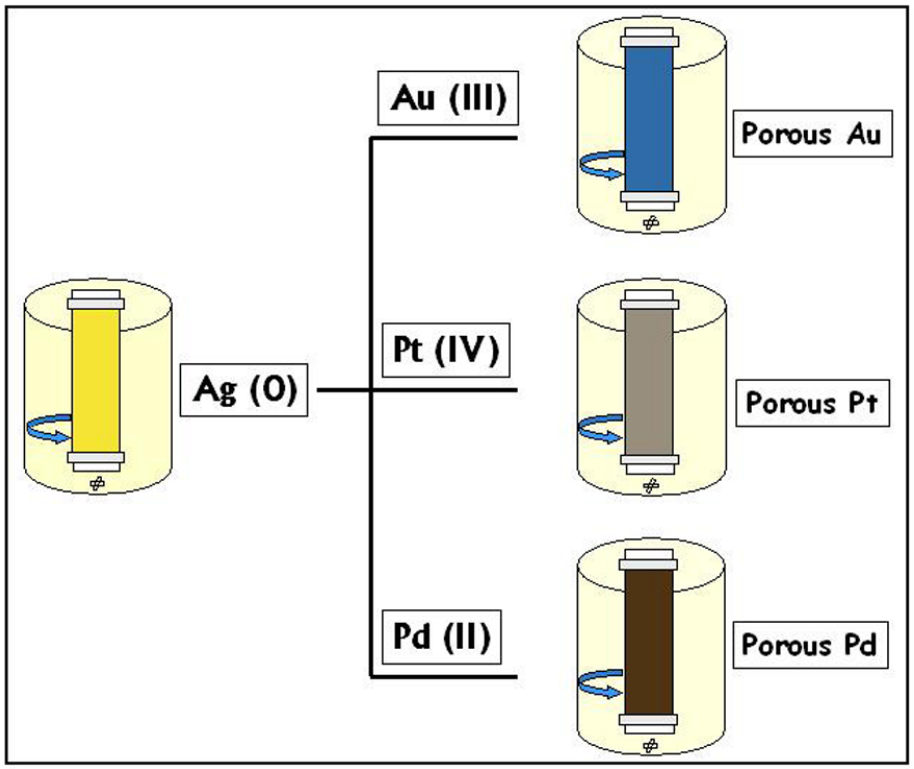

Figure 4.2 *Scheme depicting the synthesis of porous Au, porous Pt and porous Pd by the transmetallation reaction using the dialysis tubing. Tyrosine reduced silver nanoparticles, Ag (0) when dialyzed against Au (III), Pt (IV) and Pd (II) ionic solutions leads to the synthesis of respective porous nanoparticles.*

Similarly, for the fabrication of porous Pt, 20 ml of Ag NPs was dialyzed in the 12.5 kDa cut-off tubing against 10^{-4} M chloroplatinic acid (H_2PtCl_6 or Pt (IV) ions) with continuous stirring while in the case of porous Pd, 10^{-4} M palladium nitrate solution ($PdNO_3$ or Pd (II) ion) was used as the outer solution in the dialysis experiment. As in the previous case, small amount of samples from the dialysis tubing and from the outer solution were taken out intermittently, and analyzed using the above-mentioned techniques. Figure 4.2 depicts the general layout of the experiment.

4.2.1 UV-vis-NIR and Transmission Electron Microscopy analysis

The transmetallation reaction was studied using the UV-vis-NIR spectroscopy analysis and transmission electron microscopy (TEM) analysis of the samples intermittently collected from within the dialysis tubing and from the outer solutions in all the three sets of experiments involving Au (III), Pt (IV) and Pd (II) ionic solutions. The UV-vis spectra were recorded for all the solutions on a Jasco V-570 UV-vis-NIR spectrophotometer operated at a resolution of 1 nm. Samples for TEM analysis were prepared by drop-coating the nanoparticle samples at various stages of transmetallation on carbon coated copper grids. TEM measurements were performed on a JEOL model 1200EX instrument operated at an accelerating voltage of 80 kV.

The reaction between 10^{-4} M Ag NPs and 5 x10^{-5} M Au (III) ions across a 12.5 kDa dialysis tubing was monitored by time dependent UV-vis-NIR spectroscopy and TEM analysis, and is shown in Figure 4.3. The time point UV-vis-NIR absorption spectra recorded from the solution inside the dialysis tubing is shown in Figure 4.3 A. The surface plasmon resonance absorption spectrum of the as-prepared Ag NPs is centered at 408 nm (Figure 4.3 A, curve 1) [41]. As the reaction proceeds, damping of the silver plasmon absorption band is observed that shifts monotonically with time (up to 5 h of reaction, Figure 4.3 A, curve 3) to ca. 480 nm. The progressive intensity decrease and red shift in the silver plasmon absorption band is symptomatic of loss of metallic silver via oxidation of the silver nanoparticles (to Ag^+) and formation of an Ag-Au alloy phase that becomes progressively rich in gold. After 5 h of reaction (Figure 4.3 A, curve 3), an additional broad absorption band appears at 700 nm, indicating the formation of a thin shell of gold on the sacrificial silver nanoparticle.

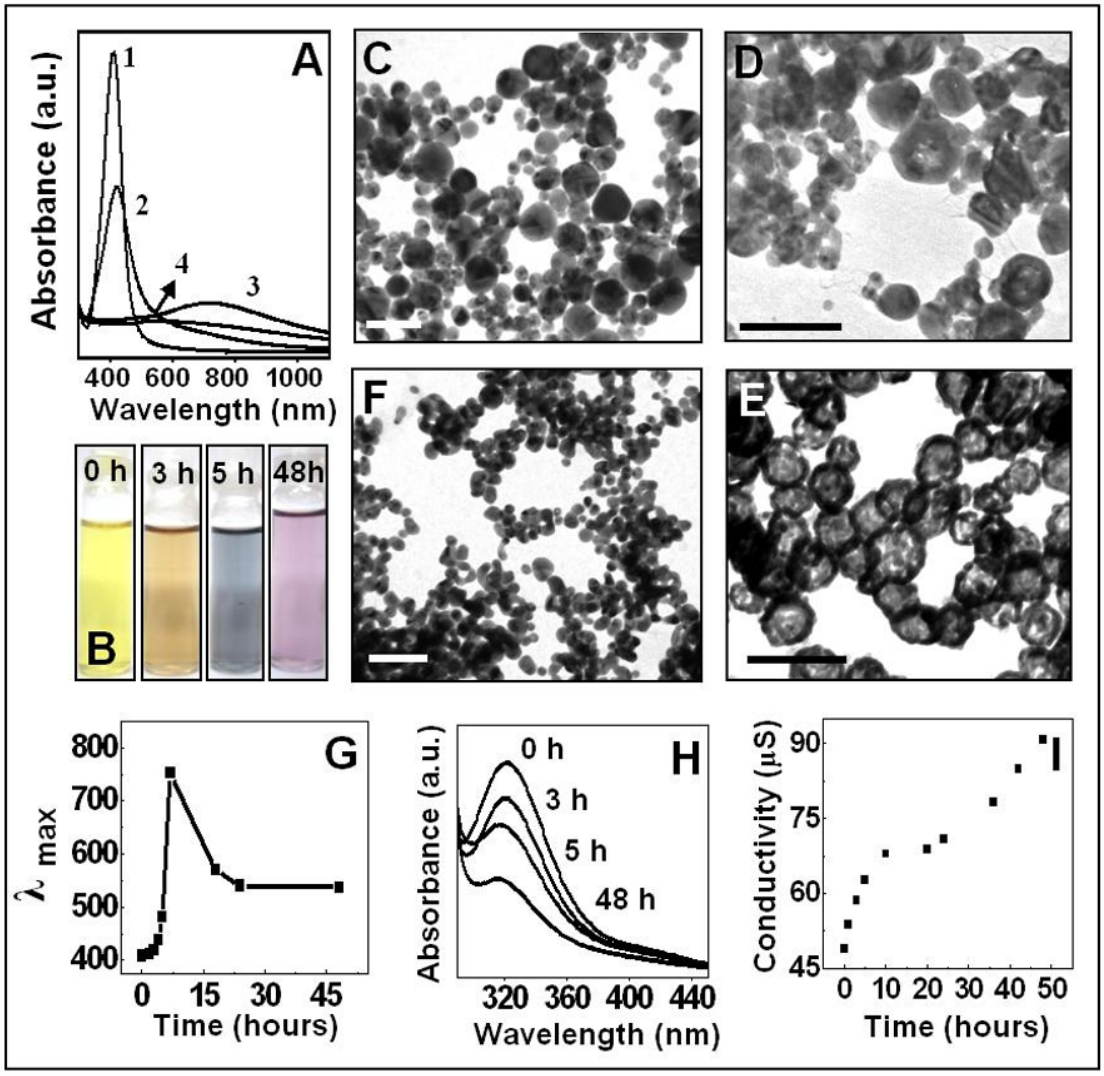

Figure 4.3 *UV-vis-NIR and transmission electron microscopy (TEM) analysis of the galvanic replacement reaction carried out between 10^{-4} M Ag NPs and 5 x 10^{-5} M Au (III) ions. Curve 1 in A corresponds to the UV-vis-NIR spectrum of the as-prepared Ag NPs, while curves 2, 3 and 4 are the absorption bands of the solution from the dialysis tubing after 3 h, 5 h and 48 h respectively. The change in the colour of the solutions with time is shown in B. C, D, E and F are TEM images corresponding to the curves 1-4 in A, respectively (scale bars in TEM images represent 100 nm). G represents the change in the λ_{max} as a function of time for the above-mentioned reaction. H and I correspond to the time dependent UV-vis-NIR absorption spectra and the conductivity measurement of the outer solution.*

These spectral changes, as a function of time, can be explained on the basis of the compositional changes taking place inside the dialysis tubing. The galvanic replacement reaction between Au (III) and Ag NPs occurs since the standard reduction potential for the $AuCl_4^-$ /Au pair (0.99 V vs standard hydrogen electrode, SHE) is higher than that of the Ag^+/Ag pair (0.80 V vs SHE). Thus, Ag NPs act as a sacrificial reducing agent in the reduction of Au (III) ions to Au (0) and in the

process, get oxidized to Ag (I). As more and more Au (III) diffuses in, there is a significant loss of metallic silver as a result of this oxidation leading to loss in intensity of the silver plasmon band. As the reduction of Au (III) ions takes place only when the ions come in contact with the surface of Ag NPs, there is a gradual deposition of metallic gold on the Ag NPs surface. As the amount of metallic gold builds up in the reaction medium, formation of Ag-Au alloy phase can be observed which is evident by the gradual red shift in the surface plasmon band at the end of 3 h of reaction along with the dampening. The positioning of the surface plasmon band between that of the metallic silver and nano gold is an indication of the alloy phase and is in agreement with literature [43]. As the reaction proceeds, loss of metallic silver results in the formation of cavities with in the template particles, rendering the nanoparticles porous with thin metallic shells of gold around them, indicated by a ~ 700 nm absorption band [22]. The increasing percentage of metallic gold, however, drives the reaction to a de-alloying phase which is characterized by a blue shift in the surface plasmon band to 540 nm (Figure 4.3 A, curve 4), which represents the formation of solid gold nanoparticles. The colour of the solution during the course of the reaction changes from yellow (Ag NPs) to light brown (Ag-Au alloy) to blue (gold shell) to pink (gold nanoparticles) as shown in Figure 4.3, B.

The observations made in the UV-vis-NIR absorption analysis are well supported by the TEM analysis (Figure 4.3, C-F), where one can clearly see the transition in the morphology of the nanoparticles as the reaction proceeds. Thus, the as-prepared Ag NPs can be seen as spherical nanoparticles with an average diameter of ~ 50 nm (Figure 4.3, C). However, as the reaction proceeds, at the end of 3 h, a large number of the Ag NPs show etching at specific locations on the particle surface and the creation of small voids (Figure 4.3, D). These voids become more prominent, and at the end of 5 h of reaction, a thin gold shell is formed around the silver nanoparticles (Figure 4.3, E). The subsequent de-alloying resulting from the continuous influx of Au (III) up to 48 h of reaction leads to the collapse of the porous gold nanoparticles to generate small irregular gold nanoparticles (Figure 4.3, F).

A simultaneous UV-vis-NIR absorption analysis of the outer solution of chloroauric acid reveals the consumption of the Au (III) ions as they diffuse into the

membrane (Figure 4.3, H). It can be observed that the intensity of the absorption band of chloroauric acid centered at 312 nm goes down as the reaction proceeds.

For each migrating Au (III) ion, three silver atoms are oxidized in the dialysis tubing, generating three Ag (I) ions, which then diffuse out. Thus, the overall ionic population of the outer solution increases. A conductivity measurement carried out for the outer solution thus reveals that as the reaction proceeds, the conductivity of the outer solution increases steadily for 20 h, reaching near saturation at around 24 h (Figure 4.3, I). Interestingly though, there is a second increment in the conductivity values towards the end of the reaction. These results can be correlated to the UV-vis-NIR absorption spectrum of the solution enclosed in the dialysis tubing (Figure 4.3, A) and the TEM analysis of the reaction mixture at the terminal stage of the reaction (Figure 4.3, F). Once the formation the thin gold shell around the Ag NPs has taken place at around 5 h of reaction, the leaching out of the silver ions from within the particles nears saturation. The steady influx of the Au (III) ions however continues. It is only at the later stages of the reaction that the concentration build up of Au (III) drives the collapse of the porous gold shell structures (Figure 4.3, F), exposing the inaccessible metallic silver to the transmetallation reaction. This in turn, results in an increased population of silver ions, which then diffuse out to contribute to the conductivity of the outer solution, and hence the second phase of rise in the conductivity is observed.

A closer look at the TEM images of the silver nanoparticles, as they acquire the porosity during the course of the reaction, reveals much about the possible mechanism of the void formation in these nanoparticles. The multiply twin nature of the tyrosine-reduced silver nanoparticles is clearly observed, with the surface topology marked with presence of the twin boundaries [44] (Figure 4.4, A). These surface defects are marked with white arrows in the figure. Higher magnification images of the nanoparticles after 3 h of reaction shows regions on the nanoparticle surface that have been etched away at certain specific locations. (Figure 4.4, B). A comparison of Figure 4.4 A and B strongly suggests that there is a correlation between the topology and position of the voids and the twins in the sacrificial silver nanoparticles. At this stage, the UV-vis-NIR spectra of the Ag NPs exhibited a peak at

419 nm indicating a small percentage of gold in the Ag-Au alloy. After 5 h of reaction, a much larger percentage of the Ag NPs shows porosity with the size of the pores also increasing with time of reaction (Figure 4.3, E). At higher magnification, one also observes that the number of pores per particle increases and a well defined gold shell has formed (Figure 4.4, C) and also that the position of the pores still bears a correlation with the multiply twinned structure of the starting sacrificial Ag np. The high magnification TEM images shown in Figure 4.4 indicate that etching of the Ag NPs during the transmetallation reaction is initiated at the twin boundaries. The twin boundaries may also provide defect sites for facile effusion of the oxidized silver ions produced as the sacrificial Ag NPs are consumed in the reaction. The porous structures formed after 5 h of reaction are of a composition at the critical limit between alloying and de-alloying (an alloy peak centered at 480 nm and a gold shell peak at 700 nm, UV-vis-NIR data in Figure 4.3, A, curve 3). Further addition of Au (III) therefore, drives the reaction to a de-alloying phase, resulting in the collapse of the porous structures into small irregular nanostructures that do not show any indication of porosity.

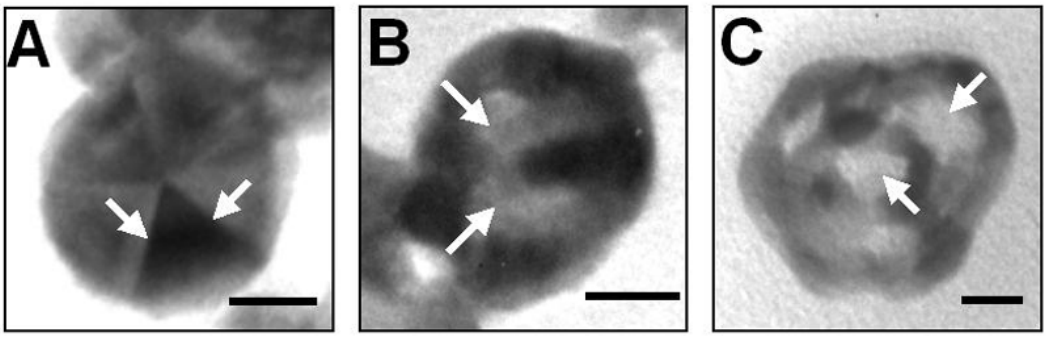

Figure 4.4 *High magnification TEM images representing the fabrication of the porous gold nanoparticles from the sacrificial silver nanoparticles. The as-prepared Ag NPs with the twin boundaries pointed with the arrows, A; the expansion of the twin boundaries to form voids after a 3 h transmetallation reaction, B; and the porous gold structures with the cavities entrapped under a gold shell after a 5 h reaction, C. Scale bars in the figure correspond to 20 nm.*

Similarly, the UV-vis-NIR absorption spectra for the galvanic replacement reaction between the sacrificial Ag NPs and 10^{-4} M Pt (IV) ions is shown in the Figure 4.5, A as a function of time. It is evident from the spectra that Pt (IV) ions too, diffuse through the dialysis tubing and lead to the oxidative loss of silver nanoparticles,

causing a gradual dampening of the silver plasmon band (Figure 4.5, A, curves 1-4). TEM analysis of the reaction as a function of time supports the UV-vis-NIR data. Thus, pure silver nanoparticles are seen as solid spheres (Figure 4.5, B and F-a) and have a characteristic surface plasmon absorption band centered at 408 nm (Figure 4.5, A, curve 1). As the reaction proceeds, at the end of 7 h of reaction a significant drop in the silver plasmon band intensity is achieved (Figure 4.5, A, curve 3), suggesting a considerable loss of metallic silver. It is evident from corresponding TEM images (Figure 4.5, C and F-b), that at this stage of the reaction a significant number of nanoparticles show formation of cavities. The complete disappearance of the silver

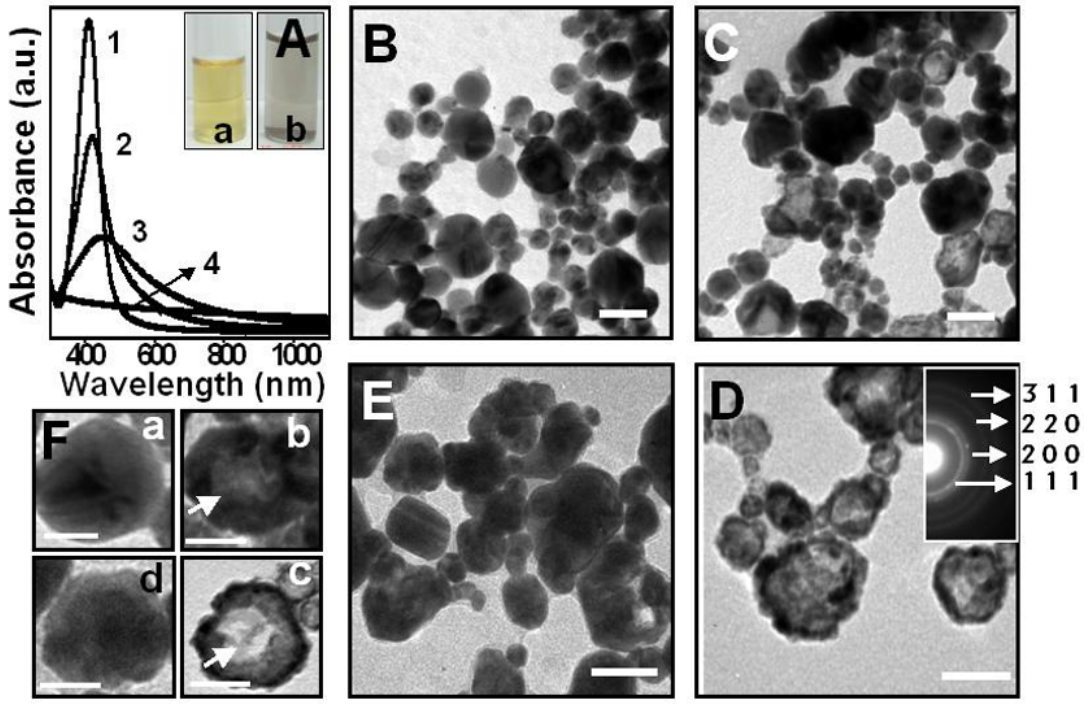

Figure 4.5 *UV-vis-NIR spectra and the TEM kinetics of the transmetallation reaction between 10^{-4} M Ag NPs and 10^{-4} M Pt (IV) solution. Curves 1, 2, 3 and 4 in A are the spectrum recorded for the pure Ag NPs, after 2 h, 7 h and 24 h of reaction. Inset A-a and A-b correspond to curves 1 and 4, respectively. B, C, D and E are the representative TEM images obtained for pure Ag NPs, and after 7 h, 24 h and 30 h of reaction, respectively. F shows the high magnification TEM images of nanoparticles at the beginning of the reaction (a) and after 7 h (b), 24 h (c) and 30 h (d) of the reaction. Scale bars in TEM images correspond to 50 nm. Inset in D is the SAED pattern recorded from the corresponding nanoparticles.*

plasmon band at the end of 24 h of the reaction (Figure 4.5, A, curve 4) corresponds to the formation of porous platinum nanoparticles, as depicted in the TEM analysis (Figure 4.5, D and F-c).The selected area electron diffraction (SAED) pattern recorded from the porous nanoparticles at the end of 24 h of transmetallation reaction

(Figure 4.5, D, inset) matched with that of platinum metal (PCPDF no. 040802) [45], hence confirming the presence of platinum in the nanoparticles. The resulting platinum nanoparticles, unlike the gold shell, do not manifest itself in the form of a distinct plasmon band. It is important to note here that due to the absence of any distinct optical signal, the reaction beyond the 24 h mark does not show any change as far as the UV-vis-NIR spectra is concerned. Although, after about 30 h of reaction, there is a significant morphology change of the particles, as observed in the TEM analysis (Figure 4.5, E and F-d), wherein the cavities created in the nanoparticles appear to have been filled to form solid nanostructures. Unlike the case of Au (III) ions, the porous platinum nanoparticles do not collapse to form smaller, pure platinum nanoparticles, as is evident from the TEM analysis. The porous platinum nanoparticles, rather, grow in size as a consequence of the deposition of atomic platinum. The progress of the reaction could be attributed to the differences in the

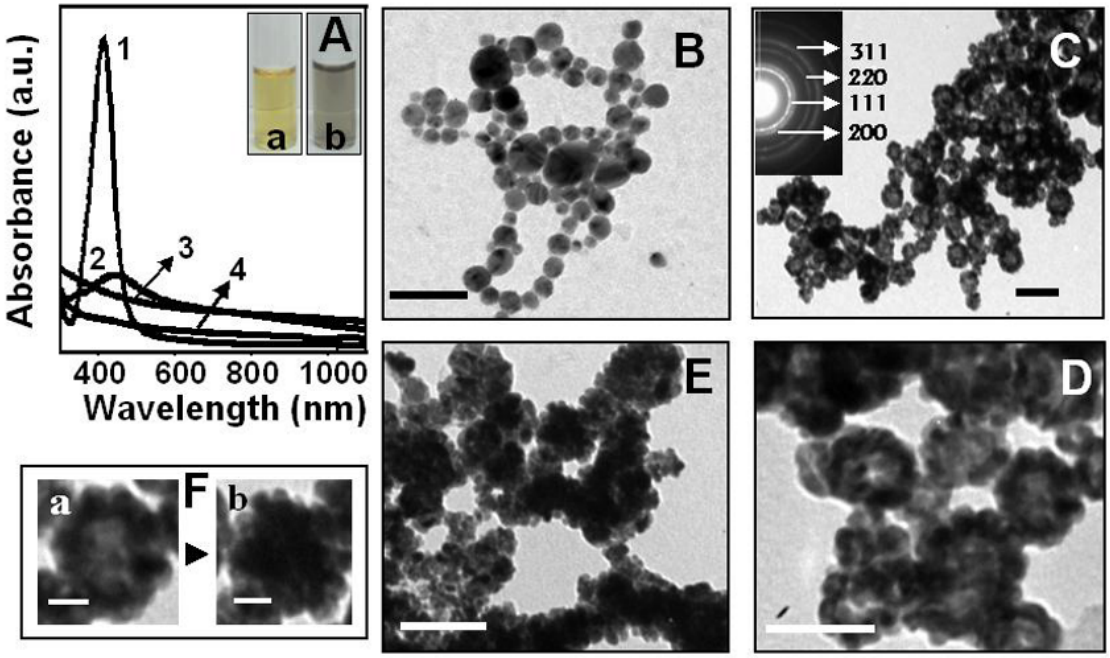

Figure 4.6 *UV-vis-NIR absorption and TEM kinetics of the transmetallation reaction between 10^{-4} M Ag NPs and 10^{-4} M Pd (II) ions. Curves 1, 2, 3 and 4 in A correspond to the absorption spectrum of pure Ag NPs and nanoparticles at 3 h, 6 h and 8 h of reaction. a and b in the inset of A correspond to curves 1 and 4, respectively. B shows the TEM images of pure Ag NPs, while C and D are the TEM images recorded at 6 h of reaction, inset of D being the SAED pattern recorded for the corresponding nanoparticles. E is the representative TEM image at the end of 8 h of reaction. F-a and F-b are the high magnification images of D and E. Scale bars in TEM images B, C and E correspond to 100 nm, D -50 nm, F -20 nm.*

redox potentials of Pt (IV) ions and the Ag NPs (Pt^{+4}/ Pt: 1.143 V v/s SHE; Ag^{+}/Ag: 0.80 V v/s SHE).

Likewise, upon dialyzing the Ag NPs against 10^{-4} M Pd (II) (Pd^{+2}/ Pd: 0.83 V v/s SHE) ions across a 12.5 kDa cut-off dialysis tubing, the oxidative consumption of the Ag NPs by the reducing Pd (II) to form atomic palladium is evident by the sharp decline in the surface plasmon band arising from the silver nanoparticles (Figure 4.6, A, curve 1). The silver plasmon band disappears completely with in 6 h of reaction (Figure 4.6, A, curve 3). However, continuing the transmetallation reaction for another couple of hours results in very broad absorption band (Figure 4.6, A, curve 4) with intensity lower than that of the 6 h band. The reaction can be kinetically followed by TEM analysis. Thus, the pure Ag NPs (Figure 4.6, B) are etched out by the diffusing Pd (II) ions resulting in the formations of cavities surrounded by a thick palladium shell at the end of 6 h of reaction (Figure 4.6, C). The porous structures so fabricated can be seen in greater details in the magnified image of the same (Figure 4.6, D and F-a). The selected area electron diffraction (SAED) pattern recorded from the nanoparticles at this stage matched well with that of metallic palladium (PCPDF no. 461043) [46], thus confirming the presence of metallic palladium in these nanostructures. It was observed that if the reaction is continued beyond this point, there is an apparent loss of the porosity of these nanoparticles, which, similar to platinum, is a consequence of the deposition of more and more metallic palladium over the porous structures (Figure 4.6, E and F-b).

4.2.2 Effect of membrane permeability and ionic concentrations on the rate of transmetallation reactions

It is obvious that the galvanic replacement reactions mentioned above are governed by the diffusion of the ionic forms of gold, platinum and palladium. Therefore the reactions and the composition of the resulting nanoparticles will be determined by the rate at which the ions can invade the dialysis tubing and get reduced at the cost of the sacrificial silver colloids. In an attempt to demonstrate the dependability of the reaction rate of a typical transmetallation process across the semi-permeable dialysis membrane, a set of experiments was performed with varying concentrations of the ionic species and varying membrane permeability. It is

noteworthy however, that it is the existence of the visible region plasmon absorption spectra of the Ag-Au nanoparticle systems, including their phase pure compositions, alloys and core shell/ hollow shell nanostructures, that enables one to spectroscopically monitor the process as is progresses through the various intermediate stages. Thus, we have limited these rate-determining experiments to the Ag NPs – Au (III) galvanic replacement reaction as the other two processes involving Pt (IV) and Pd (II) fail to provide an insight into their respective reactions in terms of the intermediate stages and the final porous nanoparticle products, spectroscopically. The results of these UV-vis-NIR experiments have been shown in the Figure 4.7, and are discussed below.

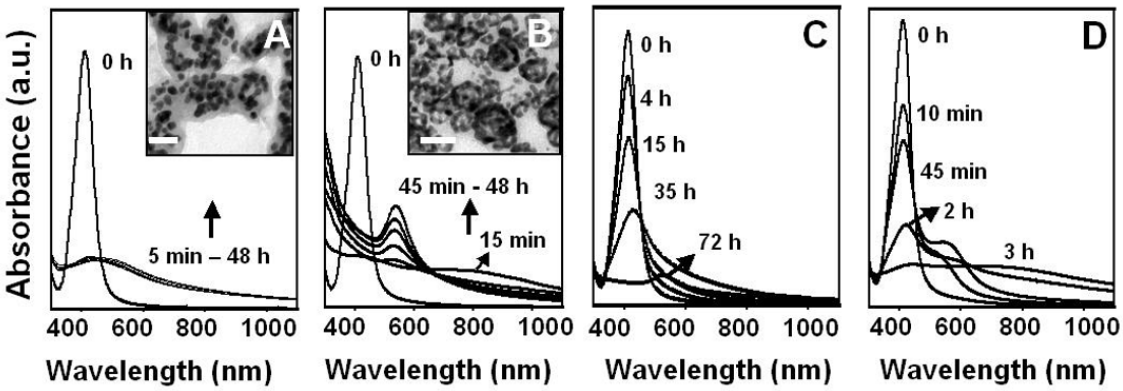

Figure 4.7 *UV-vis-NIR absorption kinetics recorded for the galvanic replacement reaction between Ag NPs – Au (III) ions with varying reaction parameters; direct addition of 5 x 10 $^{-5}$ M $HAuCl_4$ to the 10 $^{-4}$ M Ag NPs (A); Addition of higher concentration (5 x 10 $^{-4}$ M) of $HAuCl_4$ (B); transmetallation reaction across a 2.5 kDa dialysis tubing (C) and a 30 kDa dialysis tubing (D). Inset of A is the representative TEM image of the nanoparticles formed within 5 min of the direct addition of 5 x 10 $^{-5}$ M Au (III) ions to Ag NPs. Inset of B is the representative TEM image of the nanoparticles formed at the end of 15 min of reaction. Scale bars in both TEM images correspond to 50 nm.*

The significance of the semi-permeable dialysis tubing separating the sacrificial Ag NPs and the attacking ionic species of gold, platinum and palladium can be realized by carrying out the transmetallation process without the tubing. In a simple experiment, 5 x 10^{-5} M $HAuCl_4$ was added directly to the Ag NPs and the reaction was immediately followed up with the UV-vis-NIR spectroscopy. Figure 4.7, A shows the spectra recorded for the reaction. As described previously, the 0 h absorption band correspond to the surface plasmon band of the Ag NPs and is centered at 412 nm. Within 5 min of addition of the Au (III) ions a rapid dampening

of this absorption band is observed along with the appearance of a 510 nm band. Thus, the silver nanoparticles undergo rapid transition to gold nanoparticles through the oxidation of metallic silver to ionic silver and a simultaneous reduction of ionic gold to metallic gold. The intensity and the position of the new 510 nm absorption band remains constant for 48 h after the addition suggesting that the transmetallation reaction was completed in the first few minutes of the addition of the Au (III) ions itself. Thus, the galvanic replacement reaction between Ag NPs and the Au (III) ions is extremely rapid in absence of a physical barrier and a rapid transition from a purely silver phase to a gold rich phase occurs without the formation of any observable intermediate states, including nanostructures with thin gold shells. The solid gold nanoparticles formed immediately after the addition of the Au (III) ions do not show any signs of porosity (Figure 4.7, A, inset), similar to that obtained by the slow diffusion through the dialysis tubing. This experiment clearly establishes the importance of the dialysis tubing employed in our experiments as the semi-permeable barrier between the reacting species that keeps a check on the rate of ionic diffusion across it and thereby controls the overall reaction rate. It is indeed the slow rate of reaction that facilitates the creation of pores in the sacrificial Ag NPs and the subsequent thin gold shell formation.

The rate of diffusing ions also depends on its concentration outside the dialysis tubing. Thus, by increasing the concentration of the ionic solution the time required for the formation of hollow shell nanoparticles can be varied. This was demonstrated by dialyzing Ag NPs against an increased concentration of $HAuCl_4$ (5×10^{-4} M rather than 5×10^{-5} M). The UV-vis-NIR spectra reveal the appearance of the typical absorption band of a gold nano-shell centered around 700 nm at the end of 15 min itself (Figure 4.7, B), clearly indicating the enhanced rate of the reaction. Continuing the reaction further results into a rapid development of the plasmon band centered at ~ 520 nm that is characteristic of nanogold, as early as 45 min of reaction and the intensity keep increasing from that point onward up to 48 h of reaction. TEM analysis of the nanoparticles corresponding to the 15 min plasmon band shows the formation of porous gold nanoparticles (Figure 4.7, B, inset). However, a closer look reveals that the particles so formed are not as intact as that obtained with the lower concentrations of Au (III) in the previous experiments. We believe that the influx of high

concentration of ionic gold into the Ag NPs leads to a rapid de-alloying process and the consequential breakage of the porous gold nanoparticles. These results are indicative of the enhanced rate of the transmetallation reaction brought about by the increased Au (III) concentration. Similarly, with a five fold higher concentration of Pt (IV) ions (5×10^{-4} M over 1×10^{-4} M), the disappearance of the silver plasmon band was brought about in smaller time of reaction (1 h rather than 24 h).

The diffusion of the ions across the dialysis membrane is also governed by the permeability of the dialysis membrane, which in turn is decided by the pore size of the dialysis tubing. The galvanic replacement reactions discussed in the earlier part of this section for the synthesis of porous Au, porous Pt and porous Pd nanoparticles have been carried out in 12.5 kDa cut-off dialysis tubing. However, we show that the reaction kinetics can be controlled by varying the membrane permeability. Figure 4.7, C shows the UV-vis-NIR absorption spectra of a galvanic replacement reaction between the sacrificial Ag NPs and 5×10^{-5} M Au (III) ions carried out across a 2.5 kDa cut off membrane, which certainly has smaller pores. Unlike the previous experiment with 12.5 kDa cut-off membrane, the 2.5 kDa cut-off membrane slows down the reaction considerably, as evident by the extended time taken for the dampening of the silver plasmon band. The extent of red shift observed as a result of the alloying process with the metallic gold is also remarkably low. It can be observed in the spectra that after even extended period of the reaction (35 h) there is apparent formation of the gold shell nanostructures. On the other hand, Figure 4.7, D shows the spectra recorded for a similar reaction carried out through a 30 kDa cut-off dialysis tubing. It is clear from the spectra that the reaction proceeds at a much faster rate than that of the 12.5 kDa cut-off reaction. An enhanced diffusion of the Au (III) ions across the larger pores of the membrane allows rapid consumption of the metallic silver, evident by the dampening of the corresponding plasmon band within the period of 3 h.

In yet another experiment, the transmetallation reaction was carried out across two dialysis membranes instead of one. In this double dialysis experiment, one small dialysis membrane (12.5 kDa cut-off) containing 0.1 % of $NaBH_4$ solution was enclosed in a larger dialysis membrane containing 10^{-4} M Ag_2SO_4 solution and

instantly put for dialysis against 5 x 10^{-5} M $HAuCl_4$ solution (Figure 4.8, A-I). As soon as the dialysis is started, $NaBH_4$ begins to diffuse out from the innermost membrane, and reduces Ag (I) ions to yield Ag NPs. Concurrently, Au (III) ions diffuse in through the larger dialysis membrane and the transmetallation reaction between the incoming Au (III) ions and the freshly generated Ag NPs takes place as described earlier, resulting in the formation of hollow gold shell nanostructures within 2 h of reaction. At the end of this reaction time, the solution of the larger dialysis membrane turns blue (Figure 4.8, A-II) and has a broad UV-vis-NIR absorption band centered at ~ 700 nm (Figure 4.8, B, curve 2). Also, $NaBH_4$ being a strong reducing agent, is able to diffuse across the two membranes and reduce the Au (III) ions generating red colored gold nanoparticles in the outermost solution (Figure 4.8, A-II) with a sharp surface plasmon band centered at 520 nm (Figure 4.8, B, curve 3), while the innermost solution remains colorless with no signs of formation of either gold or silver nanoparticles in it (Figure 4.8, B, curve 1).

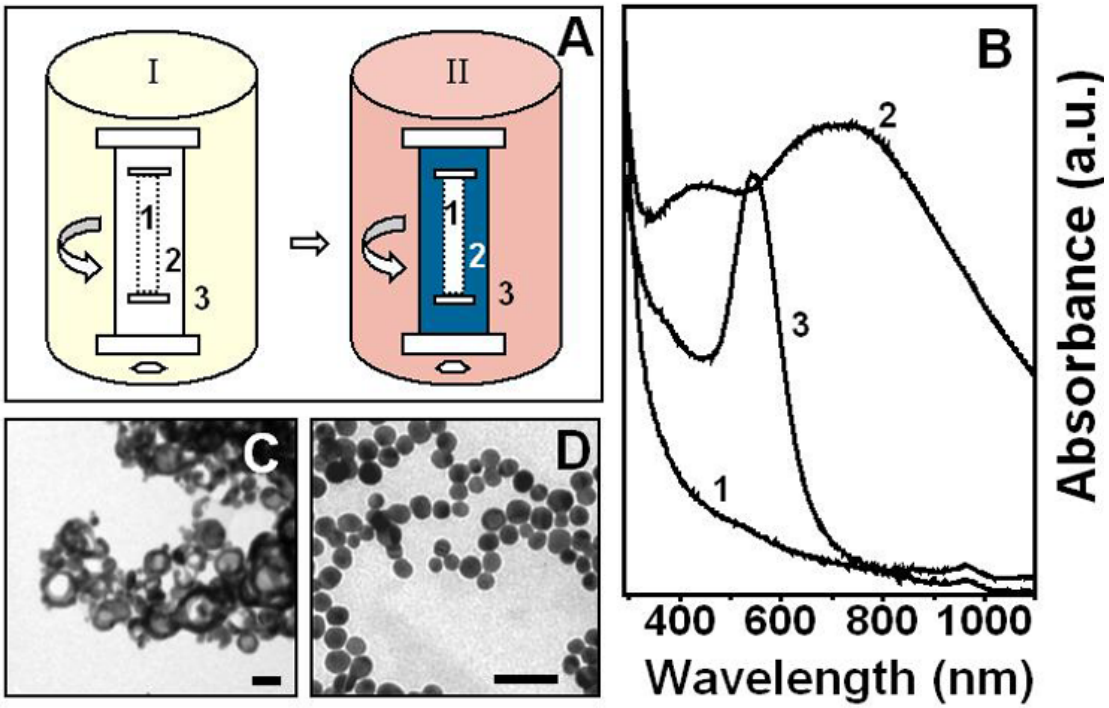

Figure 4.8 *Schematic depicting the experimental set up for the double dialysis experiment (A). The solutions in 1, 2 and 3 are $NaBH_4$ (0.1 %), 10^{-4} M Ag_2SO_4 and 5 x 10^{-5} M $HAuCl_4$, respectively that turn to porous Au (blue) and solid Au (red) after transmetallation. B is the UV-vis-NIR absorption spectra of the solutions in A-II, while C and D are representative TEM images corresponding to curve 2 and 3 in B, respectively. Scale bars in C and D correspond to 50 nm.*

The formation of hollow gold nanoparticles in the larger membrane and the solid gold nanoparticles outside of it can be confirmed by the TEM images from the respective solutions (Figure 4.8, C and D, respectively).

The double dialysis protocol for transmetallation reactions is therefore, appropriate for those experiments involving sacrificial nanoparticles that are unstable in aqueous solutions without capping agents such as cobalt and nickel nanoparticles [47]. The presence of capping agents is not desirable on the surface of the sacrificial nanoparticles as it could interfere with the transmetallation reaction, which primarily is a surface-based phenomenon. Also, the process becomes much simpler as the step involving synthesis of the sacrificial nanoparticles and their purification is omitted.

4.2.3 High-resolution transmission electron microscopy (HRTEM) and Energy dispersive X-ray (EDX) analysis

While the TEM images discussed in the section 4.2.1 suggest the formation of porous structures, they can be conclusively analyzed by the HRTEM analysis. All the HRTEM measurements were carried out on a JEOL – TEM - 2010 UHR instrument operated at a lattice image resolution of 0.14 nm.

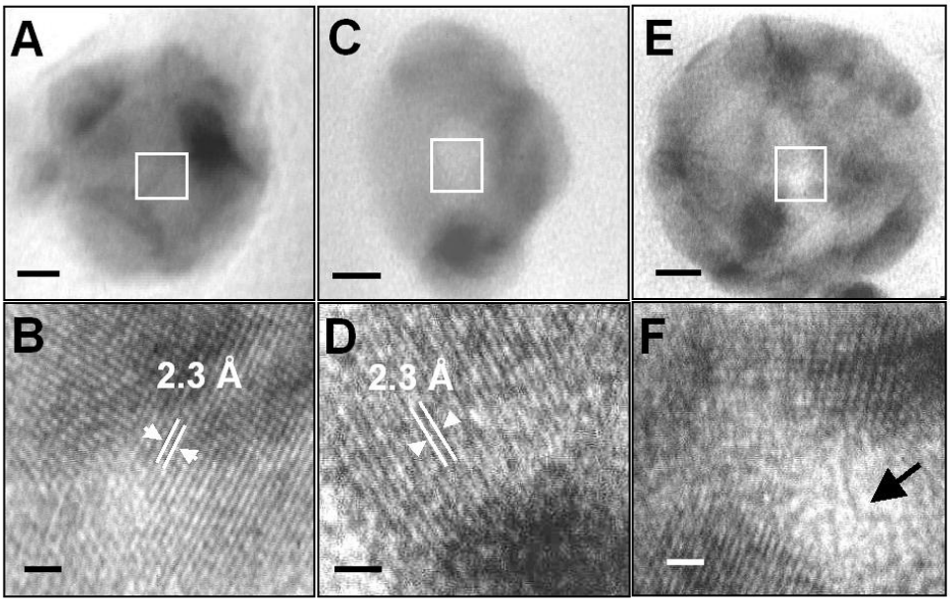

Figure 4.9 *Representative time-point HRTEM images of the nanoparticles from the reaction between 10^{-4} M Ag NPs and 5 x 10^{-5} M Au (III) using 12.5 kDa cut-off dialysis tubing; A, B-2 h; C, D-3 h; E, F- 5 h; B, D and F are the high magnification images of the regions enclosed by white boxes in A, C and E, respectively. Scale bars in A, C and E correspond to 50 Å while that in B, D and F correspond to 10 Å.*

HRTEM analysis of the porous gold nanoparticles synthesized from the transmetallation reaction between 10^{-4} M Ag NPs and 5 x 10^{-5} M Au (III) carried out through the 12.5 kDa dialysis tubing as a function of time is shown in Figure 4.9 (A, B: 2 h; C, D: 3 h and E, F: 5 h).

The presence of well-defined lattice planes in the core after 2 and 3 h of reaction indicates that the silver core is not completely oxidized at this stage of reaction (Figure 4.9 A, B and C, D). After 5 h of reaction, however, there are regions (identified by an arrow in Figure 4.9 F) in the porous structure that are free of fringes corresponding to lattice planes indicating that these are indeed cavities. The d spacing in the HRTEM images shown in Figure 4.9 B, D were determined to be 2.3 Å and correspond to the (111) lattice planes of either gold or silver (PCPDF no. 021095 for Au and 040783 for Ag) [48]. However, the similar values of the d spacing for the respective planes of gold and silver make it difficult to topographically distinguish gold and silver rich regions within these nanostructures.

Energy dispersive analysis of X-rays (EDX) measurements carried out on the sacrificial silver nanoparticles in the HRTEM instrument after 2, 3 and 5 h of transmetallation reaction yielded Au: Ag ratios of 1: 11.33, 1: 4.46 and 1: 0.9 respectively. It is clear that even after 5 h of reaction, there is still a fair percentage of silver in the porous structures. The UV-vis spectrum of this solution (Figure 4.3, A, curve 3) indicates complete damping of the silver plasmon band at 408 nm at this stage and appearance of a peak at ca. 480 nm along with the 700 nm peak. It appears likely that the 480 nm peak is due to a silver-gold alloy phase, as inferred earlier. Thus, the nanoparticles at this stage of the reaction have regions rich in the alloy phase of Ag and Au that are enclosed within the gold shell.

Similarly, HRTEM analysis of the sacrificial Ag NPs intermittently taken out from the dialysis against 1 x 10^{-4} M Pt (IV) ions across a 12.5 kDa cut-off dialysis tubing was carried out and is shown in Figure 4.10. The HRTEM images of the pure Ag NPs at the beginning of the transmetallation reaction reveal the twinned surface topography of the silver nanoparticles (Figure 4.10, A). The d spacing of the lattice planes matches well with the silver lattice planes (2.35 Å correspond to Ag (111) plane; 1.44 Å correspond to the Ag (2 2 0) plane. As the ionic Pt is reduced on the

surface of the sacrificial silver nanoparticles, deposition of metallic platinum can be observed on the surface of the Ag NPs in the form of small dark patches (Figure 4.10, B, dotted lines). The 'd' spacing at this stage matches well with the Pt (111) plane (2.25 Å; Figure 4.10, C, dotted lines) [45] and Ag (111) plane (2.34 Å; Figure 4.10, C, bold lines) [47].

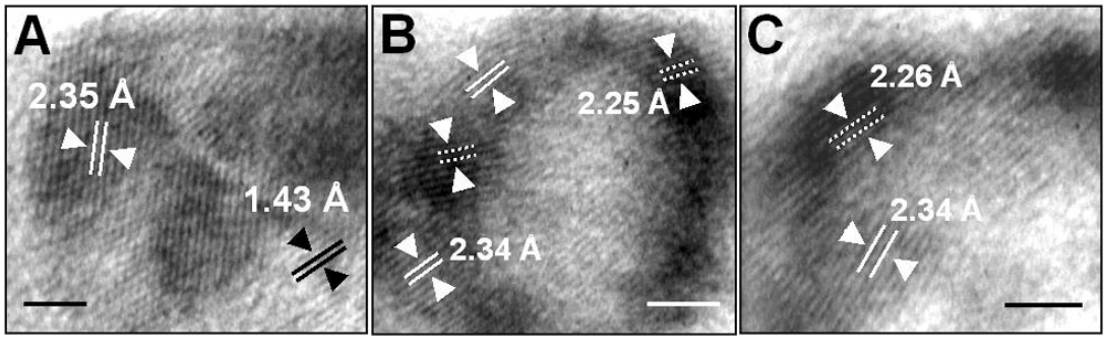

Figure 4.10 *HRTEM images corresponding to transmetallation reaction between 10^{-4} M Ag NPs and 1 x 10^{-4} M solutions of Pt (IV) ions at various stages of the reaction. A, B and C correspond to pure Ag NPs, 7 h of reaction and 24 h of reaction, respectively. Solid lines represent the lattice planes of Ag while the dotted lines represent lattice planes of Pt. Scale bars in A, B and C correspond to 20 Å.*

Thus, until this stage, there is no evidence of the formation of a complete Pt shell surrounding the sacrificial Ag NPs; also the cavities within the nanostructures are not well defined. The alteration in the nanoparticle topology is much more pronounced at the end of 24 h of reaction. Figure 4.10, C shows a part of the shell of metallic platinum formed around the silver rich inner layers. The lattice spacing corresponds to Pt (111) (2.26 Å; Figure 4.9, C, dotted lines) on the outside and Ag (111) (2.34 Å; Figure 4.10, C, bold lines) to the inside which is in agreement with the TEM image where the dark shell is observed surrounding the low contrast inner regions with a central cavity (Figure 4.5, F-c). The presence of the cavities towards the center of the nanoparticles is also clearly seen. Energy dispersive analysis of X-rays (EDX) measurements carried out on the sacrificial silver nanoparticles in the HRTEM instrument after 6, 12 and 24 h of transmetallation reaction yielded Ag: Pt ratios of 1: 0.10, 1: 0.4 and 1: 0.7 respectively, indicating a progressive increase in the Pt content of the nanoparticles with the advent of the reaction.

Galvanic replacement reaction between sacrificial Ag NPs and 1x 10^{-4} M Pd (II) across the 12.5 kDa dialysis tubing was also analyzed using time dependent

HRTEM studies (Figure 4.11). The sacrificial Ag NPs at the end of approximately 3 h of reaction show the presence of lattice planes corresponding to Ag as well as Pd. Towards the core, the particles have silver rich regions as revealed by the d spacing of 2.03 Å that matched with the Ag (200) plane (Figure 4.11, A, bold lines). On the other hand, one can make out the presence of the metallic Pd as discontinuous patches along the periphery of the particles as is evident by the d-spacing of 1.94 Å corresponding to the Pd (200) plane (Figure 4.11, A, dotted lines) [46]. With the advancement of the reaction, the cavities developed at the center of the nanoparticles are clearly visible, while the overall composition largely remains bimetallic, with the presence of both silver rich and palladium rich zones (Figure 4.11, B).

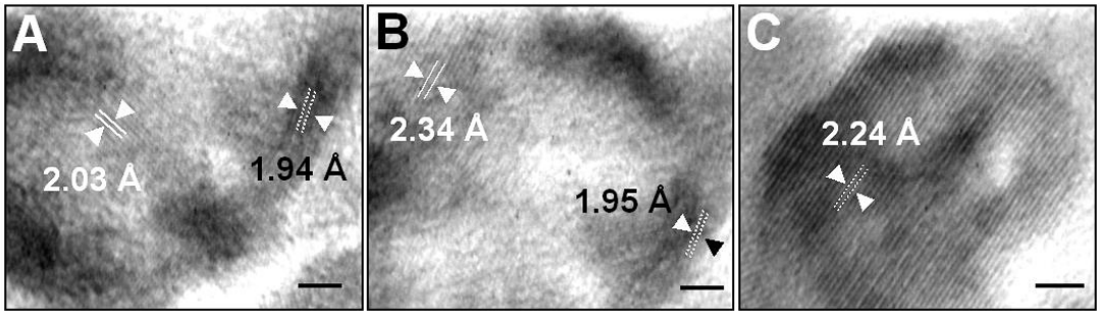

Figure 4.11 *Representative HRTEM images of the nanoparticles from the transmetallation reaction between 10^{-4} M Ag NPs and 1 x 10^{-4} M Pd (II) ions at various times intervals; A: 3 h; B: 6 h and C: 8 h. The d spacing shown with bold lines correspond to Ag while those in dotted lines represent Pd. Scale bars in A, B and C corresponds to 20 Å.*

However, with prolonged influx of the Pd (II) ions into the dialysis tubing, the nanoparticles gradually loose their porous nature as more and more metallic Pd is deposited. Eventually, the composition of these nanoparticles is dominated by palladium as is evident from the 'd' spacing of 2.24 Å that corresponds to the Pd (111) plane (Figure 4.11, C, dotted lines).

4.2.4 XPS analysis of the porous nanospheres

A comparative chemical analysis of the sacrificial Ag NPs and the porous Au nanoparticles synthesized using the transmetallation reaction was done by X-ray photoemission spectroscopy (XPS) to determine the oxidation states of silver and gold. Figure 4.12 shows the XPS analysis of the Ag NPs and porous Au coated on thin copper substrates. Figure 4.12, A and B are the XPS plots of the Ag 3d core level from Ag NPs and the porous Au respectively. The Ag 3d core level spectrum from the

sacrificial Ag NPs before the transmetallation process has begun shows the Ag $3d_{5/2}$ peak at 367.9 eV, indicating the presence of metallic silver (Figure 4.12, A).

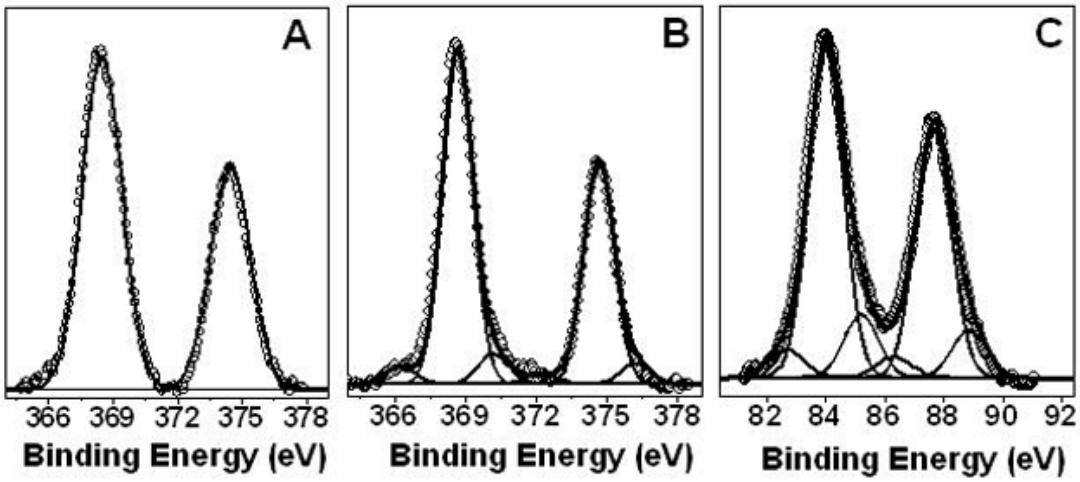

Figure 4.12 *Ag 3d core level spectrum recorded from the sacrificial Ag NPs (A) and porous Au after 5 h of the transmetallation process (B). Au 4f core level spectrum recorded from the porous Au nanoparticles (C).*

However, the Ag 3d core level spectrum from the porous Au nanoparticles could be resolved into three distinct spin orbit pairs with binding energies of 366.2 eV, 368 eV and 370. 2 eV (Figure 4.12, B). Whereas the 368 eV peak corresponds to metallic silver similar to the Ag NPs metallic silver peak, the higher energy peak at 370. 2 eV corresponds to the Ag (I) oxidation state of silver. Thus, it is clear that the transmetallation process leads to oxidation of metallic silver in the Ag NPs to Ag (I) state. This result thus is in agreement with the gradual loss of silver in the form of Ag (I) that is evident by the dampening of the SPR peak of Ag NPs with the reaction time (Figure 4.3 A). The low-intensity peak at 366.2 eV could be attributed to the silver present in the form of an alloy with gold as a result of the galvanic replacement reaction. This is in agreement with the XPS measurements performed on the Ag-Au alloy nanoparticles reported in the literature [49].

Similarly, the Au 4f core level spectra recorded from the porous Au nanoparticles after 5 h of transmetallation reaction could be resolved into three spin orbit pairs with binding energies at 82.7 eV, 84 eV and 85.2 eV (Figure 4.12, C). The 84 eV component corresponds to the metallic Au state, while the higher binding energy component (85.2 eV) correspond to the Au (I) oxidation state of the gold. The

Au (I) state represents the partially reduced gold precursors (Au (III)) present in the porous gold nanostructures. The absence of signals form the Au (III) oxidation state could be due to the very low concentrations of the Au (III) in the porous structures, as most of the precursor ions with in the dialysis membrane are already reduced at the end of 5 h of transmetallation reaction. On the other hand, the lower binding energy signal (82.7 eV) could be the contribution of Au present as an alloy with Ag in the porous nanostructures, which, at the end of 5 h of galvanic replacement reaction still have significant amount of silver as observed in the EDX measurements. The presence of the low binding energy signals of silver and gold indicates that the alloying process renders both the metals more susceptible to electron loss [49].

4.2.5 Scaled-up synthesis of porous nanospheres

For the purpose of synthesizing larger amounts of porous Au, Pt and Pd structures, a series of experiments were carried out with modified concentrations of the sacrificial Ag NPs as well as the precursor ionic solutions of gold, platinum and palladium. In one such experiment, we took one magnitude higher concentrations of sacrificial Ag NPs. Thus, instead of the 1 x 10^{-4} M Ag NPs, 1 x 10^{-3} M Ag NPs were used. The high concentration solution was made using tyrosine as the reducing agent under alkaline conditions using the protocol described by Sastry and co –workers, described earlier (Chapter IV, section 4.2), but with slight modification. Thus, while the concentration of Ag_2SO_4 and tyrosine used was 10^{-3} M, 10^{-2} M of KOH was added. After boiling, the solution turned in to a yellowish brown colour. The Ag NPs solution was then dialyzed against Millipore water for 48 h with four water changes to remove uncoordinated tyrosine and KOH molecules.

For the synthesis of high concentrations of porous Au, 10^{-3} M Ag NPs were dialyzed against 1 x 10^{-4} M Au (III) across a 12.5 kDa cut-off dialysis tubing. Within an hour of reaction the solution inside the dialysis tubing starts to turn dark brown and results in the formation of aggregates of porous Au within the dialysis tubing in ~ 48 h of reaction. The aggregates could be separated from the solution by low speed centrifugation (2000 rpm, 10 min). The aggregates after being air-dried could be collected in the form of a dry powder. The presence of the porous structures was confirmed by TEM analysis. From an experiment involving 100 ml of 10^{-3} M

sacrificial Ag NPs against 1000 ml of 10^{-4} M Au (III) ionic solution, approximately 25 mg of dry powder of porous Au NPs could be obtained.

However, many of the potential applications of the porous Au, like other nanoparticle systems, would necessitate the presence of these nanoparticles in solution form. Thus, we have attempted to synthesize the high concentration porous Au (of the order mentioned above) without triggering its aggregation in the dialysis tubing. In order to achieve this, 10^{-3} M sacrificial Ag NPs were dialyzed against 7.5 x 10^{-5} M Au (III) ionic solution instead of 1 x 10^{-4} M Au (III) solution as in earlier case. After ~ 12 h of dialysis, the Ag NPs solution appears deep brown, without any signs of aggregation, while the UV-vis-NIR absorption spectrum shows two distinct bands, one centered at 490 nm, other at 620 nm (Figure 4.13, A, curve 2). The intensity of the former band goes down after 30 h while that of the latter increases (Figure 4.13, A, curve 3). At this point the 7.5 x 10^{-5} M Au (III) solution is replaced with a fresh 5 x 10^{-5} M Au (III) solution. Within 4 h of this replacement, the colour of the solution starts turning blue and turns deep blue (characteristic of porous Au) after 10 h of replacement (Figure 4.13, A, inset-a). The solution at this stage has a broad UV-vis-NIR absorption band centered at 820 nm (Figure 4.13, A, curve 4) and there is no visible aggregation. The formation of porous Au nanoparticles is confirmed through TEM analysis, where uniform porous particles are seen with an average size of 65.7 nm (Figure 4.13, B). Thus, unlike the previous experiment where a very high concentration of Au (III) (1 x 10^{-4} M) has been used at the beginning of reaction, the relatively lower concentration prevents the aggregation of the Ag NPs.

Similar experiments involving platinum and palladium salts were also performed. Thus, whereas the transmetallation reaction of 10^{-3} M Ag NPs against 5 x 10^{-4} M Pt (IV) ions lead to an aggregation of the Ag NPs that turned porous in 24 h of reaction, a two stage transmetallation reaction against lower concentrations of Pt (IV) (2 x 10^{-4} M) resulted in stable solution of porous Pt in nearly 30 h of dialysis. In the case of both porous Pt and porous Pd too, a volume of 100 ml of Ag NPs dialyzed against 1000 ml of ionic Pt and Pd solutions yields ~ 20 mg of the respective porous nanostructures in the form of dry powder. Therefore, using higher concentrations of the sacrificial Ag NPs and the precursor ions, the yield of the porous structures can be

increased. Also, by varying the ionic concentrations and the reaction time, it is also possible to obtain highly concentrated porous structures in solution or in their powder forms.

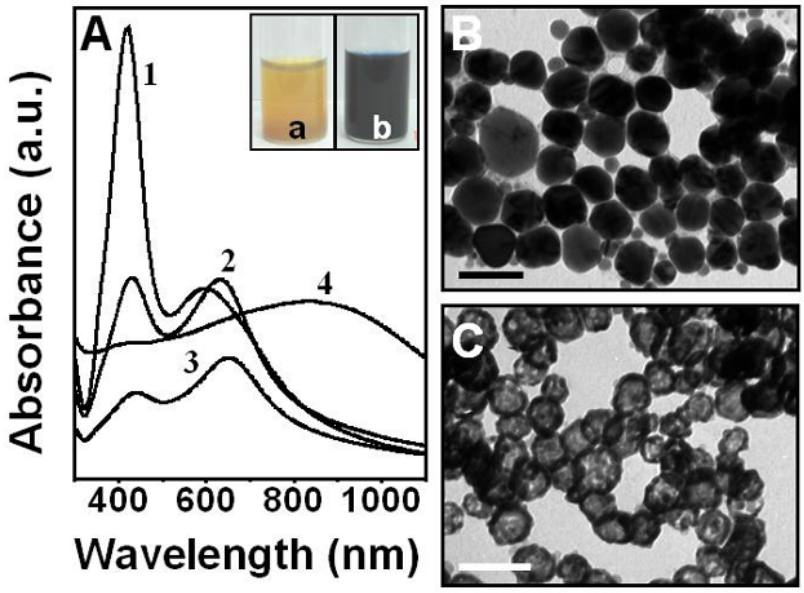

Figure 4.13 *UV-vis-NIR kinetics (A) and TEM images (B, C) from the transmetallation of reaction of 10 $^{-3}$ M Ag NPs against 7.5 x 10 $^{-5}$ M Au (III) followed by reaction against 5 x 10 $^{-5}$ M Au (III) solution. Curve 1 in A and TEM image B represent the as-prepared 10 $^{-3}$ M Ag NPs. Curves 2 and 3 correspond to spectrum recorded after 12 h and 30 h of the first phase of reaction while curve 4 is the spectrum recorded after 10 h of the second phase reaction. a and b (inset in A) correspond to curve 1 and 4. B corresponds to curve 4 in A. Scale bars in A and B correspond to 100 nm.*

A comparative particle size distribution analysis of the sacrificial nanoparticles of varying concentrations and their transmetallation products is shown in Figure 4.14 and Figure 4.15. In the case of porous Au, one can clearly observe the dependence of the size of the final product on the size and distribution of the sacrificial templates. Thus, 10 $^{-4}$ M Ag NPs have a broader size distribution, with the nanoparticle size varying from 20-75 nm (Figure 4.14, A1, A2 and A3) and the maximum percentage frequency occurring at 45 nm. The porous Au nanoparticles synthesized using these Ag NPs as the sacrificial templates for a transmetallation reaction against 5 x 10 $^{-5}$ M $HAuCl_4$ have a similar size distribution profile (Figure - 4.14, B1, B2 and B3) with the particles varying in the size range 20-70 nm and the maximum frequency at 40 nm. On the other hand, increasing the concentration of silver precursor results in much larger particle size of silver nanoparticles and a

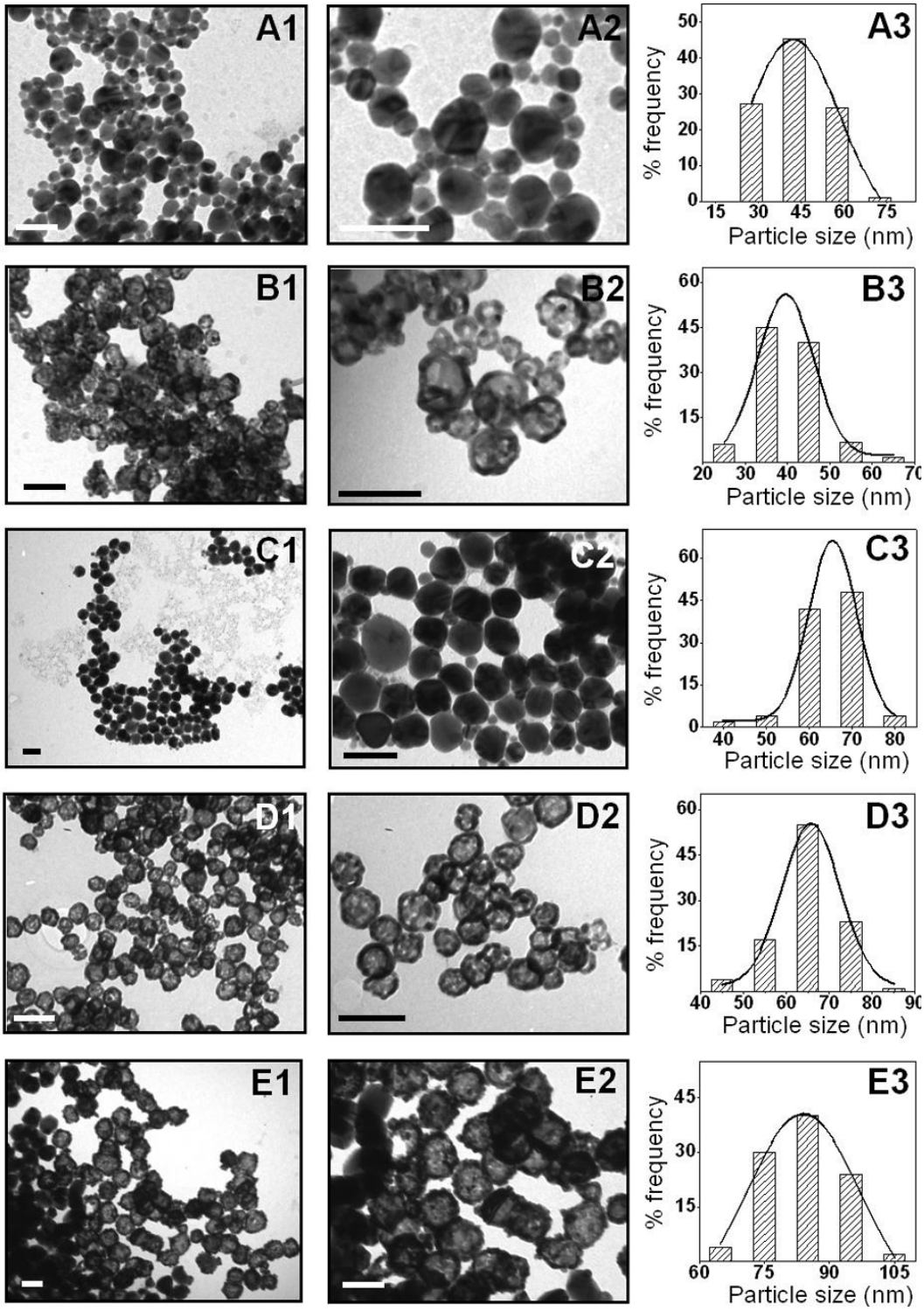

Figure 4.14 *Representative TEM images and particle size distribution of the varying concentration of Ag NPs and the porous Au nanoparticles thereof. A1, A2, A3 and B1, B2, B3 represent TEM images and particle size distributions of 1 x 10^{-4} M Ag NPs and the transmetallation product with 5 x 10^{-5} M $HAuCl_4$, respectively; C1, C2, C3 and D1, D2, D3 correspond to 10^{-3} M Ag NPs and porous Au with 7.5 x 10^{-5} M $HAuCl_4$, respectively; E1, E2, E3 correspond to the porous Au formed by transmetallation of C with 10^{-4} M $HAuCl_4$. Scale bars in TEM images correspond to 100 nm.*

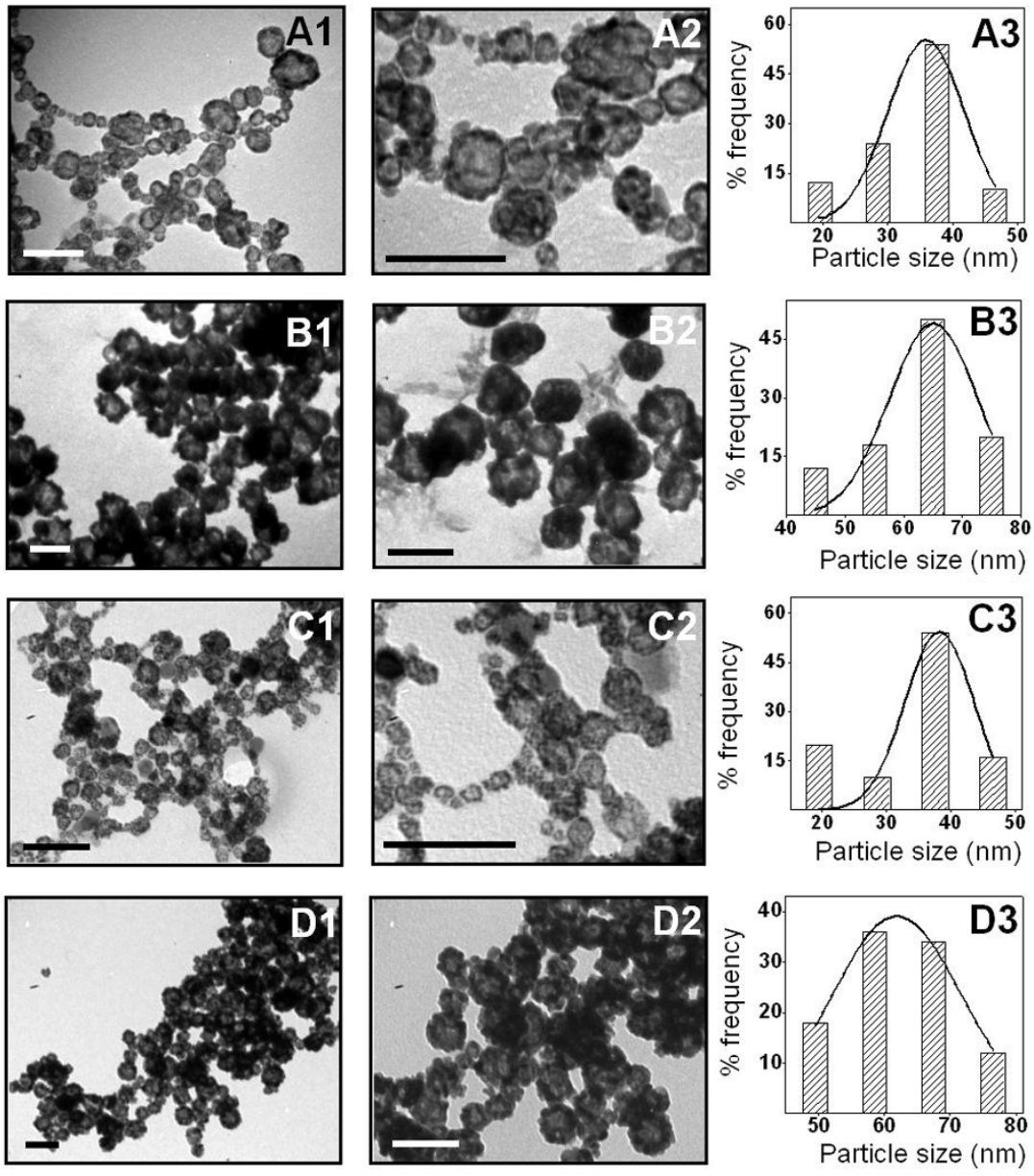

Figure 4.15 *A1, A2, A3 and B1, B2, B3 correspond to TEM images and particle size distributions of porous Pt synthesized by the transmetallation reactions involving 10^{-4} M Ag NPs/ 10^{-4} M H_2PtCl_6 and 10^{-3} M Ag NPs/ 2 x 10^{-4} M H_2PtCl_6, respectively. C1, C2, C3 and D1, D2, D3 correspond to porous Pd from the reactions involving 10^{-4} M Ag NPs/ 10^{-4} M $PdNO_3$ and 10^{-3} M Ag NPs/ 2 x 10^{-4} M $PdNO_3$, respectively. Scale bars in TEM images correspond to 100 nm.*

relatively narrow size distribution profile with an average size of 65.5 nm (Figure 4.14, C1, C2 and C3). When this batch of Ag nanoparticles is used as the sacrificial template in a two-step dialysis process against 7.5 x 10^{-5} M $HAuCl_4$ solution followed by a 10 h reaction against 5 x 10^{-5} M $HAuCl_4$ solution, the porous Au NPs form a stable solution with comparable size distribution and an average particle size of 65.7

nm (Figure 4.14, D1, D2 and D3). The small increase in the size could be attributed to the formation of thin gold shell around the silver nanoparticle with the average shell thickness ~15 nm. However, if the 10^{-3} M Ag NPs were subjected to dialysis against a much higher concentration of $HAuCl_4$ (10^{-4} M), as described previously, the porous nanoparticles aggregate at the bottom of the dialysis tubing. The particle size distribution reveals that the particle diameter has gone up significantly, and the average particle size is ~ 84 nm (Figure 4.14, E1, E2 and E3).

A similar trend in the particle size distribution is observed in the case of porous Pt and porous Pd nanoparticles also. Thus, while the porous Pt formed from the reaction between 10^{-4} M Ag NPs and 1 x 10^{-4} M Pt (IV) ions have a broad distribution profile, the average particle size remains at 35.8 nm (Figure 4.15, A1, A2 and A3). The higher concentrations of sacrificial Ag NPs and Pt (IV) ions lead to an increased nanoparticle size of 65.4 nm (Figure 4.15, B1, B2 and B3). Likewise, the lower concentration of Ag NPs/ Pd results in smaller particle sizes of porous Pd (39.4 nm, Figure 4.15, C1, C2 and C3) while the higher concentrations of the Ag NPs and the Pd precursors (2 x 10^{-4} M) generates the porous Pd nanoparticles with a relatively narrow size distribution profile and an average size of 62 nm (Figure 4.15, D1, D2 and D3).

Thus, it is clear from the discussion that the size of the porous nanoparticles synthesized by the galvanic replacement reaction depends upon that of the sacrificial nanoparticles that act as a template on which the porous nanoparticles are formed and by choosing the right sized template and precursor concentrations it is very much possible to obtain a desired size of the porous nanoparticles with tunable optical properties.

4.3 Synthesis of anisotropic porous nanostructures

This section of the chapter describes the processes developed for the synthesis of anisotropic porous structures using the galvanic replacement reaction across the semi-permeable dialysis membrane and employing anisotropic silver nanoparticles as the templates for the transmetallation process.

4.3.1 Synthesis of porous nanowires

Porous Au nanowires were synthesized by the galvanic replacement reaction between the sacrificial silver nanowires (Ag nanorods) and Au (III) ions. The silver nanowires were synthesized by the method described by Murphy and co workers [50]. Briefly, 40 µl of 0.1 M $AgNO_3$ was added to 100 ml of Millipore water with 1.5 µl of 1 M NaOH and the solution was boiled in an Erlenmeyer flask with rapid stirring for 5 min. To this boiling solution 5 ml of 0.01 M tri-sodium citrate was added and boiling was continued for an additional 10 min. Simultaneously, a second solution was-prepared by mixing 20 µl of 0.1 M $AgNO_3$ solution to 150 ml of Millipore water along with 1.5 µl of 1 M NaOH and the solution was brought to boiling. The second solution was then added to the first solution and the mixture was then boiled for 30-40 min. The solution changed from colour-less to faint yellow after the boiling. The Ag nanowires were then characterized by UV-vis-NIR spectroscopy and TEM analysis.

The citrate ions in the above reaction are performing multiple tasks. Besides reduction of the silver ions, citrate also caps the metallic silver. Even though, the silver/citrate ratio in the above reaction is similar to those reported earlier [51], the formation of anisotropic nanostructures is noteworthy. In the earlier reports with similar ratio of Ag/citrate (~1:10), the reactions were carried out at room temperature, which leads to uniform stabilization of the metallic silver and hence, a uniform growth pattern is observed. However, the elevated temperatures used in the abovementioned reaction results in alteration of the binding constants of the citrate with certain crystal faces of the silver, thereby leading to the loss of the capping citrate molecules from specific faces. This, in turn, would imply that the growth of the nanostructures would be oriented along one axis only.

The Ag nanowires thus formed were dialyzed in a 12.5 kDa cut-off against de-ionized water to get rid of all the un-coordinated citrate and unreduced silver ions prior to further use. For the fabrication of porous Au nanowires, galvanic replacement reaction was carried out between the sacrificial Ag nanowires and 5×10^{-5} M $HAuCl_4$ across a 12.5 kDa cut off dialysis membrane that was processed as described in the previous sections. The progress of reaction was observed by taking

aliquots from the dialysis membrane intermittently and analyzing them with UV-vis-NIR spectroscopy and TEM.

4.3.1.1 UV-vis-NIR and TEM analysis of the silver nanowires and the transmetallation products

The silver nanorods solution synthesized as described above appears faint yellow in colour. The UV-vis-NIR spectrum recorded from the solution is shown in Figure 4.16, A. The absorption maximum is centered at 430 nm with a pronounced tailing effect, suggesting a wide distribution of shape and size of the silver nanoparticles.

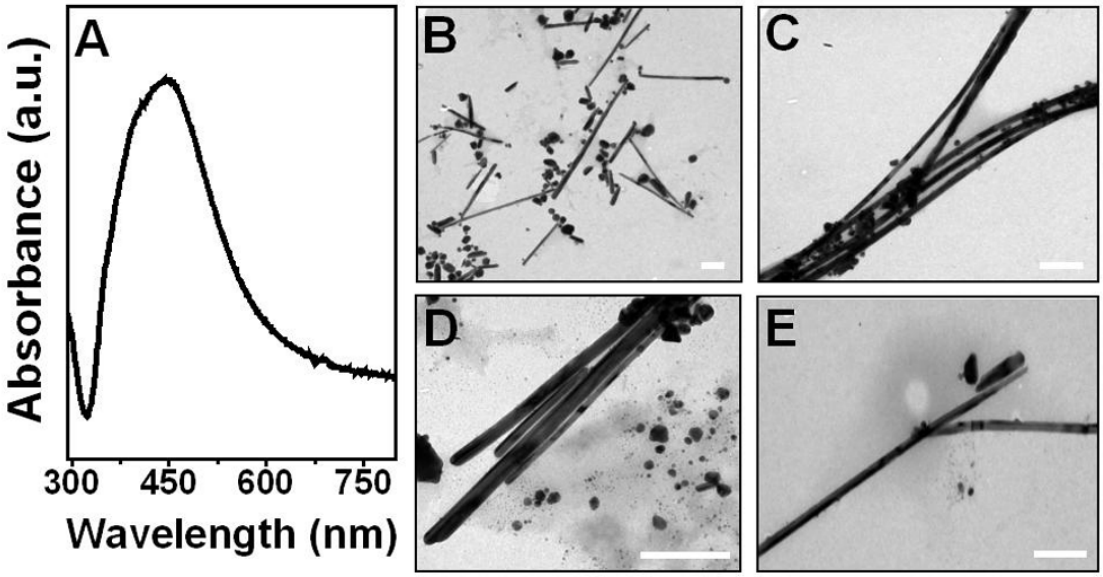

Figure 4.16 *UV-vis-NIR spectrum and TEM images of the as-prepared Ag nanorods. Scale bars in TEM images correspond to 200 nm.*

However, the presence of weak shoulders at 390 nm and 350 nm is indicative of the presence of silver nanowires in the solution [52] along with spherical nanoparticles, which generates the 430 nm peaks. The absence of a second SPR peak at ~ 570 nm which is characteristic of the sliver nanowires [52], suggests the formation of silver nanowires with aspect ratios greater than 5 [53]. The observation that there is a mixed phase of spherical silver nanoparticles and nanorods in the final solution, as indicated by the UV-vis-NIR absorption spectra, is consistent with the TEM analysis that shows the presence of large number of nanowires of silver along with irregular spherical silver nanoparticles (Figure 4.16, B-E). It is also evident that

the silver nanowires so formed have a very high aspect ratio, the length extending beyond 500 nm and the diameter ranging from 20-30 nm.

Unlike the spherical silver nanoparticles, the twin boundaries in silver nanowires are present along the length of the nanowires [52] and provide the suitable sites for the transmetallation to occur. Transmetallation reaction between the above mentioned nanowires acting as the sacrificial template and the Au (III) ions was carried across a 12.5 kDa cut-off dialysis membrane. The reaction was monitored using UV-vis-NIR spectroscopy and TEM kinetics as shown in Figure 4.17.

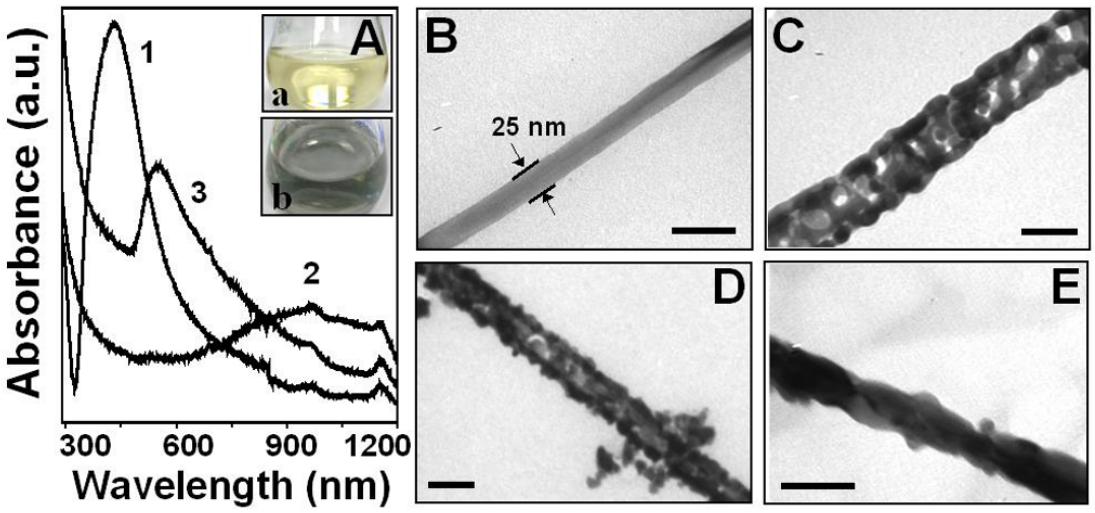

Figure 4.17 *UV-vis-NIR absorption and high magnification TEM kinetics of the transmetallation reaction between the as-prepared Ag nanorods and 5 x 10 $^{-5}$ M Au (III) ions across a 12.5 kDa cut-off dialysis membrane. Curves 1, 2 and 3 in A correspond to the plasmon absorption band recorded for as-prepared Ag nanorods, and after 3 h of reaction and 8 h of reaction. a and b in the inset of A correspond to curves 1 and 2, respectively. B, C, D and E are representative TEM images of as-prepared Ag nanorods and the reaction products at the end of 3 h, 5 h and 8 h of reaction. Scale bars in the TEM images correspond to 50 nm.*

Figure 4.17, A, curve 1 represents the transverse mode SPR absorption band arising from the as-prepared silver nanowires as has been described earlier. As the diffusion of Au (III) ions proceeds through the dialysis membrane, atomic gold gets deposited on the surface of the silver nanowire templates (Figure 4.17, B) resulting in the formation of nanotubes with uniform and smooth sheaths (Figure 4.17, C and D) as a result of which the transverse SPR component of the Ag nanowires disappears, and a new band appears at 850 –900 nm (Figure 4.17, A, curve 2). This could be attributed to the transverse mode of the tubular nano-stripes. However, as the concentration of

atomic gold builds up within the dialysis membrane, the plasmon band blue shifts to ~ 550 nm (Figure 4.17, A, curve 3), indicating the thickening of the gold layer on the nanowires as observed in the TEM also (Figure 4.17, E).

Thus, it is possible to tune the absorption of the silver nanowires from 550 nm to 900 nm depending on the composition and wall thickness of the nanowires by varying the extent of the transmetallation reaction.

4.3.2 Synthesis of triangular nanoframes

The fabrication of porous nanotriangles was achieved by the galvanic replacement reactions between the silver nanotriangles and Au (III) ions as well as Pd (II) ions. The synthesis of silver nanotriangles was done using higher concentrations of Ag ions in the reaction used for the synthesis of silver nanowires. Thus, in a typical reaction, 160 µl of 0.1 M $AgNO_3$ was added to 100 ml of de-ionized water along with 2 µl of.1 M NaOH, and the solution was boiled for 5 min in an Erlenmeyer flask with rapid stirring. 5 ml of 0.01 M tri-sodium citrate solution was added to this mixture and the solution was boiled further for another 10 min. At the same time a second solution was-prepared by mixing 80 µl of 0.1 M $AgNO_3$ to 150 ml of de ionized water in presence of 2 µl of 1 M NaOH. The solution was brought to boiling and added to the first solution. The final mixture was then boiled for another 30 min and allowed to cool down. The solution was kept at room temperature thereafter for 5 days. The Ag nanotriangles formed at the end of this period were analysed by UV-vis-NIR spectroscopy, TEM, high resolution TEM (HRTEM) and atomic force microscopy (AFM).

The triangular nanoframes were fabricated by the galvanic replacement reaction between the sacrificial silver nanotriangles and Au (III) ions and Pd (II) ions in separate experiments. The silver nanotriangles solution was dialyzed against de-ionized water across a 12.5 kDa cut-off dialysis membrane for 24 h to remove the residual silver ions as well as the un-coordinated citrate ions. In the first experiment, 20 ml of Ag nanotriangles solution was dialyzed against 200 ml of 5 x 10^{-5} M $HAuCl_4$ solution across a 12.5 kDa cut-off membrane, and the reaction was monitored kinetically using the UV-vis-NIR spectroscopy and TEM analysis. Similarly, dialysis

against 200 ml of 1 x 10^{-4} M $PdNO_3$ solution was used to fabricate Ag-Pd porous nanotriangles.

4.3.2.1 UV-vis-NIR spectroscopy and TEM analysis of silver nanotriangles and triangular nanoframes

The synthesis of triangular Ag nanoparticles was kinetically followed using UV-vis-NIR spectroscopy. The solution, immediately after boiling, was colorless but acquired a faint yellow color in nearly 12 h and showed a weak plasmon band with absorption maximum at 400 nm (Figure 4.18, A, curve 1; figure 4.19, A). This band could be attributed to the transverse surface plasmon resonance (SPR) mode of absorption of the small spherical Ag NPs formed at the early stage of reaction.

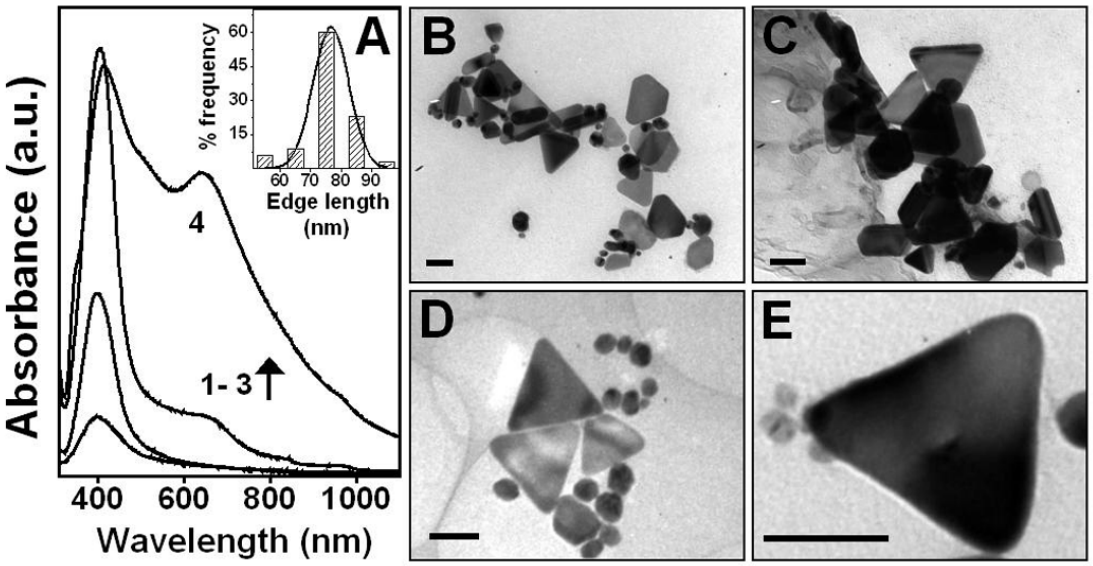

Figure 4.18 *UV-vis-NIR absorption spectra recorded for the synthesis of Ag nanotriangles as a function of time (A). Curves 1-4 are the spectra recorded after 12 h, 24 h, 48 h and 5 days of reaction, respectively. B-E is representative TEM images of Ag nanotriangles formed at the end 5 days of reaction. Inset of A shows the edge length distribution of the triangles. Scale bars in TEM images correspond to 50 nm.*

As the solution was aged, a gradual but consistent increase in the 400 nm band intensity is observed (Figure 4.18, A, curve 2) up to 24 h of reaction suggesting increased population of spherical nanoparticles in the reaction mixture.

However, at the end of 48 h a second plasmon band starts forming with the absorption maximum at 650 nm (Figure 4.18, A, curve 3) and the solution turns greenish yellow (Figure 4.19, B) indicating formation of plate like silver structures

[54]. This band grows in the intensity up to 5 days of reaction and the solution turn pale green (Figure 4.19, C). The TEM analysis of the solution at this stage reveals the presence of a large population of flat nanotriangles along with some spherical nanoparticles (Figure 4.18, B-E). The presence of the spherical nanoparticles results in the appearance of high intensity plasmon band at 410 nm (Figure 4.18, A, curve 4) even at this stage. The average edge length of the silver nanotriangles is 76 nm (Figure 4.18, A, inset), while the thickness was found to be 7-10 nm using AFM analysis (Figure 4.23, B).

As described in the previous section, citrate ions play an important role in the fabrication of the silver nanotriangles. Unlike in the case of Ag nanowires, the Ag/citrate ratio in the reaction mixture is lower is higher (~1:2). Thus, the number of capping molecules per silver atom is significantly lower than the previous case. The accompanying elevated temperatures also lead to the preferential binding of the citrate molecules to certain crystal faces only. Therefore, the growth of the nanostructures is highly oriented along certain axes only. The high concentration of silver ions ensures a prolonged growth at room temperature, allowing the kinetically controlled triangular morphology to form.

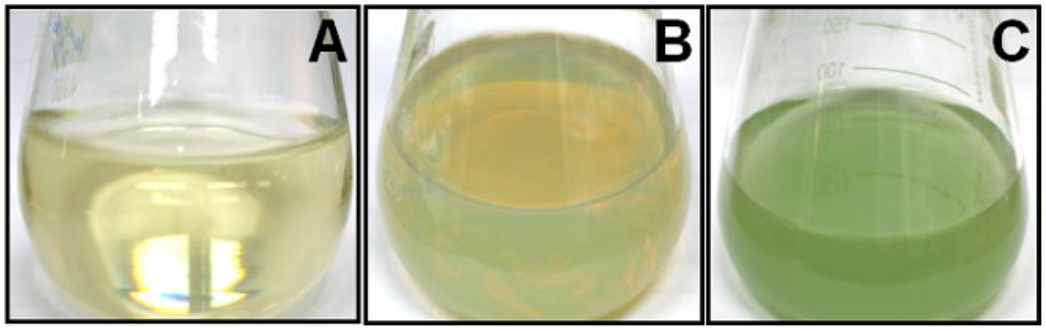

Figure 4.19 *Changing colour of the silver nanoparticles synthesized by modified seedless surfactant less protocol of Murphy [50] as a function of time (12 h, A; 48 h, B; 5 days, C) indicating the evolution of the triangular morphology.*

The transmetallation reaction of the triangular Ag nanoparticles was followed by the UV-vis-NIR spectroscopy and TEM analysis of the samples collected intermittently from the reaction mixture. The as-prepared silver nanotriangles show two SPR bands at 410 nm and 650 nm, respectively (Figure 4.20, A, curve 1). As the Au (III) ions diffuse in through the membrane and get reduced to metallic gold, the

silver nanoparticles are oxidized, resulting in the dampening of both the silver plasmon - bands up to 3 h of reaction (Figure 4.20, A, curves 2 and 3). The TEM analysis at this point reveals the formation of pinholes and cavities within the Ag nanotriangles as well as the spherical nanoparticles (Figure 4.20, C). These cavities are formed as a result of the etching of the elemental silver from the triangular nanoparticles. However, continuation of the dialysis for 5 h generates a new broad absorption band with a maximum at 850 nm (Figure 4.20, A, curve 4). The solution also changes from pale green to gray.

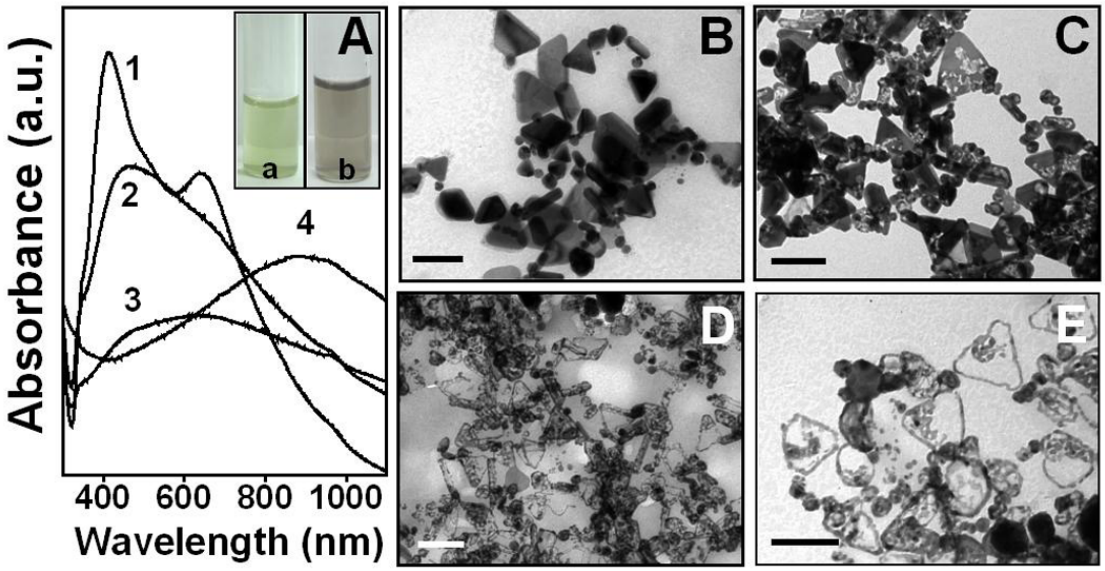

Figure 4.20 *UV-vis-NIR kinetics of the transmetallation reaction between silver nanotriangles and 5 x 10 $^{-5}$ M $HAuCl_4$ across a 12-5 kDa dialysis membrane (A). Curve 1 corresponds to the as-prepared Ag nanotriangles. Curves 2, 3 and 4 correspond to the spectrum recorded at the end of 2 h, 3 h and 5 h of reaction. Inset a and b correspond to curves1 and 4, respectively. B and C are representative TEM images corresponding to curves 1 and 3, respectively; while D and E correspond to curve 4 in A. Scale bars in TEM images represent 100 nm.*

The TEM analysis of the 5 h sample showed significant loss of metallic silver from the silver nanotriangles, which is evident by the huge cavities formed in these structures. The kinetics of the reaction in form of the gradual etching out of metallic silver can be observed much more clearly in the high magnification images of individual triangles as shown in the Figure 4.21. It is clearly observed that the oxidative loss of metallic silver begins at the atomically flat faces of the silver nanotriangles (Figure 4.21, B) and with the advent of the reaction only the nanoframes are retained (Figure 4.21, F). The Ag triangles have (111) faces on the top

and bottom surfaces. Since these planes are atomically flat, they are lower in energy than the faceted edges [39]. Therefore, a much larger energy increase in the system is observed when the Au (III) is reduced on the (111) faces rather than depositing on the edges. Thus, the triangular frame is retained while the center is etched away. The formation of these nanoframes is also a consequence of the relative thinness of the Ag nanotriangles as triangles thicker than 20 nm have been shown to form hollow nanoprisms by Xia and co-workers [40]. Lower reaction temperatures could also be contributing to the selective etching of the (111) faces and retention of the frame [39].

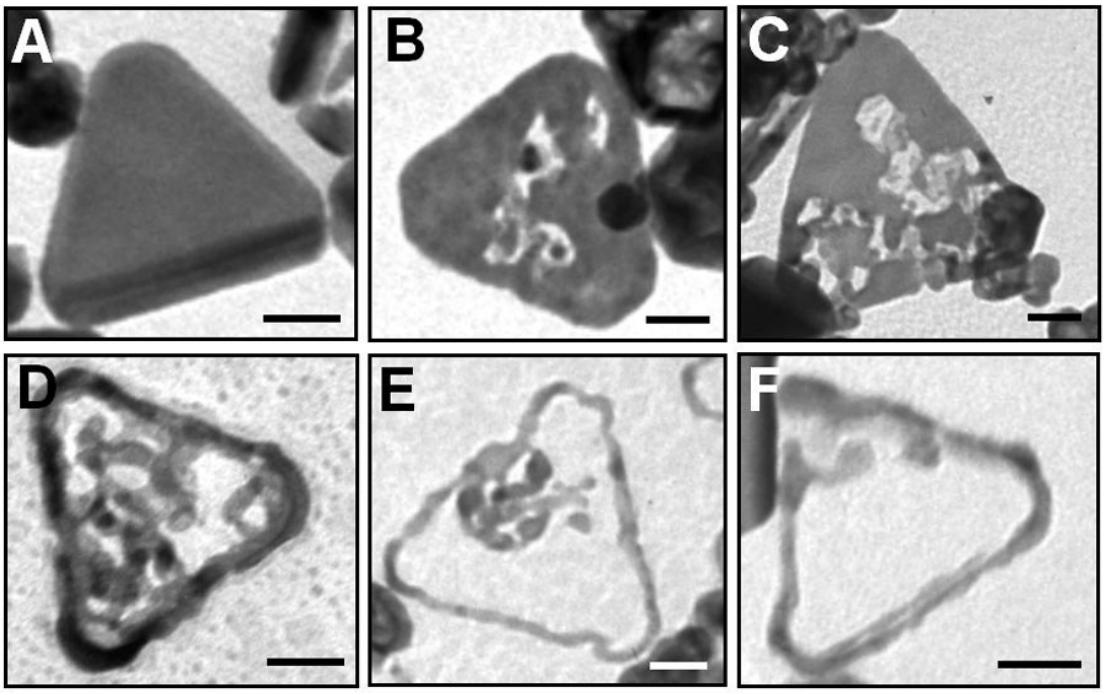

Figure 4.21 *High magnification TEM images of the Ag nanotriangles as they are etched away by the transmetallation reaction against 5 x 10 $^{-5}$ M $HAuCl_4$. Scale bars correspond to 50 nm.*

In a similar transmetallation experiment of Ag triangles against 1 x 10 $^{-4}$ M Pd (II) ions, the plasmon bands at 410 nm and 650 nm corresponding to the Ag nanotriangles are dampened within a period of 30 min of the reaction (Figure 4.22, A, curve 2) resulting in a broad absorption band after 120 min of reaction centered at 560 nm (Figure 4.22, A, curve 3). No further changes are observed in the absorption band with time suggesting the completion of the transmetallation process. It is noteworthy here, that unlike the galvanic replacement involving Au (III) ions, face selective etching is not observed under comparable conditions with Pd (II) ions as is evident

from the TEM images (Figure 4.22, B and C). The TEM images reveal that the resulting nanotriangles have smaller pinholes on the surfaces suggesting that the etching process has not resulted in complete loss of silver from the (111) faces of silver nanotriangles. Our observation is in agreement with that of Mirkin and co-workers where they could not fabricate nanoframes out of sacrificial nanotriangles using platinum ions and have attributed this to the relatively larger lattice mismatch between Pt and Ag (Pt = 3.9231 Å, Ag = 4.0862 Å) [38]. Also, the presence of Cl^-

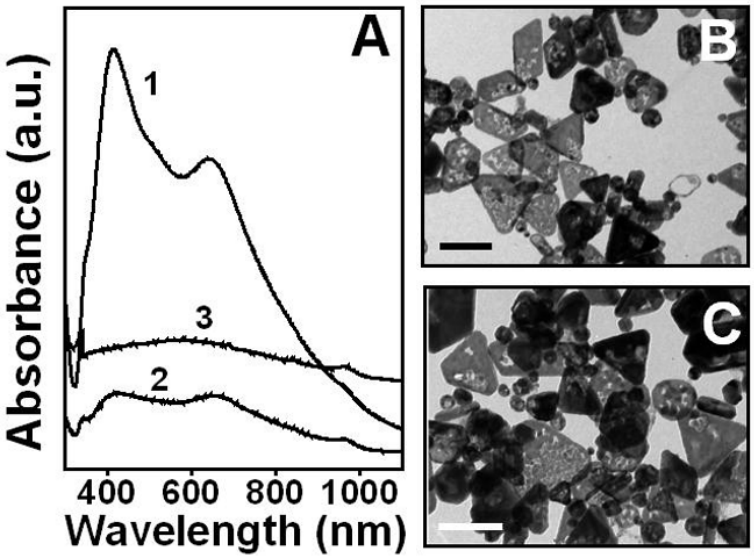

Figure 4.22 *A is UV-vis-NIR spectra recorded for the transmetallation reaction between Ag nanotriangles and 1 x 10^{-4} M Pd (II) ions. Curve 1 corresponds to the plasmon absorption of as-prepared Ag nanotriangles, while curves 2 and 3 are spectra at the end of 30 min and 120 min of the reaction. B and C are representative TEM images of the nanotriangles corresponding to curve 3 in A. Scale bars in TEM images represent 50 nm.*

ions in the gold precursor could lead to an enhanced oxidative loss of silver resulting in the formation of the nanoframes [39].

4.3.2.2 Atomic force microscopy (AFM) analysis of porous nanotriangles

The AFM analysis of Ag nanotriangles before and after subjecting to transmetallation reaction against Pd (II) solution has been shown in Figure 4.23. The AFM sample was made by drop casting 50 µl of the solution on freshly cleaved mica substrate. The 3d profile of the height image of a single nanotriangles after a 5 h reaction clearly shows the presence of well defined cavities surrounded by the triangular frame (Figure 4.23, A). The thickness of the triangle was determined by the

line profile of the height image (Figure 4.23, C). The blue lines in C correspond to the blue pointers in B, which depicts the height difference between the substrate (mica) and the Ag nanotriangle. The thickness was measured to be 8.92 nm.

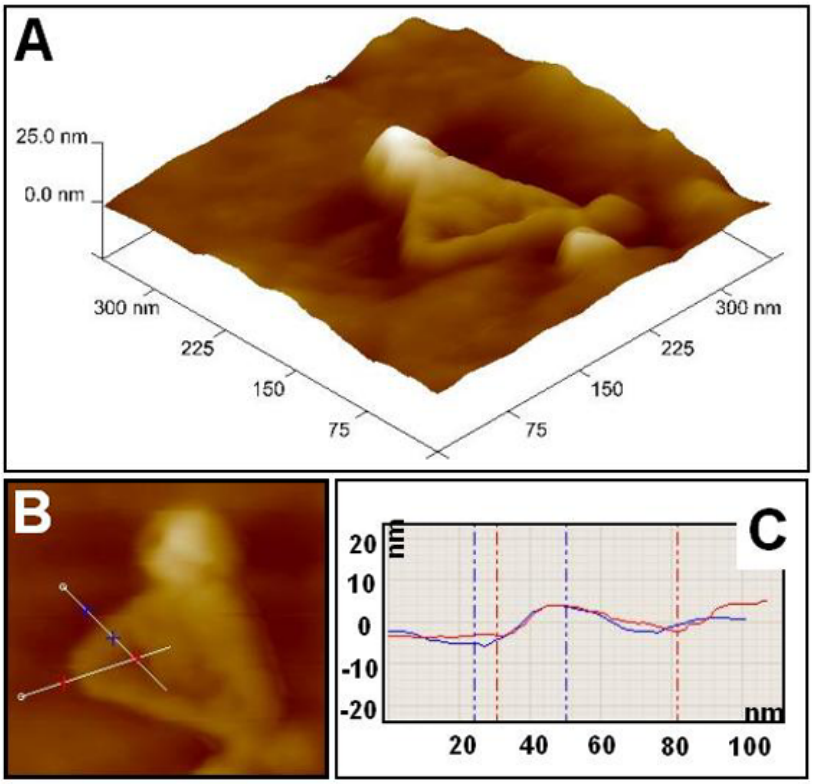

Figure 4.23 *AFM analysis of Ag nanotriangles subjected to 5 h of transmetallation against Au (III) ions. A is the 3 d profile of the height image of a single triangle with cavities. The surface profile is shown in the height image (B) and C is the relative thickness.*

The red lines in C, on the other hand, correspond to the line with red pointers in B, which compares the height of substrate and the depth of cavities formed as a result of the transmetallation process. The value so obtained is 0.9 nm, which suggests that the cavity formed in the nanotriangles runs across the whole thickness of the Ag - nanotriangle and is not merely a surface defect created by the galvanic replacement process.

4.3.2.3 High Resolution Transmission Electron Microscopy (HRTEM) analysis of silver nanotriangles and triangular nanoframes

It is the lattice mismatch between the Ag and Pd however, that allows one to perform the HRTEM analysis of the Ag nanotriangles and its transmetallation product with Pd (II) ions. The HRTEM images of a single Ag nanotriangles that has been

subjected to 120 min of transmetallation reaction against 1 x 10^{-4} M Pd (II) ionic solution has been shown in Figure 4.24, A. The areas of the nanotriangle marked as B, C and D have been magnified and are shown as Figure 4.24 B, C and D respectively. A closer look at a single Ag nanotriangle reveals the non-uniform etching process that results in loss of silver from the triangles from many different regions (Figure 4.24, A).

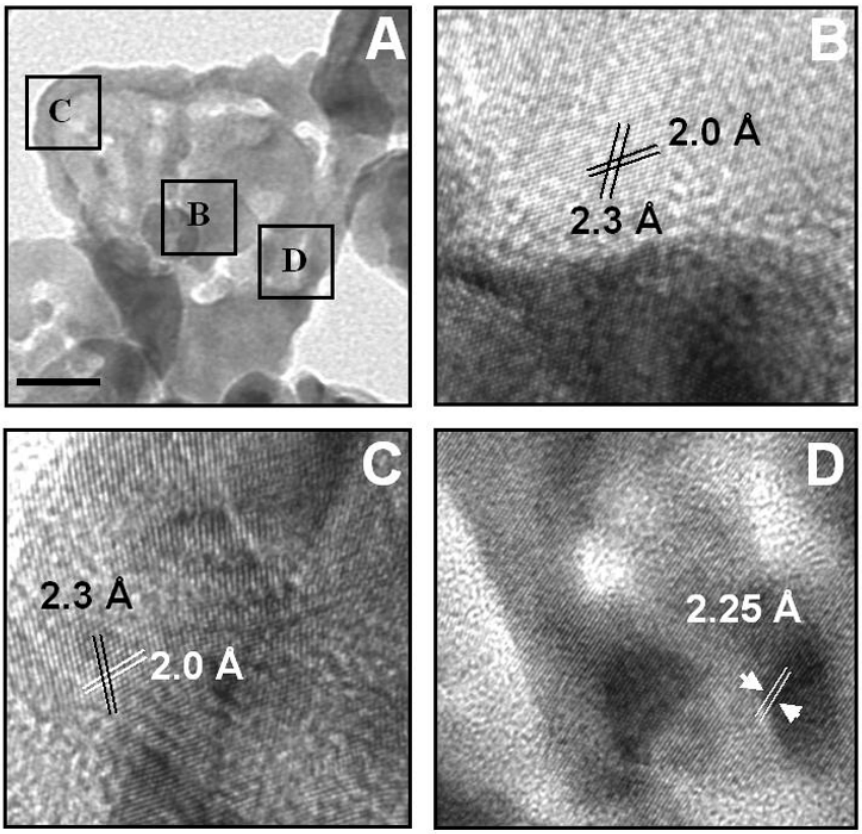

Figure 4.24 *(A) HRTEM image of an Ag nanotriangle subjected to 120 min of transmetallation reaction against 1 x 10^{-4} M ionic solution of Pd (II). Regions marked as B, C and D in A have been magnified as separate images with same labels. The scale bar in A corresponds to 20 nm. Lattice planes in images have been marked with solid lines and the respective d spacing has been written adjacent to it.*

The formation of an incomplete frame like structure can also be observed, and the edges of the triangle itself appear rough. The area marked as B in A has been magnified in Figure 4.24, B. Area B in A is the central region of the triangles, which is devoid of any cavities, suggesting that it has not been affected by the transmetallation reaction. The lattice planes are clearly seen in this area (Figure 4.24, B) and the d spacing matched that of Ag [111] plane (d = 2.3 Å) and Ag [200] plane

(d = 2.0 Å). The HRTEM image of the edge of the triangle (Figure 4.24, A, area C; C) also highlighted the presence of silver with the d spacing corresponding to Ag [111] and [200] lattice planes. However, from the regions in the triangle where cavities are seen, presence of Pd can be detected.

The presence of such cavities, seen as clear zones in Figure 4.24, A and D, is indicative of the oxidative loss of silver from these regions driven by the reduction of Pd (II) ions, which in-turn are deposited as metallic Pd in the vicinity. Thus, the lattice planes observed in Figure 4.24, D correspond to the Pd [111] as confirmed by the d spacing of 2.25 Å. Hence, it is clear from the above discussion that unlike the transmetallation reaction involving Au (III) ions, other elements such as palladium do not result into fabrication of seamless triangular nanoframes. This can be attributed to the differences in the lattice parameters of Ag and Pd / Pt.

Energy dispersive analysis of X-rays (EDX) measurements carried out on the sacrificial silver nanotriangles in the HRTEM instrument before and after the transmetallation reaction reveals the presence of palladium along with silver in the triangles. However, while the EDX recorded from the central regions devoid of cavities (Figure 4.24, B) showed insignificant amount of palladium (Ag: Pd = 1: 0.1), that from the regions surrounding the cavities (Figure 4.24, D) does show significant amount of palladium (Ag: Pd = 1: 0.35). The EDX measurements therefore, are in agreement with the HRTEM analysis, which clearly reveals the presence of palladium lattices within the Ag triangles.

4.4 Discussion

As described in the sections 4.2.1. and 4.2.2 of the chapter, the galvanic replacement reaction using silver nanoparticles as the sacrificial template could be carried out with any metal with higher reducing potential. Thus, the metal ions having a higher tendency to oxidize metallic silver would reduce by accepting the electrons released in such a process. Thus, in this study, we have used gold, platinum and palladium ions to oxidize metallic silver and generate nanostructures with porous interiors resulting from the oxidative etching of the silver from the sacrificial template and deposition of a thin shell of the oxidizing metal. The electron exchange event in the galvanic replacement reaction is a very rapid process and could lead to various

possibilities in terms of the composition and structures of the resulting products. However, the introduction of a semi-permeable dialysis membrane as a barrier between the sacrificial Ag nanoparticles and the ionic solutions of gold, platinum and palladium leads to a drastic lowering of the reaction rate, thereby facilitating an extensive control over the elemental composition of the resulting bimetallic nanostructures, and the optical properties that are a strong function of the former. Thus, one can observe and regulate the initial alloying phase and the de-alloying phase towards the later stages of the reaction. The slow transmetallation process also makes it possible to study the developing cavities and the shell, which thereby provides a means to tune the topology of the porous nanostructures and the cavity size.

The high magnification TEM analysis also points out that the defect sites in the Ag NPs, the twin boundaries, are the preferential sites for the oxidative etching of the silver and mark the sites where the cavities develop (Figure 4.4). In case of the Pt and Pd porous structures, the presence of these metals is confirmed by the HRTEM analysis that shows the lattice planes corresponding to Pt and Pd in the nanostructures and the EDX measurements as a function of time for these structures highlights the increasing Pt, Pd composition in the respective structures.

The tunability of the reaction rate and the product profile has also been demonstrated by varying the membrane permeability. These results, along with the dependability of the porous nanoparticle size (section 4.2.5) on the concentrations of the sacrificial template and the ionic precursors clearly emphasize the importance of the reaction kinetics on the fate of the products. Thus, whereas a very fast reaction does not allow the optimum morphological changes accompanying the synthesis of porous structures, a slow prolonged reaction too, is not capable of generating the desired morphologies.

The higher concentrations of the Ag nanoparticles have a narrow size distribution and therefore the resulting porous structures are quite uniform in their size distribution (section 4.2.5.), although the reactions are prolonged, as the time required for the reduction of excess of the silver is much longer.

Another interesting aspect described in the chapter is the synthesis of anisotropic sliver nanostructures and its transmetallation thereafter, resulting in some exquisite structures with porous interiors. The silver nanowires synthesized by the seedless and surfactant less protocol are known to have twin planes along the long axis of the wires [50]. The cavities are developed along the lengths of the nanowires. Prolong transmetallation reactions with Au (III) ions results in the refilling of the pores and formation of solid gold nanorods. On the other hand, slower reduction of the

Ag (I) ions by the citrate in the protocol described for nanowires synthesis leads to formation of Ag nanotriangles. Upon transmetallation against Au (III) ions, the whole of the central region of the triangle composed of the low energy [111] planes is etched away by the incoming Au (III) ions, leaving behind the triangular nanoframes. However, similar reactions with Pd (II) and Pt (IV) ions do not result in the complete etching away of the nanotriangles [111] surface, but generates voids unevenly distributed on the surface. The relatively profound mismatch between the lattice parameters of Ag and Pd/Pt is the prime cause of such sporadic transmetallation events on the surface of the triangles.

4.5 Conclusions

The chapter has illustrated a novel process developed for a highly controlled synthesis of porous nanostructures using simple galvanic replacement reactions across semi-permeable dialysis membranes. We showed that the membrane acts as a selective barrier between the sacrificial Ag nanoparticles and the ionic solutions of gold, platinum and palladium. The higher redox potential of these ions results in oxidative loss of silver and a gradual deposition of their metallic forms on the sacrificial templates, thus acquiring the shape and size of the template with well defined cavities in them. Therefore, any desired morphology and size of the bimetallic porous structures can be achieved by selecting the appropriate template, and this was proved by the fabrication of porous nanowires and nanotriangles.

The excellent control over the reaction facilitated by the dialysis membrane enabled us to study the structural changes that accompany the galvanic replacement reaction and tune the reaction conditions to suit our needs in terms of optical

properties and chemical composition of the products. The inherent ability of the dialysis membranes with variable pore sizes to segregate the ions and nanoparticles not just lead to recovery of phase pure products from within it but also overcame the drawbacks, such as formation of insoluble precipitates of ionic by-products associated with other such processes. Thus, the process described in the chapter negates the use of elevated temperatures and makes it economically more feasible than other similar methods.

The method developed by us gains much more importance in the light of the fact that there are ever-increasing reports on the synthesis of metal nanoparticles such as gold, platinum, palladium, nickel, cobalt, copper and silver with tunable size, shape and composition. To be able to manipulate materials at such small scale structurally, with great control would mean that we acquire the ability to generate novel electronic, optical and magnetic properties from these nanomaterials. Therefore, besides fabricating new materials, improving the existing nanomaterials throws open new possibilities in terms of potential applications.

4.6 References

1. (a) El-Sayed, M. A. *Acc. Chem. Res.* **2001**, *34*, 257-264. (b) Chen, S.; Yang, Y. *J. Am. Chem. Soc.* **2002**, *124*, 5280.

2. (a) Lee, K. S.; El-Sayed, M. A. *J. Phys. Chem. B* **2006**, *110,* 19220. (b) Acharya, G.; Chang, C.; Savran, C. *J. Am. Chem. Soc.* **2006**, *128*, 3862.

3. (a) Mandal, S.; Roy, D.; Chaudhari, R. V.; Sastry, M. *Chem. Mater.* **2004**, *16*, 3714. (b) Lu, L. et al *J. Mater. Chem*. **2004**, *14*, 1005.

4. (a) Luo, X.; Morrin, A.; Killard, A. J.; Smyth, M. R. *Electroanalysis* **2006**, *18*, 319. (b) Wang, J. *Analyst* **2005**, *130*, 421.

5. (a) Rosi, N. L.; Mirkin, C. A. Chem. Rev. **2005**, *105*, 1547. (b) Li, H. *et al., Angew. Chem. Int. Ed*. **2005**, *44*, 5100. (b) Tkachenko, A. G.; Xie, H.; Coleman, D.; Glomm, W.; Ryan, J.; Anderson, M. F.; Franzen, S.; Feldheim, D. L. *J. Am. Chem. Soc.* **2003**, *125*, 4700.

6. (a) Qin, J.; Jo, Y.; Ihm, J. E.; Kim, J.; Muhammed, M. *Langmuir* **2005**, *21,* 9346-9351. (b) Kannan, R. *et al* J. *Am. Chem. Soc*. **2006**, *128*, 11342. (c) Everts, M**.** *et al Nano. Lett*. **2006**, 6, 587-591. (c) Pankhurst, Q. A.; Connolly, J.; Jones, S. K.; Dobson, J. *J Phys D: Appl. Phys.* **2003**, *36,* R167.

7. (a) Kelly, K. L.; Coronado, E.; Zhao, L. L.; Schatz, G. C. *J. Phys. Chem. B.* **2003**, *107,* 668.

8. (a) Yamada, K.; Tokumoto, Y.; Nagata, T.; Mafune, F**.** *J. Phys. Chem. B* **2006**, *110,* 11751-11756. (b) Tsuji, M.; Hashimoto, M.; Nishizawa, Y.; Kubokawa, M.; Tsuji, T. *Chem. Eur. J.* **2005**, *11*, 440.

9. (a) Sastry, M.; Swami, A.; Mandal, S.; Selvakannan, P. R. *J. Mater. Chem*. **2005**, *15*, 3161. (b) Wiley, B.; Sun, Y.; Mayers, B.; Xia, Y. *Chem. Eur. J.* **2005**, *11*, 454. (c). Kou, X. et al J. *Phys. Chem. B.* **2006**, *110,* 16377. (d) C. J. Murphy, N. R. Jana, *Adv. Mater*. **2002**, *14*, 80.

10. (a) Klaus, T.; Joerger, R.; Olsson, E.; Granqvist, C. G. *Proc. Nat. Acad. Sci. USA* **1999**, *96*, 13611. (b) Mukherjee, P. *et al., Angew. Chem. Int. Ed.* **2001**, *40*, 3585. (c) Shankar, S. S.; Rai, A.; Ankamwar, B.; Singh, A.; Ahmed, A.;

Sastry, M. *Nat. Mater*. **2004**, *3*, 482. (d) Willner, I.; Baron, R.; Willner, B. *Adv. Mater.* **2006**, *18*, 1109.

11. (a) Jensen, T. R.; Kelly, L.; Lazarides, A.; Schatz, G. C. *J. Cluster Sci.* **1999**, *10*, 295. (b) Kottmann, J. P.; Martin, O. J. F.; Smith, D. R.; Schultz, S. *Phys. Rev. B* **2001**, *64*, 235402. (c) Sosa, I. O.; Noguez, C.; Barrera, R. G. *J. Phys. Chem. B* **2003**, *107*, 6269. (d) Murphy, C. R.; Jana, N. R. *Adv. Mater.* **2002**, *14*, 80. (e) Kim, F.; Song, J. H.; Yang, P. *J. Am. Chem. Soc.* **2002**, *124*, 14316.

12. (a) Lee, K. S.; El-Sayed, M. A. *J. Phys. Chem. B* **2006**, *110,* 19220. (b) Haes, A. J.; Van Duyne, R. P. *J. Am. Chem. Soc***. 2002**, *124*, 10596.

13. (a) Hirsch, L. R.; Stafford, R. J.; Bankson, J. A.; Sershen, S. R.; Rivera, B.; Price, R. E.; Hazle, J. D.; Halas, N. J.; West, J. L. *Proc. Nat. Acad. Sci. USA* **2003**, *100*, 13549. (b) El-Sayed, I. H.; Huang, X.; El-Sayed, M. A. *Nano Lett.* **2005**, *5*, 829.

14. Shankar, S. S.; Rai, A.; Ahmed, A.; Sastry, M. *Chem. Mater.* **2005**, *17*, 566.

15. Loo, C.; Lowery, A.; Halas, N.; West, J.; Drezek, R. *Nano Lett*. **2005**, 5, 709.

16. (a) Dick, L. A.; McFarland, A. D.; Haynes, C. L.; Van Duyne, R. P. *J. Phys. Chem. B* **2002**, *106*, 853. (b) Miranda, M. M. *Chem. Phys. Lett.* **2001**, *340*, 437.

17. (a) Shi, A. C.; Masel, R. I. *J. Catal.* **1989**, *120*, 421. (b) Falicov, L. M.; Somorjai, G. A. *Proc. Natl. Acad. Sci. USA* **1985**, *82*, 2207.

18. (a) Maroun, F.; Ozanam, F.; Magnussen, O. M.; Behm, R. J. *Science* **2001**, 293, 1811. (b) Heemeier, M.; (b) Carlsson, A. F.; Naschitzki, M.; Schmal, M; Bäumer, M.; Freund, H. J. *Angew. Chem. Int. Ed.* **2002**, *41*, 4073. (c) Alexeev, O. S.; Gates, B. C. *Ind. Eng. Chem. Res.* **2003**, *42*, 1571. (d) Link, S.; Wang,Z. L.; El-Sayed, M. A. *J. Phys. Chem. B* **1999**, *103*, 3529. (e) Sun, S.; Murray, C. B.; Weller, D.; Folks, L.; Moser, A. *Science* **2000**, *287*, 1989.

19. (a) Jackson, J. B.; Halas, N. J. *J. Phys. Chem. B* **2001**, *105*, 2743. (b) Sun, Y.; Xia, Y. *Anal. Chem.* **2002**, *74*, 5297. (c) Kim, S. W.; Kim, M.; Lee, Y. W.; Hyeon, T. *J. Am. Chem. Soc.* **2002**, *124*, 7642.

20. (a) Pardridge, W. M. *Curr. Opin. Pharmacol.* **2006**, *6*, 494. (b) Tenne, R.; Homyonfer, M.; Feldman, Y. *Chem. Mater.* **1998**, *10*, 3225.

21. (a) Ren, N.; Wang, B.; Yang, Y.; Zhang, Y. H.; Yang, Y.L.; Yue, Y. H.; Gao, Z.; Tang, Y. *Chem. Mater.* **2005**, *17,* 2582. (b) Ogihara, H.; Sadakane, M.; Nodasaka, Y.; Ueda, W. *Chem. Mater.* **2006**, *18*, 4981.

22. (a) Schwartzberg, A. M.; Olson, T.; Talley, C. E.; Zhang, J. Z. *J. Phys. Chem. B* **2006**, *110,* 19935. (b) Oldenburg, S. J.; Averitt, R. D.; Westcott, S. L.; Halas, N. J. *Chem. Phys. Lett.* **1998**, *288*, 243. (c) Halas, N. J. *Optics and Photonics News* **2002** August 26.

23. Loo, C.; Lowery, A.; Halas, N.; West, J.; Drezek, R. *Nano Lett.* **2005**, *5*, 709.

24. Liu, Z.; Searson, P. C. *J. Phys. Chem. B* **2006**, *110,* 4318.

25. (a) Graf, C.; Blaaderen, A. *Langmuir* **2002**, *18,* 524. (b) Skirtach, G. A. *et al., Nano Lett.* **2005**, *5*, 1371.

26. (a) Bruzzone, S.; Malvaldi, M.; Arrighini, G. P.; Guidotti, C. *J. Phys. Chem. B* **2006**, *110,* 11050. (b) Prodan, E.; Nordlander, P.; Halas, N. J. *Nano. Lett.* **2003**, *3*, 1411.

27. Chen, J.; Saeki, F.; Wiley, B.; Cang, H.; Cobb, M. J.; Li, Z.; Au, L.; Zhang, H.; Kimmey, M.J.; Li, X.; Xia, Y. *Nano Lett.* **2005**, *5*, 473.

28. (a) Liao, H.; Nehl, C. L.; Hafner, J. H. *Nanomedicine* **2006**, *1*, 201. (b) Tovmachenko, O. G.; Graf, C.; Heuvel, D. J.; Blaaderen, A.; Gerristen. H. *Adv. Mater.* **2006**, *18*, 91.

29. Sun, y.; Xia, Y. *Anal. Chem.* **2002**, *74*, 5297.

30. Kim, S. W.; Kim, M.; Lee, W. Y.; Hyeon, T. *J. Am. Chem. Soc.* **2002**, *124*, 7642.

31. Liang, H. P.; Zhang, H. M.; Hu, J. S.; Guo, Y. G.; Wan, L. J.; Bai, C. L. *Angew. Chem. Int. Ed.* **2004**, *43*, 1540.

32. Teng, X.; Liang, X.; Rahman, S.; Hong, Y. *Adv. Mater*. **2005**, *17*, 2237.

33. (a) Chah, S.; Fendler, J. H.; Yi, J. *J. Colloid Interface Sci.* **2002**, *250*, 142. (b) Caruso, F.; Caruso, R. A.; Mohwald, H. *Science* **1998**, *282*, 1111. (c) Caruso, F.; Spasova, M.; Maceira, V.; Marzan, L. M. *Adv. Mater*. **2001**, *13*, 1090. (d) Oldenburg, S. J.; Averitt, R. D.; Westcott, S. L.; Halas, N. J. *Chem. Phys. Lett.* **1998**, *248*, 243. (e) Dhas, N. A.; Suslick, K. S. *J. Am. Chem. Soc*. **2005**, *127*, 2368.

34. Murthy, V. S.; Cha, J. N.; Stucky, G. D.; Wong, M. S. *J. Am. Chem. Soc.* **2004**, *126*, 5292.

35. Yin, Y.; Rioux, R. M.; Erdonmez, C. K.; Hughes, S.; Somorjai, G. A.; Alivisatos, P. *Science* **2004**, *304*, 711.

36. Qian, L.; Yang, X. *Colloids and Surfaces A* **2005**, *260*, 79.

37. Sun, Y.; Meyers, B.; Xia, Y. *Adv. Mater*. **2004**, *15*, 651.

38. Liang, H. P.; Guo, Y. G.; Zhang, H. M.; Hu, J. S.; Wan, L. J.; Bai, C. L. *Chem. Commun*. **2004**, 1496.

39. Metraux, G. S.; Cai, Y. C.; Jin, R.; Mirkin, C. A. *Nano. Lett.* **2003**, *3*, 519.

40. Selvakannan, P. R.; Sastry, M. *Chem. Commun*. **2005**, 1684.

41. Sun, Y.; Xia, Y. *J. Am. Chem. Soc.* **2004**, *126*, 3892.

42. Selvakannan, P. R.; Swami, A.; Srisathiyanarayanan, D.; Shirude, P. S.; Pasricha, R.; Mandale, A. B.; Sastry, M. *Langmuir* **2004**, *20,* 7825.

43. Link, S.; Wang, Z. L.; El-Sayed, M. A. *J. Phys. Chem. B* **1999**, *103*, 3529.

44. Bogels, G.; Meekes, H.; Bennema, P. *J. Phys. Chem. B* **1999**, *103,* 7577.

45. Swanson, T. *Natl. Bur. Stand. (U. S.)*. **1953**, *1 (31)*, 539.

46. Kern, A.; Eysle, W.; Minera. *Natl. Bur. Stand. (U. S.)*, **1953**, *1 (31)*, 540.

47. (a) Bala, T.; Bhame, S. D.; Joy, P. A.; Prasad, B. L. V.; Sastry, M. *J. Mater. Chem*. **2004**, *14*, 2941. (b) Maaz, K.; Mumtaz, A.; Hasanain, S. K.; Ceylan, A. *J. Magn. Magn. Mater.* **2007**, *308*, 289. (c) Green, M.; Brien, P. *Chem. Commun*. **2001**, 1912.

48. (a) Davey, Z. *Kristallogr. Kristallgeom. Kristallphys. Kristallchem.* **1926**, *63*, 316. (b) Jung, Z. *Kristallogr. Kristallgeom. Kristallphys. Kristallchem.* **1926**, *64*, 423.

49. Wang, A. Q.; Liu, J. H.; Lin, S. D.; Lin, T. S.; Mou, C. Y. *J. Catal*. **2005**, *233*, 186.

50. Caswell, K. K.; Bender, C. M.; Murphy, C. J. *Nano Lett.* **2003**, *3*, 667.

51. Henglein, A.; Giersig, M. *J. Phys. Chem. B* **1999**, *103*, 9533-9539.

52. (a) Bhattacharraya, S.; Saha, S. K.; Chakravorty, D. *Appl. Phys. Lett.* **2000**, *290*, 2120. (b) Zhu, J. J.; Liao, X, H.; Zhao, X. N.; Chen, H. Y. *Mater. Lett*. **2001**, *49*, 91. (c) Sun, Y.; Yin, Y.; Mayers, B. T.; Herricks, T.; Xia, Y. *Chem. Mater*. **2002**, *14*, 4736.

53. Ah, C. S.; Hong, S. D.; Jang, D. J. *J. Phys. Chem. B* **2001**, *105*, 7871.

54. (a) Washio, I.; Xiong, Y.; Yin, Y.; Xia, Y. *Adv. Mater*. **2006**, *18*, 1745. (b) Maillard, M.; Giorgio, S.; Pileni, M. P. *J. Phys. Chem. B* **2003**, *107,* 2466. (c) Jin, R.; Cao, Y. C.; Hao, E.; Me´traux, G. S.; Schatz, G. C.; Mirkin, C. A. *Nature*, **2003**, *425*, 487. (d) Mock, J. J.; Barbic, M.; Smith, D. R.; Schultz, D. A.; Schultz, S. *J. Chem. Phys.* **2002**, *116*, 6755.

Chapter V

Biological Applications of Porous Nanoparticles

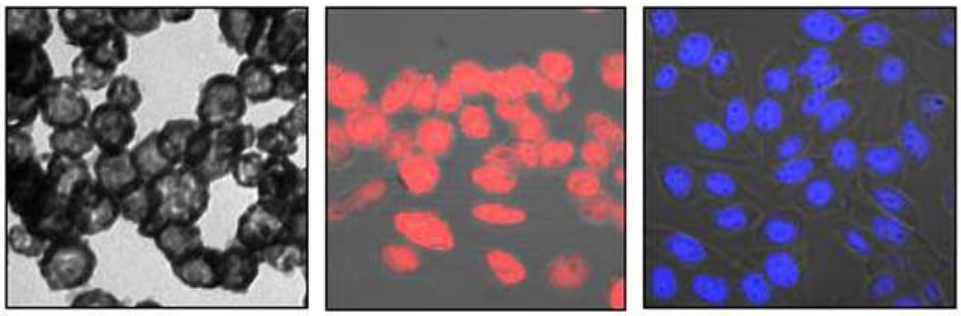

Porous metallic nanoparticles possess unique optoelectronic properties due to their structure and composition. Most remarkable of these are the enhanced surface area and the cavities within the nanostructures. These properties have been exploited in this chapter to develop new cell imaging methodologies and delivery protocols for ligands confined within the nanoporous cavities of gold. Porous gold nanoparticles therefore are interesting in improving the efficiency and sensitivity of the existing sensing and diagnostic techniques in comparison with their solid metal counterparts.

Part of the work described in this chapter has been published: Shukla, S.; Priscilla, A.; Banerjee, M.; Bhonde, R. R.; Ghatak, J.; Satyam, P. V.; Sastry, M. *Chem. Mater.* **2005**, *17*, 5000.

5.1 Introduction

Michael Faraday ‘s work is believed to be the first documented effort towards understanding nanoparticles, which came much later than the first known applications of nanotechnology in colored glasses and ancient therapeutic medicines. Thus, the simplest of the applications developed without much insight into nanotechnology *per se*, lead to the development of an altogether new field of research with extensive inclusion of diverse areas such as physics, chemistry, mathematics, engineering, biology and medicine. What followed was a plethora of new concepts, understanding and applications, that encircled all the above-mentioned disciplines of science and technology. As the understanding of the ‘nano-world’ grew, it fueled extensive research towards development of novel materials, with tunable properties and that, in turn, lead to development of novel application of nanomaterials. Thus, starting from the straightforward applications of nanoparticles such as aggregation mediated optical changes [1] to highly intricate plasmonics [2] and magnetic data storage devices [3] have come up in the last decade or so.

The new technologies based on nanoparticles have often provided significant advantages over those involving conventional materials and have imparted higher efficiency, sensitivity, selectivity and portability over conventional technologies. Hence, there is an ever-growing literature on the newer applications involving metal nanoparticles [4], metal oxides [5], non-metallic oxides [6], composites [7], semiconductor nanoparticles [8] and magnetic nano materials [9] of different shapes, sizes, compositions and structures.

All these classes of nano materials have specific properties and hence, specific applications. Thus, while gold, silver and copper nanoparticles have found applications due to their visible region absorption spectrum and field enhancement effects in various optical chemical and biological sensors [10], quantum dots have emerged as highly sensitive fluorescent markers for *in vivo* biological applications [11]. Similarly, platinum, palladium, nickel, cobalt, gold and their nano-composites have been proved to be highly efficient catalysts [12]. Non-metallic oxides such as TiO_2, SiO_2, ZrO_2, $BaTiO_3$ etc have found applications in paints and coatings [13], cosmetics [14], and sensors [15] as well as more sophisticated applications such as

read write memory devices [16], sensitive electronics [17] and mechanical applications [18]. Similarly, magnetic nanoparticles such as Fe_3O_4, Fe_2O_3, Co and Ni, CrO_2 have been used in bio-diagnostics [19] and drug delivery applications [20], as MRI contrast agents [21], catalysts [22], in bio-separation [23] and pollutant filtration protocols [24]. Besides, in a carrier fluid, magnetic nanoparticles constitute magnetic fluids, which have many interesting applications such as high vacuum seals [25], dampers [26] etc. Likewise, inorganic nano-crystals like $CaPO_4$ etc have been used for biomedical implants [27].

As mentioned earlier, nanoparticle properties can be tuned based on their size, shape, structure and composition. Thus, an entirely different set of properties could be achieved by altering any of these parameters. Therefore, based on the differences in the shape, size, composition and structure of nanoparticles, high degree of specificity in the applications could be obtained. For example, while spherical gold nanoparticles have been used as optical sensors in the visible region [28], anisotropic gold nanoparticles such as nano rods and nano triangles have been used for such purposes in the Near-IR (NIR) region of the electromagnetic spectrum [29]. Similar applications of silver colloids have also been studied by El-Sayed and co-workers [30]. Sastry and co-workers have shown that gold nanotriangles could be used for optical coatings on thermal shields due to their property of NIR absorption [31]. Also, these anisotropic nanoparticles can be used in cancer hyperthermia and as substrates for SERS at higher wavelengths. Similarly, platinum nanoparticles show catalytic specificity based on their crystal structures [32, 12c]. Besides, uptake of nanoparticles by living cells is also influenced by the shape and size of the nanoparticles as demonstrated by Chan and co-workers [33].

Apart from morphology, compositional variations too provide unusual properties to the nanomaterials. Bimetallic nanoparticles are an important class of nanomaterials that often have improved properties than their constituent metals and hence, have improved functionality. These include, core-shell and alloy nanoparticles and have been used for various applications including bio-diagnostics and catalysis. Hollow shell nanoparticles are a subclass of the bimetallic nanoparticles, which have added advantage of enhanced surface area, low density and cost effectiveness.

Therefore, these materials have been used for improved catalysis [34], cell imaging [35] and drug delivery applications [36].

Life sciences research has benefited tremendously from the development of new methods for diagnosis, sensors, therapeutics and imaging technologies. Amongst the inorganic nanoparticles, gold nanoparticles are arguably the most widely used nanoparticle system in biological applications and have been used for immobilization of enzymes [37], antibodies [38], chemotherapeutic agents [39], and fluorescent probes [40] for both *in vitro* and *in vivo* applications [41]. The strongly enhanced surface plasmon resonance of gold nanoparticles at optical frequencies makes them excellent scatterers and absorbers of visible light [42]. In addition, the choice of gold nanoparticles in biological applications stems from the known and well-documented biocompatibility of gold nanoparticles [43]. The use of gold sols in ancient medicines suggests that the compatibility of the gold nanoparticles was recognized in those days too. The ability of the nanogold surface to bind a wide range of biomolecules, including proteins, antibodies and nucleic acids through thiol or amine groups, presents another advantage of using gold nanoparticles for biochemical sensing and detection [44], medical diagnostics, and therapeutic applications [45]. Besides, the facile synthesis protocols also makes gold highly attractive for the above mentioned purposes.

Another technologically important application of gold nanoparticles has been its use as a contrast agent in cellular and biological imaging protocols where it improves the sensitivity and diagnostic ability of imaging by site specific labeling of tissues or cells of interest [46]. Cell imaging utilizing immunotargeted contrast agents provides anatomical details of cell and tissues that can be used for diagnosis of cellular disorders. Traditionally, synthetic dyes and fluorophore such as malachite green and rhodamine 6G have been used as the contrast agents [47]. More recently, quantum dots have gained importance for cell imaging protocols due to their size dependent fluorescent properties [48]. However, cytotoxicity of the semiconductor materials remains a major issue with their use [49]. Therefore, colloidal gold becomes much more important as a nontoxic contrast agent with non-susceptibility to photobleaching or thermal and chemical denaturation which has been the major

drawback associated with chemical flourophores [50]. Gold nanospheres in the size range commonly employed (40 nm) show an absorption cross-section 5 orders higher than conventional absorbing dyes, while the magnitude of light scattering by 80-nm gold nanospheres is 5 orders higher than the light emission from strongly fluorescing dyes [51].

Gold nanoparticles have already shown promising application as contrast agents based on techniques such as multiphoton plasmon resonance microscopy [46, a], photoacoustic tomography [46, b], optical coherent tomography (OCT) [52], photothermal interference contrast microscopy [53] and confocal reflectance microscopy [46, c]. However, the plasmon absorption of gold nanoparticles (500- 550 nm) is too narrow for *in vivo* applications. As has been discussed in the previous chapter, introduction of anisotropy shifts the plasmon absorption of gold nanoparticles to NIR regions. Thus, gold nanorods and nanoshells that absorb in the NIR region of electromagnetic spectra are more useful for *in vivo* applications as the tissue transmissivity is the highest in this region of the spectrum [54] and therefore it does not interfere with the absorption by nanoparticles. Hence, gold nanoshells have been increasingly used not just for cancer imaging and diagnostic applications but their ability to convert absorbed light into localized heat that can be readily employed for therapy based on photothermal destruction of cancerous cells. Hirsch *et al*. have shown the application of silica core-gold shells for photothermal destruction of breast carcinoma cells *in vitro* as well as solid tumors *in vivo* [55]. Similarly, Loo *et al.* have shown simultaneous imaging and therapy of the breast cancers using anti Her 2 antibody labeled gold shells [56]. El-Sayed and co-workers have demonstrated photothermal destruction of cancer cells using localized heating of gold nanoparticles by Argon laser [57].

In this chapter, we have shown that porous gold nanoparticles (porous Au NPs) synthesized by a controlled transmetalation reaction in a dialysis bag, described in the previous chapter, have the ability to conjugate with higher quantities of ligands due to it enhanced surface area. We also illustrate that besides the known applications of such gold shell structures as contrast agents in cell imaging, porous gold nanoparticles can be used as carriers of chemical fluorophore and lead to more stable

fluorescent signals. Besides, the cavities present within these porous structures can be used to conceal ligand molecules and its delivery. Thus, the porous gold nanostructures can act as 'Trojan horse' and therefore could have many interesting implications. The chapter also explores the possibilities of using porous nanoparticles for sustained release of chemotherapeutic agents such as antibiotics and drug molecules, which in itself has emerged as a highly challenging field. We have also demonstrated that the transmetalation products are biocompatible by showing tolerance of mammalian cells towards these nanoparticle systems.

Clearly, the chapter explores the four aspects of the porous nanoparticles viz., enhanced surface area, cavities for concealment, sustained release of molecules trapped in it and biocompatibility issues. By showing various applications of the porous nanoparticles, we have discussed each of these advantages associated with the porous metal nanoparticles.

5.2 Porous gold nanoparticles for cell imaging applications

Presence of a rough surface and cavities within is expected to result in increased surface area of the porous gold nanoparticles. This, in turn, would mean that the porous gold nanoparticles have the ability to bind higher quantities of ligand molecules than the solid counterparts. We have used a fluorophore, Propidium Iodide (PI) to show that the surface area of the porous old nanoparticles is indeed higher than that of the solid gold nanoparticles. The PI conjugated porous gold nanoparticles have also been used for cell labeling as discussed below.

5.2.1 Demonstration of increased surface area with Propidium Iodide

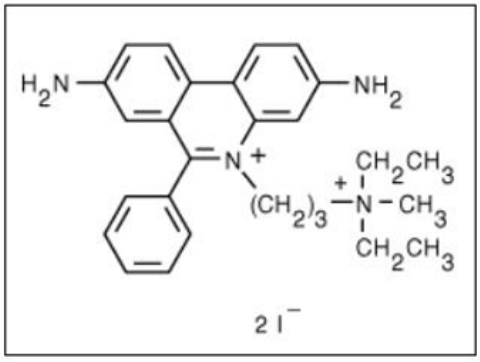

Scheme 5.1 *Chemical structure of Propidium Iodide (PI).*

Propidium Iodide (PI) or Phenanthridinium, 3,8-diamino-5- [3-(diethylmethylammonio) propyl]-6-phenyl-, diiodide is a conventional fluorophore used for cell staining protocols and yields a strong fluorescence emission at 590 nm when excited at 485 nm [58]. The structure of PI is given as Scheme 5.1. A PI only stain fixed cells and is generally used to distinguish live cells from dead cells in a cell culture population. In a typical experiment, 25 mg/ml stock solution of propidium iodide (Sigma, St. Louis, MO, USA) was prepared in phosphate buffer saline (PBS). 500 µl of the PI stock solution was added to 2 ml of porous gold and solid gold nanoparticle solutions. The porous gold NPs were prepared by the reaction of Ag NPs in a 12.5 kDa cutoff dialysis bag with 5 x 10^{-4} M $HAuCl_4$ solution (Figure 5.1, A) as described earlier (Chapter IV) while solid gold NPs were prepared by the sodium borohydride reduction of aqueous chloroauric acid solution as described elsewhere [59], resulting in nanoparticles of size 6.5 ± 0.7 nm (Figure 5.1, B). Similarly 500 µl of PI was added to 2 ml of PBS as a control. These solutions were incubated for 3 h at room temperature under continuous stirring and then centrifuged at 14,000 rpm for 30 min. While the supernatants were collected for fluorimetric analysis, the pellets thus obtained in each case were washed thrice with PBS to remove unbound PI molecules (if any). The washed pellets were then re-suspended in 100 µl of PBS and used for cell staining.

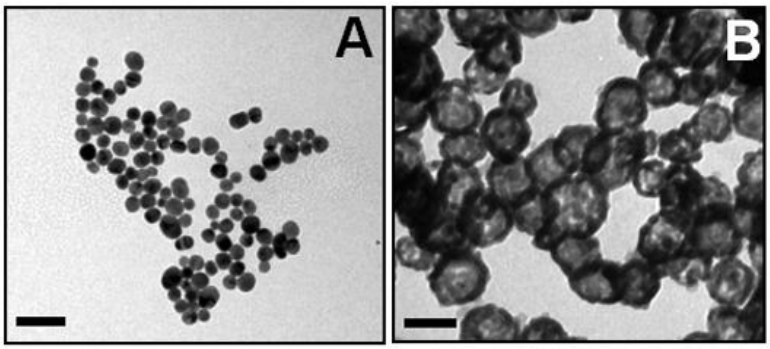

Figure 5.1 *Representative TEM images of $NaBH_4$ reduced solid Au NPs (A) and Porous Au NPs (B). The scale bars correspond to 50 nm.*

Fluorescence measurements of the supernatants collected from the porous and solid gold nanoparticle solutions were performed on a Fluoroskan Ascent fluorimeter by recording the emission at 590 nm after exciting the solutions at 485 nm and are shown in Figure 5.2. The difference in fluorescence intensities of the as-prepared PI

solution and the supernatant after removal of the Au NPs after centrifugation was used to quantify the binding of PI to the porous and solid gold NPs.

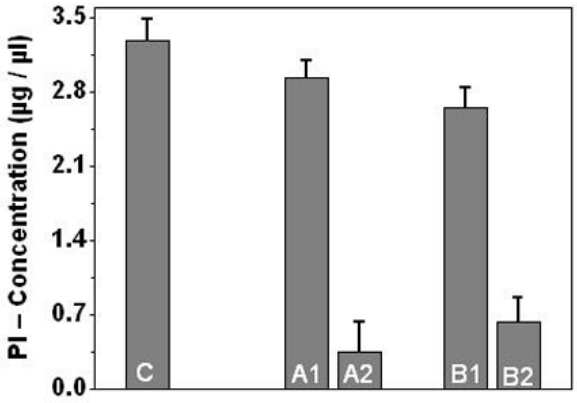

Figure 5.2 *PI concentration in the bound and unbound fractions as calculated from the fluorescence intensities of the respective solutions. C is the uncoordinated PI in the solution; A1 and A2 correspond to the PI concentrations in the supernatants and in the fraction bound on solid Au NPs. B1 and B2 correspond to the concentrations of free and bound fractions of PI on porous Au NPs, respectively.*

The concentrations of PI in the unbound fractions were calculated using a standard fluorescence curve of PI whereas the concentrations of the bound fractions were determined by re-dispersing the pellets in equivalent volume of PBS and subsequently measuring the fluorescence intensity.

The concentration of PI from the supernatants collected from the PI-porous Au NPs (2.5 ± 0.13 µg/µl) and PI-solid Au NPs conjugates (2.7 ± 0.11 µg/µl) are found to be less than that of the control (3.02 ± 0.14 µg/µl), suggesting that a certain fraction of the PI is bound to the nanoparticles in solution and has settled down during centrifugation. The lower fluorescence intensity from the supernatant of the porous structures (Figure 5.2, C) than that of solid gold nanoparticles (Figure 5.2, B) indicates further that the binding of PI to the porous gold nanoparticles is much higher than that to the solid gold nanoparticles as depicted by the concentrations of the bound fractions of PI (0.34 ± 0.28 µg/µl for solid Au NPs and 0.62 ± 0.22 µg/µl for porous Au NPs).

5.2.2 Porous gold-PI conjugate for fixed cells staining

Measuring the fluorescence of the residual PI in the supernatants of porous and solid gold NPs is an indirect approach of determining enhanced binding of PI to

the porous Au NPs. A more direct way of ascertaining the same is the measurement of the fluorescence from the PI associated with the respective nanoparticles. This was achieved by using pellets obtained after the centrifugation to stain mammalian cells and recording the fluorescence intensity from the stained cells. Flow cytometry was then employed to quantitatively analyze the differences in the fluorescence intensities associated with porous Au NPs and solid Au NPs.

5.2.2.1 Cell culture

Chinese Hamster Ovary (CHO) cells were cultured and maintained in tissue in culture grade Nunclon flasks containing Dulbecco`s Modified Eagle Medium (DMEM; Gibco, Grand Island, NY, USA) supplemented with 10% Fetal calf serum (FCS; Trace Biosciences PTY Ltd., New South Wales, Australia) and antibiotics (penicillin 200 U/ml and streptomycin 0.2 mg/ml) at 37 °C in 5% CO_2-incubator.

5.2.2.2 Cell fixation

The CHO cells were dislodged with trypsin, washed with PBS, pelleted down at 2000 rpm and then fixed with 4% paraformaldehyde (w/v) in PBS (pH 7.2) for 10 min at 4 ^{o}C. This results in the death of the CHO cells. The fixed cells were then washed twice with PBS.

5.2.2.3 Cell staining with PI-labeled nanoparticles and microscopic studies

The fixed CHO cells were subjected to RNase (5 mg/ml, USB, Amersham Life technologies, Cleveland, Ohio) treatment for 20 min at room temperature to avoid RNA contamination. The PI-labeled porous and solid gold nanoparticle solutions were then added to the cell suspensions and incubated at room temperature for 90 min in the dark. After incubation, the cells were washed with PBS to remove uncoordinated nanoparticle-PI conjugates. Stained as well as unstained cell preparations were cytospined (Shandon, cytospin 3) on glass slides and mounted with fluorescent mounting medium. The slides were stored in the dark at 4 ^{o}C until analysis. Similarly, CHO cells were also incubated with PI conjugated with porous platinum nanoparticles (porous Pt NPs) synthesized by the galvanic replacement process involving sacrificial silver nanoparticles and Pt (IV) ions, as described in Chapter IV.

5.2.2.4 Microscopic analysis of the fixed CHO cells incubated with PI-nanoparticles conjugates

Fluorescence microscopic analyses of the fixed CHO cells incubated with PI conjugated porous Au NPs, solid Au NPs and porous platinum nanoparticles (porous Pt NPs) carried out at different magnifications is shown in Figure 5.2. It is evident from the fluorescence microscopy that the amount of PI loaded on the nanoparticles varies significantly. The cells incubated with the solid Au NPs-PI pellet shows much lower fluorescence intensity than those incubated with porous Au NPs-PI conjugates. This is in good agreement with the fluorescence intensity recorded for the supernatants of these nanoparticle-PI pellets.

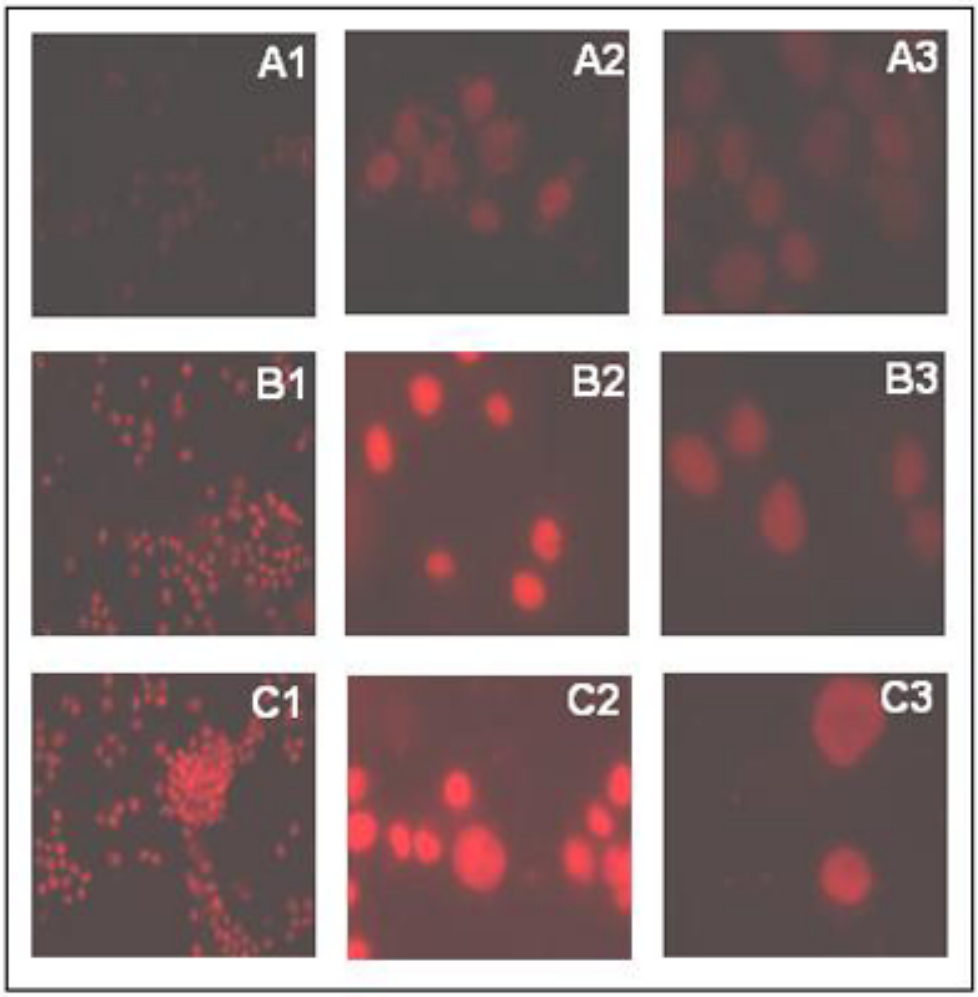

Figure 5.3 *Fluorescence microscopic images of fixed CHO cells incubated with PI conjugated solid Au NPs (A1, A2, A3), PI-porous Au NPs (B1, B2, B3) and PI-porous Pt nps (C1, C2, C3). The magnifications are 20x (A1, B1, C1), 60x (A2, B2, C2) and 100x (A3, B3, C3).*

Thus, supernatants collected from the solid Au NPs-PI conjugate (Figure 5.2, B) showed higher fluorescence intensity suggesting that smaller amount of PI was bound to the nanoparticles, which results in the lower fluorescence observed from the cells under the fluorescence microscope (Figure 5.2, A1, A2 and A3). On the other hand, the supernatant collected from the porous Au NPs-PI conjugate showed lower fluorescent intensity (Figure 5.2, C) as more PI is bound to the pellet in this case than that in solid Au NPs. The higher amount of PI associated with the porous Au NPs pellet results in an increased fluorescence recorded in the fixed CHO cells incubated with it (Figure 5.3, B1, B2, B3).

Interestingly, CHO cells incubated with porous Pt NPs-PI conjugate shows the maximum fluorescence in the microscopic analysis (Figure 5.3, C1, C2, C3). However, cytotoxicity issues associated with the use of heavy elements such as platinum prevents the use of these nanoparticles in biological applications.

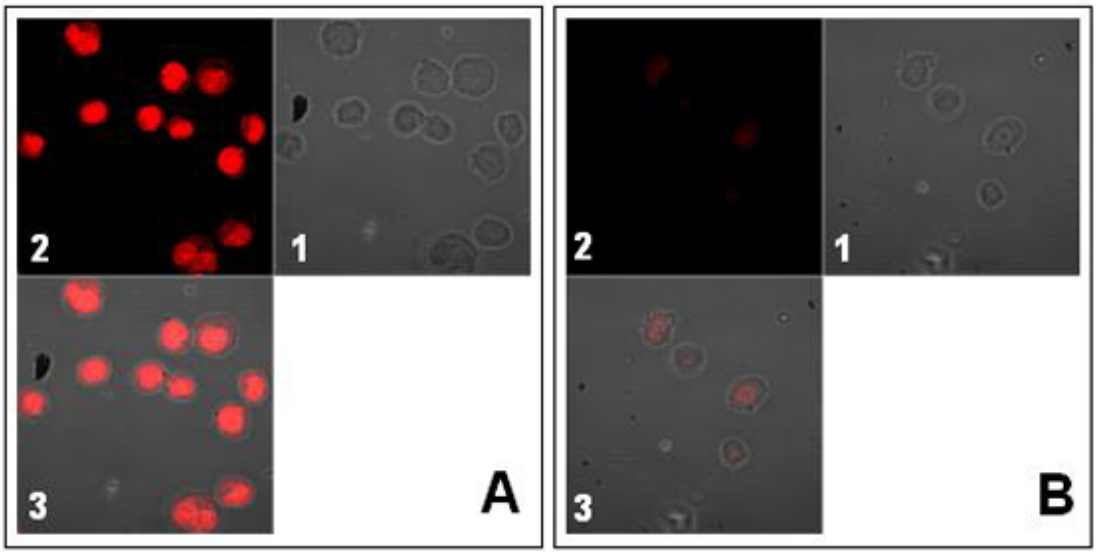

Figure 5.4 *Confocal microscopic images of fixed CHO cells stained by porous Au NPs-PI conjugates (A-1, 2, 3) and solid Au NPs-PI conjugates (B-1, 2, 3). Images A-1 and B-1 are the phase contrast images of the CHO cells; A-2 and B-2 are the fluorescent images; A-3 and B-3 are the superimposition of respective phase contrast and fluorescent images.*

Similarly, confocal-laser-scanning-microscopic (CFLSM) analysis was performed to compare the fluorescence emission from the fixed CHO cells incubated with porous Au NPs-PI conjugate and solid Au NPs-PI conjugates. The confocal images of the stained cells are shown in the Figure 5.4. The cell morphology can be seen more clearly in the respective phase contrast images (Figure 5.4, A-1 and B-1).

Fluorescent images highlight the differences in the fluorescence emission from the fixed cells. Thus, while cells incubated with the conjugation of porous Au NPs and PI are seen bright red in the fluorescent image (Figure 5.4, A-2), those incubated with solid Au NPs-PI complex show only faint red fluorescence (Figure 5.4, B-2). The superimposed images of the CHO cells reveal that the fluorescence is emitted from the cells only, and that the nanoparticles act as the carriers of the fluorescent probes into the mammalian cells (Figure 5.4, A-3 and B-3).

5.2.2.5 Flow cytometry analysis of the nanoparticles-PI stained cells

The increase in the fluorescence due to enhanced binding of PI with porous Au NPs was also quantified using Fluorescence-Activated Cell Sorting (FACS) analysis (FACS Vantage instrument, Becton–Dickinson, Canada).

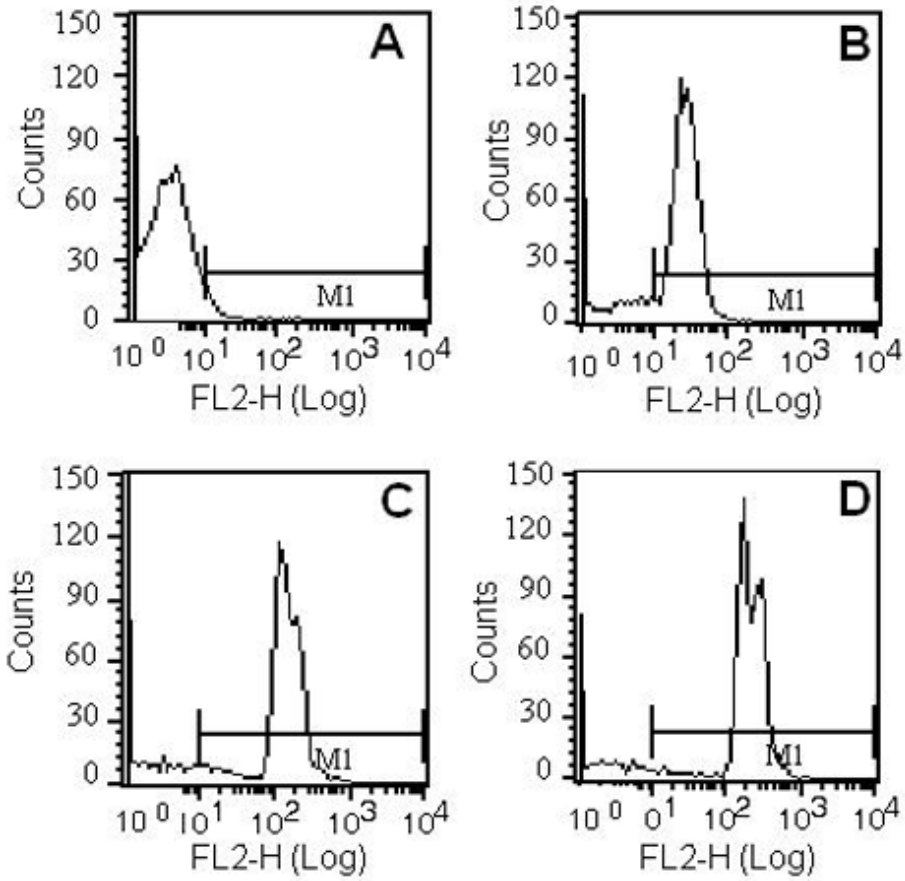

Figure 5.5 *FACS analyses of unstained cells (A), solid Au NPs-PI conjugate stained cells (B), porous Au NPs-PI conjugate stained cells (C) and porous Pt-PI conjugate stained CHO cells (D). x- axis is the mean fluorescence intensity in Log scale, y- axis correspond to the cells count.*

For the FACS analysis, equal number of cells labeled with solid Au NPs-PI conjugates and porous Au NPs-PI conjugates were analyzed and the mean fluorescence intensity measured for equal number of cells counted. Similar number of porous Pt NPs-PI labeled CHO cells were also analyzed using FACS for comparison. The plots obtained from the FACS analysis are shown in Figure 5.5. The x-axis in the FACS data plots represents the fluorescence intensity plotted in log scale recorded for 10,000 CHO cells analyzed in each case, while the y-axis represents the number cells counts. Figure 5.5, A represents the plot obtained for unstained CHO cells, showing residual intrinsic fluorescence of cells while B, C and D represents the FACS data obtained from the cells stained by solid Au NPs-PI, porous Au NPs-PI and porous Pt NPs-PI conjugates. The marker M1 is always set such that the intrinsic fluorescence is lower than 5 % of the fluorescence intensity from the dye. Here, the intrinsic fluorescence was observed to be 1.3 %. The FACS analysis reveals that cells stained with solid Au NPs-PI conjugate, porous Au NPs-PI conjugate and porous Pt NPs-PI conjugate have the mean fluorescence intensities of 24.61, 128.69 and 188.41 respectively.

Thus, it is clear that CHO cells stained with porous Au NPs-PI conjugates show much higher fluorescence than those stained with the solid Au NPs-PI conjugates, suggesting higher binding of PI on the porous Au surface. These results are in good agreement with the fluorescent imaging data discussed previously and are therefore symptomatic of the enhanced surface area of the porous gold nanoparticles over that of the solid gold nanoparticles. As is observed in the fluorescence microscopy images, cells stained with porous Pt NPs- PI conjugates show even higher values of mean fluorescence intensities.

5.2.3 Porous gold-PI conjugate for live cells staining

In the previous section it was showed that PI could be conjugated with gold nanoparticles (both solid and porous) and be used for cell staining procedures. However, PI is known as a fixed cell stain and is used to demarcate fixed cells from the live cells. The cell membrane excludes PI from entering into a live cell and therefore, only when the membrane integrity is lost, as in the case of fixed cells, the

dye is able to enter the cells [60]. However, nanoparticles based non-specific uptake of the dye PI was studied in the following experiment.

5.2.3.1 Live cell staining with PI and nanoparticle-PI conjugates

For live cell staining, PI- labeled porous gold nanoparticles and PI-labeled solid gold nanoparticles were incubated with live CHO cells at 37 ^{o}C for 30 min and the excess unbound PI-nanoparticles conjugates were washed away with PBS. These cells were then stained separately with Hoechst stain-33342 (12.5 μg / ml) and Mitotracker stain; these stains are conventionally used for live cell staining [58] and the experiments were done to establish the viability of the cells after PI-nanoparticles conjugate treatment. After washing with PBS, the cells were fixed and mounted as described previously. Similarly, live CHO cells were incubated with unconjugated pure PI to check the uptake of PI.

5.2.3.2 Confocal Laser Scanning Microscopy (CFLSM)

Live CHO cells incubated with porous Au NPs-PI conjugate, solid Au NPs-PI conjugate and pure PI were viewed under confocal microscope to determine the uptake of PI in the live cells.

Figure 5.6 shows the confocal images of the live CHO cells stained by PI under varying conditions. PI is known to stain only fixed (dead) cells. Live cells, when incubated with pure PI, therefore, exclude the dye and are not stained at all, as evident by the absence of any red fluorescence (Figure 5.6, A). PI conjugated with solid Au NPs also, does not lead to staining of live CHO cells (Figure 5.6, B). On the contrary, live CHO cells, when incubated with PI complexed to porous Au NPs, show excellent staining by PI (Figure 5.6, C-2). To rule out the possibility of cell death during the incubation with nanoparticles resulting into uptake of PI, cell viability was demonstrated using secondary staining with Hoechst stain-33342 and Mitotracker dyes. As shown in the Figure 5.6, C-2, live CHO cells incubated with porous Au NPs-PI complex are stained with PI and therefore appear red. These cells when observed under confocal microscope with red filter show excellent blue staining by Hoechst stain-33342, suggesting that the cells are indeed alive (Figure 5.6, C-3). A superimposition of the two fluorescent images reveals that same cells have been

stained by PI as well as Hoechst stain-33342 and therefore appear pink. Similarly, viability assay carried out with Mitotracker as the secondary stain results in the live cells appearing green (Figure 5.6, C-3). Upon superimposition, live CHO cells stained with PI show dual fluorescence (Figure 5.6, C-4). The cell viability was also supported by the Trypan blue exclusion assay, where live cells did not allow the blue stain to enter, which otherwise resulted in the blue stain of the dead cell population.

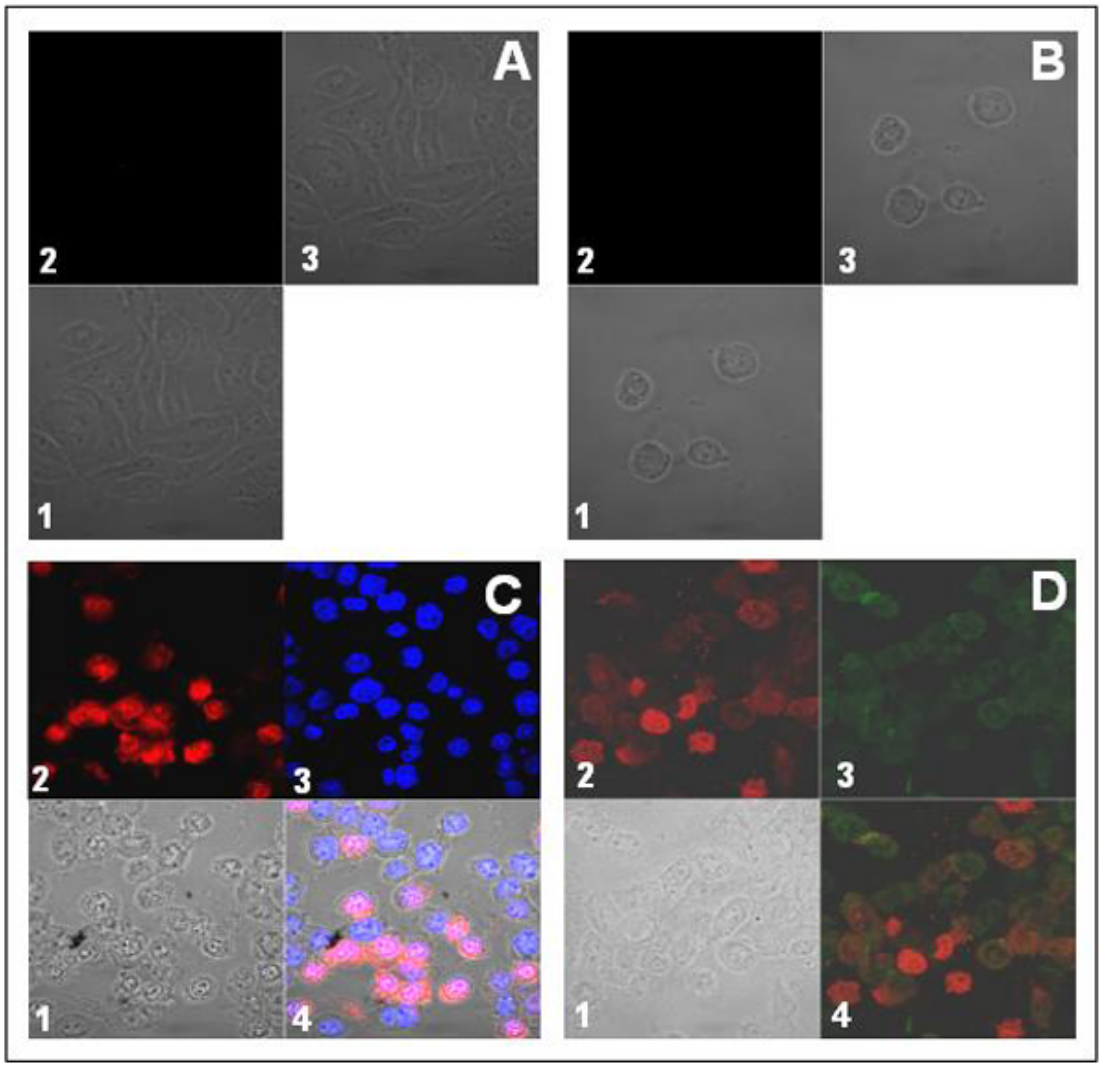

***Figure* 5.6** *Confocal images of live CHO cells stained with pure PI (A) and PI conjugated with solid Au NPs (B). Images 1, 2 and 3 correspond to the phase contrast image, fluorescence and superimposed image of the two, respectively. C and D show the secondary staining of live CHO cells stained with porous Au-PI conjugate by Hoechst stain – 33342 and Mitotracker dyes, respectively. Images 1, 2, 3 and 4 in C and D correspond to phase contrast image, primary staining, secondary staining and superimposition of the three images, respectively.*

The observation that entry of PI into live cells was facilitated by only porous nanoparticles and not the solid nanoparticles is exciting. The cell membrane has the ability to exclude PI from entering into the live cells and it is only when the membrane integrity has been lost that PI is able to enter a cell, thus, PI staining is used to distinguish between the dead and live cells in a culture medium.

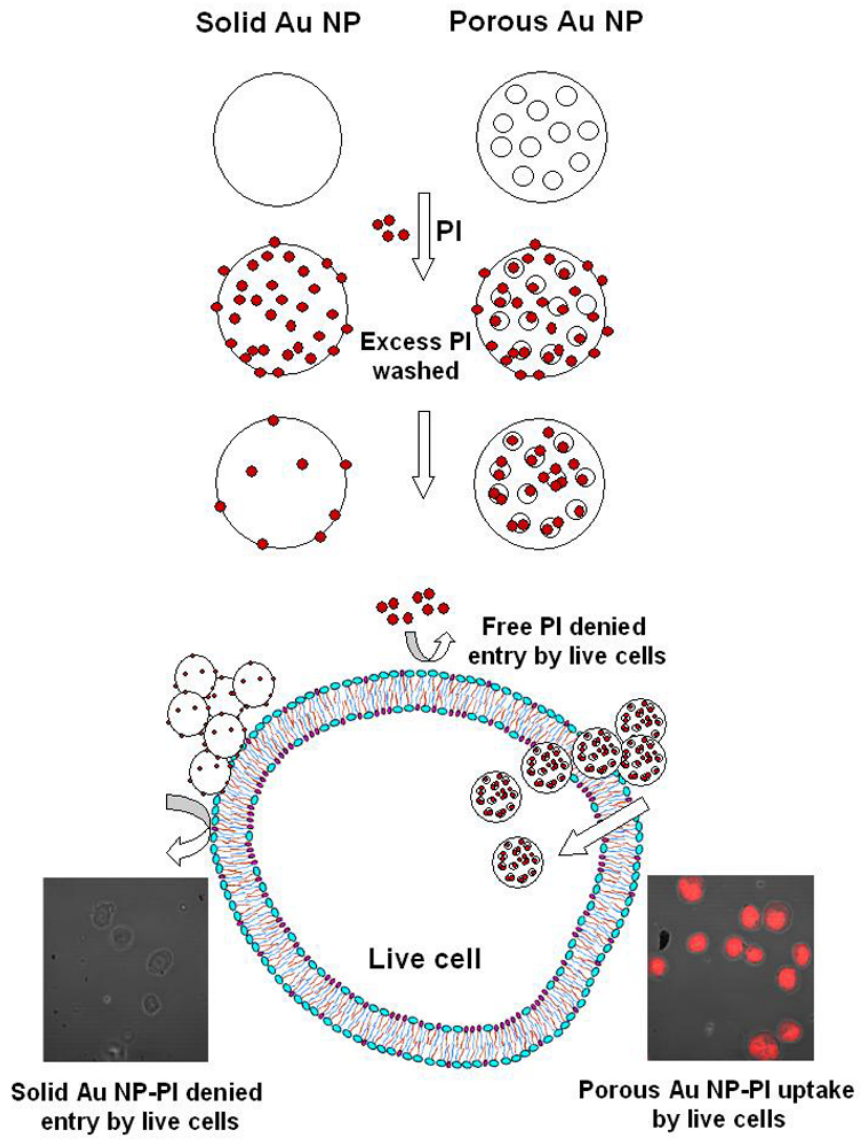

Scheme 5.2 *Live CHO cell staining using PI-nanoparticles conjugates. Pure PI as well as solid gold-PI conjugates are restricted by the cell membrane whereas PI loaded within the cavities of porous gold nanoparticles is able to enter the cell as revealed by the fluorescence image on the right.*

However, nonspecific uptake of nanoparticles into the cells, in principle, is expected to facilitate the entry of any ligand molecule associated with the nanoparticle

into the cell. Under such conditions, PI loaded on the solid gold nanoparticles would have entered the live CHO cells. However, absence of any fluorescence signal from the cell under CFLSM suggests that the PI bound on the solid gold nanoparticles does not stain cells and the plasma membrane is still able to exclude the PI molecules present on the nanogold surface from entering the cells.

On the other hand, the ability of PI loaded on the porous Au NPs to stain the live CHO cells indicates that porous Au NPs are able to penetrate the cells resulting in red fluorescence emission from these cells. This suggests that the cell membrane is not able to detect the presence of PI molecules on the nanoparticles and thus is not able to exclude it. The fact that the porous nanoparticles have numerous small cavities in its structure points towards confinement of the residual PI molecules within the cavities after thorough washing had removed the surface bound and loosely held PI molecules. The confinement of PI in the cavities prevent detection of its presence by the intact cell membrane of the live CHO cells, resulting the uptake of the PI laden porous Au NPs. Thus, porous nanoparticles acts as 'Trojan Horse' capable of concealing ligands within its cavities and releasing them as and when required. The staining of live cells by porous Au NPs-PI conjugate has been depicted in scheme 5.2.

Thus, while the fixed-cell-staining is an evidence of enhanced surface area of the porous Au NPs over their solid counterparts, live-cells-staining using PI loaded on porous nanoparticles underlines the importance of the cavities present with in the Au porous nanoparticles. This phenomenon is of technological significance as metal nanoparticles have been increasingly sought for applications in drug delivery protocols. The ability of porous nanoparticles to confine the ligands within the cavities could be used to protect it from chemical/ physical denaturation during the delivery process.

5.3 Porous gold nanoparticles for enzyme immobilization

Nanoparticle mediated enzyme immobilization has been demonstrated previously. For example, pepsin and trypsin, fungal protease [37], horseradish peroxidase [61] etc. have been immobilized on gold and other inorganic nanoparticles surface. Immobilization of enzymes leads to better thermal and chemical stability as

well as makes the recovery of the biocatalyst easier, which reduces the loss of precious biocatalyst after completion of the reactions [37]. Gold nanoparticle have gained considerable interest in such immobilization procedures as in other biological applications chiefly due to the ease with which the nanogold surface can be decorated with biomolecules and its biocompatibility. Like other surface associated phenomenon, binding of the biomolecules also would increase with increasing surface area. Thus, we carried out enzyme immobilization experiments to determine if the porous structures could be a better substrate in terms of loading and activity of the biocatalysts.

5.3.1 Immobilization of Amylase on porous gold nanoparticles

Amylases are the hydrolytic enzyme derived from animal, fungal and plant sources that catalyze the hydrolysis of (α 1-4) glycosidic linkages of polysaccharides to yield dextrins, oligosaccharides, maltose and D-glucose [62]. These enzymes are classified according to the manner in which the glysosidic bond is attacked. α-Amylases are used to hydrolyze glycogen, the reserve carbohydrates in animals, when the blood glucose levels are low. Salivary amylase, a major component of human salivary secretions, possesses multiple functions in the oral cavity. It is the only enzyme in the saliva capable of degrading oligosaccharides, which are used by the oral microflora for nutritional purposes. The structural neighbor, β-amylase, breaks down starch during the germination of seeds (rich in starch) into sugars. These sugars constitute the chief energy source in the early development of the plant. β-Amylase is able to break down the α-1, 4 linkages of starch polymers in plants and seeds. Amylase is also used in industry. It is used in brewing and fermentation industries for the conversion of starch to fermentable sugars, in the textile industry for designing textiles, in the laundry industry in a mixture with protease and lipase to launder clothes, in the paper industry for sizing, and in the food industry for preparation of sweet syrups, to increase diastase content of flour, for modification of food for infants, and for the removal of starch in jelly production.

For loading Amylase on the gold nanoparticles, stock solution of Amylase was prepared in the phosphate buffer solution (0.1 M, pH 7.0). The pH of solid Au NPs and porous Au NPs was adjusted to 7 prior to addition of enzyme solution in it.

Amylase solution was mixed with equal volumes of solid Au NPs and porous Au NPs to obtain a final concentration of 5 IU/ml of enzyme in the mixture. The mixture of nanoparticles and enzyme was incubated for 12 h at 4 ^{0}C. After the incubation period, the nanoparticles – enzyme solution was centrifuged at 15000 rpm for 20 min. The supernatant was collected separately, while the pellets were resuspended in phosphate buffer of pH 7. The enzyme activity was determined in the supernatants and pellet obtained from both solid gold nps as well as porous Au NPs. For control experiments, enzymatic activity for similar concentration of enzyme in phosphate buffer of pH 7 was determined.

5.3.2 Enzymatic activity determination

Amylase activity was determined by using a standard Amylase Reagent Kit (Teco Diagnostics, Anaheim, CA, US). The kit is based on a modified version of Wallenfels's protocol [ref] where p-Nitrophenyl-D-Maltohepatoside (PNPG7), is used as a substrate. The test is performed in a kinetic mode with a very short lag time.

The enzymatic reaction sequence employed in the assay of amylase is as follows:

$$\text{PNPG7} \xrightarrow{\text{amylase}} \text{PNPG3} + \text{Maltotetraose}$$

$$\text{PNPG3} \xrightarrow{\text{glucoamylase}} \text{PNPG1} + \text{Glucose}$$

$$\text{PNPG1} \xrightarrow{\text{glucosidase}} \text{p-Nitrophenol} + \text{Glucose}$$

Amylase hydrolyzed p-Nitrophenyl D-maltohepatoside (PNPG7) to p-Nitrophenylmaltotriose (PNPG3) and maltotetraose. Glucoamylase hydrolyzes PNPG3 to p-Nitrophenylglycoside (PNPG1) and glucose. Then PNPG1 is hydrolyzed by glucosidase to glucose and p-Nitrophenol, which produces a yellow colour. The rate of increase in absorbance is measured at 405 nm and is proportional to the amylase activity in the sample.

25 µl of the samples (supernatants and re-dispersed pellets) were added to 1 ml of the reconstituted reagent provided with the kit taken in pre-warmed (37 ^{0}C) 96-well plates and plates were read under spectrophotometer at 405 nm immediately after addition and then after every 60 seconds up to 3 min. The mean absorbance difference

per minute was determined and the enzyme activity in terms of IU/ml was calculated as:

$$\text{IU/ml amylase in sample} = \frac{\Delta \text{ Abs./min x TV}}{\text{M.M.A. x S.V. x L.P.}}$$

Where:

Δ Abs./min = Absorbance difference per minute

TV = Total reaction volume

M.M.A. = Millimolar absorptivity of p-Nitrophenol (8.5)

SV = Sample volume

LP = Light path in cm

Appropriate controls were taken to negate the absorbance, if any, by the nanoparticles solution at 405 nm. The values obtained in the amylase assay performed as described above are plotted as Figure 5.7. The activity of free amylase in solution was determined to be 3.84 ± 0.05 IU/ml (Figure 5.7, a). Centrifugation of the free enzyme lead to slight precipitation, which after redispersal gave only negligible enzymatic activity and could be considered as particulate impurities (Figure 5.7, b).

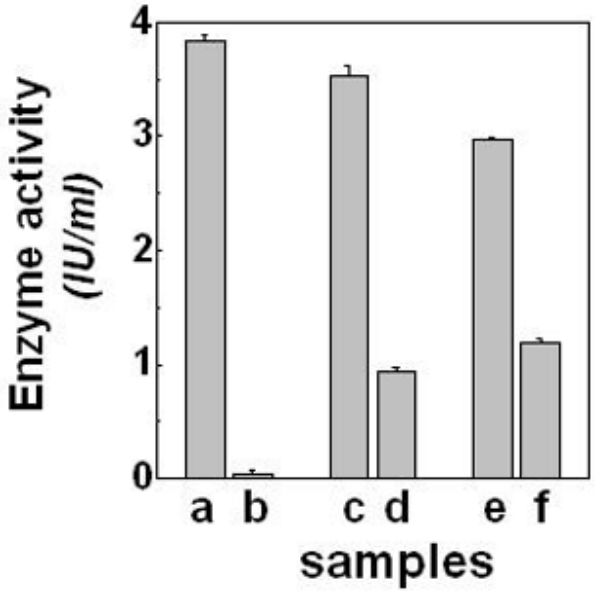

Figure 5.7 *Amylase activity in IU/ml measured after immobilization of the enzyme on solid Au NPs and porous Au NPs. Activity recorded from free amylase in solution a, b; solid Au NPs c, d; porous Au NPs e, f. a, c and d are the activity recorded from the respective supernatants, while b, d and f correspond to the enzyme activity from the pellets after centrifugation.*

Conjugating amylase with solid gold nanoparticles, on the other hand results in the loss of free enzyme from the solution. The residual amylase activity in the supernatant after the centrifugation was estimated to be 3.5 ± 0.08 IU/ml (Figure 5.7, c). The fraction of amylase, which was bound to the nanoparticles surface, gave an enzymatic activity of 0.93 ± 0.03 IU/ml (Figure 5.7, d). These values suggest that only a small fraction of the total enzyme added to the gold nanoparticle solution was bound to the nanoparticle surface. There was a larger decrease in the free enzyme activity in the supernatant when amylase was added to the porous gold nanoparticles solution (Figure 5.7, e). Thus, the activity was estimated to have fallen to 2.98 ± 0.01, suggesting that a larger fraction of enzyme was bound to the porous gold nanoparticles in comparison with the solid gold nanoparticles. This was supported by the enzyme activity measured from the redispersed pellet of porous nanoparticles following the centrifugation, where the enzyme activity was measured to be 1.19 ± 0.03 IU/ml (Figure 5.7, f), which is higher than that obtained from the solid gold nanoparticles.

Although, porous gold nanostructures show an enhanced loading of the enzyme than their solid counterparts, the values are not significantly apart as in the case of the fluorescence intensity observed in the case of propidium iodide loading discussed earlier. These results could be attributed to the composition of the porous gold nanoparticles synthesized by the transmetalation reaction between the sacrificial silver nanoparticles and the Au (III) ions. As has been illustrated previously using EDX, XPS data and the UV-vis-NIR absorption spectra, there is still a fair amount of silver in the porous nanoparticles. The presence of silver in the nanoparticles could well be the reason behind the lower conjugation of the biomolecules such as enzymes, which have a very high binding affinity with the gold surfaces. However, it could be turn into an advantage as binding of ligands to the gold or silver rich regions with in the porous structures could facilitate selectivity in functionalization of nanoparticles.

The lower activities could also result due to the steric hindrance experienced by the substrate molecules when complexing with the surface bound enzymes as against the free enzyme molecules in the solution [63]. However, immobilization of the enzymes on the solid substrates including metal nanoparticles has been shown to

enhance the thermal and ionic stability of the enzyme and is therefore interesting [37, 64]. Such immobilization of enzymes and other biological molecules are important in developing miniaturized sensors and diagnostic tools with high specificity and accuracy [65]. Hence, enhanced binding ability of the porous nanoparticles along with their unique opto-electronic properties could have sweeping implications in the development of more efficient nanoparticle based sensors.

5.4 Cytotoxicity studies of porous gold nanoparticles

Porous gold nanoparticles are promising materials for various biological applications including cell imaging protocols and carriers for biomolecules such as enzymes as illustrated above. The enhanced surface area and nano-cavities offered by these nanoparticles have potential applications in drug delivery applications. However, the applicability of nanoparticle system in clinical and diagnostic applications depends upon the biocompatibility of the nanoparticles and therefore there is an increasing literature available on the biocompatibility studies of various nanomaterials including metallic [43], semiconductor [49] and oxides nanoparticles [66] as well as carbon nanotubes [67]. Gold nanoparticles [68] and its ionic precursors, both Au (I) [69] and Au (III) [69b, c; 70], have been studied extensively by many groups for their biocompatibility and cytotoxicity effect.

Recently, Sastry and co-workers have done a detailed evaluation of the immunological response of cells on exposure to the gold nanoparticles and elucidated the mode of internalization [43, a]. It has been demonstrated that the gold nanoparticles synthesized by sodium borohydride reduction do not show any visible cytotoxicity upto 100 μM concentration in macrophages, which are actively phagocytotic cells. Furthermore, it has been shown that they do not elicit any stress-induced production of proinflammatory cytokines TNFα or IL-1β in the macrophages. At higher concentrations, the gold nanoparticles inhibit the secretion of reactive oxygen species (ROS) and reactive nitrite species (RNS). Murphy and co-workers, on the other hand, have elucidated that citrate reduced gold nanoparticles of an average size of 18 nm are non-toxic up to a concentration of 200 μM while gold salts ($HAuCl_4$) are up to 90% toxic at this concentration [43, b].

There is a lot of interest in exploring the antimicrobial activity of various nanoparticles systems, particularly in application such as antimicrobial surface coatings, food additives, filters and packaging materials [71]. Metal nanoparticles have been also used as the carriers of antibiotics and other chemotherapeutic agents, as they result in the slow release of these molecules in the medium or inside body, which often is an advantage [72]. However, such applications should also mean that the nanoparticles itself are not toxic to the normal microbial flora of the body and only the targeted cells are killed. Here, we have explored the biocompatibility of porous gold nanoparticles with mammalian cell lines as well as microbial cell cultures.

5.4.1 Biocompatibility of porous gold nanoparticles with mammalian cell lines

The cytotoxicity studies of porous gold nanoparticles were performed in the CHO epithelial cell line as well as NIH 3T3 mouse embryonic fibroblast cell line. Cells of both the cell lines were cultured in Dulbecco's modified Eagle's medium (DMEM) supplemented with 10% fetal calf serum (FCS), 100 units/mL penicillin, 100 μg/mL streptomycin, and 2 mM glutamine. The cells were incubated in a humidified atmosphere of 5% CO_2 and 95% air at 37 °C. Actively growing cells were seeded with density around 1 x 10^5 cells/well in a 96-well tissue culture plate. The cells were treated with different concentrations of porous gold nanoparticles (10, 25 and 50 μM) for 48 h.

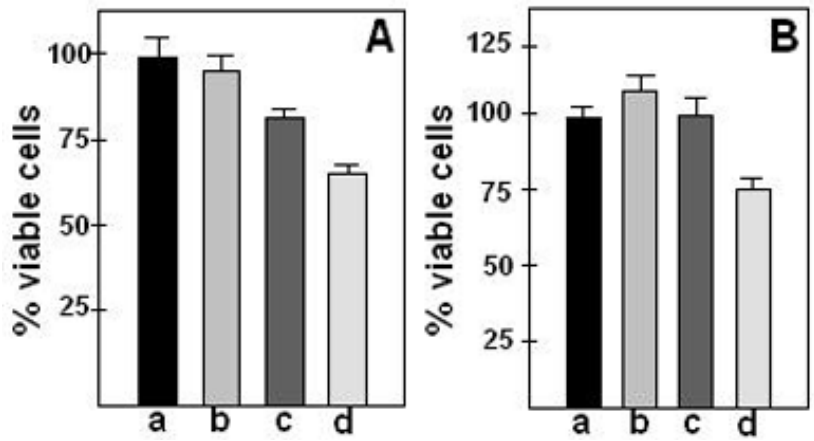

Figure 5.8 *MTT assay for determination of the cytotoxicity of the porous gold nanoparticles on CHO epithelial cell line (A) and NIH 3T3 mouse fibroblast cell line (B) after 48 h of exposure. Bars a, b, c and d correspond to the porous gold concentration of 0, 20, 50 and 100 μM, respectively.*

The control cells were not treated with porous gold nanoparticles and were kept in the same volume of phosphate buffer saline (PBS, pH-7.4) for the same period of time. After the end of the exposure time, the cell viability was checked using the 3-(4,5-dimethylazol-2-yl)-2,5- diphenyl-tetrazolium bromide (MTT) assay [44]. The MTT assay is based on the optical detection of the purple colored formazan at 570 nm, which is formed by the enzymatic reduction of yellow tetrazolium MTT. All experiments were performed 3 times in quadruplets, and their average has been shown as cell-viability percentage in comparison with the control experiment. The porous gold untreated controls were considered to be 100% viable. The MTT assay carried out on CHO and NIH 3T3 cell lines has been shown in the Figure 5.8.

As evident in Figure 5.8, A, CHO epithelial cells exhibit slightly enhanced cytotoxicity with increasing concentrations of porous gold nanoparticles in the culture media after an exposure of 48 h. The control cell population unexposed to porous gold nanoparticles was considered as 100 % cell viability (Figure 5.8, A, a). With respect to the control cell population, CHO cells show more than 80 % cell viability up to the porous gold concentration of 50 μM for 48 h (Figure 5.8, A, b & c). However, at higher concentration of 100 μM, the cell viability reduces to 66 % with respect to the control cell population. The cell viability is lower in comparison to that obtained with borohydride reduced gold nanoparticles [43, a] or citrate reduced gold nanoparticles [43, c] and could be attributed to the presence of considerable quantities of metallic silver in the porous structures and absence of a capping agent. It has been demonstrated earlier that the presence of capping molecules such as polyethylene glycol [73] and amino acids [74; 43, a] renders the nanoparticles more biocompatible. Porous Au NPs, on the other hand, do not retain the tyrosine capping of the sacrificial silver nanoparticles once the gold shell has formed. This is supported by the weak nitrogen signal obtained from the XPS spectra of the porous Au NPs.

Lower concentrations of porous gold nanoparticles added into the culture media containing NIH 3T3 cells leads to a slightly elevated cell viability (Figure 5.8, B, b & c). This could result from an enhanced enzymatic activity in the cells due to the stress like conditions within the cells due to the exposure to the metal

nanoparticles. At higher concentrations (100 μM), though, cell viability reduces to 76 % (Figure 5.8, B, d).

In another experiment it was demonstrated that CHO cells not exposed to the nanoparticles retain the monolayer growth pattern even after 24 h (Figure 5.9, A). On the contrary, exposure of CHO cells with 50 μM of porous Au NPs leads to breaking of the monolayer and formation of small aggregates of cells within 24 h as shown in Figure 5.9, B. The aggregating cells start forming discrete cell masses within 48 h of growth. Although, the exact mechanism leading to the cell aggregation is not clear at this point, it reflects the alteration in the cell-cell and cell-substrate interactions, which could be a manifestation of the altered protein profile of the mammalian cells and need further studies.

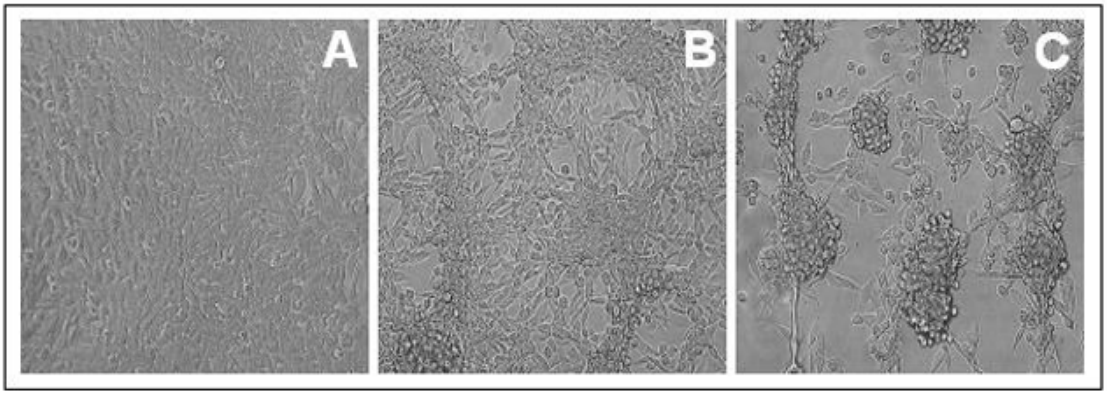

Figure 5.9 *Phase contrast microscopy images of CHO epithelial cell cultures; A corresponds to 24 h old culture; B and C correspond to cells exposed to 50 μM porous Au NPs for 24 h and 48 h, respectively.*

Although, the MTT assay elucidates that the porous nanoparticles leads to cell death in both the cultures, it does so only on prolonged exposure of 48 h at reasonably high concentrations. Thus, prolonged exposures of high concentrations of porous gold nanoparticles for *in vitro* and *in vivo* applications could lead to cytotoxicity. However, it has been demonstrated that the porous nature of the particles provides them with enhanced surface area over the solid gold nanoparticles, which obviously mean that they can carry higher amounts of ligands on the surface than the solid gold nanoparticles. Thus, the high surface area offered by the porous nanoparticles over the solid counterparts obliviates the use of high concentrations of porous gold

nanoparticles for applications such as cell imaging and drug delivery that require nanoparticle interaction with live cells.

5.4.2 Non toxic nature of porous gold nanoparticles on microbial cultures

The microbial cytotoxicity of the porous gold nanoparticles was tested against *E.coli* HB101 culture, a susceptible strain devoid of plasmids. The seed culture of bacterium was grown in 100 ml of Luria broth medium at 37 ^{o}C for 12 h. Three flasks containing 100 ml of fresh Luria broth were prepared with 100 μM each of silver nanoparticles, porous gold nanoparticles and silver sulphate, respectively. Similarly, a fourth flask with equivalent volume of sterile water was prepared as a control. All the solutions, including silver nanoparticles, porous gold nanoparticles and silver sulphate were autoclaved prior to addition in the Luria Broth. All the flasks were inoculated with 1 ml of the 12 h old seed culture and incubated at 37 ^{o}C. Samples were withdrawn from the cultures periodically and their optical density was recorded at 660 nm to measure the bacterial growth, which is shown in Figure 5.10.

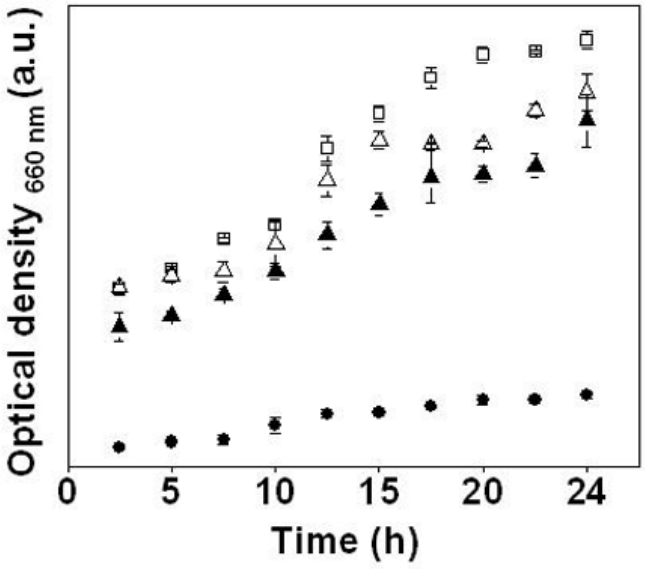

Figure 5.10 *Optical density of bacterial cell cultured in presence of only medium (□), in presence of porous gold nanoparticles (Δ), silver nanoparticles (▲) and silver ions (●) over a period of 24 h.*

Bacterial cells grown only in medium shows a typical sigmoid growth curve over a period of 24 h (Figure 5.10, -□-). Silver ions (Ag (I)) and silver nanoparticles have been shown to have antimicrobial properties and therefore have found

application as antimicrobial agents [75]. Thus, *E.coli* cells, cultured in Luria broth supplemented with the silver ions, showed drastic reduction in the microbial cell populations as reflected by the lower optical density recorded at 660 nm (Figure 5.10, -●-). Similarly, silver nanoparticles illustrate a more restricted growth in the microbial growth as compared to the control (Figure 5.10, -▲-). In presence of porous Au NPs however, there is no significant inhibition of the bacterial growth as reflected by the optical density at 660 nm (Figure 5.10, -Δ-). These results elucidate that the porous gold nanoparticles are not toxic to the microbial cells. The significance of this observation lies in the fact that the porous nanoparticles can therefore be used for applications such as plasmid DNA transfer in the bacterial cells without inhibiting the growth. Also, application of porous gold nanoparticles as a carrier of antibiotics and other chemotherapeutic agents appears more promising as there is no apparent toxic effect of the metal nanoparticles itself on the normal gut flora and only the targeted pathogenic microbes targeted with the chemotherapeutic ligand molecules will be affected.

The increased surface area and the cavities within the structure renders the porous gold nanoparticles advantageous over other nanoparticles of choice despite the slight toxicity showed against mammalian and microbial cells. Increased loading of the ligands and the ability to conceal molecules within the cavities makes the porous nanoparticles much more promising for a wide range of applications including drug delivery applications, biomolecules immobilization and catalysis.

5.5 Discussion

Porous metal nanoparticles are a special class of nanoscale metals that offer increased surface area, low density and cost effectiveness over their solid counterparts. Their unique structure and composition impart the porous nanoparticles with interesting optoelectronic properties that are very different from the solid nanoparticles. Therefore, one immediately recognizes that such porous nanoparticles can present improved potential for the existing protocols involving conventional nanoparticles besides developing novel applications. This chapter attempts to elaborate the improved functionality that can be achieved using porous metal nanoparticles.

Nanotechnology has had tremendous impact on life sciences research in terms of emergence of new sensing, diagnostic and therapeutics protocols involving nanoparticles. Gold nanoparticles are arguably the most studied and applied nanoparticles system in biological research due to the ease of synthesis, known biocompatibility and their ability to bind strongly through the amine or thiol functional groups to a wide variety of biomolecules and other ligands. In this chapter, porous gold nanoparticles synthesized using controlled transmetallation reaction have been shown to possess improved surface area and functionality over solid gold nanoparticles. The higher surface area is reflected in the enhanced concentrations of ligands bound on the surface of the porous nanoparticles.

Conjugation of fluorophore, Propidium Iodide (PI), to the nanoparticles was carried out to establish the enhanced surface area of porous nanoparticles. Cells incubated with porous gold nanoparticles appeared to emit increased red fluorescence than those incubated with borohydride reduced solid gold nanoparticles. This could be attributed to the higher quantities of PI associated with the porous gold nanoparticles as compared to the borohydride reduced gold nanoparticles. Similar experiments with porous platinum nanoparticles showed even higher binding of PI. These observations were supported by the fluorescence-assisted cell sorting (FACS) analysis that indicated five-fold increase in the fluorescence intensity from the cells stained with porous gold NPs-PI complex.

The application of nanoparticles conjugated fluorophore has so far been restricted to Fluorescence Resonance Energy Transfer (FRET) mediated fluorescence quenching for detection of specific molecular recognition events [76]. Florescent molecules have been shown to undergo radiative and non-radiative decay processes on the gold nanoparticles and its vicinity [77]. Both radiative and non-radiative decay rates are expected to depend critically on the nanoparticles size, distance between the fluorescent molecules to the nanoparticle surface etc [78]. It is known that dye molecules that have absorption bands in the same frequency range as the plasma frequency of the metal particle can strongly affect the absorption spectra of the particles [79]. At the same time quenching of the excited state by the conductive metal surface that results in energy transfer to the metal surface has been reported

earlier [80]. The probability of this Forster energy transfer depends on the overlap of the fluorescence band of dye molecule with the absorption band of the acceptor. In the present case, PI fluorescence band at 580 nm is near the nanogold surface plasmon band at 520 nm and one expects effective energy transfer from the excited molecule to the gold surface. Thus, the low fluorescence intensities observed from the CHO cells under the confocal microscope could also be due to the partial quenching of the fluorescence of the PI molecules conjugated on the solid gold nanoparticles surface. Porous gold nanoparticles, on the other hand, show surface plasmon absorption band at ~700 nm, which therefore, does not lead to efficient quenching of PI fluorescence and hence cells incubated with PI complexed to porous gold nanoparticles appear bright red under CFLSM.

Sensitivity of the fluorescence-based assays has also been enhanced by numerous methods including surface-enhanced fluorescence on metal nanostructures (SFE) [81] where fluorescence enhancement occurs when a fluorophore is localized near the surface of metallic nanoparticles [82]. SEF is believed to take place through the coupling of the fluorophore with radiating plasmon from the metallic particles [83]. Silver nanoparticles have been reported to enhance fluorescence of the dyes associated to its surface through SFE [81]. Presence of considerable amounts of silver in the porous nanoparticles was shown by the EDX and XPS analysis in the previous chapter. The high fluorescence intensity from PI conjugated porous nanoparticles, could be, in part, attributed to the enhancement due to the metallic silver present in the porous structures. Although, the points discussed above need to proved with more experimentation, together with the enhanced surface area, they make the porous gold nanoparticles highly potential contrast agents for cell imaging applications.

Another interesting aspect of the porous gold nanoparticles was their ability to stain live CHO cells with PI, a stain that is known to stain only the fixed cells. The inability of the cell membrane to exclude the PI conjugated porous nanoparticles from entering the live cells, while at the same time, inhibiting PI bound to solid gold nanoparticles is highly intriguing. It is evident from these results that solid gold nanoparticles present the conjugated PI molecules on the surface, and the cell membrane is able to sense and exclude the PI from the cell similar to the exclusion of

pure uncoordinated PI in a separate experiment. However, repeated washing with buffer after conjugating the porous nanoparticles with PI gets rid of most of the surface bound PI molecules. Uptake of porous nanoparticles into cells and the subsequent observation of fluorescence from the cells suggest that porous nanoparticles were able to carry concealed PI molecules into the cells. The cavities present in the porous nanoparticles can be therefore used for concealing such molecules and deliver them into cells. Previously, it has been demonstrated that gold nanoparticles decorated with specific signaling peptides were capable of entering the cell nucleus [84]. It was demonstrated that presence of certain specific peptides only could guide the nanoparticles to the nucleus, whereas in their absence the nanoparticles were delivered to the endosomes. In this case, gold nanoparticles were actively taken up by the cells irrespective of the peptides bound on the surface, although the fate of the nanoparticles within the cells was decided by the specific peptides. However, in case of solid and porous gold nanoparticles, it was the presence of PI on the surface that governed the uptake of nanoparticles. It is clear that porous nanoparticles could act as excellent carriers of wide range of ligands for both in vitro and in vivo applications. Such nano-container could be used to control the microenvironment of the fluorophore and other confined ligands and to protect them from unwanted chemical interactions with substrates in the external medium. The presence of plasmon absorption band in the near infrared regions of the electromagnetic spectrum would mean that these nanoparticles could absorb heat and therefore have applications in therapies like cancer hyperthermia. Together with capability to bind drug molecules within, NIR absorption could facilitate temperature dependent release of anticancer drugs like doxorubicine and thus provide dual effect against cancerous cells.

5.6 Conclusions

This chapter illustrates applications of porous gold nanoparticles based on their unique structure based properties. The improved surface area and cavities within the metal nanoparticles facilitates applications of these nanoparticles as contrast agents in cell imaging protocols and carriers that could act as ‘Trojan Horse’ in drug delivery applications. These very characteristics of the porous nanoparticles promises

to improve the efficiency of existing devices and techniques based on the conventional solid gold nanoparticles. The chapter also addresses the issues relating to the cytotoxicity of the porous gold nanoparticles and shows that they are reasonably biocompatible with mammalian cell lines as well as bacterial cultures. It has been shown that the porous gold nanoparticles have huge potential for a wide range of applications.

5.7 References

1. (a) Mirkin, C. A.; Letsinger, R. L.; Mucic, R. C.; Storhoff, J. J. *Nature* **1996**, *382*, 607. (b) Lim, M.; Schnablegger, H.; Mann, S. *Nature* **1999**, *402*, 393. (c) Wessels, J. M. *J. Am. Chem. Soc.* **2004**, *126*, 3349.

2. (a) Maier, S. A.; Brongersma, M. L.; Kik, P. G., Meltzer, S.; Requicha, A. A. G.; Atwater, H. A. *Adv. Mater.* **2001**, *13*, 1501. (b) Wabuyele, M.B.; Vo-Dinh, T. *Anal. Chem*. **2005**, *77*, 7810. (c) Stranik, O.; McEvoy, H. M.; McDonagh, C.; MacCraith, B. D. *Sensors and Actuators, B*, **2005**, *107*, 148.

3. (a) Tour, J. M. *et al., J. Am. Chem. Soc*. **2003**, *125*, 13279. (b) Gubin, S. P.; Spichkin, Y. I.; Yurkov, G. Y.; Tishin, A. M. *Russ. J. Inorg. Chem*. **2002**, *47*, S32.

4. (a) Pérez-Juste, J.; Pastoriza-Santos, I.; Liz-Marzán, L. M.; Mulvaney, P. *Coord. Chem. Rev.* **2005**, *249*, 1870. (b) Huber, D. L. *Small*, **2005**, *1*, 482. (c) Wiley, B.; Sun, Y.; Mayers, B.; Xia, Y. *Chem. Euro. J.* 2005, 11, 454. (d) Kim, K. S.; Demberelnyamba, D.; Lee, H. *Langmuir* **2005**, *20*, 556.

5. (a) Jana, N. R.; Chen, Y.; Peng, X. *Chem. Mater*. **2001**, *16*, 3931. (b) Wang, X.; Chen, X.; Gao, L.; Zheng, H.; Ji, M.; Tang, C.; Shen, T.; Zhang, Z. *J. Mater. Chem.* **2004**, *14*, 905.

6. (a) Niederberger, M.; Pinna, N.; Polleux, J.; Antonietti, M. *Angew. Chem. Int. Ed.* **2004**, *43*, 2270. (b) Zhang, H. F.; Wang, C. M.; Buck, E. C.; Wang, L. S. *Nano Lett.* **2003**, *3*, 577. (c) Hakuta, Y.; Ura, H.; Hayashi, H.; Arai, K. *Indust. Engg. Chem. Res.* **2005**, *44*, 840.

7. (a) Hu, X.; Wang, T.; Qu, X.; Dong, S. *J. Phys. Chem. B* **2006**, *110*, 853. (b) Kim, B. S.; Qiu, J. M.; Wang, J. P.; Taton, T. A. *Nano Lett*. **2005**, *5*, 1987.

8. (a) Sun, X.; Li, Y. *Angew. Chem. Int. Ed.* **2004**, *43*, 3827. (b) Mao, C. *et al*., *Science*, **2004**, *303*, 213. (c) Goldberger, J.; He, R.; Zhang, Y.; Lee, S.; Yan, H.; Choi, H. J.; Yang, P. *Nature* **2003**, *422*, 599.

9. (a) Gupta, A. K.; Gupta, M. *Biomater*. **2005**, *26*, 3995. (b) Jana, N. R.; Chen, Y.; Peng, X. *Chem. Mater*. **2004**, *16*, 3931. (c) Dumestre, F.; Chaudret, B.; Amiens, C.; Renaud, P.; Fejes, P. *Science*, **2004**, *303*, 821.

10. Liu, J.; Lu, Y. *J. Am. Chem. Soc.* **2004**, *126*, 12298. (b) Yonzon, C. R.; Jeoung, E.; Zou, S.; Schatz, G. C.; Mrksich, M.; Van Duyne, R. P. *J. Am. Chem. Soc.* **2004**, *126*, 12669. (c) Taurozzi, J. S.; Tarabara, V. V. *Env. Engg. Sc.* **2007**, *24*, 122.

11. (a) Chen, W.; Zhang, J. Z.; Joly, A. G. *J. Nanosci. Nanotechnol.* **2004**, *4*, 919. (b) Edgar, R. *et al., Proc. Natl. Acad. Sci*. *USA* **2006**, *103*, 4841. (c) Zhang, C. Y.; Yeh, H. C.; Kuroki, M. T.; Wang, T. H. *Nature Mater.* **2005**, 4, 826.

12. Mei, Y., Sharma, G., Lu, Y., Ballauff, M. Drechsler, M.; Irrgang, T.; Kempe, R. *Langmuir* **2005**, *21*, 12229. (b) Astruc, D.; Lu, F.; Aranzaes, J. R. *Angew. Chem. Int. Ed.* **2005**, *44*, 7852. (c) Narayanan, R.; El-Sayed, M. A. *J. Phys. Chem. B* **2005**, *109*, 12663.

13. (a) Pradell, T.; Molera, J.; Bayés, C.; Roura, P. *Appl. Phys. A* **2006**, *83*, 203. (b) José-Yacamán, M.; Rendón, L.; Arenas, J.; Serra Puche, M. C. *Science* **2006**, *273*, 223. (c) Baglioni, P.; Giorgi, R. *Soft Matter* **2006**, *2*, 293.

14. (a) Cengiz, E.; Wissing, S. A.; Muoller, R. H.; Yazan, Y. *Intl. J. Cosmetic Sci.* **2006**, 28, 371. (b) Villalobos-Hernández, J. R.; Muoller-Goymann, C. C. *Intl. J. Pharmaceutics* **2006**, *322*, 161.

15. (a) Osterloh, F.; Hiramatsu, H.; Porter, R.; Guo, T. *Langmuir* **2004**, 20, 5553. (b) Manera, M.G.; Cozzoli, P.D.; Curri, M. L.; Leo, G.; Rella, R. *Synth. Metals* **2005**, *148*, 25.

16. (a) Murphy, T. E.; Chen, D.; Phillips, J. D. *Appl. Phys. Lett.* **2004**, *85*, 3208. (b) Seager, C. H.; Mcintyre, D. C.; Warren, W. L.; Tuttle, B. A. *Appl. Phys. Lett.* **1996**, *68*, 2660.

17. (a) Qi, L.; Lee, B. I.; Samuels, W. D.; Exarhos, G. J.; Parler Jr., S. G. *J. Appl. Polymer. Sci.* **2006**, *102*, 967. (b) Huang, L. *et al*., *J Appl. Phys*. **2006**, *100*, 34316.

18. (a) Park, H. S. *et al., Macromol. Res*. **2006**, *14*, 430. (b) Fechine, P. B. A. *et al., Mater Chem. Phys*. **2006**, *96*, 402.

19. (a) Boas, G. *Biophotonics Intl.* **2005**, *12*, 42. (b) Mornet, S.; Vasseur, S.; Grasset, F.; Duguet, E. *J. Mater. Chem.* **2004**, *14*, 2161. (c) Bogue, R. *Sensor Rev*. **2005**, *25*, 249. (d) Zhao, X.; Tapec-Dytioco, R.; Wang, K.; Tan, W. *Anal. Chem*. **2003**, *75*, 3476.

20. (a) Wagner, K. *et al., Appl. Organomet. Chem*. **2004**, *18*, 514. (b) Yang, J.; Park, S. B.; Yoon, H. G.; Huh, Y. M.; Haam, S. *Intl. J. Pharmaceut.* **2006**, *324*, 185. (c) Saito, R. *et al., Expt. Neurol*. **2005**, *196*, 381.

21. (a) Will, O. *et al., Lancet Oncology* **2006**, *7*, 52. (b) Veiseh, O. *et al., Nano Lett*. **2005**, *5*, 1003. (c) Rockall, A. G. *et al*., *J. Clinic. Oncol*. **2005**, *23*, 2813.

22. (a) Luo, J.; Kariuki, N.; Han, L.; Wang, L.; Zhong, C. J.; He, T. *Electrochim. Acta.* **2006**, *51*, 4821. (b) Guczi, L. *et al., Appl. Catal. A* **2005**, *291*, 116. (c) Tsang, S.C.; Caps, V.; Paraskevas, I.; Chadwick, D.; Thompsett, D. *Angew. Chem. Int. Ed.* **2004**, *43*, 5645.

23. (a) Yang, H. H. *et al*., *Anal.Chem*. **2004**, *76*, 1316. (b) Ito, A.; Shinkai, M.; Honda, H.; Kobayashi, T. *J. Biosci. Bioengg.* **2005**, *100*, 1. (b) Ho, K. C.; Tsai, P. J.; Lin, Y. S.; Chen, Y. C. *Anal. Chem.* **2004**, *76*, 7162.

24. (a) Elliott, D. W.; Zhang, W. X. *Environ. Sci. Technol*. **2001**, *35*, 4922. (b) Kumbhar, A.; Chumanov, G. *J. Nanopart. Res*. **2005**, *7*, 489.

25. (a) Massart, R.; Rasolonjatovo, B.; Neveu, S.; Cabuil, V. *J. Mag. Mag. Mater.* **2007**, *308*, 10. (b) Sekine, K.; Mitamura, Y.; Murabayashi, S.; Nishimura, I.; Yozu, R.; Kim, D. W. *Artificial Organs* **2007**, *27*, 892.

26. (a) Yang, G.; Spencer Jr., B. F.; Jung, H. J.; Carlson, J. D. *J.Engg. Mechanics* **2004**, *130*, 1107. (b) Hou, B. L. *Acta Armamentarii* **2006**, *27*, 613.

27. (a) Wutticharoenmongkol, P.; Sanchavanakit, N.; Pavasant, P.; Supaphol, P. *Macromol. Biosci*. **2006**, *6*, 70. (b) Vallet-Regí, M.; Arcos, D. *Curr. Nanoscience* **2006**, *2*, 179.

28. (a) Lee, K. S.; El-Sayed, M. A. *J. Phys. Chem. B* **2006**, *110,* 19220. (b) Haes, A. J.; Van Duyne, R. P. *J. Am. Chem. Soc***. 2002**, *124*, 10596. (a) Hirsch, L. R.; Stafford, R. J.; Bankson, J. A.; Sershen, S. R.; Rivera, B.; Price, R. E.; Hazle, J. D.; Halas, N. J.; West, J. L. *Proc. Natl. Acad. Sci. USA* **2003**, *100*, 13549. (b) El-Sayed, I. H.; Huang, X.; El-Sayed, M. A. *Nano Lett.* **2005**, *5*, 829.

29. (a) Dick, L. A.; McFarland, A. D.; Haynes, C. L.; Van Duyne, R. P. *J. Phys. Chem. B* **2002**, *106*, 853. (b) Miranda, M. M. *Chem. Phys. Lett.* **2001**, *340*, 437. (c) Orendorff, C. J.; Gole, A.; Sau, T. K.; Murphy, C. J. *Anal. Chem.* **2005**, *77*, 3261.

30. Lee, K. S.; El-Sayed, M. A. *J. Phys. Chem. B* **2006**, *110*, 19220.

31. Shankar, S. S.; Rai, A.; Ahmed, A.; Sastry, M. *Chem. Mater.* **2005**, *17*, 566.

32. (a) Shi, A. C.; Masel, R. I. *J. Catal.* **1989**, *120*, 421. (b) Falicov, L. M.; Somorjai, G. A. *Proc. Natl. Acad. Sci. USA* **1985**, *82*, 2207. (c) Narayanan, R.; El-Sayed, M. A. *Langmuir* **2005**, *21*, 2027.

33. Chithrani, B. D.; Ghazani, A. A.; Chan, W.C.W. *Nano Lett.* **2006**, *6*, 662.

34. (a) Liang, H. P.; Guo, Y. G.; Zhang, H. M.; Hu, J. S.; Wan, L. J.; Bai, C. L. *Chem. Commun*. **2004**, 1496. (b) Arnal, P. M., Comotti, M., Schuoth, F. *Angew. Chem. Int. Ed*. **2006**, *45*, 8224.

35. (a) Chen, J.; Saeki, F.; Wiley, B.; Cang, H.; Cobb, M. J.; Li, Z.; Au, L.; Zhang, H.; Kimmey, M.J.; Li, X.; Xia, Y. *Nano Lett.* **2005**, *5*, 473. (b) Ntziachristos, V.; Bremer, C.; Weissleder, R. *Eur. Radiol.* **2003**, *13*, 195-208.

36. (a) Sham, J. O. H.; Zhang, Y.; Finlay, W.H.; Roa, W.H.; Loobenberg, R.; *Intl. J. Pharmaceu.* **2004**, *269*, 457. (b) Hadinoto. K.; Phanapavudhikul, P.; Kewu, Z.; Tan, B. H. *Ind. Eng. Chem. Res.* **2006,** *45,*3697.

37. (a) Mandal, S.; Phadtare, S.; Sastry, M. *Curr. Appl. Phys*. **2005**, *5*, 118. (b) Phadtare, S.; Shah, S.; Prabhune, A.; Wadgaonkar, P.P.; Sastry, M. *Biotech. Prog.* **2004**, *20*, 1817. (c) Phadtare, S.; Vinod, V. P.; Wadgaonkar, P. P.; Rao, M.; Sastry, M. *Langmuir* **2004**, *20*, 3717.

38. (a) Lee, K. B.; Kim, E. Y.; Mirkin, C. A.; Wolinsky, S. M. *Nano Lett.* **2006**, *4*, 1869. (b) Nam, J. M.; Thaxton, C. S.; Mirkin, C. A. *Science* **2003**, 301, 1884. (c) Kim Thanh, N. T.; Rosenzweig, Z. *Anal. Chem*. **2002**, *74*, 1624.

39. (a) Radt, B.; Smith, T. A.; Caruso, F. *Adv. Mater.***2004**, *16*, 2184. (b) Otsuka, H.; Nagasaki, Y.; Kataoka, K. *Adv. Drug Del. Rev*. **2003**, *55*, 403.

40. (a) Taton, T. A.; Mirkin, C. A.; Letsinger, R. L. *Science* **2000**, *289*, 1757. (b) Makarova, O.V.; Ostafin, A.E.; Miyoshi, H.; Norris Jr., J. R.; Meisel, D. *J. Phys. Chem. B* **1999**, *103*, 9080.

41. (a) Driskell, J. D.; Kwarta, K. M.; Lipert, R. J.; Porter, M. D.; Neill, J. D.; Ridpath, J. F. *Anal. Chem.* **2005**, *77*, 6147. (b) Sokolov, K.; Follen, M.; Aaron, J.; Pavlova, I.; Malpica, A.; Lotan, R.; Richards-Kortum, R. *Cancer Res*. **2003**, *63*, 1999. (c) Cognet, L.; Tardin, C.; Boyer, D.; Choquett, D.; Tamarat, P.; Lounis, B. *Proc. Natl. Acad. Sci*. *USA* **2003**, *100*, 11350.

42. (a) McConnell, W. P.; Novak, J. P.; Brousseau, L. C., III; Fuierer, R. R.; Tenent, R. C.; Feldheim, D. L. *J. Phys. Chem. B* **2000**, *104*, 8925. (b) Kreibig, U.; Vollmer, M. *Optical Properties of Metal Clusters* Springer: New York, **1995** and references therein. (3) Faraday, M. *Philos. Trans. R. Soc. London* **1857**, *147*, 145.

43. (a) Shukla, R.; Bansal, V.; Chaudhary, M.; Basu, A.; Bhonde, R. R.; Sastry, M. *Langmuir*, **2005**, *21*, 10644. (b) Connor, E. E.; Mwamuka, J.; Gole, A.; Murphy, C. J.; Wyatt, M. D. *Small* **2005**, *1*, 325.

44. (a) Riboh, J. C.; Haes, A. J.; McFarland, A. D.; Yonzon, C. R.; Van Duyne, R. P. *J. Phys. Chem. B* **2003**, *107*, 1772. (b) Shafer-Peltier, K. E.; Haynes, C. L.; Glucksberg, M. R.; Van Duyne, R. P. *J. Am. Chem. Soc*. **2003**, *125*, 588.

45. Rosi, N. L.; Mirkin, C. A. *Chem. Rev.* **2005**, *105*, 1547.

46. (a) Yelin, D.; Oron, D.; Thiberge, S.; Moses, E.; Silberberg, Y. *Optics Express*, **2003**, *11*, 1385. (b) Wang, Y. *et al*., *Nano Lett.* **2005**, *4*, 1689. (c) Sokolov, K. *et al*., *Cancer Res.* **2003**, *63*, 1999. (d) El-Sayed, I. H.; Huang, X.;

El-Sayed, M. A. *Nano Lett.* **2005**, *5*, 829. (e) Grainger, R.G. *Brit. J. Rad.* **1882**, *55*, 1.

47. Bugaj, J. E.; Achilefu, S.; Dorshow, R. B.; Rajagopalan, R. *J. Biomed. Opt.* **2001**, *6*, 122.

48. Bruchez Jr., M.; Moronne, M.; Gin, P.; Weiss, S., Alivisatos, A. P. *Science*, **1998**, *281*, 2013. (b) Chan, W. C. W.; Nie, S. *Science*, **1998**, *281*, 2016. (c) Voura, E. B.; Jaiswal, J. K.; Mattoussi, H.; Simon, S. M. *Nature Med.* **2004**, *10*, 993.

49. (a) Lovrić, J. *et al*., *J. Mol. Med.* **2005**, *83*, 377. (b) Hoshino, A. *et al., Nano Lett.* **2005**, *4*, 2163. (c) Shiohara, A.; Hoshino, A.; Hanaki, K. I.; Suzuki, K.; Yamamoto, K. *Microbiol. Immunol.* **2004**, *48*, 669.

50. Landsman, M. L. J.; Kwant, G.; Mook, G. A.; Zijlstra, W. G. *J. Appl. Phys.* **1976**, *40*, 575.

51. Jain, P. K.; Lee, K. S.; El-Sayed, I. H.; El-Sayed, M. A. *J. Phys. Chem. B* **2006**, *110*, 7238.

52. (a) Chen, J.; Saeki, F.; Wiley, B.; Cang, H.; Cobb, M. J.; Li, Z.; Au, L.; Zhang, H.; Kimmey, M.J.; Li, X.; Xia, Y. *Nano Lett.* **2005**, *5*, 473. (b) Loo, C. *et al.*, *Technol. Cancer Res. Treat.* **2004**, *3*, 33.

53. Boyer, D.; Tamarat, P.; Cognet, L.; Orrit, M.; Lounis, B. *Procd. SPIE Intl. Soc. Opt. Engg.* **2003**, *121*, 4962.

54. Weissleder, R. *Nature biotechnol.* **2001**, *19*, 316.

55. Hirsch, L.R. *et al., Proc. Natl. Acad. Sci. USA* **2003**, *100*, 13549.

56. Loo, C.; Lowery, A.; Halas, N. J.; West, J.; Drezek, R. *Nano Lett.* **2005**, *5*, 709.

57. Huang, X., Jain, P. K.; El-Sayed, I. H.; El-Sayed, M. A. *Photochem. Photobiol*. **2006** (In press). (b) Huang, X., El-Sayed, I. H.; Qian, W.; El-Sayed, M. A. (2006) *J. Am. Chem. Soc*. **2006**, *128*, 2115.

58. Jones, K. H.; Senft, J. A. *J. Histochem. Cytochem.* **1985**, *33*, 77.

59. Patil, V.; Malvankar, R. B.; Sastry, M. *Langmuir*, **1999**, *15*, 8197.

60. Flanigan, R. C.; Pavlik, E. J.; Van Nagell, Jr.; Keaton, K.; Kenady, D. E. *J. Urol.* **1986**, *135*, 1091.

61. Xu, Q.; Mao, C.; Liu, N. N.; Zhu, J. J.; Sheng, J. *Biosens. Bioelectron.* **2006**, *22*, 768.

62. Burtis, C. A.; Ashwood, E. R. *Tietz Textbook of Clinical Chemistry, 3rd ed.* Philadelphia: W. B. Saunders Company, **1999**, 689.

63. Lundqvist, M.; Sethson, I.; Jonsson, B. H. *Biochem.* **2005**, *44*, 10093.

64. (a) Verma, A.; Simard, J. M.; Rotello, V. M. *Langmuir* **2004**, *20*, 4178. (b) Aubin-Tam, M. E.; Hamad-Schifferli, K. *Langmuir* **2005**, *21*, 12080.

65. (a) Tang, D. P. *et al*., *Anal. Biochem.* **2004**, *333*, 345. (b) Liu, J.; Lu, Y. *J. Am. Chem. Soc.* **2004**, *126*, 12298. (c) Zhang, J.; Oyama, M. *J. Electroanal. Chem.* **2005**, *577*, 273.

66. (a) Brunner, T. J. *et al., Environ. Sci. Technol.* **2006**, *40*, 4374. (b) Gurr, J. R.; Wang, A. S. S.; Chen, C. H.; Jan, K. Y. *Toxicol.* **2005**, *213*, 66.

67. (a) Shvedova, A. A. *et al.,* J. Toxicol. Environ. Health **2003**, *66*, 1909. (b) Jia, G. *et al., Environ. Sci. Technol.* **2005**, *39*, 1378. (c) Wörle-Knirsch, J. M.; Pulskamp, K.; Krug, H. F. *Nano Lett*. **2006**, *6*, 1261.

68. (a) Goodman, C. M.; McCusker, C. D.; Yilmaz, T.; Rotello, V. M. *Bioconjug. Chem.* **2004**, *15*, 897. (b) Connor, E. E.; Mwamuka, J.; Gole, A.; Murphy, C. J.; Wyatt, M. D. *Small* **2005**, *1*, 325. (c) Bhattacharya, R.; Mukherjee, P.; Xiong, Z.; Atala, A.; Soker, S.; Mukhopadhyay, D. *Nano Lett.* **2004**, *4*, 2479. (d) Tsoli, M.; Kuhn, H.; Brandau, W.; Esche, H.; Schmid, G. *Small* **2005**, *1*, 841.

69. (a) Grootveld, M.; Blake, D. R.; Sahinoglu, T.; Claxson, A. W.; Mapp, P.; Stevens, C.; Allen, R. E.; Furst, A. *Free Radical Res. Commun.* **1990**, *10*, 199. (b) Gleichmann, E.; Kubicka-Muranyi, M.; Kind, P.; Goldermann, R.; Goerz, G.; Merk, H.; Rau R. *Rheumatol. Int.* **1991**, *11*, 219. (c) Griem, P.; Gleichmann, E. Z. *Rheumatol*. **1996**, *55*, 348.

70. (a) Mirabelli, C. K.; Johnson, R. K.; Sung, C. M.; Faucette, L. F.; Muirhead, K.; Crooke, S. T. *Cancer Res.* **1985**, *45*, 32. (b) Cossu, R.; Matovic, Z.; Radanovic, C.; Ponticelli, G. *Farmaco* **1994**, *49*, 301. (c) Svensson, A.; Moller, H.; Bjorkner, B.; Bruze, M.; Leden, I.; Theander, J.; Ohlsson, K.; Linder, C. *BMC Dermatol*. **2002**, *2*, 2.

71. (a) Alt, V. *et al*., *Biomaterials* **2005**, *25*, 4383. (b) Lok, C. N. *et al*., *J. Prot. Res.* **2006**, *5*, 916. (c) Panácöek, A. *et al*., *J. Phy. Chem. B* **2006**, *110*, 16248. (d) Wagener, M. *Surf. Coat. Intl. Part A: Coatings J.* **2005**, *88*, 355.

72. (a) Kreuter, J. *J. Cont. Rel.* **1991**, *16*, 169. (b) Cavallaro, G.; Fresta, M.; Giammona, G.; Puglisi, G.; Villari, A. *Intl. J. Pharma.* **1994**, *111*, 31. (c) Kyriacou, S. V.; Brownlow, W. J.; Xu, X. H. N. *Biochemistry* **2004**, *43*, 140. (d) Lecaroz, C.; Gamazo, C.; Blanco-Prieto, M. J. *J. Nanosci. Nanotechnol.* **2006**, *6*, 3296.

73. (a) Fang, C.; Shi, B.; Pei, Y. Y.; Hong, M. H.; Wu, J.; Chen, H. Z. *Euro. J. Pharma. Sci.* **2006**, *27*, 27. (b) Sun, X. *et al*., *Biomacromol.* **2006**, *6*, 2541. (c) Veiseh, O. *et al*., *Nano Lett.* **2005**, *5*, 1003.

74. (a) You, C. C.; De, M.; Han, G.; Rotello, V. M. *J. Am. Chem. Soc.* **2005**, *127*, 12873. (b) Won, J. *et al*., *Science* **2005**, *309*, 121. (c) Abad, J. M.; Mertens, S. F. L.; Pita, M.; Fernández, V. M.; Schiffrin, D. J. *J. Am. Chem. Soc.* **2005**, *127*, 5689. (d) Eguchi, A. *et al*., *J. Cont. Rel.* **2005**, *104*, 507.

75. Cho, K. H.; Park, J. E.; Osaka, T.; Park, S. G. *Electrochim. Acta* **2005**, *51*, 956. (b) Strohal, R.; Schelling, M.; Takacs, M.; Jurecka, W.; Gruber, U.; Offner, F. *J. Hospt. Infect.* **2005**, *60*, 226. (c) Silver, S.; Phung, L. T. *J. Ind. Microbiol. Biotechnol.* **2005**, *32*, 587. (d) Furno, F. *J. Antimicrob. Chemo.* **2004**, *54*, 1019.

76. (a) Oh, E. *et al., J. Am. Chem. Soc.* **2005**, *127*, 3270. (b) Willard, D. M.; Carillo, L. L.; Jung, J.; Van Orden, A. *Nano Lett*. **2001**, *1*, 469. (c) Dubertret, B.; Calame, M.; Libchaber, A. J. *Nature Biotechnol*. **2001**, *29*, 365. (d) Maxwell, D. J.; Taylor, J. R.; Nie, S. *J. Am. Chem. Soc*. **2002**, *124*, 9606. (e) Oh, E. *et al., Angew. Chem. Int. Ed*. **2006**, *45*, 7959.

77. (a) Dulkeith, E. *et al*., *Phys. Rev. Lett.* **2002**, *89*, 203002-1. (b) Bizzarri, A. R.; Cannistraro, S. *J. Phys. Chem. B* **2006**, *110*, 16491. (c) Gueroui, Z.; Libchaber, A. *Phys. Rev. Lett*. **2004**, *93*, 166108-1.

78. (a) Andreussi, O.; Corni, S.; Mennucci, B. Tomasi, J. *J. Chem. Phys.* **2004**, *121*, 10190. (b) Anger, P.; Bharadwaj, P.; Novotny, L. *Phys. Rev. Lett.* **2006**, *96***,** 113002.

79. Makarova, O. V.; Ostafin, A. E.; Miyoshi, H.; Norris, Jr. J. R. *J. Phys. Chem. B* **1999**, *103*, 9080.

80. (a) Whitmore, P. M.; Robota, H. J.; Harris, C. B. *J. Chem. Phys.* **1982**, *77*, 1560. (b) Waldeck, D. H.; Alivisatos, A. P.; Harris, C. B. *Surf. Sci.* **1985**, *158*, 103.

81. (a) Zhang, J.; Malicka, J.; Gryczynski, I.; Lakowicz, J. R. *J. Phys. Chem. B* **2005**, *109,* 7643. (b) Lakowicz., J. R. *Anal. Biochem*. **2005**, *337*, 171. (c) Lakowicz, J. R. *Anal. Biochem*. **2001**, *298*, 1. (d) Gryczynski, I.; Malicka, J.; Shen, Y. B.; Gryczynski, Z.; Lakowicz, J. R. *J. Phys. Chem. B* **2002**, *106*, 2191. (e) Malicka, J.; Gryczynski, I.; Fang, J.; Kusba, J.; Lakowicz, J. R. *Anal. Biochem*. **2003**, *315*, 160. (f) Gersten, J. I.; Nitzan, A. *Surf. Sci.* **1985**, *158*, 165.

82. (a) Kamat P. V. *J. Phys. Chem. B* **2002**, *106*, 7729. (b) Kulakovich, O.; Strekal, N.; Yaroshevich, A.; Maskevich, S.; Gaponenko, S.; Nabiev, I.; Woggon, U.; Artemyev, M. *Nano Lett.* **2002**, *2*, 1449. (c) Geddes, C. D.; Cao, H.; Gryczynski, I.; Gryczynski, Z.; Fang, J. Y.; Lakowicz, J. R. *J. Phys. Chem. A* **2003**, *107*, 3443

83. (a) Kreibig, U.; Vollmer, M. *Optical Properties of Metal Clusters*; Springer-Verlag: Berlin and Heidelberg, Germany, **1995**. (b) Kerker, M.; Blatchford, C. G. *Phys. Rev. B* **1982**, *26*, 4082. (c) Zhang, J.; Whitesell, J. K.; Fox, M. A. *J. Phys. Chem. B* **2003**, *107*, 605.

84. (a) Tkachenko, A. G. *J. Am. Chem. Soc.* **2003**, *125*, 4700. (b) De La Fuente, J. M.; Berry, C. C. *Bioconjug. Chem.* **2005**, *16*, 1176.

Chapter VI

Conclusions

This chapter describes the salient features of the thesis and briefly discusses the future scope of the work presented in the thesis.

6.1 Summary of the work

Nanotechnology research has come a long way in terms of developing applications for the improvement of the existing technologies. There is an ever-increasing need to develop new materials to cope with the growing challenges and opportunities presented by the availability of more sophisticated techniques. This thesis emphasizes upon developing novel strategies for the assembly of nanoparticles as well as developing new materials with enhanced functionalities. The thesis also explores the potential of these nanoparticles for novel biological applications.

The first part of the thesis investigates the role of nucleobases, which are the building blocks of deoxy ribose nucleic acid (DNA) in the assembly of nanoparticles. DNA based nanoparticle assemblies have gained tremendous importance over the last decade. The programmability, specificity, reproducibility and flexibility provided by DNA molecule have been prime reasons for its choice as a nano-scale template. Most of the existing strategies pertaining to such nanoparticle assemblies are based on electrostatic interactions of pre-formed nanoparticles or their precursors with the uniformly charged sugar phosphate backbone of DNA molecules, which leads to uniform, nonspecific metallization of DNA. However, for the fabrication of molecular interconnects for the futuristic nano-devices it is often desirable to achieve more complex patterns of metallization. Such complexity can be acquired by bringing in the sequence specificity into play.

Despite the extensive literature on differential interactions of nucleobases, nucleosides and nucleotides with metal precursors and nanoparticles alike, there have been only a few attempts towards achieving sequence specific metallization of DNA. The work discussed in the thesis therefore, focuses on the study of nucleobases-metal ion interactions. Using an extremely sensitive isothermal titration calorimetry (ITC) analysis it has been showed that the heat of interaction of silver ions with nucleobases differ significantly, the overall order of strength being $C > G > A \geq T$. These studies are then extended to short single strand oligonucleotides, C24 and T24 having similar length and charge density of sugar phosphate backbone but dissimilar base composition. The ITC analysis reveals that the former has significantly higher exothermicity than the latter, in accordance with the results obtained for the

nucleobases and suggests that silver ions indeed prefer binding to the nucleobases over the sugar-phosphate backbone as indicated by the differences in the heat of interaction values. This is in agreement with the previous studies that have categorized silver ions amongst the cations with higher affinity towards nucleobases over the sugar phosphate backbones.

These results suggest a new approach to generate patterned metallic nanowires based on the sequence of DNA molecule. To realize this, synthetic DNA sequences **C_{30}-T_{40}-C_{30}** and **C_{20}-T_{20}-C_{20}-T_{20}-C_{20}** were metallized with silver using tyrosine-mediated reduction of silver ions in alkaline conditions. The position of cytosine and thymine determines the sites along the length of the DNA where metallization takes place as cytosine binds silver ions strongly whereas thymine rich zones do not. Thus, in the first case, TEM analysis reveals formation of silver nanoparticle 'doublets' at the C_{30} regions separated by a distance consistent with the length of T_{30} regions. With the second oligonucleotide, 'triplets' of silver nanoparticles are observed at positions corresponding to three C_{20} regions separated with two intermittent regions corresponding to T_{20} segments.

The thesis also illustrates a new process for the fabrication of porous metallic nanostructures, which have added advantages of low density and higher specific surface area besides the properties exhibited by the bimetallic nanoparticles. The method employs a galvanic replacement process between sacrificial silver nanoparticles and metallic ions with higher redox potential, across a semi-permeable dialysis membrane. The controlled rate of ionic diffusion across the membrane leads to control over the reaction kinetics thereby facilitating observation of the various phases of the transmetalation process leading to the porous nanostructures. The slow process also gives a control over the bimetal composition as well as the size of cavities within the porous nanoparticles. Using this method porous gold, porous platinum and porous palladium nanoparticles have been synthesized and it has been illustrated that the formation of cavities takes place preferentially at the twin boundaries on the surface of silver nanoparticles. We have also demonstrated that the rate of reaction and the particle size can be tuned by varying concentrations of precursors and permeability of the dialysis membrane.

Similarly, anisotropic porous metal nanoparticles *viz.* porous nanowires and porous nanotriangles of gold and palladium have been fabricated by employing the respective anisotropic templates of silver.

The thesis also illustrates biological applications of the porous gold nanoparticles synthesized using the transmetalation process. The enhanced surface area of the porous gold nanoparticles over conventional solid gold nanoparticles has been demonstrated by the increased fluorescence associated with the porous gold-propidium iodide (PI) conjugate over that of solid gold-PI conjugate using fluorescence spectroscopy, fluorescent microscopy and fluorescence activated cell sorting analysis. Moreover, it has also been demonstrated that the PI conjugated with porous gold nanoparticles is able to stain live mammalian cells (CHO cells), which otherwise exclude pure PI and solid gold nanoparticles bound PI. This ability of porous gold nanoparticles to facilitate PI uptake in live cells has been attributed to the cavities within the metallic nanostructures, which avert the detection of PI molecules by the cell membrane.

The enhanced surface area of the porous gold nanoparticles is also evident from the increased loading of amylase over the conventional gold nanoparticles. The cytotoxicity issues pertaining to the biological applications of the porous gold nanoparticles have also been addressed and it has been shown that these nanoparticles are reasonably biocompatible to mammalian cell lines upto a concentration of 50 μM for 48 h incubation periods. It was also found that the porous nanoparticles do not exhibit any significant bactericidal effects on normal microbial flora of body such as *E. coli*.

6.2 Scope for future work

The work presented in the thesis has huge potential for future applications. The study of the interactions of the nucleobases with various metal nanoparticles and ions could pave the way for sequence dependent metallization of the DNA molecule. There is extensive literature on the ability of metallic ions to interact differentially with the sugar phosphate backbone and the bases, which could be exploited to acquire site specific metallization of the DNA molecules resulting in molecular wires with more complex composition and properties.

Porous gold nanoparticles have huge potential in biological research as a carrier of ligands, drugs and fluorophores. The ability of the porous structures to conceal these ligands within could be used for targeted therapies against intracellular parasites like *Plasmodium* spp. and pathogens such as *Mycobacterium* spp. The near infra red (NIR) absorption along with enhanced surface area and pores make them attractive candidates for a combined chemo-hypothermal cancer therapy, where anticancer chemotherapeutic agents such as doxorubicine could be loaded on the porous gold nanostructures and released using laser mediated heat treatment. Porous nanoparticles are also promising in the improvement of current sensing and diagnostic techniques based on solid gold nanoparticles due to the enhanced surface area and unique optical properties. At a more basic level, optical properties of fluorophore confined within the cavities could be studied to understand the enhancement and dampening effects of the metal surfaces.

Biocompatibility of the nanoparticles is an important issue that needs to be addressed prior to their application in biological research. Although, the thesis has demonstrated preliminary results regarding the same, a more detailed analysis needs to be performed, including the mechanism of nanoparticles uptake in the animal cells, and the long term effects of their accumulation inside the living systems.

Porous platinum and porous palladium nanoparticles are promising candidates for improved catalysis and applications such as hydrogen storage in the fuel cell technology as well as sensing applications for hydrogen and other gases. They not just offer enhanced specific surface area for such applications but also promise economical feasibility to processes involving costly metal catalysts such as platinum and palladium due to their lower density. Their catalytic ability could also be used to improve the current nanoparticle-based pollution control filters and membranes.

List of Publications

1. Gaurishankar, A.; **Shukla, S**.; Pasricha, R.; Ganesh, K. N.; Sastry, M. DNA and PNA as Templates for Building Nano-assemblies via Electrostatic Complexation with Gold Nanoparticles. ***Current Applied Physics***, 2, 105, **2004**.

2. Gaurishankar, A.; **Shukla, S**.; Ganesh, K. N.; Sastry, M. Isothermal Titration Calorimetry Studies on the Binding of DNA Bases and PNA Base Monomers to Gold Nanoparticles. ***Journal of American Chemical Society***, 126, 13186, **2004**.

3. **Shukla, S**.; Priscilla, A.; Banerjee, M.; Bhonde, R. R.; Ghatak, J.; Satyam, P. V.; Sastry, M. Porous Gold Nanospheres by Controlled Transmetallation Reaction: A Novel Material for Application in Cell Imaging. ***Chemistry of Materials,*** 17, 5000, **2005**.

4. **Shukla, S**.; Sastry, M. An Isothermal Titration Calorimetry Analysis into Differential Affinities of DNA Nucleobases for Ag (I) ions: Towards Sequence Dependent DNA Metallization. ***Journal of American Chemical Society*** (communicated), **2007**.

5. **Shukla, S**.; Pasricha, R.; Sastry, M. Hollow/Porous Anisotropic Metal Nanostructures Through Controlled Transmetallation Across a Dialysis Membrane. ***Small*** (communicated), **2007.**